Nuclear forces at the extremes

Aldric Revel

Normandie Université

THÈSE

Pour obtenir le diplôme de doctorat

Spécialité PHYSIQUE

Préparée au sein de l'Université de Caen Normandie

Les forces nucléaires à l'extreme

Présentée et soutenue par
Aldric REVEL

Thèse soutenue publiquement le 27/09/2018 devant le jury composé de		
Mme SANDRINE COURTIN	Professeur des universités, Institut Hubert Curien	Rapporteur du jury
M. JEROME GIOVINAZZO	Directeur de recherche au CNRS, Centre d'Etudes Nucléaires de Bordeaux	Rapporteur du jury
Mme FRANCESCA GULMINELLI	Professeur des universités, UNIVERSITE CAEN NORMANDIE	Président du jury
M. ELIAS KHAN	Professeur des universités, INSTITUT DE PHYSIQUE NUCLEAIRE D'ORSAY	Membre du jury
M. ALEXANDRE OBERTELLI	Chargé de recherche HDR, GSI Darmstadt - Allemagne	Membre du jury
M. OLIVIER SORLIN	Directeur de recherche au CNRS, 14 GANIL de CAEN	Directeur de thèse
M. MIGUEL MARQUES	Chargé de recherche au CNRS, UNIVERSITE CAEN NORMANDIE	Co-directeur de thèse

Thèse dirigée par OLIVIER SORLIN et MIGUEL MARQUES, Grand accélérateur national d'ions lourds (Caen)

UNIVERSITÉ CAEN NORMANDIE

ED 591 PSIME

GANIL laboratoire commun CEA/DRF spiral2 CNRS/IN2P3

Acknowledgment

First, I would like to acknowledge all the people working in GANIL and LPC for welcoming me in their laboratory for a little more than three years. And I would like to thank especially my group leaders, Abdou and Nigel.

I would also like to acknowledge my two supervisors, Olivier and Miguel, for all their support and advice during those three years and half working together. I would also like to thank them especially for giving me the opportunity to present my work in several conferences around the world.

During those three years of PhD, I have been working within the R3B and SAMURAI international collaborations. I would therefore like to thank all the members of those collaborations and more especially Nakamura-san, Kondo-san, Yasuda-san for their support in the analysis of the RIKEN data and for welcoming me at TiTech for two weeks, and also Christoph and Thomas for the their support in the analysis of the GSI data.

I also want to thank all my fellow PhD and Post-doc colleagues for all the coffee breaks and also for all the drinks shared when it was more than needed. I give my best wishes to the PhD that will finish in the coming years and more specifically to Armel, Belen, Blaise, Louis, Quentin, Simon and Valerian.

I also would like to say thank you to my family for supporting me for 26 years and especially to my parents, Thierry and Catherine, and my brothers, Adrien and Guillaume. I also thank Amelia, for being there every step of the way and for supporting me everyday.

Finally, I would like to acknowledge all the people I met and worked with during my PhD. It has been a pleasure and I am sure we will cross paths again in the near future.

Contents

List of Figures

List of Tables

Chapter 1

Introduction

Contents

Nuclear physics is not a new science. However, after almost one century of research, the atomic nucleus is still not fully understood and new unexpected properties are emerging frequently. Trying to understand the structure and the evolution of the nucleus depending on its constituents is one of the fundamental goals of nuclear physics. Nevertheless, describing the interaction between nucleons is extremely hard to achieve, even for light nuclei where the number of nucleons is small.

Historically, fundamental properties of the nucleus have been investigated by reducing the N-body problem to independent nucleons located in a mean field built in an auto-coherent way. This approach allowed to explain several phenomena observed experimentally such as the magic numbers associated to certain configurations of nucleons particularly stable, and lead to the shell model of the nucleus.

However, even if the stable nuclei are the most abundant on earth, their diversity (nearly 300) represents only a small fraction of the existing nuclei (see Fig. 1.1). Today, nearly 3000 nuclei have been observed experimentally and it is expected that the same amount still remains to be observed. Those nuclei have a limited lifetime after which they decay mainly via β decay. For a given Z number, the more (or the less) neutrons we count away from the equilibrium

value, and the less stable the nucleus becomes, until reaching a threshold where even in its ground state the nucleus is not bound anymore and decays in a very short time by emitting nucleons. This limit is called neutron dripline (or proton dripline, respectively) and the nuclei around this region usually exhibit very different behavior compared to the stable nuclei.

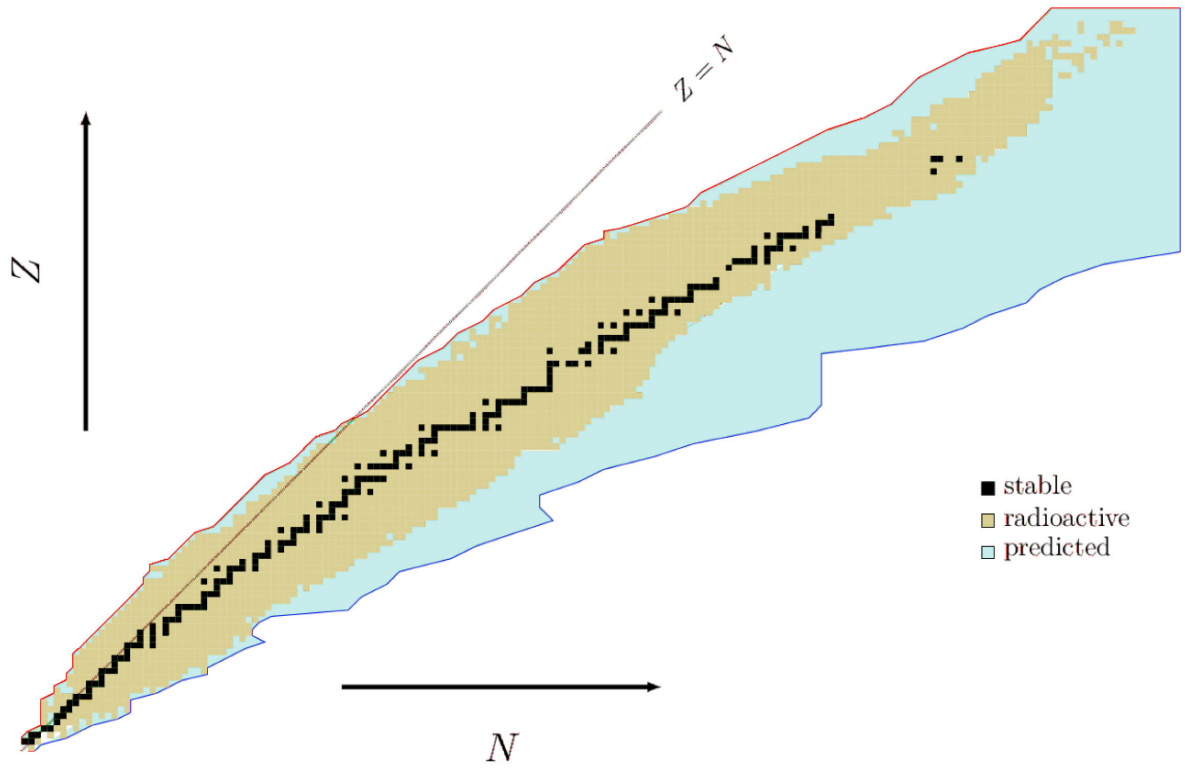

Figure 1.1: *Chart of the nuclides representing with black squares stable nuclei, light yellow neutron-rich or neutron-deficient nuclei already produced in terrestrial laboratories, and in light blue nuclei not studied yet. The limits of proton and neutron particle stability (or driplines), predicted by theoretical models, are shown with red and blue lines, respectively.*

One of the major research goals of modern nuclear physics is to explore those regions where the neutron to proton imbalance is reaching extreme values in order to determine the exact position of the dripline. Studying the properties of the nuclei in those regions gives us information on the evolution of their structure while approaching (sometimes even crossing) the limits of existence. The results obtained can then be compared to existing theoretical models and if needed, used to correct or justify the development of new models. A single look at Fig.1.1 shows the huge work that still needs to be done, in particular around the neutron dripline. Indeed, the neutron dripline has been reached experimentally only for nuclei with a proton number Z lower than ten.

In this document, we will be investigating the nucleon-nucleon interaction toward the neutron dripline. In practice, the dripline can be reached by changing the proton to neutron ratio but also by increasing the excitation energy of a nucleus beyond the nucleon(s) emission thresholds. This work can be divided in two studies: the n-n interaction in the core+xn systems and the evolution of the p-n interaction in the Fluorine isotopic chain. Indeed, we will start by exploring the n-n interaction in nuclei for very high energy unbound states of ^{18}C

and ^{20}O (that can be seen as ^{14}C+4n and ^{16}O+4n, respectively). And we will then study the evolution of the p-n interaction in the Fluorine isotopic chain by comparing results from ^{26}F and ^{28}F, the latter being an unbound system. All the nuclei, be there bound or unbound, are studied using knockout reactions, meaning that a nucleon is removed from a nucleus in order to populate the system of interest.

This document is divided in five chapters. In the first one, we will present the particularities of the study of nuclei at the neutron dripline as well as the motivations of such studies. We will then describe the different techniques and observables used in order to explore unbound states. In a third chapter, we are presenting the experimental principle and setups used during this work in order to populate the nuclei of interest as well as the simulations used to understand and interpret the data. In the fourth chapter, we are presenting our results and interpretation on the n-n pairing in unbound states of ^{18}C and ^{20}O. And finally, in the last chapter, we are presenting our results and interpretation on the evolution of the p-n interaction in the Fluorine isotopic chain between ^{26}F and ^{28}F.

1.1 Toward the neutron dripline

1.1.1 General properties of nuclei

In this section, we are focusing on the description of the lightest nuclei $Z \leq 10$. Since we will be investigating those nuclei, we start by describing the characteristics of stable nuclei before comparing them to those of neutron-rich ones.

Despite a limited number of isotopes for each chemical element, light nuclei can be very different from each other. Stable nuclei have the following characteristics:

- The N/Z ratio between their number of neutrons and protons varies slightly varying around 1.
- The binding energy between the nucleons is similar for all the nuclei and is around 8 MeV/nucleon. The separation energies for one proton (S_p) or one neutron (S_n) are also very similar.
- Their radius can be described by the empirical formula $R = r_0 A^{1/3}$ [10], where r_0 is the effective radius of a nucleon ($r_0 \approx$1.2 fm) and A is the total number of nucleons. Such description assumes an homogeneous distribution of the nucleons in the nucleus (independently of their nature).
- The presence of several bound excited states. Those states, whose excitation energies vary from one isotope to the other, usually decay by the emission of γ-rays.

While moving away from stability those properties change rapidly and nuclei become unstable, with shorter and shorter lifetimes. If the lifetime of the nuclei close to stability is varying from a few years to a few seconds, the lifetime of the neutron rich nuclei is dropping rapidly under the second and they survive only a few milliseconds approaching the dripline. The N/Z ratio for nuclei outside the valley of stability can vary from 0.6 to 4 and their

separation energies $S_{n,p}$ vary from 40 to 0 MeV [11].

When the ratio reaches extreme values, the radial distributions of protons and neutrons can decouple massively and give raise to exotic phenomena such as the neutron halo: in those nuclei, the radial distribution of neutrons shows a tail that spreads much further than the proton one. Those nuclei can therefore be represented as a light core around which one or several neutrons are orbiting. A similar phenomenon can be observed for proton halos in the case where N/Z is very low. However, in that case this manifestation is less obvious due to the Coulomb barrier that does not allow protons to have a spatial wave function as spread as the one of neutrons.

In our study, we are interested by the light neutron-rich nuclei and in particular nuclei that have such a large excess of neutrons that are unbound (^{28}F). For a stable nucleus, the proton and neutron potentials have similar characteristics, except for the Coulomb contribution, that makes the proton potential less deep. If the number of neutrons increases, the proton potential becomes deeper due to the attractive *n-p* interaction [11]. Therefore the separation energy for the protons becomes larger while the one for the neutrons becomes smaller, its value reaching zero close to the dripline.

Moreover, bound excited states become more and more rare while moving toward the neutron dripline. The last bound isotopes of an element usually do not have any bound excited state. This is why the study of neutron-rich nuclei usually requires to do spectroscopy of unbound states.

1.1.2 Structure in nuclear physics

Nuclei, like all the subatomic particles, follow the rules of quantum mechanics. In particular, their evolution is governed by the Shrödinger equation. Considering the simple case of a particle with mass m in a potential depending only on its position, the Shrödinger equation can be written as follows [12]:

$$-\frac{\hbar^2}{2m}\Delta\psi(\vec{r},t) + V(\vec{r})\psi(\vec{r},t) = i\hbar\frac{\partial\psi(\vec{r},t)}{\partial t} \tag{1.1}$$

where $V(\vec{r})$ is the potential in which the particle is and $\psi(\vec{r},t)$ its wave function. In the case of a problem with several particles interacting with each other, the problem is more complex since the potential felt by each particle is a function of the state of all the others. This interdependence is known as the N-body problem and is encountered in numerous fields of physics. The complexity of this problem increases with the number of particles. It is possible to solve it analytically for very small number of particles but it remains unsolvable exactly in its general case. We therefore solve it numerically using different methods that have been developed. We can give as example for light nuclei the techniques called *ab initio*: NSCM (No Core Shell Model), GFMC (Green Function Monte Carlo), Coupled Cluster... However, those different techniques encounter sometimes different problems that can be conceptual or due to numerical convergence.

Another difficulty, proper to nuclear physics, adds itself to the problem: there is no analytic form for the interaction potential between two nucleons inside a same nucleus fundamentally

speaking. Quantum chromodynamics [13] is the theory that studies, in a fundamental level, the strong interaction that confines the quarks inside the nucleus. This theory allowed to treat problems up to four nucleons but shows some numerical limitations when the systems become more complex. Moreover all the models used in nuclear physics are based on effective interaction potentials.

Historically, the model that encountered a big success and allowed us to better understand nuclei is the model of independent particles. In this model, particles are considered entirely independent one from another and are sitting in a mean potential (also called mean field). In this context, we can express the wave function of the system such as the sum of the wave functions of each independent particle that composes the system. The Hamiltonian of the system can be expressed as follows:

$$\hat{H} = \sum_{i=1}^{N} \hat{T}_i + \sum_{i=1}^{N} \sum_{j>i}^{N} \hat{V}_{ij} \approx \sum_{i=1}^{N} \hat{T}_i + \hat{U}_i \tag{1.2}$$

where $\hat{H}$ is the Hamiltonian of the system, $\hat{T}_i$ is the kinetic part associated to the particle i, $\hat{V}_{ij}$ the interaction potential between particles i and j, and $\hat{U}_i$ the effective potential felt by particle i.

Considering that the potential has spherical symmetry and by adding the spin-orbit term, it is possible to show [12] that the energy levels of the system can be obtained as the sum of the energies e_{nlj} of the independent particles. Those energies e_{nlj} are obtained using the diagram presented in Fig. 1.2. Each combination of quantum numbers n, l and j characterizes what is called an orbital. The latter can contain at most $2j+1$ nucleons with the same energy, depending on the orbital. The total energy is obtained by filling the orbitals with the nucleons of the system. In this model, neutrons and protons are decoupled and are filling a similar diagram independently. To build those diagrams, we order the orbitals from the lower to the higher energy, so that an independent particle located on a higher orbital has systematically more energy than any other particle located in a lower orbital. The nucleons of the last occupied orbital are called valence nucleons, the others being sometimes called core nucleons.

In this model, the ground state of a nucleus is obtained by minimizing the total energy, i.e. by following the order of the orbitals while filling them with the nucleons of the nucleus of interest. In order to obtain the different excited states of a nucleus, one needs to modify the ground-state configuration by promoting one or several valence nucleons into higher orbitals. To distinguish the different configurations, we are using in this entire document the following notation:

$$\pi(nlj)^{N_p} \otimes \nu(nlj)^{N_n},$$

where $\pi(nlj)$ and $\nu(nlj)$ depict the valence protons and the valence neutrons, respectively and N_p and N_n how many of them are located in those orbitals. All the lower orbitals below the valence ones are supposed to be fully filled, which allows the use of a condensed notation.

There are pairing effects between nucleons of a same orbital that tend to lower their individual energy when they are paired. This effect is directly visible by looking at the nuclear chart (Fig. 1.3), and is the origin of the pattern that can be observed while following the

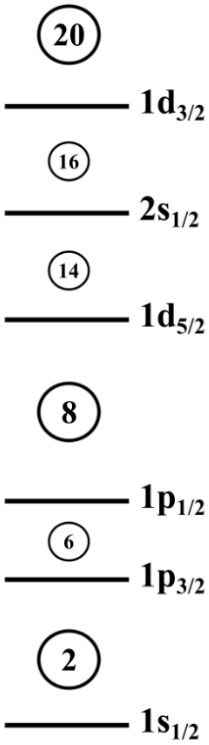

Figure 1.2: *Energy levels of a model with independent particles. Each level (also called orbital) is characterized by the quantum numbers nlj. The orbitals are classified from bottom to top by increasing energy. The numbers between orbitals correspond to the number of nucleons used if all the lower energy orbitals are filled.*

neutron dripline: some isotopes with an even number of neutrons are bound while isotopes with one neutron less are unbound.

The historical model that has been used to reproduce the nuclei from the valley of stability using the assumption of independent particles is the shell model [14]. It allows to derive in particular the so called magic numbers. Nuclei with a magic number of nucleons (2, 8, 20, 28, 50, 82, 126) show singular properties that have been observed experimentally. For example, Fig. 1.4 shows the evolution of the neutron separation energy (S_n) for nuclei with an even number of neutrons as a function of their neutron number. We observe sharp drops at each magic number (in particular for 50, 82 and 126), meaning that it is much harder to remove a neutron when the neutron number corresponds to a magic number.

In the diagram presented in Fig. 1.2, the magic numbers correspond to the number of nucleons necessary to fill entirely certain orbitals: $1s_{1/2}$, $1p_{1/2}$, $1p_{3/2}$... Those orbitals are characterized by an important separation energy compared to the orbital above, meaning that transferring a nucleon to the next orbital would cost a lot of energy.

However, this simple model shows its limits while moving away from stability. The separation energy between two orbitals and even their order can change while moving toward the neutron dripline. If we take as an example the Oxygen isotopic chain, several experimental studies [15–17] show that the numbers $N = 14$ and $N = 16$ behave like magic numbers while

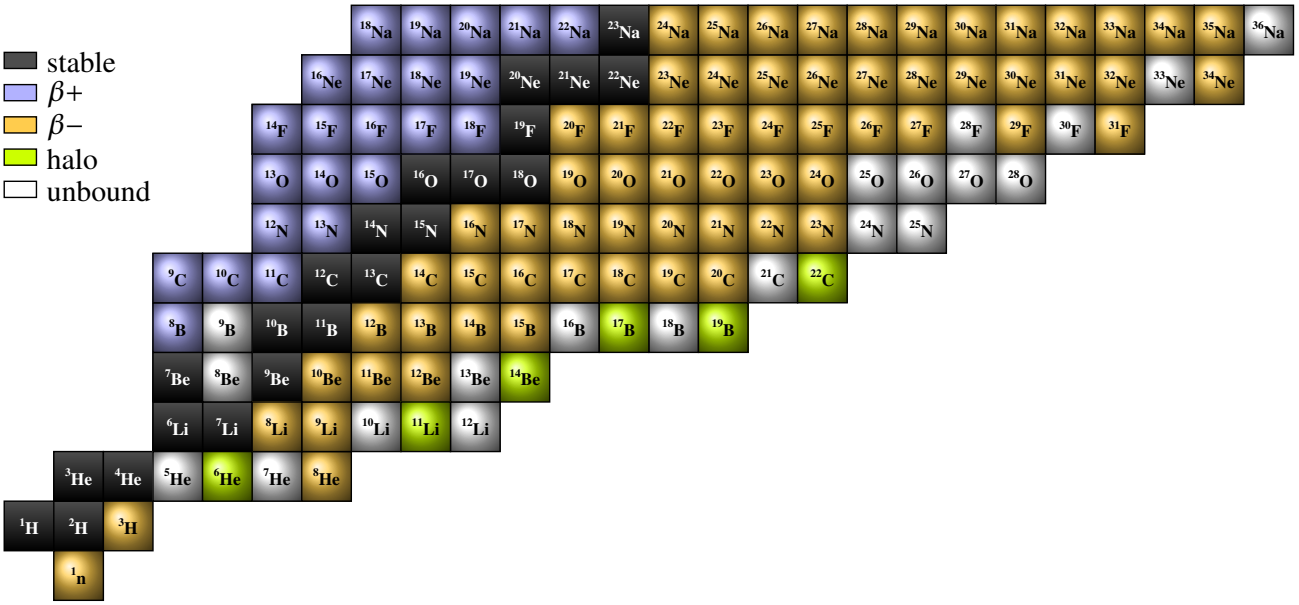

Figure 1.3: *Nuclear chart for light nuclei.*

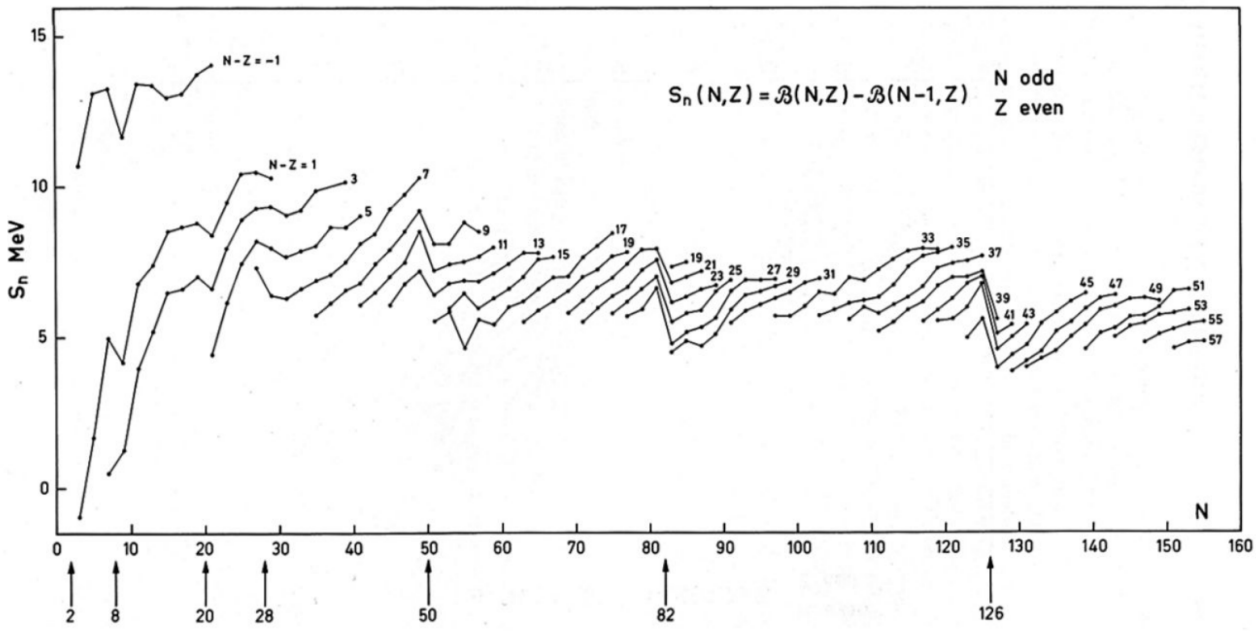

Figure 1.4: *Evolution of the neutron separation energy for nuclei with an even number of neutrons as a function of their neutron number. The arrows located below the horizontal axis correspond to the magic numbers (figure taken from [1]).*

the magic number $N = 20$ disappears [18]. Different theoretical calculations [19, 20] explain this phenomenon from the evolution of the energies of the independent particle orbitals.

1.1.3 Unbound nuclei and resonant states

Nuclei close to the dripline are weakly bound and most of the time do not have any bound excited state. It is the case for example for nuclei such as ^{6}He or ^{11}Li, that do not have any bound excited states below the two neutron emission threshold (S_{2n}). In this conditions, excited states can manifest themselves as resonances. Past the dripline, nuclei become unstable with respect to the emission of particles even in their ground state. However, in the case of unbound nuclei located close from the emission thresholds, it is possible to observe resonant states, their lifetime τ being generally associated to the width of the resonance Γ due to the Heisenberg uncertainty principle:

$$\Gamma \times \tau \sim \hbar \tag{1.3}$$

For an unstable system with respect to the emission of one neutron, the relative energy spectra of the fragment-neutron system can reveal the presence of resonant states. A well known example is the one of the unbound Helium isotopes. For example ^{7}He, which ground state has been observed as a resonance since the sixties [21]. The difficulty to observe those states is that they have very short lifetimes (of the order of 10^{-21} s). As a consequence, the measurement of the energy of those states can only be done in an indirect way, using reactions, by observing the decay products and/or other particles involved in the reaction.

If we consider only the fragment-neutron relative movement during the decay, the apparition of a resonant state depends entirely on the shape of the potential felt by the neutron. For a neutron with an angular orbital ℓ, the effective potential is given by [22]:

$$V_{eff}(r) = V_N(r) + V_\ell(r) = V_N(r) + \frac{\hbar^2 \ell(\ell+1)}{2\mu r^2} \tag{1.4}$$

where r is the fragment-neutron distance, μ the reduced mass, V_N the attractive nuclear potential created by the fragment and V_ℓ the repulsive centrifugal potential, that depends quadratically on the angular momentum. The larger is the angular momentum ℓ, the higher is the centrifugal barrier, which implies the confinement of the neutron in the potential for a longer time since the penetrability of the barrier is inversely proportional to its height [23]. As a consequence, for $\ell > 0$, we obtain resonant states which lifetime τ increases (and width decreases) with a larger ℓ. But for neutrons with angular momentum equal to zero, the contribution from the V_ℓ term disappears and there is no more centrifugal barrier (see Fig. 1.5). It is therefore impossible to observe resonant states in that case. However, if an increase of the cross-section is observed toward 0 energy, we talk of virtual states [24].

In fact, such a description is too simple, since only the relative fragment-neutron movement is taken into account and that no assumption is made on the internal structure of the fragment. Indeed, models that take into account the coupling between the different configuration of the fragment predict the existence of an $\ell = 0$ resonance [1]. However this simple vision allows us to obtain information on the structure of unbound states.

In this description, resonant and virtual states are treated like the diffusion of a neutron on the fragment. The differential cross-section in relative energy (E_{rel}) for a partial wave with an angular momentum ℓ can be expressed as follows:

$$\frac{d\sigma_\ell}{dE_{rel}} = \frac{4\pi}{k_{rel}^2}(2\ell+1)\sin^2\delta_\ell(E_{rel}) \tag{1.5}$$

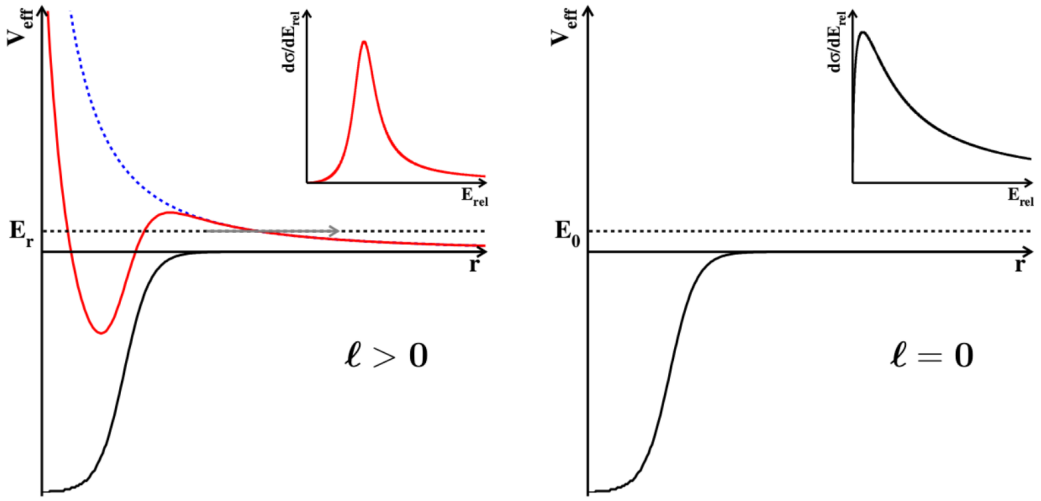

Figure 1.5: *On the left, effective potential felt by a neutron with an $\ell > 0$ angular momentum. We notice that it shows a centrifugal barrier (in dashed blue line) that can confine the neutron and induce the formation of resonant states that can be observed. On the right, case where $\ell = 0$, no centrifugal barrier is felt by the neutron. The insets on the top right of each figure represent the kind of differential cross-section in relative energy that we obtain in each case.*

where k_{rel} is the wave number linked to the fragment-neutron relative momentum and δ_ℓ is the phase of the wave ℓ induced by the potential on the neutron wave function. In the case of a resonance with $\ell > 0$, the phase will be negligible for all the partial waves except for the resonant ℓ component. The cross-section will display a maximum at an energy E_r with a width Γ. In that case, the shape of the phase in Eq. 1.5 leads to a Breit-Wigner distribution and the two parameters E_r and Γ allow to entirely characterize the unbound state.

For virtual states, at low energy, it is possible to link the phase with the scattering length a_s. This parameter gives us a measurement of the attractive potential ability to bind the system: it is positive for bound states and negative for unbound states. At very low energy ($k_{rel} \to 0$), we can do the following approximation:

$$\delta_0 \approx -a_s k_{rel} \tag{1.6}$$

In such conditions, the cross-section displays a maximum very close from the neutron emission threshold, with a tail that spreads to higher energies (see Fig. 1.5). We can link qualitatively the scattering length to the corresponding resonance energy using the following approximation [25]:

$$E_r \approx \frac{\hbar^2}{2\mu a_s^2} \tag{1.7}$$

We obtain therefore for example that a scattering length a_s =-20 fm corresponds to a resonance energy of about E_r =50 keV for A$\sim$9. However this formula can be used only in the limit case $k_{rel} \to 0$, and is used here only to give a comparison with the resonance energy.

1.2 The nucleon-nucleon interaction inside the nucleus

1.2.1 General properties of the nucleon-nucleon interaction

We present here the general properties of the nucleon-nucleon interaction in a qualitative way. The intensity of the interaction between two nucleons depends on several parameters:

- The strongest intensity for the interaction is obtained when the wave functions of the two nucleons show the larger spatial overlap. This is happening when two nucleons have the same number of nodes (characterized by the quantum number n) and the same angular orbital momentum ℓ.
- The nuclear interaction depends on the spins of the nucleons. The proton-neutron interaction, in particular, is the largest for a proton and a neutron with anti-aligned spins for $\ell \neq 0$, i.e. for $s_1 = 1/2$ and $s_2 = -1/2$. For example, the proton-neutron $\pi d_{5/2} \otimes \nu d_{3/2}$ interaction will be stronger than the $\pi d_{5/2} \otimes \nu d_{5/2}$ interaction.
- Empirically, it has been shown that the intensity of the nuclear force inside a nucleus is inversely dependent on the size of the nucleus. This dependence is a function of $A^{-1/3}$ or $A^{-2/3}$ depending whether the nucleons are located at the surface or at the center of the nucleus. We can understand it qualitatively from the fact that when the size increases, nucleons 'meet' less often, decreasing therefore their interaction which has a short range. An important consequence from this decreasing of the nuclear interaction when the size of the nucleus increases is that the modification of the nuclear structure will occur much faster in light nuclei compared to heavier ones.
- Since the nucleus is made of neutrons and protons, there are two isospin values: T=0 and T=1. However, the T=0 value can be obtained only for a proton-neutron system while the T=1 value can be obtained for proton-proton, proton-neutron or neutron-neutron system. The effective interaction will therefore be stronger for a proton-neutron system than for a system with two identical nucleons.

1.2.2 Empirical determination of the proton-neutron interaction

The proton-neutron interaction, for given orbitals, can be obtained experimentally from the structure of odd-odd nuclei (odd number of protons and odd number of neutrons). We also need to assume that the chosen nucleus can be seen as an inert core to which only one neutron and one proton are added. This method can therefore only be applied to nuclei with a core possessing a strong shell closure. Indeed in that case, the core excitations are at very high energy and their influence on the valence proton and neutron is negligible.

We can take as an example the ^{38}Cl nucleus. It can be seen as a ^{36}S doubly-magic core on top of which a proton is added in $\pi d_{3/2}$ and a neutron in $\nu f_{7/2}$. The coupling of those two nucleons gives four negative parity states with spin $J^\pi = 2^-, 3^-, 4^-, 5^-$. We will now determine their binding energy (BE) resulting from adding independently one proton and one neutron to the ^{36}S core. Adding one proton in $\pi d_{3/2}$ gives us ^{37}Cl which binding energy is known. Therefore we can determine the gain in binding energy resulting from adding a proton in $\pi d_{3/2}$ to the ^{36}S core:

$$BE(^{37}\mathrm{Cl}) - BE(^{36}\mathrm{S}) = S_p(^{37}\mathrm{Cl}) \tag{1.8}$$

In a similar way, adding one neutron in $\nu f_{7/2}$ gives us ^{37}S and the resulting binding energy gain can be expressed as follows:

$$BE(^{37}\mathrm{S}) - BE(^{36}\mathrm{S}) = S_n(^{37}\mathrm{S}) \tag{1.9}$$

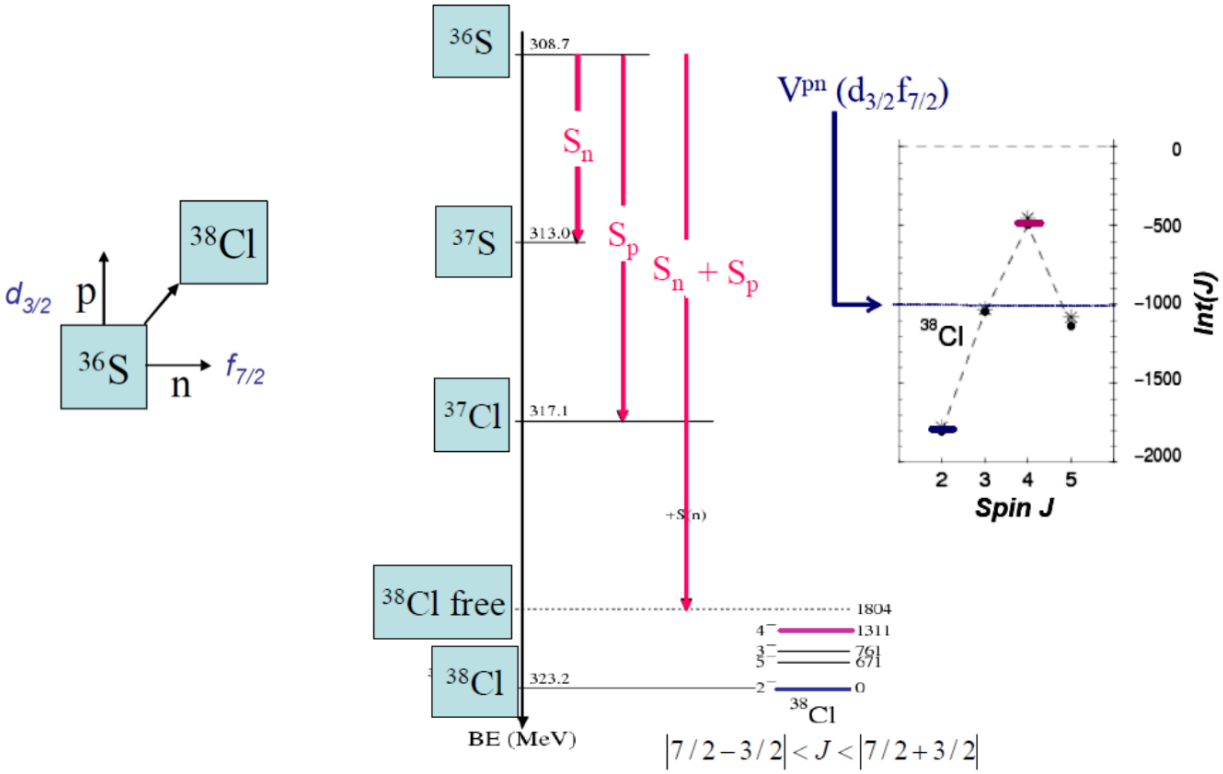

Figure 1.6: *Determination of the interaction energy $\pi d_{3/2} \otimes \nu f_{7/2}$ from the structure of ^{38}Cl extracted from [2]. Int(J) are the interaction energies defined as the difference between the reference value BE(^{38}Cl) and the real binding energy of the J spin state. The weighted average of those interaction energies $V^{pn}(d_{3/2}f_{7/2})$ is an approximation of the monopole energy.*

Finally, adding those two terms to the ^{36}S nucleus binding energy, we obtain the ^{38}Cl nucleus binding energy assuming that the neutron in $\nu f_{7/2}$ and the proton in $\pi d_{3/2}$ do not interact with each other. This can be written such as:

$$BE(^{38}\mathrm{Cl}_{free}) = BE(^{36}\mathrm{S}) + S_n(^{37}\mathrm{S}) + S_p(^{37}\mathrm{Cl}) \tag{1.10}$$

Comparing now this value to the binding energies of the four states obtained experimentally for ^{38}Cl, we obtain the interaction energy between the proton in $\pi d_{3/2}$ and the neutron in $\nu f_{7/2}$ coupled to a given spin (assuming that the gain in energy is only due to the proton and the neutron that have been added). We note those interaction energies $Int(J)$. The results for ^{38}Cl, extracted from [2], as well as an illustration of the method are presented in Fig. 1.6. We then define the weighted average V^{pn} of the interaction energies, called monopole energy. It can be expressed in the following way:

$$V^{pn} \approx \frac{\sum_j (2J+1) \times Int(J)}{\sum_j (2J+1)} \tag{1.11}$$

In the case discussed here, we have been able to determine the $V^{pn}(d_{3/2}f_{7/2})$ value that is of about -1 MeV, which is close from the value predicted by shell-model calculations (-1.19 MeV). The monopole interaction is characterizing the average change of the binding energies due to the nucleon-nucleon interaction inside the nucleus, an essential element in order to understand the evolution of the shell closures. However it is often complicated to determine it using the technique that we just presented due to several constraints. Indeed, not only the core used (A,Z) needs to have a strong shell closure, but also the nuclei ($A+1$,Z), (A,$Z+1$) and ($A+1$,$Z+1$), needed in the calculation, cannot be deformed. Otherwise we would not be dealing with single particle states and the calculation presented here would have no sense since the states for which the interaction energies are calculated would show too many correlations. And finally, the last condition is obviously knowing experimentally all the states from the multiplet involved which often requires the use of different experimental techniques.

We can also notice the parabolic shape of the interaction energy curve as a function of the spin J. This is due to the quadrupole interaction that will be discussed in the following.

1.2.3 Effective single particle energies

We determined in the previous section the intensity of the monopole interaction $V^{pn}(d_{3/2}f_{7/2})$ equal to -1 MeV. Assuming that the inert core approximation is valid, adding protons in $\pi d_{3/2}$ to a ^{36}S core will bind the neutrons in $\nu f_{7/2}$ by -1 MeV by proton added. This can be observed by looking at the effective "single particle" energies (ESPE). Those ESPE depict the mean effect of the other nucleons on a nucleon in a given orbital, meaning the variations of the binding energies induced by the monopole interaction alone. The ESPE of an occupied orbital is defined such as the energy needed to remove one of its nucleons, while the ESPE of an empty orbital corresponds to the binding energy gained while filling it with nucleons. For nuclei close to a shell closure, the ESPE will be similar to the experimental binding energies. However this is not true for nuclei that are strongly correlated or deformed. In the case discussed here, we are close from the doubly magic ^{36}S and the equivalence between ESPE and binding energy can be considered valid in a first approximation.

When adding four protons in $\pi d_{3/2}$, we expect that ESPE($\nu f_{7/2}$) will shift by the quantity $4V^{pn}(d_{3/2}f_{7/2})$, meaning -4 MeV. This value can be compared to the one obtained from the experimental binding energies of neutrons in $\nu f_{7/2}$:

- for Z=16 (0 in $\pi d_{3/2}$) and N=21 (1 in $\nu f_{7/2}$), i.e. $S_n(^{37}\mathrm{S})$=4.303 MeV
- for Z=20 (4 in $\pi d_{3/2}$) and N=21 (1 in $\nu f_{7/2}$), i.e. $S_n(^{41}\mathrm{Ca})$=8.363 MeV

Therefore:

$$S_n(^{41}Ca) - S_n(^{37}S) \approx 4 \text{ MeV} \tag{1.12}$$

We obtain then a gain of binding energy of nearly 4 MeV when adding four protons in $\pi d_{3/2}$. The two methods to determine the monopole interaction are in good agreement if the conditions described earlier are fulfilled.

1.2.4 Quadrupole interaction and nucleus deformation

On top of the monopole interaction, nuclei can gain binding energy through deformation. This gain of energy comes from the quadrupole interaction. Indeed, while filling a new orbital, the experimental binding energy is often found stronger than the ESPE deduced from the monopole interaction alone. Taking back the example of the $\nu f_{7/2}$ orbital, experimentally, the protons in $\pi d_{3/2}$ have been found more bound than predicted by the ESPE($\pi d_{3/2}$). This quadrupolar gain of energy reaches its maximum in the middle of the orbital. We confirm, as mentioned before, that in case of shell closure (here $\nu f_{7/2}$ completely empty or full) experimental proton binding energies are equal to ESPE($\pi d_{3/2}$).

For those nuclei with closed shell, nucleons occupy all the possible magnetic sub-states and therefore adopt a spherical shape. When those shell closures disappear, nucleons can move in an extended valence space and adopt more configurations, implying more than one orbital, with some that are more favorable than the one of the inert core. Nucleons from different orbitals mix and maximize their quadrupole energy, leading to deformed structures. We understand that in those cases where strong correlations exist, the determination method of the monopole interaction described earlier is not valid anymore.

1.3 The *n*-*n* interaction in core+x*n* nuclei

In the previous section, we have been mainly interested in the *p*-*n* interaction. However, pairing interactions between identical particles play a major role in nuclear physics. Therefore, we propose to discuss the *n*-*n* and *p*-*p* interactions in this section.

Pairing interactions play crucial roles in atomic nuclei and quantum many-body physics in general [26]. In finite nuclei, two-neutron and/or two-proton pairing are responsible for the odd-even staggering observed in the binding energy of atomic masses and for the fact that all even nuclei have a $J = 0^+$ ground state. Pairing correlations also imply a smoothing of the level occupancy around the Fermi energy surface, an enhancement of pair transfer probabilities (see e.g. Refs. [27, 28]), as well as a superfluid behavior in nuclear rotation [29] and vibration [30]. When moving from the interior to the surface of the neutron-rich nuclei ^{11}Li [31], ^{6}He and ^{18}C [32], a transition from BCS (Bardeen Cooper-Schrieffer) [33] to BEC (Bose-Einstein Condensation) [34] pairing has been predicted to possibly occur. On a larger nuclear-matter scale, pairing plays a major role in the modeling of the rotation, magnetization and cooling of neutron stars [35].

Recently, the formation of tetra-neutron resonances, either from an ensemble of four interacting neutrons [36] or from the coupling of four neutrons inside atomic nuclei [37] were proposed on the basis of experimental results. If confirmed, tetra-neutron excitations would require a higher range of (four-body) nucleon interactions [38], with expected important consequences in the description of finite nuclei, of nuclear matter [39] and in the determination of neutron captures in the Big Bang [40] and in neutron-star mergers. Despite of its tremendous importance, the real observation of the decay of paired or tetra nucleons is still lacking or very scarce as difficult to evidence. By generalizing the Ikeda conjecture [41], initially proposed to account for the presence of α cluster states close to α emission thresholds, such two- or

four-nucleon resonances would similarly appear at energies close to the corresponding emission thresholds [42]. The sudden promotion of nucleons beyond those thresholds, using a suitable reaction mechanism, would allow the study of such few-nucleon correlations.

Tremendous efforts have been made during the last decades to extract information on proton correlations from the decay of two-proton emitters [43–46]. In such nuclei, the Coulomb barrier traps the unbound protons during a time that is long enough to allow the detection of protons distinctly to the formation of the emitter. This emission was first described as a possible di-proton decay in the form of a ^{2}He [47], in analogy with α decay. However, after having unfolded the strong final-state interaction (FSI) component, the observed proton-proton angular distributions in ^{45}Fe [48] and ^{54}Zn [49] rather point to a three-body decay [44], in which the two protons are emitted (not necessarily paired) from a mixed filling of *pf* shells. These relatively weak proton correlations may be inferred from the fact that the studied nuclei were far from closed shells and that protons may lose their initial correlation when traversing the high Coulomb barrier while escaping the nucleus.

Other approaches were carried out by observing the decays of the unbound ^{6}Be [50], ^{12}O [51], ^{15}Ne[52], ^{16}Ne and ^{19}Mg [53]. A progressive transition from correlated to sequential two-proton decay was clearly observed in Ref. [50] as a function of the excitation energy of ^{6}Be. Sequential decay was also observed in ^{12}O. In all cases, however, the decay patterns are subject to strong Coulomb FSI between the two protons and the core, especially blurring the observation of nuclear correlations at low relative energies.

To circumvent the problems caused by the Coulomb interaction, the study of two-neutron emission was carried out in neutron-rich core+n+n systems that are unbound either in their ground state (^{10}He [54], ^{13}Li [54, 55], ^{16}Be [56] and ^{26}O [17, 57, 58]) or in excited states beyond the two-neutron threshold (^{8}He [59], ^{14}Be [7, 60] and ^{24}O [61, 62]). The decay of excited states of ^{8}He [59], ^{14}Be [7, 60] and ^{24}O [62], as well as the ground-state decay of ^{10}He [54], all show very convincing signatures of sequential decay through intermediate core-n resonances. First observations of a di-neutron decay from the ground states of ^{13}Li [55] and ^{16}Be [56] were claimed on the basis of the observed small n-n energies and angles, as compared to a three-body phase-space decay, with no interaction between the emitted neutrons. However, the need to go beyond the di-neutron simplification and to use realistic n-n FSI, in direct and/or sequential decays, has been pointed out in Ref. [63]. Indeed, the attractive nature of the n-n interaction can give rise to small relative n-n energies and angles, hereby mimicking a di-neutron decay.

An additional motivation for studying $2p$ or $2n$ decay emissions, is to find whether the Ikeda conjecture, introduced above, can hold for two-nucleon systems as well, as proposed in Ref. [42]. Such $2p$ and $2n$ narrow resonances have been very recently found in ^{15}F [64] and ^{26}O[17], respectively. However, their $2p$ or $2n$ decay pattern could not be studied because of the too weak $2p$ branch for ^{15}F and the too low relative energy of the two neutrons for ^{26}O. We will show that a narrow resonance is found in our work for ^{28}F, for which the $2n$ decay pattern could be characterized.

1.4 From ^{26}F to ^{28}F: evolution of the *p*-*n* interaction

As mentioned previously, nucleon-nucleon interactions are responsible for the major changes in nuclear structure observed while moving toward the dripline. The $N = 20$ shell closure disappears for $Z \leq 14$ and a new gap at $N = 16$ is emerging for nuclei with $Z \sim 8$, explaining the position of the dripline at $A = 24$ for the Oxygen isotopes. However, adding only one proton in order to form a Fluorine isotope allows us to bind six additional neutrons since ^{31}F is the last bound Fluorine isotope (note that ^{28}F and ^{30}F are unbound due to pairing effects). It is therefore important to have a good understanding of the nucleon-nucleon interaction in this region in order to be able to predict properly the structure of those nuclei close to the dripline. We are interested in this section in ^{26}F and ^{28}F.

We start with ^{26}F, which offers the opportunity to study different aspects, as discussed earlier in this chapter, of the nucleon-nucleon interaction far from stability. Indeed, this nucleus has all the conditions required so that the approximations nedeed for such a study are valid. ^{26}F can be seen as a doubly magic ^{24}O core to which we added one deeply bound proton ($S_p(^{25}F) = -15.1(3)$ MeV [65]) in $\pi d_{5/2}$ and one unbound neutron ($S_n(^{25}O) = 770(20)$ keV [66]) in $\nu d_{3/2}$. The fact that the first excited state of ^{24}O is located at an excitation energy of 4.47 MeV [67] and that the sub-shells $\pi d_{5/2}$ and $\nu d_{3/2}$ are well separated in energy compared to the others allow us to use the single-particle approach necessary to the determination of the $\pi d_{5/2} \otimes \nu d_{3/2}$ interaction such as presented in section 1.2. From the $\pi d_{5/2} \otimes \nu d_{3/2}$ coupling, results a $J^\pi = 1^+, 2^+, 3^+, 4^+$ multiplet, whose energies must be determined in order to study the influence of the proximity of the continuum on the corresponding *p*-*n* interaction. Indeed, once those states identified and characterized, we will be able using the method described in section 1.2.2 for ^{38}Cl to determine the intensity of the $\pi d_{5/2} \otimes \nu d_{3/2}$ interaction. Finally, adding one proton in $\pi d_{5/2}$ to ^{24}O gives ^{25}F which binding energy is known to be $BE(^{25}F) = -183.38(8)$ MeV. In a same way, adding one neutron in $\nu d_{3/2}$ to ^{24}O gives ^{25}O which is unbound with a neutron emission threshold of $S_n(^{25}O) = 0.77(2)$ MeV. Then we obtain the binding energy of $^{26}F_{free}$ (see section 1.2.2):

$$BE(^{26}F_{free}) = BE(^{24}O) + S_p(^{25}F) + S_n(^{25}O) = BE(^{25}F) + S_n(^{25}O) \tag{1.13}$$

We need now to determine the energies of the four states ($J^\pi = 1^+, 2^+, 3^+, 4^+$) resulting from the $\pi d_{5/2} \otimes \nu d_{3/2}$ coupling. Energies for the bound $J^\pi = 1^+, 2^+$ and 4^+ states were measured using different techniques [68–70]. In particular, the spin assigments of the ground state (1^+) [68, 71] and of the weakly bound isomeric state (4^+ at 643 keV) [68] were proposed from their decay pattern to low- and high-energy spin values, respectively, in the daughter nucleus ^{26}Ne. Also an unbound state was recently proposed to be the missing $J^\pi = 3^+$ state [3]. In this work, ^{26}F was populated from ^{27}Ne via proton knockout at GSI. In such reaction, we expect the proton to be knocked-out mainly from the $\pi d_{5/2}$ orbital, while the neutron remains in $\nu d_{3/2}$, and therefore populating the states of the $J^\pi = 1^+, 2^+, 3^+, 4^+$ multiplet. Among those states, only the 3^+ has been found to be unbound, and decaying into ^{25}F+n.

Since the $J^\pi = 1^+, 2^+, 3^+, 4^+$ multiplet has been observed experimentally , we can turn to experimental interaction energies $Int(J)$, that correspond to the interaction between a $\pi d_{5/2}$ proton and $\nu d_{3/2}$ neutron above the ^{24}O core coupled to different spin orientations J. We can define this quantity such as:

$$Int(J) = BE(^{26}F)_J - BE(^{26}F_{free}) \tag{1.14}$$

J	$Int(J)$ [MeV]		
	exp	IM-SRG	USDA
1	-1.85(13)	-2.24(07)	-2.47
2	-1.19(14)	-1.86(05)	-1.51
3	-0.45(19)	-0.53(04)	-0.69
4	-1.21(13)	-1.56(04)	-1.54
V^{pn}	-1.06(8)	-1.41(02)	-1.40

Table 1.1: *Experimental and calculated interaction energies, $Int(J)$, between a $\pi d_{5/2}$ proton and a $\nu d_{3/2}$ neutron in ^{26}F. Calculated results are obtained from USDA and IM-SRG shell-model calculations (adapted from [3]).*

where $BE(^{26}\mathrm{F})_J$ is the energy of a given J^π state in ^{26}F. Values of $Int(1,2,4)$ obtained in [68] and $Int(3)$ obtained in [3] are listed in Table 1.1 and shown in Fig. 1.7. The corresponding effective experimental monopole interaction (see section 1.2.2) amounts to $V^{pn}_{exp} \approx -1$ MeV.

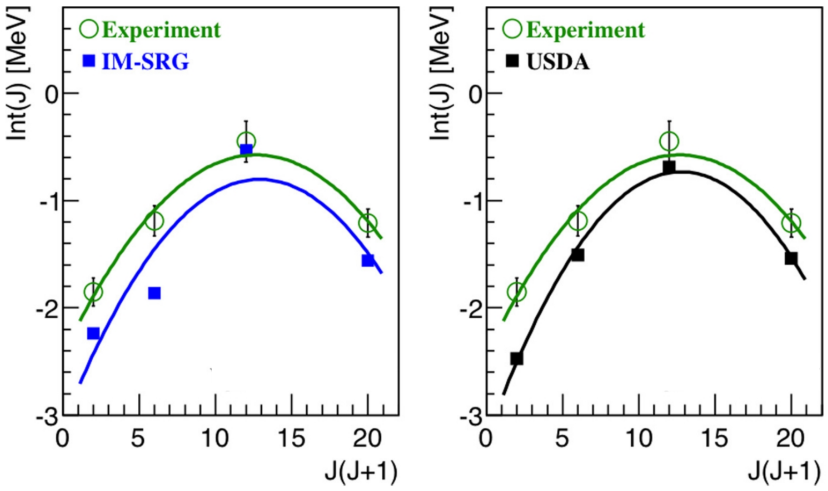

Figure 1.7: *Experimental interaction energies corresponding to the $\pi d_{5/2} \otimes \nu d_{3/2}$ coupling in ^{26}F. $Int(J)$ (green cicles), are plotted as a function of $J(J+1)$ and compared to calculations using the IM-SRG procedure (left) and the USDA interaction (right). Fitted parabolas are drawn to guide the eye (taken from [3]).*

The results from the USDA and IM-SRG calculations for the monopole interaction (V^{pn}) amount to about -1.4 MeV. This is larger than the experimental value of -1.06 MeV, pointing to a smaller monopole interaction as compared to calculations. As seen in Table 1.1 and Fig. 1.7, the amplitude of the multiplet parabola of USDA is also larger than in experiment, while the energy of $J = 3$ is in good agreement. This suggests that the residual energy that lifts the degeneracy between the J components of the multiplet is smaller than calculated. Both effects of smaller monopole and residual interactions, as compared to calculations, could be interpreted (with a word of caution concerning the S_n value of ^{26}F and its consequence on a possible shift in excitation energy of the resonance) as an effect of the proximity of the continuum on the effective proton-neutron interaction.

We are aiming now to perform the same kind of study for ^{28}F. Then by comparing the results for ^{28}F and ^{26}F, we will get information on the evolution of the $\pi d_{5/2} \otimes \nu d_{3/2}$ interaction while moving further toward the dripline. Indeed while moving from ^{26}F to ^{28}F, we expect to be filling the $\nu d_{3/2}$ by adding two additional neutrons as shown in Fig. 1.8. In the case of ^{28}F, we are therefore left with a proton in $\pi d_{5/2}$ and a hole in $\nu d_{3/2}$. This coupling results in a $J^\pi = 1^+, 2^+, 3^+, 4^+$ multiplet whose energies must be determined.

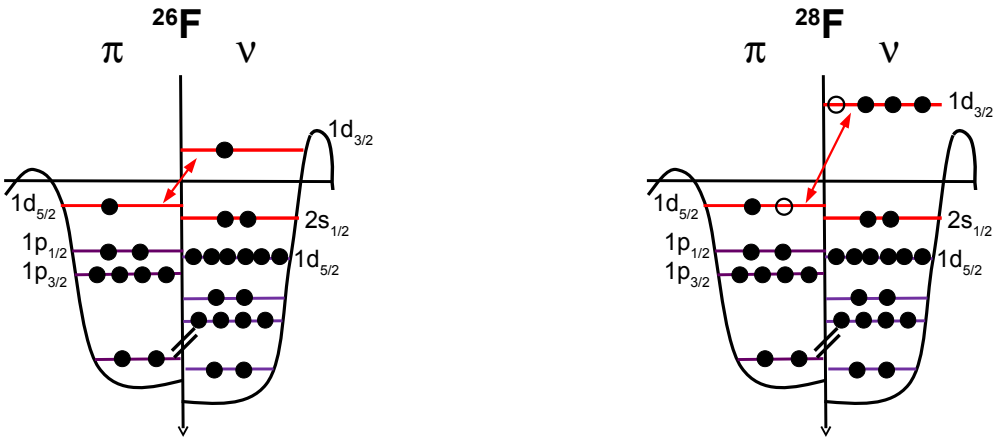

Figure 1.8: *Expected ground state configurations for ^{26}F and ^{28}F.*

However, performing such study on ^{28}F reveals itself to be even more challenging than in the case of ^{26}F. Indeed, while in ^{26}F only the $J^\pi = 3^+$ state was unbound, in ^{28}F all the states are unbound as the nucleus is unbound itself. ^{28}F can be seen as a ^{28}O core to which we added one deeply bound proton in $\pi d_{5/2}$ and remove one unbound neutron in $\nu d_{3/2}$. The interaction energies $Int(J)$ for ^{28}F can be expressed following Eq. 1.14:

$$Int(J) = BE(^{28}\mathrm{F})_J - BE(^{28}\mathrm{F}_{free}) \tag{1.15}$$

where $BE(^{28}\mathrm{F}_{free})$ is given by:

$$BE(^{28}\mathrm{F}_{free}) = BE(^{28}\mathrm{O}) + S_p(^{29}\mathrm{F}) - S_n(^{27}\mathrm{O}) = BE(^{29}\mathrm{F}) - S_n(^{27}\mathrm{O}) \tag{1.16}$$

However, the $S_n(^{27}\mathrm{O})$ value is unknown. This is a problem that should not stop us in our study since ^{27}O is also currently being studied, in the data from the same SAMURAI21 experiment that will be presented in chapter 5, giving hope for a value in the near future that could allow us to determine the interaction energies ($Int(J)$).

Another difficulty might be added to the one already mentioned. Indeed, it is known that the large shell gap at $N = 20$ is disappearing for neutron-rich nuclei [72–74]. The change in shell structure around $N = 20$ is known to be a result of the tensor force, which is strongly attractive for the $\pi d_{5/2} \otimes \nu d_{3/2}$ coupling and strongly repulsive for the $\pi d_{5/2} \otimes \nu f_{7/2}$ coupling [75–77]. For nuclei in the region of $N \sim 20$ and $Z \leq 13$, the reduced $N = 20$ gap allows pf intruder configurations to compete with standart sd-only configurations if the gain in correlation energy is of the same order as the size of the shell gap [78–80]. This has led to the establishment of the "island of inversion", a region of nuclei near $N = 20$ for which the

intruder configuration is dominant in the ground state.

The island of inversion was originally thought to be including nuclei with $10 \leq Z \leq 12$ and $20 \leq N \leq 22$ [18]. In more recent years, it has become clear that the island extends further, and a lot of experimental effort has been put forth to determine its boundaries [81]. On the low-N and high-Z sides of the island, it is generally agreed that ground-state intruder components fade away for $Z \geq 13$ and $N \leq 18$. Until now, the low-Z shore of the island of inversion has been almost completely unexplored. A measurement of bound states in ^{27}F, which lies on the island's western border at $N = 18$, has hinted a pf-shell contribution to its excited state structure [82], but mass measurements [70] indicate that ^{27}F ground state is primarily sd shell. For the heavier ($N \geq 19$) Fluorine isotopes, lying within the island's southern shore, only one study is available, on ^{28}F populated from ^{29}Ne($-1p$) [4].

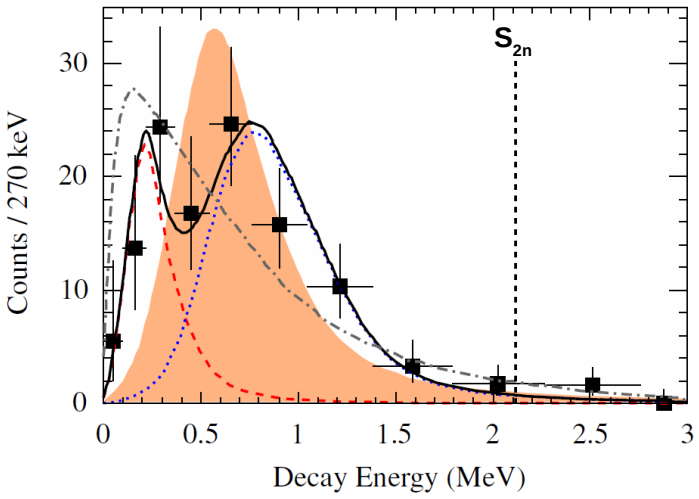

Figure 1.9: *Relative (or decay) energy spectrum for $^{27}F+n$ coincidences (extracted from [4]). The filled squares with error bars are the measured data, and the dashed red and dotted blue curves represent the 220 keV and 810 keV simulation results, respectively. The solid black curve is the sum of the two resonances, with the ratio of 220 keV resonance to the total area being 28%. The filled orange curve is a simulation of a single resonance at 590 keV, and the gray dot-dashed curve is the best fit of a single s-wave (a_s=-0.05 fm). The two neutron emission threshold (S_{2n}) has also been added.*

We will now describe in more detail the results obtained previously on ^{28}F [4]. In this study, ^{28}F has been populated via the knockout of a proton in ^{29}Ne at NSCL (National Superconducting Cyclotron Laboratory). The relative energy spectrum obtained is presented in Fig. 1.9. Assuming the presence of only two resonances, the fit of the data leads to two resonance energies, at 220(50) keV and 810 keV, even if the possibilty of more resonances is not ruled out. Also no γ-ray transitions were observed in coincidence, so the states observed were assumed to feed the ground state of ^{27}F. However, the data suffer from very low statistics and large error bars. Indeed, the two-resonance hypothesis is only based on one data point at around 500 keV, with large error bars, that looks like a local minimum but could equally be a statistical fluctuation. Moreover, as discussed in Ref. [4], by comparing the relative energy spectrum to the response of the experimental setup in Fig. 1.10, it is clear that the data are strongly distorted by the resolution and the acceptance. In particular, the width of the observed data is almost entirely due to the experimental resolution and the shape of the data

above ∼0.8 MeV is dominated by the limited acceptance at higher relative energies.

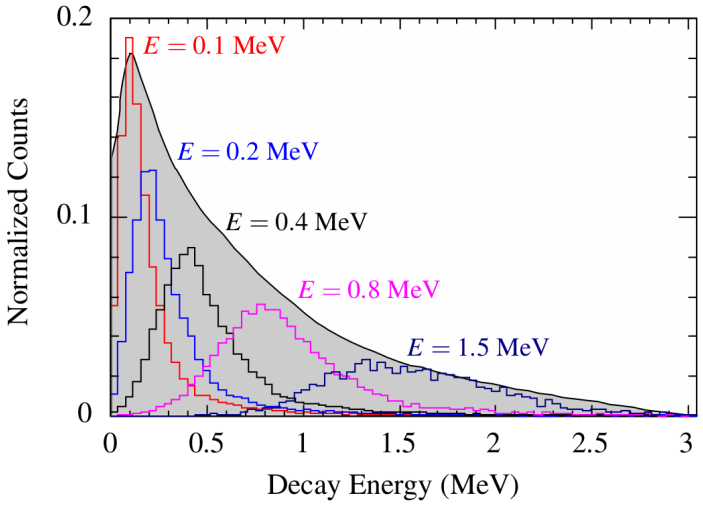

Figure 1.10: *Simulated resolution and acceptance of the experimental setup (figure taken from [4]). Each colored histogram was generated by simulating a ^{28}F breakup at the indicated energy and then folding in detector resolution and acceptance cuts. The shaded curve was generated by simulating a ^{28}F breakup with the relative energy uniformly distributed from 0-3 MeV and folding in acceptance and resolution. The colored histograms are all normalized to a total area of unity, and the shaded curve was arbitrarily scaled to fit within the same panel.*

The binding energy of ^{28}F, deduced from the experimental results assuming that the ground state was the structure at about 220 keV, was then compared and found in good agreement with USDA and USDB calculations. However as mentioned in Ref. [4], for a given nucleus, good agreement between experiment and USDA/USDB theory indicates a ground-state configuration that is primarily *sd* shell. In contrast, a nucleus with significant ground-state intruder components would be poorly described by the USDA/USDB shell model, leading to the conclusion that pf-shell intruder components play only a small role in the ground-state structure of ^{28}F, leaving it therefore out of the island of inversion.

The information extracted from this first attempt to study the structure of ^{28}F did not lead to clear answers. And there is no doubt that improvements on the resolution, statistics and acceptance would allow us to get a clearer picture of the structure of ^{28}F. However, this result gives us an idea of the complexity of such study.

We will present in chapter 5 our results on ^{28}F not only using this same reaction ^{29}Ne$(-1p)$, but also populating it from ^{29}F$(-1n)$, where both the resolution and the statistics have been largely improved compared to previous studies of unbound nuclei in general.

Chapter 2

Analysis techniques of fragment+xn systems

Contents

In this chapter we will discuss the experimental principle, requiring the detection of the incident beam and outgoing fragment and neutron(s), and the observables that will be constructed in order to extract the physical quantities. Indeed, these are the kind of coincidence events that are characteristics of the decay of an unbound state. We will introduce first the principle of neutron(s) detection, which is a key point in such kind of analysis. Then we will present the different observables used for the study of two-body and three-body unbound states.

2.1 The principle of neutron(s) detection

The detection of neutron(s) is a key step for the study of neutron-rich unbound states. It is therefore crucial to understand fully the principle of neutron(s) detection that will be used in our analysis. Indeed, we are investigating in this document unbound states that are decaying by emitting neutron(s) (see Fig. 2.1). The fact that the neutron is neutral makes it hard to detect. Their detection is possible only through the strong interaction, with cross-sections much lower than the corresponding atomic processes involved in charged-particle detection. Their detection is therefore not direct but induced by the recoil signal of a particle due to a nuclear reaction.

In our experiments, neutrons were detected after a collision with a nucleus from the detector material (plastic scintillators in our case). However, since in most reactions the

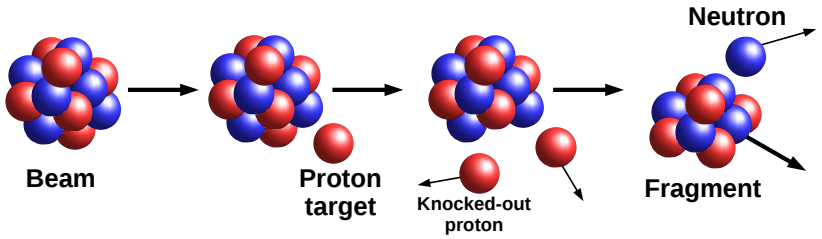

Figure 2.1: *Principle of the reaction of interest where a nucleus of the beam is undergoing a knock-out reaction in order to populate unbound states that will decay via the emission of neutron(s). We take here the example of a proton knockout with a proton target.*

neutron survives in the exit channel, a same neutron can be detected several times in the neutron detector by interacting successively in different locations. And even when the neutron interacts only once, outgoing charged particles from that interaction can propagate to neighboring detector modules. This phenomenon, the generation of signals in several detectors due to the passage of one single neutron, is known as cross-talk. The low neutron detection efficiencies and the occurrence of cross-talk makes extremely difficult the study of unbound resonances that decay through the emission of more than one neutron.

In this work, we are interested mainly in two types of decay mechanisms, the $1n$ and the $2n$ decay. The $1n$ decay remains relatively simple since only one neutron needs to be detected and therefore in that case only the first interaction occurring can be considered (all the hits due to cross-talk arriving later). However, for the $2n$ decay channel, since two neutrons have to be detected in order to have access to the full kinematics of the reaction, it is crucial to distinguish the *true* hits from the case where several hits originate from the same neutron. A list of the different possible cases when several hits are registered in the neutron detector are presented in Fig. 2.2.

In order to identify such kind of events, we applied algorithms in order to suppress as much cross-talk events as possible while optimizing the selection of real $2n$ events, sometimes a difficult compromise.

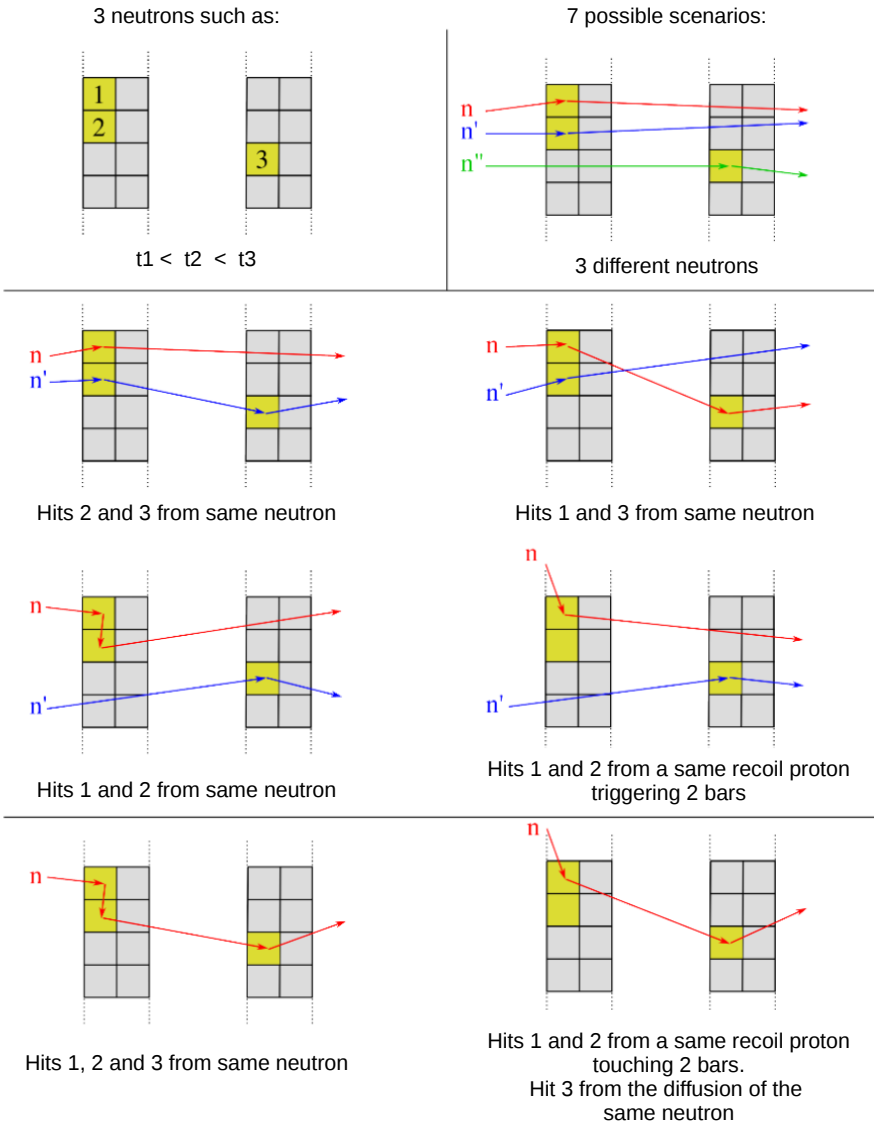

Figure 2.2: *The cross-talk principle: sketch of all the possible scenarios for the detection of 3 hits in the neutron detectors (adapted from [5]).*

2.2 Two-body unbound systems

In this section, we are focusing on the treatment of the coincidence between a nucleus of the beam, a fragment and a neutron. We will present the properties of the fragment-neutron non-resonant contribution before developing the different observables that characterize an unbound system.

2.2.1 Non-resonant contributions

Definition

Let us consider two particles that are part of the exit channel of a given reaction, with four-momenta p_1 and p_2. In an ideal case in which they do not 'see' each other, their momentum distributions should be independent, $d\sigma/dp_1$ and $d\sigma/dp_2$, and these distributions

would lead to a non-resonant component in the two-particle observables, the one we would like to estimate. If we can select exit channels in which only one of them is emitted, we could measure them. However, when they are mostly emitted together, as is the case of two neutrons in the breakup of borromean two-neutron haloes, or the unbound resonance we have described, we have only access to the two-particle cross-section, which we can write as:

$$\frac{d^2\sigma}{dp_1 dp_2} = \frac{d\sigma}{dp_1}\frac{d\sigma}{dp_2} \times C(p_1, p_2) \tag{2.1}$$

The factor $C(p_1, p_2)$ is often called the "correlation function", but it should simply be seen as the effect of the mutual presence of both particles in the final state. The main mechanisms that may modify the momenta p_1 and p_2 of the particles we measure can be classified in three categories:

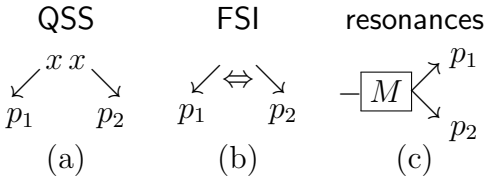

(2.2)

the quantum statistical symmetries for identical particles (a), the final-state interaction for interacting particles (b), and the formation of resonances decaying into those particles (c). In the case of two neutrons we have (a,b) because they are identical fermions and subject to the strong interaction, in the case of fragment+proton we have (b) through the Coulomb interaction, and in the case of fragment+n we may have (c) if the unbound system has resonances.

Event mixing

Independently of the mechanism modifying the momenta, if we want to extract its effect $C(p_1, p_2)$ from the experimental coincidences $d^2\sigma/dp_1 dp_2$, we need to estimate the 'independent distributions' of Eq. (2.1), i.e. how the two-particle observable would look like without the correlation/interaction. If we mix particles from different events we should expect to wash out any correlation, since a particle 1 has not 'seen' a particle 2 from a different event, they did not coexist. The added bonus of these 'virtual pairs' is that they are built from particles that have been detected, so our independent distributions will include the experimental acceptances.

This technique has been extensively used in a wide range of energies in both nuclear and particle physics, and has effectively extracted the correlation signals from two-particle coincidences (leading usually to the source size for QSS and FSI, and for resonances to their mass and width). However, when the correlation is very strong, just mixing the events is not enough. In order to understand why, let us 'mix' Eq. (2.1). Mixing particle 1 with all other particles 2 corresponds to integrating the two-particle distribution over particle 2:

$$\begin{aligned}\frac{d\sigma_{\otimes}}{dp_1} &= \int \frac{d^2\sigma}{dp_1\,dp_2}\,dp_2 \\ &= \frac{d\sigma}{dp_1}\int C(p_1,p_2)\,\frac{d\sigma}{dp_2}\,dp_2 \\ &= \frac{d\sigma}{dp_1}\,\langle C\rangle(p_1) \end{aligned} \tag{2.3}$$

We have used the definition of $C(p_1, p_2)$ in Eq. (2.1) and then used the fact that the independent distributions are independent of each other. By mixing events we obtain $d\sigma_{\otimes}/dp_1$, which is the independent distribution we are looking for times $\langle C\rangle(p_1)$. The same stands for particle 2, so in general we obtain:

$$\frac{d\sigma_{\otimes}}{dp} = \frac{d\sigma}{dp} \times \langle C\rangle(p) \tag{2.4}$$

The unexpected factor represents the average correlation, with all the other 'virtual' partners, of a particle with four-momentum p. When the correlation function is small, or when it acts on a very small portion of the data set, this average correlation will be $\langle C\rangle \approx 1$, and therefore the standard mixing technique will succeed:

$$C(p_1,p_2) \approx \frac{d^2\sigma/dp_1dp_2}{(d\sigma_{\otimes}/dp_1)\,(d\sigma_{\otimes}/dp_2)} \tag{2.5}$$

This is the case in most of the applications of the technique, in which particles are weakly correlated, or very few of them are strongly correlated.

Residual correlations

The correlation factor in Eq. (2.4) represents the residual correlations that 'survive' the event mixing. If we know it is going to be significantly larger than 1, or if we do not know but do not want to make *a priori* assumptions, it is better to take it into account. In general, mixing the events will lead us to underestimate, more or less, the correlation function:

$$\frac{d^2\sigma/dp_1dp_2}{(d\sigma_{\otimes}/dp_1)\,(d\sigma_{\otimes}/dp_2)} \leq C(p_1,p_2) \tag{2.6}$$

However, if we are able to calculate the residual correlation factor, then we can use it as a weight of the events we mix and remove the residual correlations completely:

$$\underbrace{\frac{d^2\sigma/dp_1dp_2}{(d\sigma_{\otimes}/dp_1)\,(d\sigma_{\otimes}/dp_2)}}_{\times\frac{1}{\langle C\rangle(p_1)}\frac{1}{\langle C\rangle(p_2)}} = C(p_1,p_2) \tag{2.7}$$

The problem, of course, is that in order to construct the correlation function we have to use the correlation function! We need an iterative algorithm, that will construct successive correlation functions using the weights calculated with the preceding one. And, to make

things a bit more complex, there is a subtle detail in the calculation of the weights that can be deduced from Eq. (2.3):

$$\begin{aligned} \langle C\rangle(p_1) &= \int C(p_1,p_2)\,\frac{d\sigma}{dp_2}\,dp_2 \\ &= \int C(p_1,p_2)\,\frac{d\sigma_{\otimes}/dp_2}{\langle C\rangle(p_2)}\,dp_2 \end{aligned} \tag{2.8}$$

In order to calculate the weights of particle 1 we would use the correlation function plus the 'independent' distribution of particle 2, but experimentally we cannot measure it. So we will have to add a second loop in the iteration algorithm, since in order to calculate the average correlation of one particle for a given step we have to use the average correlation of all the other particles...

The iterative technique

The previous integral equations help to understand the principle, but in practice we are measuring a given number N of two-particle coincidences:

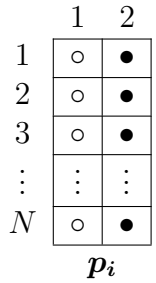

How do we proceed? First we project the 8-dimensional space into 1 dimension:

$$(p_i,p_j) \;\rightarrow\; x_{ij} \tag{2.9}$$

which is the relative observable we are going to study, and that should contain the correlation we want to extract. For n-n pairs it may be the relative momentum, for fragment-n pairs their relative energy, for example. Eq. (2.7) becomes:

$$\frac{\sigma(x_{12})}{[\sigma_{\otimes}(x_{12})]_{w_{12}}} \;=\; C(x_{12}) \tag{2.10}$$

The numerator is the measured two-particle distribution, and the denominator the distribution obtained through event mixing, with $N(N-1)$ virtual pairs, weighted by:

$$w_{12} \;=\; w_1\,w_2 \;=\; \frac{1}{\langle C\rangle(p_1)}\,\frac{1}{\langle C\rangle(p_2)} \tag{2.11}$$

Each particle must have an associated weight, therefore we have to build an array of $2N$ weights with the correlation function:

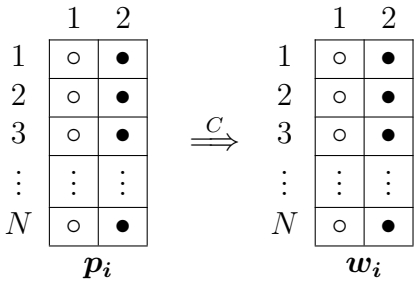

that will allow us to build the correlation function. We initialize the first weights to 1, build the first 'mixed' distribution, divide the data by that distribution to obtain the first correlation function, that is used to calculate the second weights... and after a big enough number of steps we should obtain the correlation function:

$$\begin{aligned} w^{(1)}=1 \;&\rightarrow\; [\sigma_{\otimes}]_{w^{(1)}} \rightarrow \frac{\sigma}{[\sigma_{\otimes}]_{w^{(1)}}} = C^{(1)} \\ \rightarrow\; w^{(2)} \;&\rightarrow\; [\sigma_{\otimes}]_{w^{(2)}} \rightarrow \frac{\sigma}{[\sigma_{\otimes}]_{w^{(2)}}} = C^{(2)} \\ \rightarrow\; w^{(3)} \;&\rightarrow\; \cdots \rightarrow \frac{\sigma}{[\sigma_{\otimes}]_{w^{(n)}}} = C^{(n)} \end{aligned} \tag{2.12}$$

For the calculation of the array of weights, Eq. (2.8) becomes:

$$\langle C\rangle^{(n)}(p_i) \;=\; \frac{1}{N-1}\sum_{j=1\neq i}^{N}\frac{C^{(n-1)}(x_{ij})}{\langle C\rangle^{(n)}(p_j)} \tag{2.13}$$

This is the second loop of iterations, since we calculate this array at every step (beyond the first) of the general iteration, and for the calculation of each weight $1/\langle C\rangle^{(n)}(p_i)$ we need the weights $1/\langle C\rangle^{(n)}(p_j)$ of all possible partners, that at the same time will need the former.

Application

In order to illustrate this technique, we use in this paragraph the example of the construction of the distribution of the non-resonant events in a relative energy spectra for the (^{29}F,^{27}F+n) reaction. In practice, the two loops described by the equations (2.12,2.13) have to be iterated a sufficient number of times in order to reach a convergence criteria determined by the user (an example of the effect of the different iterations is presented in Fig. 2.3). The result obtained gives us the shape of the non-resonant distribution with very high statistics compared to the data (of the order of N^2 virtual pairs). The statistical error of this distribution is therefore negligible, but its amplitude has to be determined from the comparison with the experimental one.

In the case of a relative energy spectrum, we assume that the non-resonant distribution needs to remain lower than the data in the limit of the error bars for the whole energy range (positive correlations). This fact allows us to establish an upper limit to the contribution of the uncorrelated events in the relative energy spectrum. However, the resonances observed in the correlated spectrum can sometimes have long tails at high energy, therefore creating events over the whole energy range. The real proportion of the non-resonant contribution is therefore usually smaller than the one obtained with such a normalization. Fig. 2.3 shows the

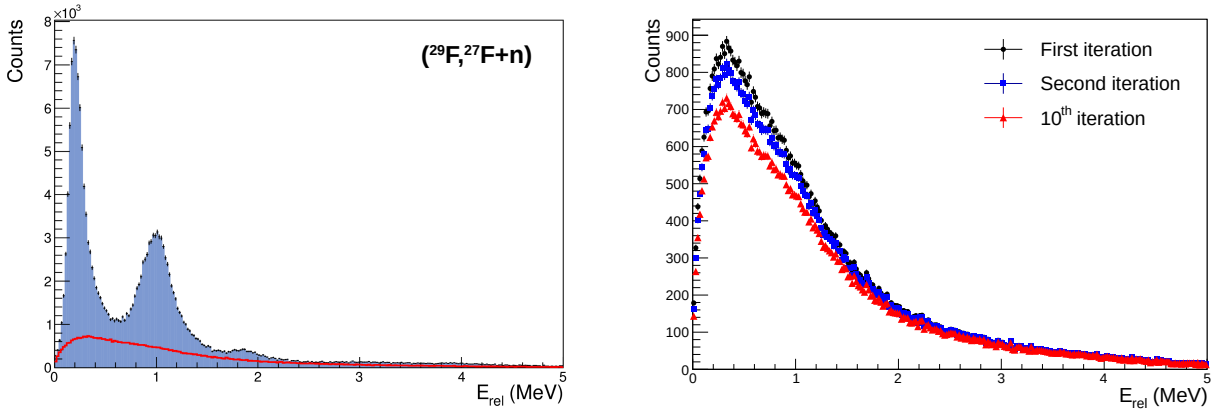

Figure 2.3: *On the left, relative energy spectrum and non-resonant distribution for the (^{29}F,^{27}F+n) reaction. The non-correlated distribution has been maximized in order to reach the data points in some areas of the spectrum without going above it. On the right, the superposition of the non-resonant distributions obtained for different iterations of the algorithm are presented.*

relative energy spectrum as well as the maximized non-resonant contribution ($C \geq 1$) for the (^{29}F,^{27}F+n) reaction.

In fact, the exact proportion of non-resonant events is determined by making a fit taking into account this background as well as the different resonances observed, but this technique will be described in more detail later. However, the maximization of the non-resonant distribution allows us to obtain indications on the presence or not of resonances in the spectra. Indeed, the shape of the non-resonant contribution being non trivial, and the resolution of the experimental setup degrading with the relative energy, it can be sometimes difficult to spot wide or high-energy resonances. This is even more true in the case of reaction channels involving the knockout of several nucleons where the signal over non-resonant contribution ratio can become very low. In that case, we can plot the difference or the ratio of the data over the non-resonant contribution in order to enhance some structure in the spectrum. Fig. 2.4 shows an example of those two approaches for the (^{29}F,^{27}F+n) reaction.

2.2.2 Invariant-mass method

We are investigating unbound states that immediately decay after being populated, making impossible the direct measurement of their "mass". Therefore, we use the invariant-mass method in which the measurement of the complete kinematics of the reaction is necessary. Indeed, we need for this method to detect all the decay products of the reaction and measure their momenta.

The relativistic relation linking the mass m, the momentum $\vec{p}$ and the energy E of a system is as follows:

$$E = \sqrt{p^2c^2 + m^2c^4} \tag{2.14}$$

In the following, we will assume $c = 1$. This formula can be used to express the mass of a

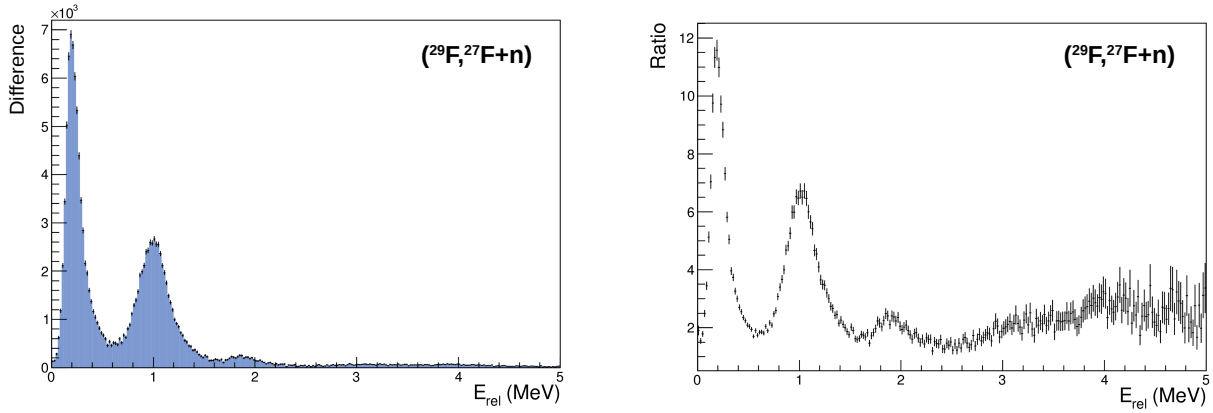

Figure 2.4: *On the left, results from the subtraction of the maximized non-resonant contribution from the relative energy spectra for the (^{29}F,^{27}F+n) reaction. On the right, correlation function, (i.e. ratio between the relative energy spectrum and the maximized non-resonant distribution for the same reaction).*

system from a four-vector $(E, \vec{p})$:

$$m^2 = (E, \vec{p})^2 = E^2 - p^2 \tag{2.15}$$

And we can derive from this formula the invariant mass M_{inv} for a N-body unbound system such as:

$$M_{inv} = \sqrt{\left(\sum_{i=1}^{N} E_i\right)^2 - \left(\sum_{i=1}^{N} \vec{p}_i\right)^2} \tag{2.16}$$

where E_i is the energy of particle i and $\vec{p}_i$ its momentum.

M_{inv} being the mass of the system, we can derive the expression of the relative energy E_{rel} between the particles by subtracting from it the mass of each particle in its rest frame m_i:

$$E_{rel} = M_{inv} - \sum_{i=1}^{N} m_i \tag{2.17}$$

If the unbound state is decaying by emitting only one neutron, Eq. 2.17 for a two-body fragment+n system becomes:

$$E_{rel} = \sqrt{m_A^2 + m_n^2 + 2\left(E_A E_n - |\vec{p_A}||\vec{p_n}|cos\theta\right)} - m_A - m_n \tag{2.18}$$

where m_A and m_n are the rest masses of the fragment of atomic mass number A and the neutron, E_A and E_n are their total energies, $|\vec{p_A}|$ and $|\vec{p_n}|$ are their momenta norm and θ is their relative angle.

If the fragment is populated in its ground state, we have then $E_{exc} = S_n + E_{rel}$ where E_{exc} is the excitation energy of the A+1 nucleus and S_n is its neutron emission threshold. However, the reaction can also lead to the production of the fragment in one of its excited states that subsequently decays to the ground state by the emission of a γ-ray of energy E_γ. In the latter

case, a coincidence between the neutron and the de-exciting γ-ray is observed. We can therefore propose the following expression for the excitation energy:

$$E_{exc} = S_n + E_{rel}(+E_\gamma) \tag{2.19}$$

2.3 Three-body unbound systems

In this part, the three-body correlations in the decay of high-energy unbound states are explored. In particular, a method for analyzing triple coincidence events (fragment+n+n) from kinematically complete experiments is described. The method incorporates the techniques of intensity interferometry [83] and Dalitz plots [84] and allows the estimation of the n-n distance and time delay between the emission of the two neutrons. As will be seen, the latter is related to the presence of fragment-n final-state interactions (FSI) in the exit channel. In principle, the present approach is also sensitive to the energies and lifetimes of these resonances.

2.3.1 Phase space

In order to identify the correlations emerging from the interaction between particles, we need to seperate them from the basic correlations imposed by energy and momentum conservation, that are independent of the nature of the particles. The latter are given by the N-body phase space, on top of which we will add what we call "physical correlations", or simply "correlations". Our model is an interacting three-body phase-space model that has been developed for the analysis of triple correlations. In brief, the experimental relative energy distribution is used as input to generate events $\vec{p}_{f,n,n}(E_{rel})$ following three-body phase-space [85]. The final momenta of the three particles generated are then filtered to include all experimental effects (like energy resolution, angular acceptance, or cross-talk rejection). In order to illustrate the method used, we are using the result of the simulation for the reaction ^{21}O(p,pn)^{20}O* where unbound states above the $2n$ emission threshold are populated. As mentioned earlier, the experimental relative energy distribution is used as input to generate our events. Therefore, we can first look at the experimental relative energy distribution for our reaction when the ^{20}O* is decaying with the emission of two neutrons (^{18}O+n+n), see Fig 2.5.

In our simulation, the available energy for the decay is selected according to this experimental distribution. Before implementing correlations in our model to make it more realistic, we are describing in the following sections the different observables that we use in our analysis in order to investigate three-body correlations.

2.3.2 Observables

In order to investigate three-body correlations, we need to define the observables that are used in our analysis.

Invariant masses and Dalitz plots

Correlations in three-particle decays have been extensively studied in particle physics by means of Dalitz plots of the particle energies (E_i, E_j) or the squared invariant masses of particle

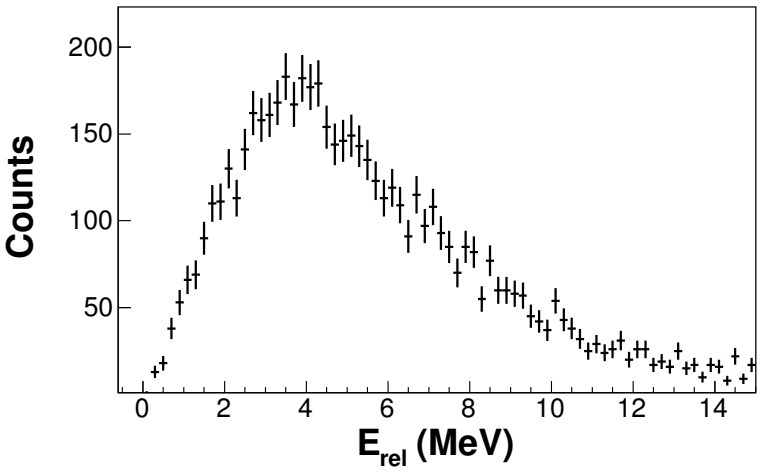

Figure 2.5: *Experimental relative energy spectrum of the decay* ^{18}O*+n+n.*

pairs (M_{ij}^2, M_{jk}^2), with $M_{ij}^2 = (P_i + P_j)^2$. In these representations, FSI/resonances lead to a non uniform population of the surface within the kinematic boundary defined by energy-momentum conservation and relative energy [84]. The classic example of such an analysis is the three-body decay of an unstable particle [86]. In the present case, the fragment+n+n system exhibits a distribution of relative energies. Consequently, the value of E_{rel} associated with each event will lead to a different boundary for the Dalitz plot, and the resulting plot containing all events cannot be easily interpreted. We thus introduce a normalized invariant mass:

$$m_{ij}^2 = \frac{M_{ij}^2 - (m_i + m_j)^2}{(m_i + m_j + E_{rel})^2 - (m_i + m_j)^2} \tag{2.20}$$

which ranges from 0 to 1 (E_{ij} from 0 to E_{rel}) for all events and exhibits a single kinematic boundary.

We can now, using Eq. 2.20, compute the fragment-n and n-n invariant masses. The Dalitz plot can be obtained by simply representing m_{fn}^2 as a function of m_{nn}^2. Since we have two neutrons involved in the decay, we fill two times the Dalitz plot for each event, one time for each neutron. In the absence of any correlations above the phase-space kinematics, the plot exhibits a uniform population as can be seen in Fig. 2.6 (a). The projections over the normalized invariant masses, Fig. 2.6 (b,c), both show a regular bell shape from 0 to 1 with a maximum at around 0.5. We can also notice that the distribution of those two variables is minimum and equal to 0 at m_{ij}^2 equal to 0 and 1.

Angular coordinates

In order to study the decay mechanism, one can also look at the angular correlations between the three particles involved in the decay. We define two angles θ_{nn} and $\theta_{f/nn}$ such as presented in Fig. 2.7, θ_{nn} being the angle between the two neutron momenta $\vec{p}_{n_1}$ and $\vec{p}_{n_2}$ and $\theta_{f/nn}$ being the angle between the fragment momentum and the relative momentum of the two neutrons. Their cosines can be expressed as a function of the momenta of the particles involved in the decay $\vec{p_f}$, $\vec{p_{n_1}}$ and $\vec{p_{n_2}}$ for the fragment, the first neutron n_1 and the second neutron n_2, respectively (see Eq. 2.21 and Eq. 2.22). Since there are two different ways (noted here "a" and "b") to label

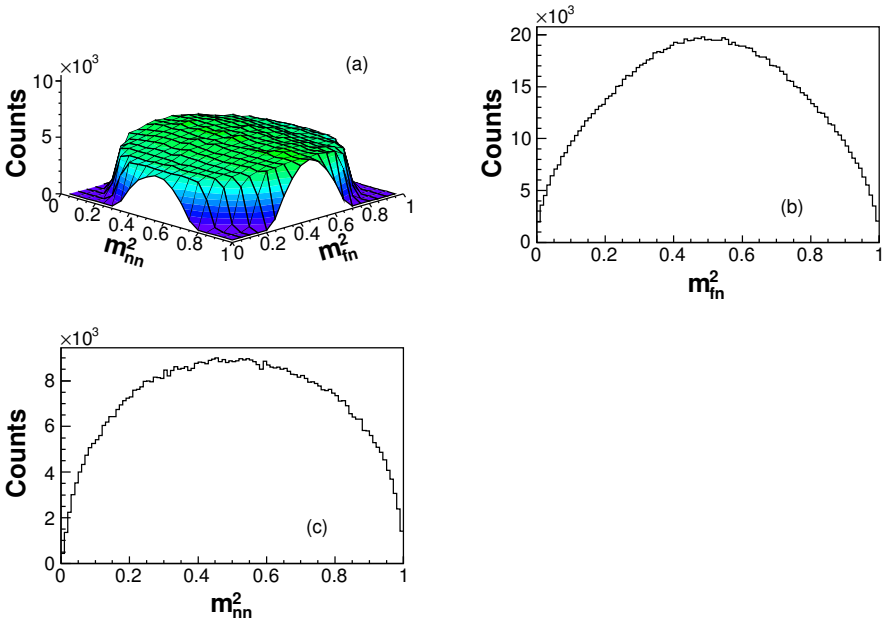

Figure 2.6: *Dalitz plot (a) of the ^{18}O+n+n events from the simulation of a phase-space decay for E_{rel} =0-12 MeV. The projections over the normalized invariant masses are presented in (b) and (c) for m^2_{fn} and m^2_{nn}, respectively. We observe that the projections are not identical because of the mass asymmetry of the three particles (m_A, m_n, m_n).*

the neutrons involved in the decay, we compute $\theta_{f/nn}$ with both and add them in the same histogram.

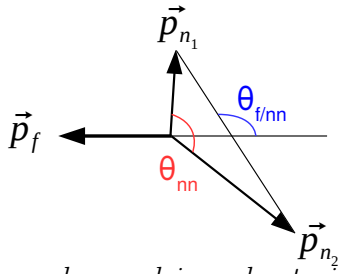

Figure 2.7: *Definition of the two angles used in order to investigate three-body correlations as a function of the momenta of the three particles involved, $\vec{p}_f$, $\vec{p}_{n_1}$ and $\vec{p}_{n_2}$ for the fragment, the first neutron and the second neutron, respectively.*

$$cos(\theta_{nn}) = \frac{\vec{p_{n_1}} \cdot \vec{p_{n_2}}}{|\vec{p_{n_1}}|\,|\vec{p_{n_2}}|} \tag{2.21}$$

$$cos(\theta_{f/nn})_{a/b} = \frac{(\vec{p_{n_{1/2}}} - \vec{p_{n_{2/1}}}) \cdot \vec{p_f}}{\left|\vec{p_{n_{1/2}}} - \vec{p_{n_{2/1}}}\right|\,|\vec{p_f}|} \tag{2.22}$$

In the absence of correlations above the phase-space kinematics, plotting $cos(\theta_{nn})$ as a function of $cos(\theta_{f/nn})$ results in a rather uniform population of the plot like shown in Fig. 2.8(a). However, we can observe structures at the boundaries ($cos(\theta_{f/nn}) = \pm 1$ and $cos(\theta_{nn}) = \pm 1$) due to kinematic conditions. The projection on the $cos(\theta_{f/nn})$ variable (Fig. 2.8(b)) shows a

slight bell shape with a maximum at 0, whereas the projection on $cos(\theta_{nn})$ (Fig. 2.8(c)) presents a slowly decreasing slope from -1 to 1 with a drop at around 1.

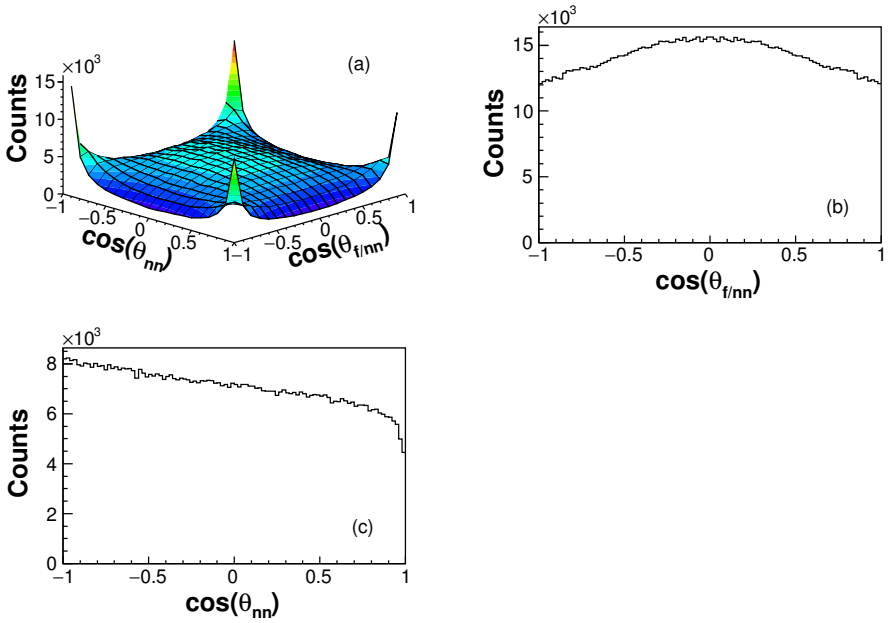

Figure 2.8: *Two dimensional plot of $cos(\theta_{nn})$ as a function of $cos(\theta_{f/nn})$ (a) for the ^{18}O+n+n events from the simulation of a phase-space decay for E_{rel} =0-12 MeV. The projections over $cos(\theta_{f/nn})$ and $cos(\theta_{nn})$ are presented in (b) and (c), respectively.*

Jacobi coordinates

Another system of coordinates that is often used in order to study three-body correlations are the Jacobi coordinates [55, 87], where the energy and the angular correlations between the reaction products are described by the hyperspherical Jacobi vectors $\vec{X}$ and $\vec{Y}$ and their conjugate momenta $\vec{k}_x$ and $\vec{k}_y$. The Jacobi coordinates can be defined in two independent ways, the "T" and the "Y" systems that are presented in Fig. 2.9.

In the "Y" system, the fragment is represented by the particle 2 and in the "T" system by the particle 3. The Jacobi coordinates are expressed as follows:

$$\vec{X} = \vec{r}_1 - \vec{r}_2 \tag{2.23}$$

$$\vec{Y} = \frac{m_1\vec{r}_1 + m_2\vec{r}_2}{m_1 + m_2} - \vec{r}_3 \tag{2.24}$$

$$\vec{k}_x = \frac{m_2\vec{p}_1 - m_1\vec{p}_2}{m_1 + m_2} \tag{2.25}$$

$$\vec{k}_y = \frac{m_3(\vec{p}_1 + \vec{p}_2) - (m_1 + m_2)\vec{p}_3}{m_1 + m_2 + m_3} \tag{2.26}$$

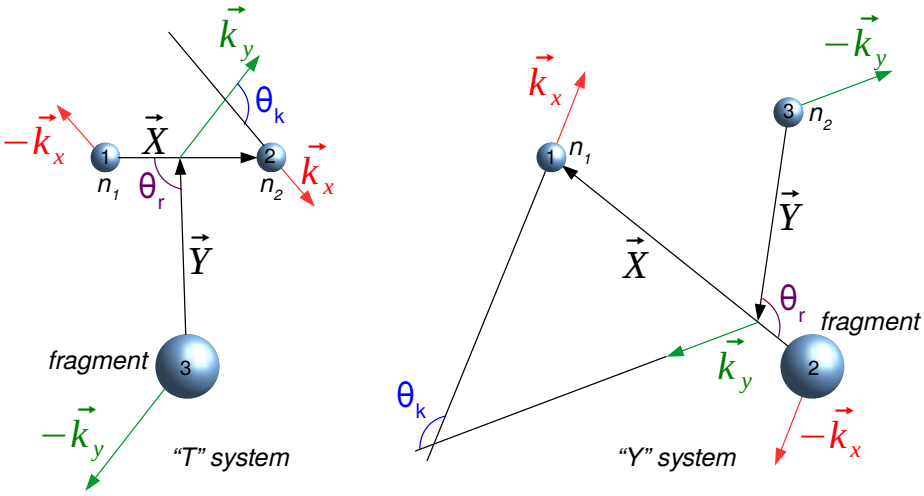

Figure 2.9: *"T" (left) and "Y" (right) Jacobi systems for the fragment+n+n three-body system in coordinate and momentum spaces.*

where m_i is the mass of each particle in its rest frame, r_i its position vector and p_i its momentum vector.

As shown in [87], the complete correlation information can be described by two observables that are E_x/E_{rel} and θ_k such as:

$$E_x = \frac{(m_1 + m_2)k_x^2}{2m_1m_2} \tag{2.27}$$

$$\theta_k = \frac{\vec{k}_x \cdot \vec{k}_y}{|\vec{k}_x||\vec{k}_y|} \tag{2.28}$$

In the case of a two-neutron decay, for each event there are two ways (noted as "a" and "b" in the following) to label the neutrons leading to two different values for the $[E_x/E_{rel}, cos(\theta_k)]$ coordinates. Therefore, we compute both and add them in the same histogram. This produces a symmetry over $cos(\theta_k)$ for the "T" system.

We propose now to present the expression of the $[E_x/E_{rel}, cos(\theta_k)]$ coordinates for the two different systems "T" and "Y" explicitly in the case of a $2n$ decay. We obtain for the "T" system:

$$\vec{k}^T_{x_{a/b}} = \frac{\vec{p}_{n_{1/2}} - \vec{p}_{n_{2/1}}}{2} \tag{2.29}$$

$$\vec{k}^T_{y_{a/b}} = \frac{m_f(\vec{p}_{n_{1/2}} + \vec{p}_{n_{2/1}}) - 2m_n\vec{p}_f}{2m_n + m_f} \tag{2.30}$$

noting that $\vec{k}^T_{y_a} = \vec{k}^T_{y_b}$. From which we can derive:

$$E^T_{x_{a/b}} = \frac{(k^T_{x_{a/b}})^2}{m_n} \tag{2.31}$$

$$\theta^T_{k_{a/b}} = \frac{\vec{k}^T_{x_{a/b}} \cdot \vec{k}^T_{y_{a/b}}}{|\vec{k}^T_{x_{a/b}}||\vec{k}^T_{y_{a/b}}|} \tag{2.32}$$

We can also compute the $[E_x/E_{rel}, cos(\theta_k)]$ coordinates for the "Y" system in the same way:

$$\vec{k}^Y_{x_{a/b}} = \frac{m_f \vec{p}_{n_{1/2}} - m_n \vec{p}_f}{m_n + m_f} \tag{2.33}$$

$$\vec{k}^Y_{y_{a/b}} = \frac{m_n(\vec{p}_{n_{1/2}} + \vec{p}_f) - (m_n + m_f)\vec{p}_{n_{2/1}}}{2m_n + m_f} \tag{2.34}$$

From which we can derive:

$$E^Y_{x_{a/b}} = \frac{(m_n + m_f)(k^Y_{x_{a/b}})^2}{2m_n m_f} \tag{2.35}$$

$$\theta^Y_{k_{a/b}} = \frac{\vec{k}^Y_{x_{a/b}} \cdot \vec{k}^Y_{y_{a/b}}}{|\vec{k}^Y_{x_{a/b}}||\vec{k}^Y_{y_{a/b}}|} \tag{2.36}$$

We present in Fig. 2.10, the results of the $2n$ phase-space decay of ^{20}O into ^{18}O for the "Y" system (right) and the "T" system (left). By comparing those results to the two sets of variables developed in the previous sections (Fig. 2.6 and Fig. 2.8), we notice that the E_x/E_{rel} variables for the "T" and the "Y" systems are equivalent to the normalized invariant masses m^2_{nn} and m^2_{fn}, respectively. And that the $cos(\theta_k)$ variables for the "T" and the "Y" systems are similar to the $cos(\theta_{f/nn})$ and $cos(\theta_{nn})$ variables, respectively. However, in the case of the $cos(\theta_k)$ variable for the "T" system, the relation with $cos(\theta_{nn})$ is not direct since the $cos(\theta_k)$ distribution is flat and, instead of showing a dip toward 1 (like $cos(\theta_{nn})$), it shows it toward -1.

Relative momentum and correlation function

In the n-n part of the three-body decay, we can also be interested by their relative momenta, that offer a way to probe the n-n correlations by using intensity interferometry. This technique is based on the principle that the wave function of relative motion of light identical particles, when emitted independently in close proximity in space-time, is modified by the final-state interaction (FSI) and quantum statistical symmetries (QSS). Following on from previous application to stellar interferometry [88], the two-particle correlation function was introduced to describe the influence of FSI and QSS on the emission probability of two particles with momenta $\vec{p}_1$ and $\vec{p}_2$ [89]. Since both effects are governed by the space-time characteristics of the source, the correlation function C, defined as the ratio between the measured two-particle distribution and the product of the independent single-particle distributions, provides a snapshot of the particle emission region. C can be expressed by rearranging Eq. 2.1 as follows:

$$C(\vec{p}_1, \vec{p}_2) = \frac{d^2n/dp_1 dp_2}{(dn/dp_1)(dn/dp_2)} \tag{2.37}$$

The projection onto the relative three-momentum $q_{12} = |\vec{p}_1 - \vec{p}_2|$ is commonly used, where the experimental distribution of pairs is divided by a reconstructed distribution of uncorrelated

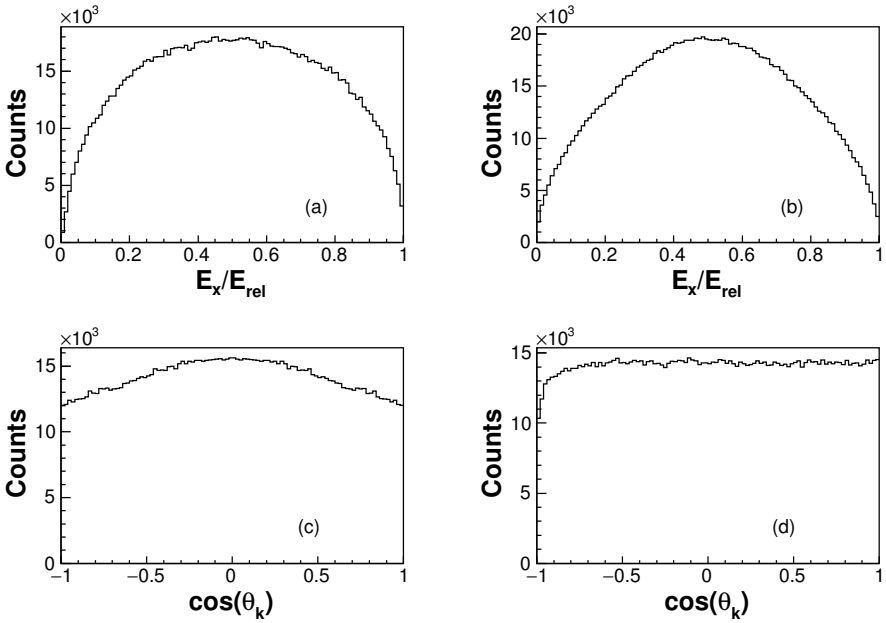

Figure 2.10: *"T" (left) and "Y" (right) Jacobi coordinates of the ^{18}O+n+n events from the simulation of a phase-space decay for E_{rel} =0-12 MeV. The "T" system $[E_x/E_{rel}, cos(\theta_k)]$ coordinates are presented in (a) and (c), respectively and the "Y" system $[E_x/E_{rel}, cos(\theta_k)]$ coordinates in (b) and (d), respectively.*

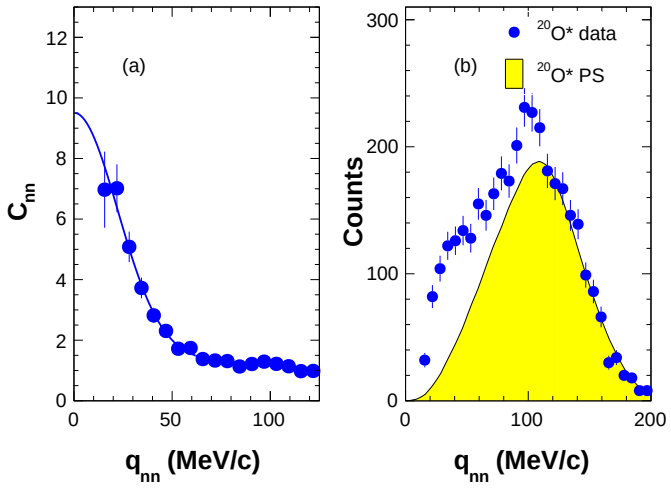

Figure 2.11: *(a) Two-neutron correlation function for E_{rel}=3.7-12 MeV of $^{20}O^*$ 2n decays. The solid line is traced to guide the eye. (b) Numerator (measured relative momentum distribution, blue points) and denominator (phase space, yellow) of C_{nn} for the $^{20}O^*$ case.*

pairs normalized so that C goes to 1 at high q, where effects of FSI and QSS should vanish. The deviation of C from 1 thus reflects the structure of the source. Other effects, arising from the form of the single-particle distributions or the experimental acceptances, are eliminated by the denominator of Eq. 2.37.

In our case, we are looking at n-n correlations. We can therefore write the n-n correlation

function C_{nn} such as:

$$C_{nn} = \frac{\sigma_{exp}(q_{nn})}{\sigma_{PS}(q_{nn})} \tag{2.38}$$

The numerator $\sigma_{exp}(q_{nn})$ corresponds to the experimental distribution and contains all the interaction effects. The denominator $\sigma_{ps}(q_{nn})$ can be obtained by the simulation of a phase-space decay and contains all the other effects such as kinematic constraints and experimental filter. The correlation function for the ^{20}O decay into ^{18}O by the emission of two neutrons is presented in Fig. 2.11(a). In Fig. 2.11(b), the two distributions $\sigma_{exp}(q_{nn})$ and $\sigma_{PS}(q_{nn})$ are shown, where the attractive effect of the n-n FSI at q_{nn} values below 100 MeV/c becomes clear.

2.3.3 Decay mechanisms and event generators

In the previous section, we presented a set of different observables used in order to study three-body correlations. Those observables have been used to illustrate the result of a three-body phase-space decay from a simulation. And by comparing it to the experimental data (Fig. 2.11 (b)), it is obvious that correlations beyond the phase space need to be implemented in the simulation in order to be able to reproduce what we observed in the experiment. In this section, we are therefore describing two decay mechanisms, and the model used in order to implement them into the simulation. Indeed, when a two-neutron decay occurs, mainly two modes are possible: the direct decay, in which the two neutrons are emitted at the same time, and the sequential decay, in which one neutron is emitted first, populating then a resonance in the intermediate nucleus that is decaying later (depending on the lifetime of the state) by emitting the second neutron. The model used does not include the microscopic structure of the initial state, and treats the effects of FSI and resonances on the fragment+2n phase-space decay phenomenologically. A description of the model can be found in [7, 59, 90]. We are summarizing and illustrating it in the following sections.

Direct decay

We start by the direct decay in which the two neutrons n_1 and n_2 are emitted at the same time. As mentioned before, the n-n FSI effects have to be added to the three-body phase-space decay simulation previously discussed (see section 2.3.1). To do so, we used the formalism from [91] which takes explicitly into account the influence of the two-nucleon proximity on the effects of their interaction. A simplified form of the two-particle cross-section can be expressed using a modified version (projection) of Eq. 2.1 such as:

$$\sigma(q_{nn}) \approx \sigma_0(q_{nn})\, C_{nn}(q_{nn}) \tag{2.39}$$

where σ_0 corresponds to the two-particle cross-section that the particles would exhibit if there were no influence between them and C_{nn} is the correlation function that can be expressed as follows:

$$C_{nn}(q_{nn}) \approx \int W(r_{nn})\, F(r_{nn}, q_{nn})\, dr_{nn} \tag{2.40}$$

where W is the spatial distribution of the source depending on the distance r_{nn} between the neutrons, here taken as a Gaussian, and F is the correlation factor that contains the effect of the s-wave n-n FSI as well as the effects of the Fermi statistics for identical particles (even if it is negligible in the case of nucleon pairs [91]). The correlation function can be thus seen as

a probability distribution $P(q_{nn})$ to accept the event following the form of the n-n correlation function C_{nn}, that depends on the space-time parameters (r_{nn}^{rms}, τ) of a Gaussian two-neutron source[1]. However, since in the case of a direct decay the two neutrons are emitted at the same time, we have $\tau = 0$ and therefore C_{nn} only depends on the relative distance between the neutrons r_{nn}^{rms}. And as discussed in [91], the correlation function of a Gaussian source becomes analytical. The validity of this assumption is discussed in [59] where it is shown that very different source distributions such as Gaussian, Yukawa-like, or spherical all lead roughly to similar Gaussian-like distributions for $W(r_{nn})$. Moreover, in our model, internal momentum correlations in the source ($W(r_{nn}, q_{nn})$) are assumed to be small or to have minor impact on C_{nn} after averaging over the whole source and are therefore neglected. The fact that this formalism has been used successfully in order to describe in an accurate way the low energy peaks observed in the n-n FSI of previous works [7, 56, 90, 92, 93] confirms the validity of the approximations made in our model.

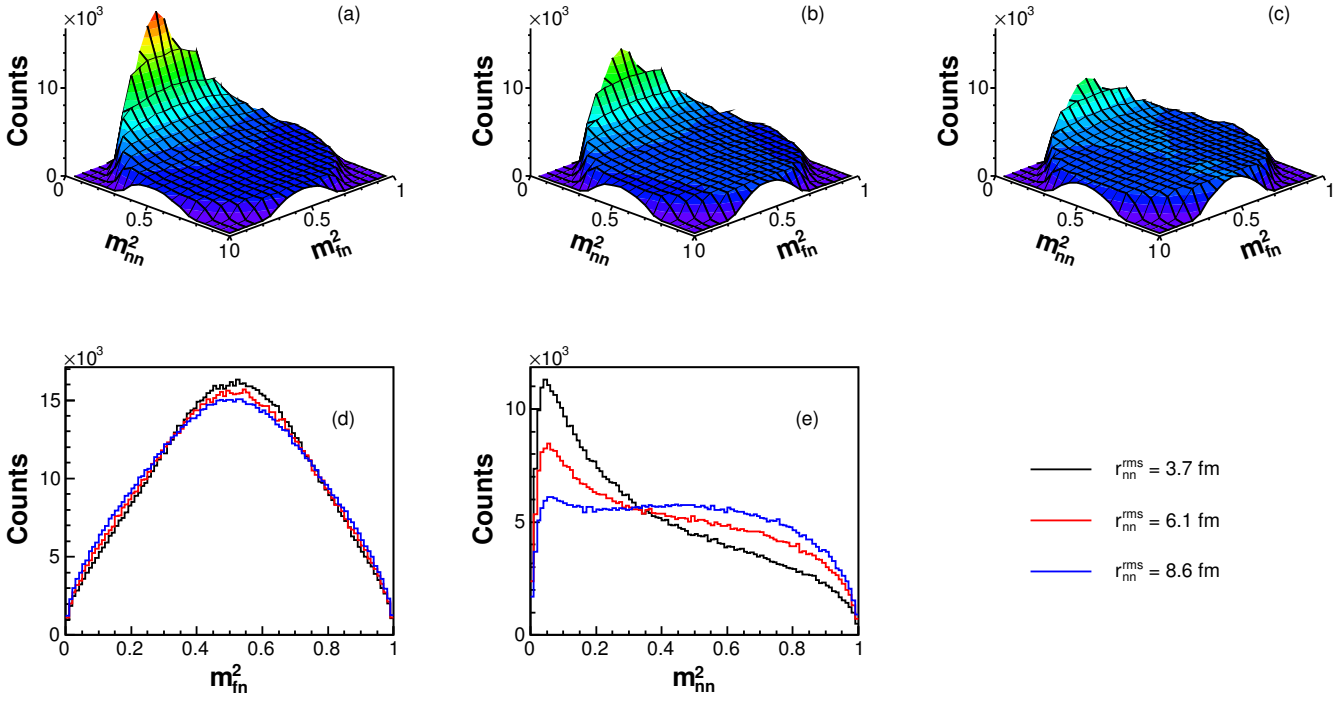

Figure 2.12: *(a), (b), (c) Dalitz plots for the ^{18}O+n+n direct decay for E_{rel} =0-12 MeV from the simulation with a source size of r_{nn}^{rms} =3.7, 6.1 and 8.6 fm, respectively. The projections onto the normalized invariant masses m_{fn}^2 (d) and m_{nn}^2 (e) are displayed for the three different r_{nn}^{rms} values.*

We can now observe how the n-n FSI is affecting the three-body phase-space decay where the only free parameter in our simulation is the average size of the source r_{nn}^{rms}. We take as an example the $2n$ decay of ^{20}O into ^{18}O. The results for different r_{nn}^{rms} are presented in the following for all the observables described in the previous section: the normalized invariant masses

[1]If the neutron volume $w(r_n)$ is taken as a Gaussian of width σ, and the neutrons move independently, the relative distance distribution $W(r_{nn})$ is also Gaussian with sigma $\sqrt{2}\sigma$ and $r_{nn}^{rms} = \sqrt{6}\sigma$.

(Fig. 2.12), the angular coordinates (Fig. 2.13), the Jacobi coordinates (Fig. 2.14) and the correlation function (Fig. 2.15). We are now describing the effects of the n-n FSI on each observable.

Dalitz plots - As we can observe in Fig. 2.12(a, b, c, e), the n-n FSI appears as a concentration of events at low m^2_{nn} (< 0.25), corresponding to small relative momenta. We also notice that a smaller source size shows a signal with higher amplitude. On the contrary, the m^2_{fn} variable (Fig. 2.12(d)) does not seem to be affected significantly.

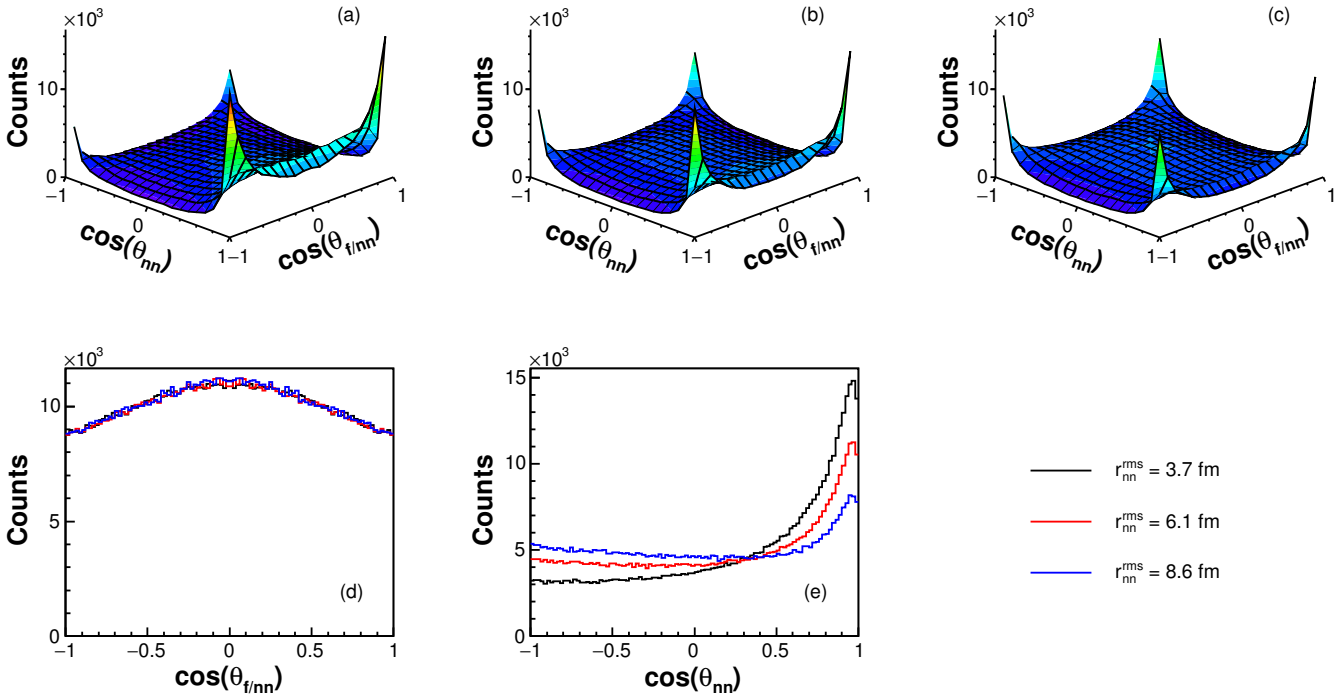

Figure 2.13: *(a), (b), (c) Two dimensional plots of $cos(\theta_{nn})$ as a function of $cos(\theta_{f/nn})$ for the ^{18}O+n+n direct decay for E_{rel} =0-12 MeV from the simulation with a source size r^{rms}_{nn} =3.7, 6.1 and 8.6 fm, respectively. The projections onto the $cos(\theta_{f/nn})$ (d) and $cos(\theta_{nn})$ (e) are displayed for three different r^{rms}_{nn} values.*

Angular coordinates - We can observe in Fig. 2.13(a, b, c, e) that the n-n FSI appears at small θ_{nn} angles and that the smaller the source size, the bigger the signal observed. On the contrary, as for m^2_{fn}, the $\theta_{f/nn}$ (d) variable seems to be unaffected by the n-n FSI.

Jacobi coordinates - As mentioned in the previous section, the Jacobi coordinates are directly comparable to the normalized invariant masses and to the angle coordinates. We observe in Fig. 2.14(b,c) that the E_x/E_{rel} observable in the "Y" system and the $cos(\theta_k)$ observable in the "T" system are not affected by the n-n FSI. However, the E_x/E_{rel} observable in the "T" system (a) is affected by the n-n FSI in the same way as the m^2_{nn} variable with a concentration of events at $E_x/E_{rel} < 0.25$. The θ_k variable in the "Y" system shows a concentration of events at large angles ($cos(\theta_k) < -0.5$). In both cases, the smaller the source

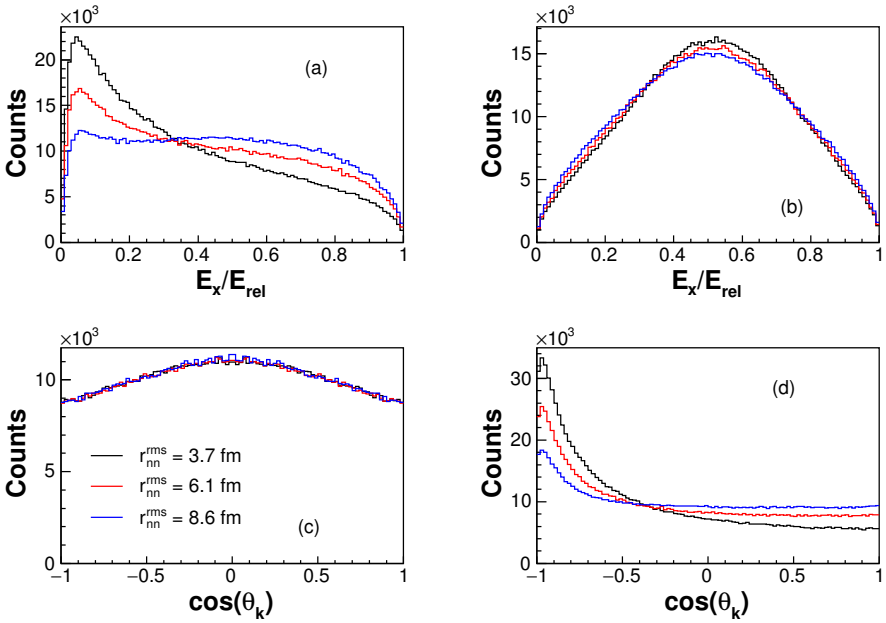

Figure 2.14: *"T" (left) and "Y" (right) Jacobi coordinates of the ^{18}O+n+n events from the simulation of a two-neutron direct decay for E_{rel} =0-12 MeV. The "T" system $[E_x/E_{rel}, cos(\theta_k)]$ coordinates are presented in (a) and (c), respectively and the "Y" system $[E_x/E_{rel}, cos(\theta_k)]$ coordinates in (b) and (d), respectively. The results of three different source sizes r_{nn}^{rms} are presented.*

size, the bigger the signal observed.

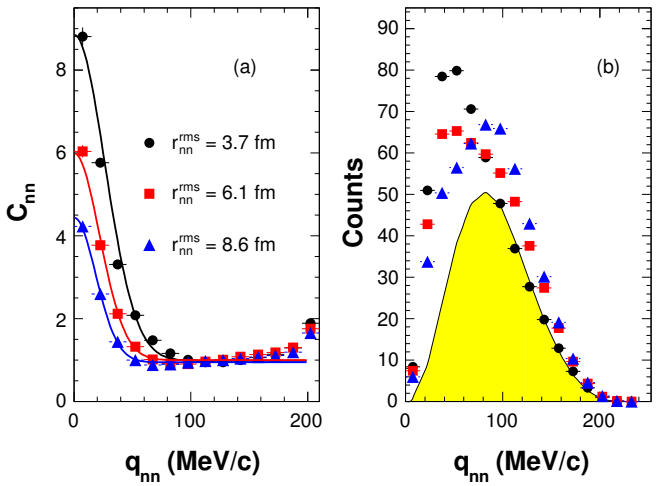

Figure 2.15: *(a) Two-neutron correlation functions and (b) relative momentum distribution (numerator of C_{nn}) and phase space (denominator of C_{nn} in yellow) for the ^{18}O+n+n direct decay for E_{rel} =0-12 MeV from the simulation for three different source sizes r_{nn}^{rms}. Lines has been added in (a) with the only purpose to guide the eye.*

Correlation function - As we can see in Fig.s 2.11(a) and 2.15(a), the *n-n* FSI is characterized by an accumulation of events at low q_{nn}, creating a strong deviation from the phase space distribution presented in Figs. 2.11(b) and 2.15(b). We also observe that the smaller the size of the source, the stronger the signal. It also seems that the shape of C_{nn} is directly linked to

the size of the emitting source in the case of a direct decay. With this method, it is hoped to directly deduce information on the size of the emitted pair, provided that the decay is direct.

Sequential decay

The other decay mechanism considered is the $n + n$ sequential decay, in which one neutron is emitted before the other. In order to simulate such a mechanism, the events are generated following twice the two-body phase space through a fragment-n resonance of energy E_r and width Γ (Breit-Wigner as presented previously in this chapter), followed by the interaction between the two emmited neutrons once the resonant state has decayed. In that case, the emission of the neutrons cannot be considered simultaneous ($\tau \neq 0$) and therefore a space-time analysis is needed, meaning that n-n FSI depends on the space-time parameters (r_{nn}^{rms}, τ). As discussed in [91], this leads to the fact that C_{nn} is not analytical anymore.

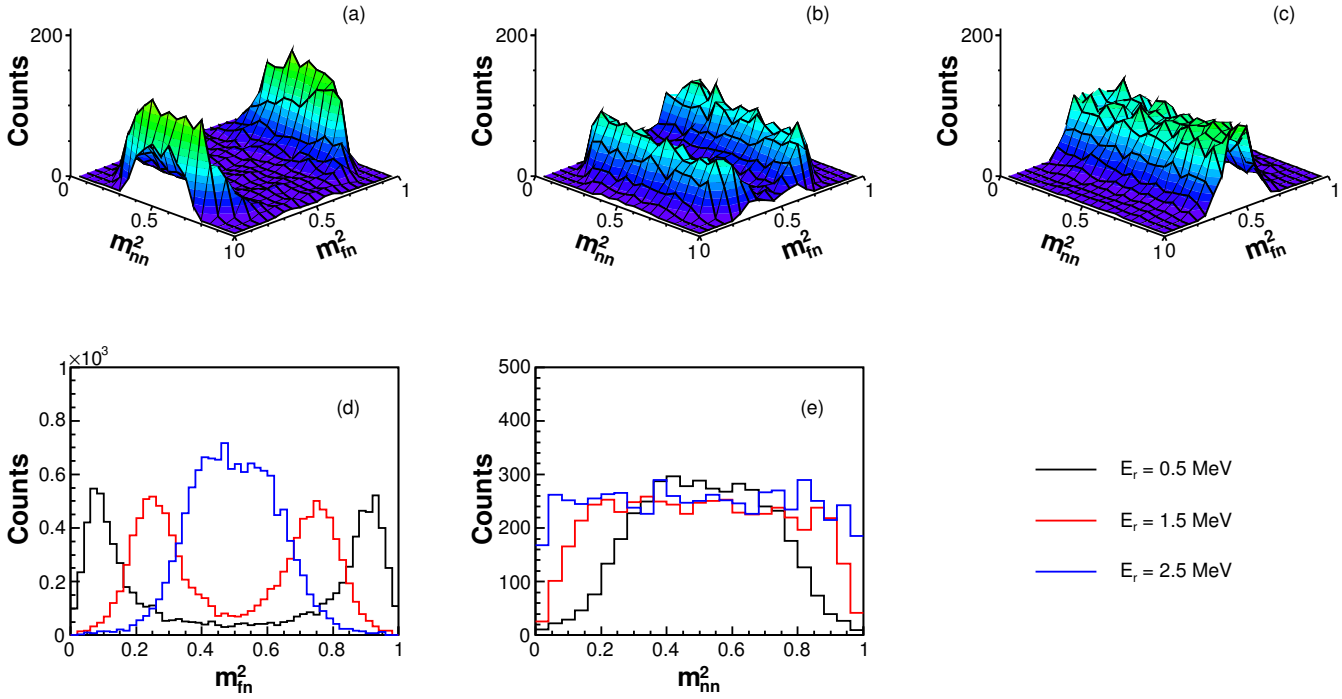

Figure 2.16: *(a), (b), (c) Dalitz plots of the ^{18}O+n+n sequential decay for E_{rel} =5.3-7.2 MeV from the simulation for E_r =0.5 MeV, E_r =1.5 MeV and E_r =2.5 MeV, respectively (r_{nn}^{rms} =6.1 fm and Γ_r =0.5 MeV being fixed). The projections onto the normalized invariant masses m^2_{fn} (d) and m^2_{nn} (e) are displayed for three different E_r values.*

We are then left with four parameters: r_{nn}^{rms}, τ, E_r and Γ. The number of parameters can be reduced, as it has been shown in [59] for the well-known ^{7}He resonance, to three by equating the delay induced in the neutron emission with the lifetime of the fragment-n resonance, leading to:

$$\tau = \frac{\hbar c}{\Gamma} \tag{2.41}$$

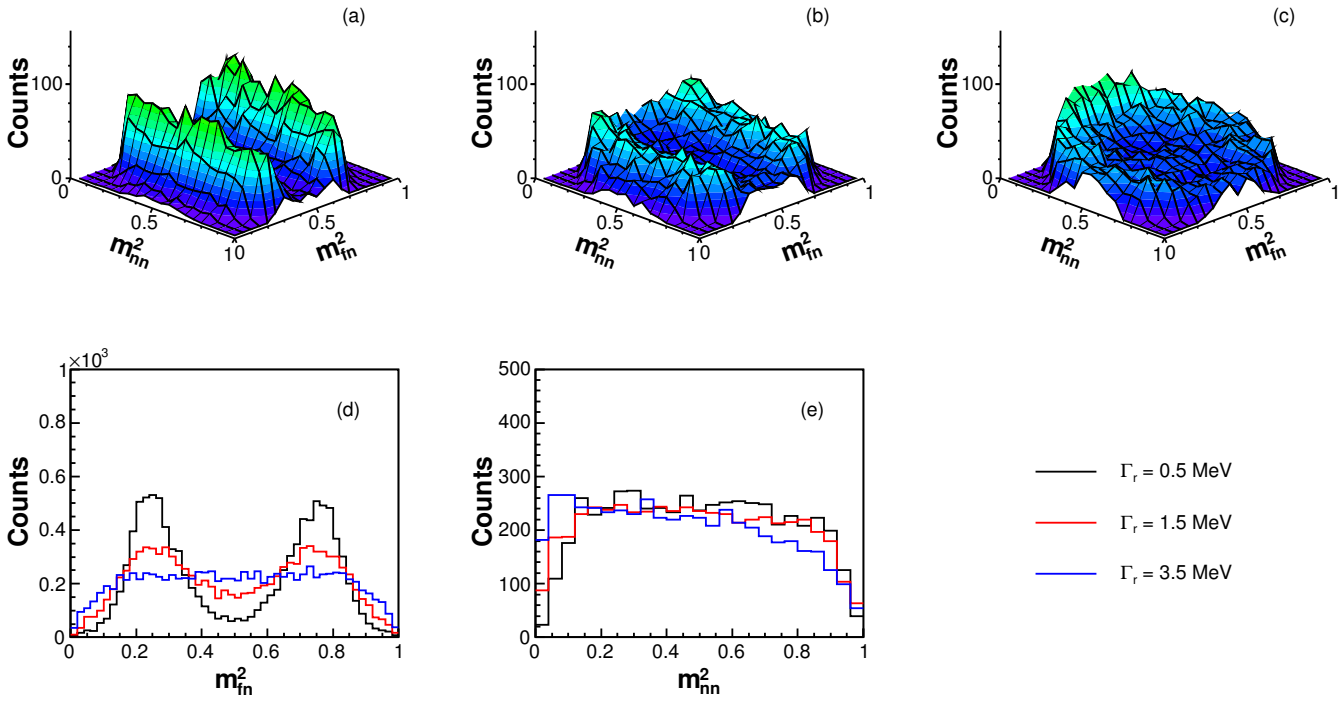

Figure 2.17: *(a), (b), (c) Dalitz plots of the ^{18}O+n+n sequential decay for E_{rel} =5.3-7.2 MeV from the simulation for Γ_r =0.5 MeV, Γ_r =1.5 MeV and Γ_r =3.5 MeV, respectively (r^{rms}_{nn} =3.9 fm and E_r =1.5 MeV being fixed). The projections onto the normalized invariant masses m^2_{fn} (d) and m^2_{nn} (e) are displayed for three different Γ_r values (the black curve here corresponds to the red curve in Fig. 2.16).*

In this case, the only free parameters of the sequential decay are (r^{rms}_{nn}, E_r, Γ).

The results of the sequential $2n$-decay simulation of ^{20}O into ^{18}O for 5.3< E_{rel} <7.2 MeV are presented in the following for all the observables mentioned before: the normalized invariant masses (Fig. 2.16, Fig. 2.17), the angular coordinates (Fig. 2.18, Fig. 2.19), the Jacobi coordinates (Fig. 2.20, Fig. 2.21) and the correlation function (Fig. 2.22). We are now discussing the effects observed for different resonance energies and widths on each observable.

Dalitz plots - We can observe on Fig. 2.16(a, b, c, d) that the sequential decay is characterized by ridges on the Dalitz plot and by double humped structures (except when the centroid of the resonance is in the middle of the decay energy range) in the projection over m^2_{fn}. Since we fill up two times the m^2_{fn} histogram, one time for each neutron n_1 and n_2, we observe two symmetrical wings in (d) as $m^2_{fn_1} \approx 1 - m^2_{fn_2}$. The position of the bands/wings is directly related to their energies compared to the maximum energy (E_{rel}) available in the system. Looking at Fig. 2.16(e), we see that the energy of the resonance E_r also has an influence on m^2_{nn}. Indeed, the smaller the resonance energy is, the narrower the m^2_{nn} distribution is, due to the kinematic boundaries of the three-body decay.

Looking now at the influence of the resonance width Γ on the m^2_{fn} variable (Fig. 2.17(a, b,

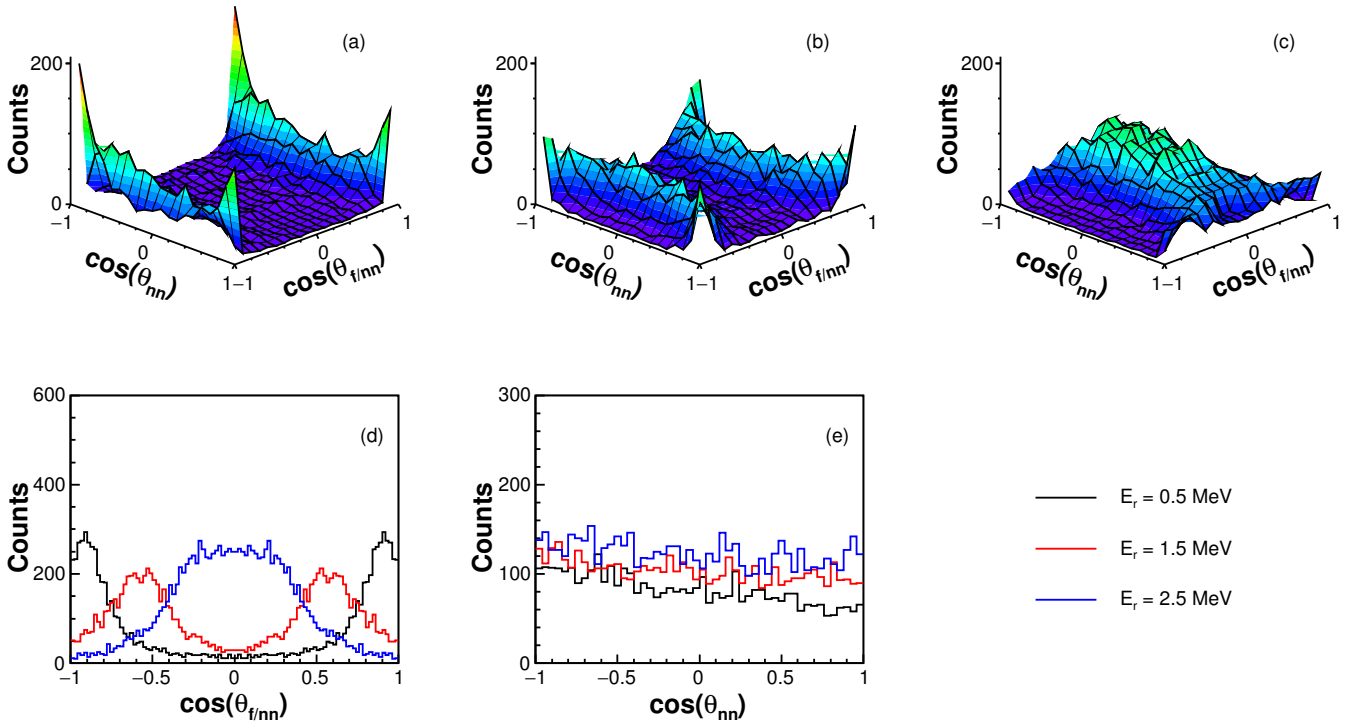

Figure 2.18: *(a), (b), (c) Two dimensional plots of $cos(\theta_{nn})$ as a function of $cos(\theta_{f/nn})$ for the ^{18}O+n+n sequential decay for E_{rel} =5.3-7.2 MeV from the simulation with E_r =0.5 MeV, E_r =1.5 MeV and E_r =2.5 MeV, respectively (r_{nn}^{rms} =6.1 fm and Γ_r =0.5 MeV being fixed). The projections onto the $cos(\theta_{f/nn})$ (d) and $cos(\theta_{nn})$ (e) are displayed for three different E_r values.*

c, d)), we observe that the wider the resonance is, the wider the wings are. Since $\Gamma \propto 1/\tau$, wider resonance also means shorter lifetime and therefore that the two neutrons, even if emitted sequentially, remain close from each other when the second neutron is emitted, as we can observe in Fig. 2.17(a, b, c, e) where a signal appears at low m_{nn}^2 due to the n-n FSI. The wider the resonance is, the bigger this signal is.

We can conclude by saying that n-n FSI are revealed by the m_{nn}^2 observable and that the m_{fn}^2 variable is sensitive to the sequential decay mechanism. Therefore, using a two-dimensional analysis we can have access to information on the decay mechanism involved in the reaction.

Angular coordinates - Looking now at the angular correlations in Fig. 2.18, we see that the sequential decay is characterized by bands on the two dimensional plot (a), (b), (c) and by wings on the projection over $cos(\theta_{f/nn})$ (d). The position of the bands/wings observed is depending on the resonance energy and on the maximum energy E_{rel} available in the system. However, the $cos(\theta_{nn})$ observable (e) does not seem to be affected at all by the sequential decay mechanism.

We are investigating in Fig. 2.19 the influence of the resonance width on the angular coordinates. We observe that similarly to the case of the normalized invariant masses m_{fn}^2,

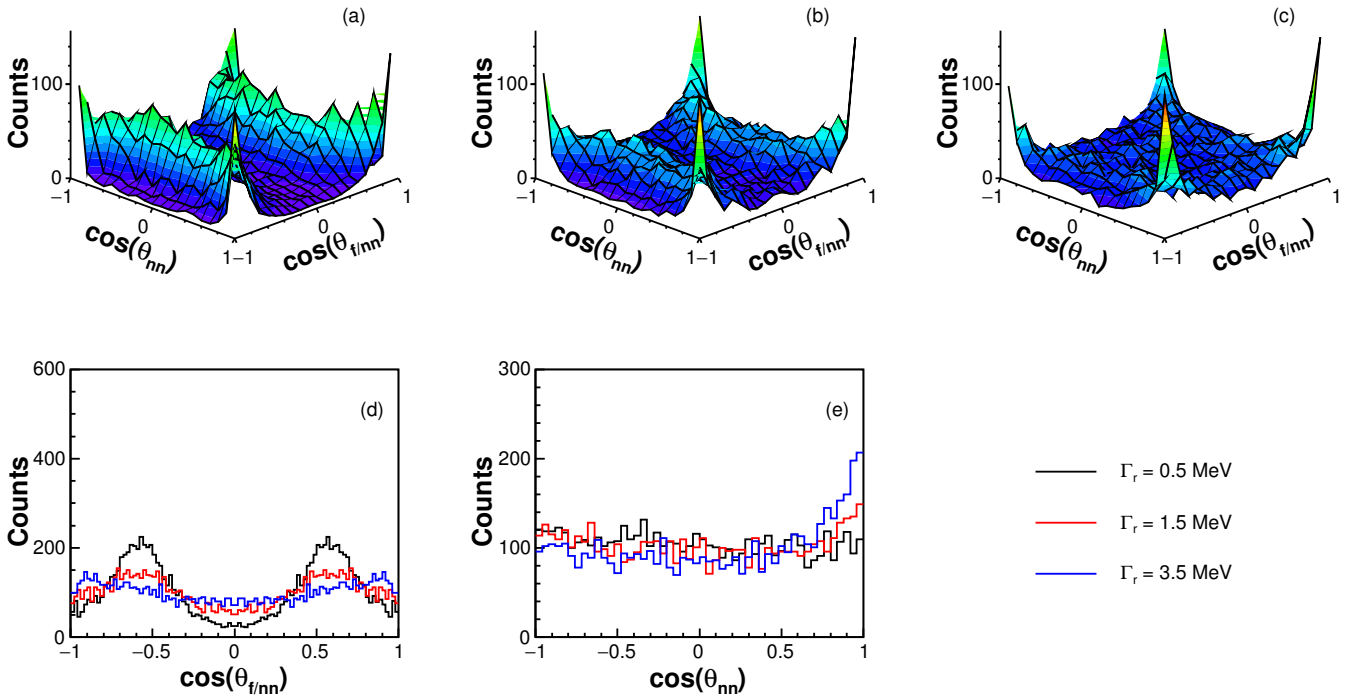

Figure 2.19: *(a), (b), (c) Two dimensional plots of $cos(\theta_{nn})$ as a function of $cos(\theta_{f/nn})$ for the ^{18}O+n+n sequential decay for E_{rel} =5.3-7.2 MeV from the simulation with Γ_r =0.5 MeV, Γ_r =1.5 MeV and Γ_r =3.5 MeV, respectively (r_{nn}^{rms} =3.9 fm and E_r =1.5 MeV being fixed). The projections onto the $cos(\theta_{f/nn})$ (d) and $cos(\theta_{nn})$ (e) are displayed for three different Γ values.*

wider resonances lead to wider structures in the $cos(\theta_{f/nn})$ (d) variable. Also a wide resonance (short lifetime) allows *n*-*n* FSI to survive as we can observe in the projection over $cos(\theta_{nn})$ (e) where a signal arises at low angles.

Jacobi coordinates - As discussed in the previous section, the Jacobi coordinates are analog to the normalized invariant masses and to the angular coordinates as can be seen in Fig. 2.20 and Fig. 2.21. Indeed we observe the same effects of the resonance energy and width as observed previously using the two other sets of coordinates. The E_x/E_{rel} (a) and $cos(\theta_k)$ (d) in the "T" and "Y" system, respectively, are sensitive to the *n*-*n* FSI whereas E_x/E_{rel} (b) and $cos(\theta_k)$ (c) in the "Y" and "T" system, respectively, are sensitive to the characteristics of the sequential decay.

Correlation function - Looking at Fig. 2.22 (b), we observe that the q_{nn} distribution is influenced by the resonance energy E_r. Indeed, we see that the higher E_r is, the narrower the q_{nn} distribution is which is due to the kinematic boundaries of the three-body decay. This effect is also revealed in the *n*-*n* correlation function (a) where a signal appears at low q_{nn} when E_r increases.

Fig. 2.23 shows that a small resonance width Γ induces the rising of signal at low q_{nn}. As we discussed earlier, such a signal is characteristic of *n*-*n* FSI. This observation is agreeing with

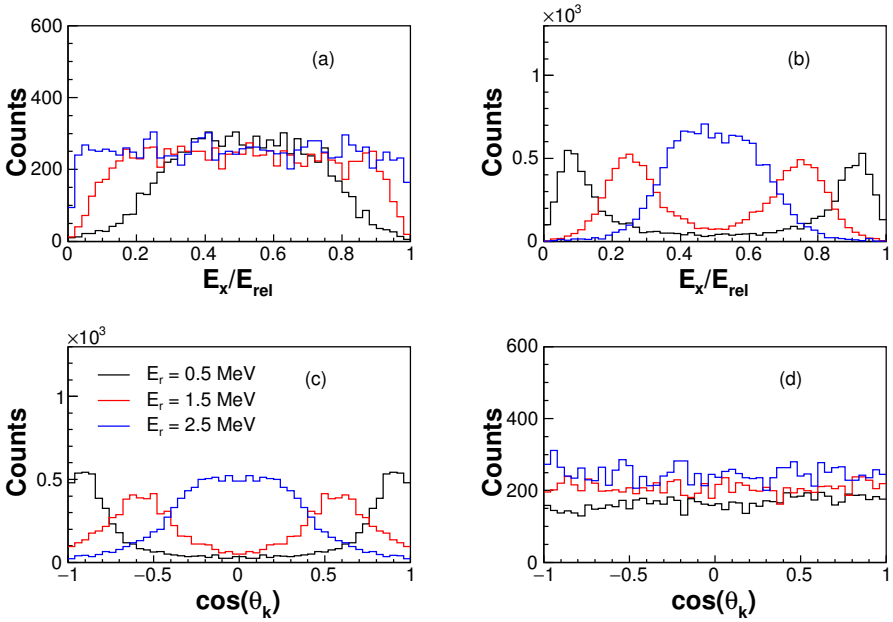

Figure 2.20: *"T" (left) and "Y" (right) Jacobi coordinates of the ^{18}O+n+n events from the simulation of a two-neutron sequential decay for E_{rel} =5.3-7.2 MeV with r_{nn}^{rms} =6.1 fm and Γ_r =0.5 MeV. The "T" system $[E_x/E_{rel}, cos(\theta_k)]$ coordinates are presented in (a) and (c), respectively and the "Y" system $[E_x/E_{rel}, cos(\theta_k)]$ coordinates in (b) and (d), respectively. The results of three different resonance energies E_r are shown.*

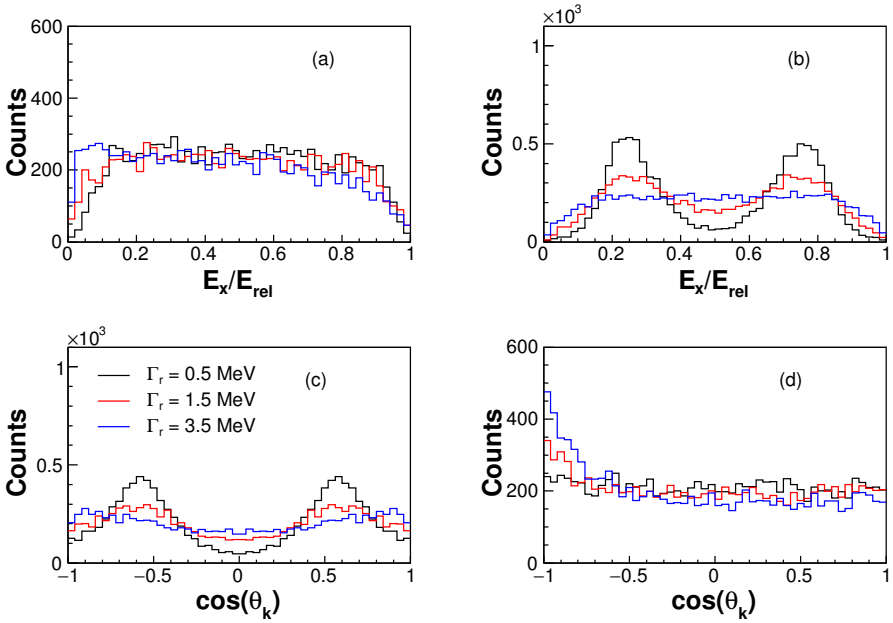

Figure 2.21: *"T" (left) and "Y" (right) Jacobi coordinates of the ^{18}O+n+n events from the simulation of a two-neutron sequential decay for E_{rel} =5.3-7.2 MeV with r_{nn}^{rms} =3.9 fm and E_r =1.5 MeV. The "T" system $[E_x/E_{rel}, cos(\theta_k)]$ coordinates are presented in (a) and (c), respectively and the "Y" system $[E_x/E_{rel}, cos(\theta_k)]$ coordinates in (b) and (d), respectively. The results of three different resonance widths Γ are shown.*

what we observed already in the other observables. We also observe that the amplitude of the

signal observed for the sequential decay is smaller than the one observed for the direct decay (Fig. 2.15) for the same distance r_{nn}^{rms}.

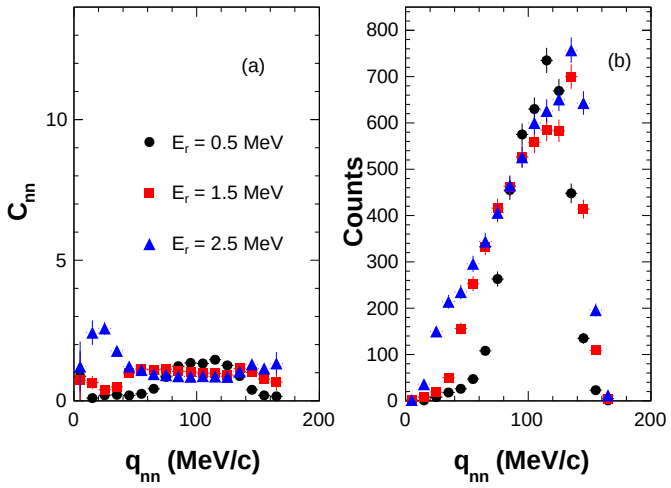

Figure 2.22: *(a) Two-neutron correlation functions and (b) relative momentum distribution (numerator of C_{nn}) for the ^{18}O+n+n sequential decay for E_{rel} =5.3-7.2 MeV from the simulation with r_{nn}^{rms} =6.1 fm, Γ_r =0.5 MeV and three different resonance energy values E_r.*

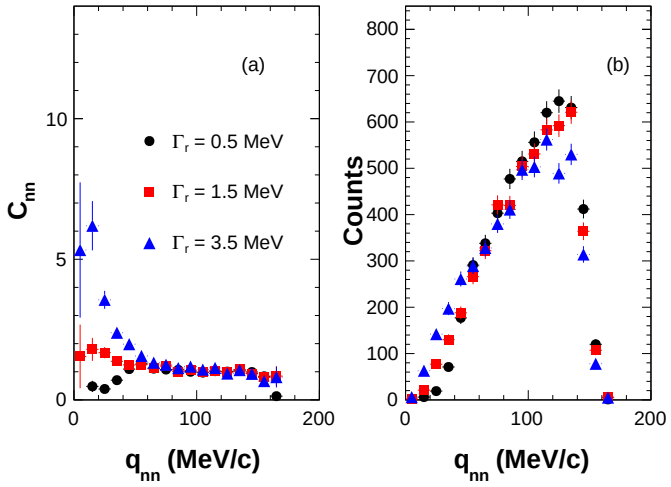

Figure 2.23: *(a) Two-neutron correlation functions and (b) relative momentum distribution (numerator of C_{nn}) for the ^{18}O+n+n sequential decay for E_{rel} =5.3-7.2 MeV from the simulation with r_{nn}^{rms} =3.9 fm, E_r =1.5 MeV and three different resonance width Γ values.*

Chapter 3

Experimental method and setup

Contents

As we discussed in the previous chapter, this thesis is focused on the study of neutron unbound states of neutron-rich nuclei. In order to conduct such a study, we introduced in the previous chapter the invariant-mass method [94] which is a key element in the investigation of neutron unbound states. Indeed, the invariant mass M_{inv} corresponds to the mass of the unbound state before the decay. Then by subtracting the masses of the different decay products, we obtain the relative energy E_{rel} of the system which is the energy available for the decay, sometimes also referred to as the decay energy E_d.

However, we need first to populate the unbound states. This is done in inverse kinematics at beam velocity using knockout reactions, where one or several nucleons are suddenly removed after interaction with the target. Because we are working in inverse kinematics, the decay products are also emitted at approximately the beam velocity.

In order to compute the invariant mass, we need to have access to the four-momenta of all the decay products involved in the reaction. This is achieved by using a complex set of detectors to track and select the beam, and detect the charged fragment, neutron(s) and eventually γ-rays in coincidence. Two different setups, that will be described in the following sections, have been used during this thesis in order to conduct such kind of experiments: R3B-LAND at GSI and SAMURAI at RIKEN.

3.1 Population of unbound states

The reaction mechanism is crucial since it has an influence on the production rate as well as the properties of the populated states. There are several techniques that can lead to the production of unbound states such as inelastic scattering, transfer reactions, fusion-evaporation reactions, and also knockout reactions, that have been used during our experiments and will be presented in more detail in this section. In order to populate exotic or unbound nuclei close to the dripline and study the properties of the populated states, it is necessary to work in two steps, that we are describing below.

We start by producing a high-energy radioactive beam of neutron-rich nuclei (secondary beam) close to the dripline. The best way in order to obtain such a beam with a sufficient intensity is by fragmentation of a high-energy stable beam (primary beam). The characteristics of the radioactive beam produced (energy, intensity, purity and spatial spread) are key parameters that are conditioning the success of an experiment. Indeed, those characteristics are influencing the number of events N_{evt} measured during the experiment. We can express N_{evt} such as:

$$N_{evt} = N_{inc}\ \rho\ x\ \sigma\ \epsilon \tag{3.1}$$

where N_{inc} is the number of incoming ions (that depends on the duration of the experiment and on the beam intensity), ρx is the thickness of the reaction target taking into account its density, σ is the reaction cross-section (probability that an incoming ion interacts with an ion of the target, that is energy dependent) and ϵ is the experimental setup detection efficiency. In order to successfully perform an experiment, one should try to maximize N_{evt}, to have a good resolution and ensure a good selection of the events of interest.

We saw in the previous section that in order to use the invariant-mass method, we need to be able to detect and characterize all the products of the reaction. However the detection of gammas and neutrons for example is far from being 100% efficient. It appears then that some factors of Eq. 3.1 are highly constrained by the experimental setup. We therefore need to try to maximize the other parameters.

We chose in our experiments to use direct reactions in inverse kinematics from a high-energy radioactive beam. Being at high energy (typically around 430 MeV/nucleon at GSI and around 230 MeV/nucleon at RIKEN) allows the use of thicker targets in order to maximize the interaction probability of the beam. And working in inverse kinematics facilitates the detection of all the reaction products as they are focused in the forward direction.

In order to populate unbound states, we chose to use knockout reactions of one or several

nucleons. At high energies, the cross-section for such reactions is rather high (10-100 mb). High-energy knockout reactions also have the advantage of being sudden, meaning that it is a one-step process where the final state is influenced by the initial state, and nucleons that are not involved in the knockout reaction are spectators and therefore unaffected. Since the initial state directly influences the final state, populating the same system from different knockout reactions (hence different incoming ions) allows us to do a selection on the final state.

The secondary beams used in our experiments as well as the nuclei studied using knock-out reactions are presented in Fig. 3.1. We sum up here the different reactions studied: ^{29}Ne(p,2p)^{28}F$^{(*)}$, ^{29}F(p,pn)^{28}F$^{(*)}$, ^{27}F(p,pn)^{26}F$^{(*)}$, ^{19}N(p,2p)^{18}C$^{(*)}$ and ^{21}O(p,pn)^{20}O$^{(*)}$. As we can see already, we have the chance to populate ^{28}F via two different knockout reactions, which could help us to have a complete picture of its structure.

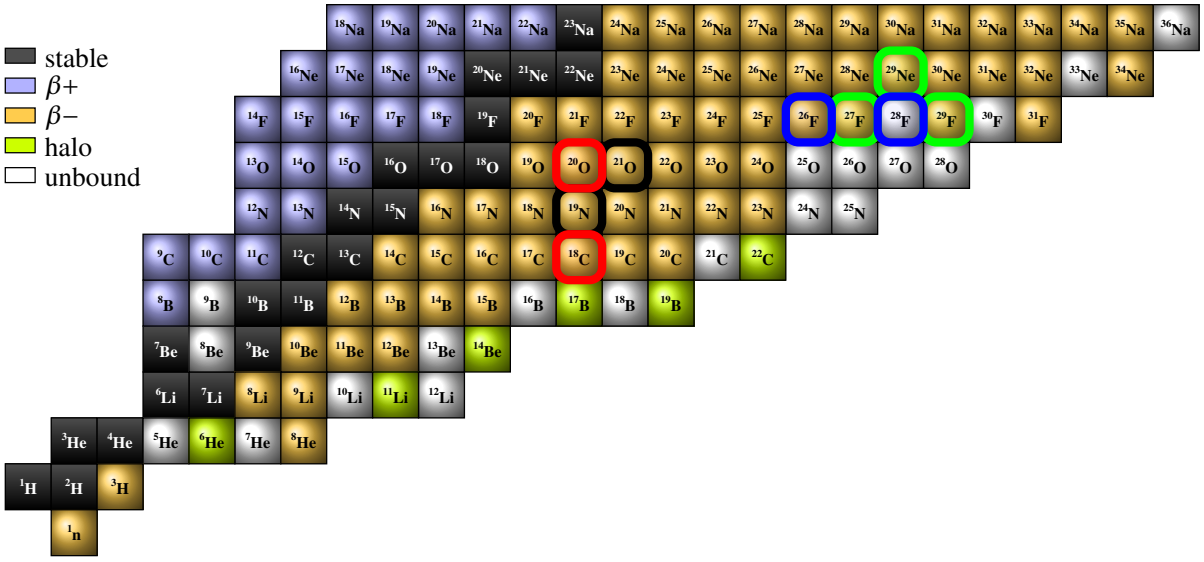

Figure 3.1: *Nuclei studied during this thesis at RIKEN (blue square) and GSI (red square). The secondary beams used to populate them are also presented in green and black squares for RIKEN and GSI, respectively.*

As mentioned earlier, the data presented in this document have been taken in two different laboratories (GSI and RIKEN). This choice to use two different facilities and setups has been made due to the capabilities of each accelerator to produce the desired beams and also due to the available setups.

3.2 General principle

One of the key observables to investigate and characterize unbound states is the relative energy introduced in section 2.2.2. And in order to access it, we need to be able to identify and measure the momenta of all the products involved in the decay of an unbound system.

We present in Fig. 3.2 the typical setup used during our experiments.

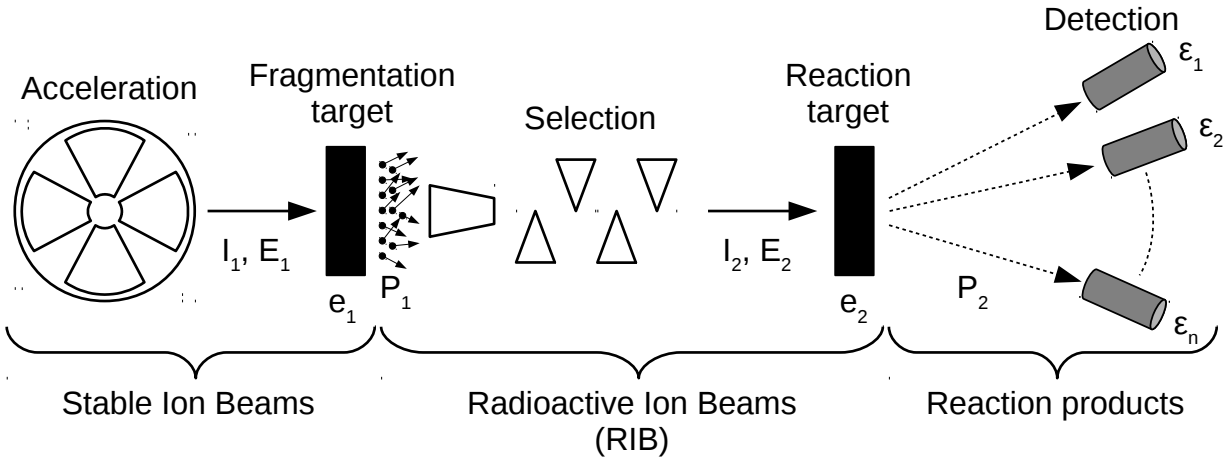

Figure 3.2: *Sketch of the general principle used during our experiments.*

The first step is to accelerate a stable beam to high energy and send it onto the fragmentation target in order to produce a big variety of radioactive isotopes. However we are not interested by all the radioactive isotopes produced. A $B\rho$ selection is then applied using a succession of dipole magnets. By doing such a selection, the ions are separated according to their mass to charge ratio (A/Z). Indeed, while traveling through a dipole magnet, the Lorentz force equals the centripetal force which keeps the particle of charge number Z and mass number A on a circular orbit with radius ρ, leading to the following conditions:

$$B\rho = C\frac{A}{Z}\beta\gamma \tag{3.2}$$

where B is the strength of the magnetic field, β is the velocity of the ion and γ is the associated Lorentz factor. The constant C is given by:

$$C = \frac{uc}{e} = 3.1 \text{ Tm} \tag{3.3}$$

This formula is only valid for high-energy beams for which the ions are fully stripped. Otherwise the charge number Z of the ion has to be replaced by the charge q. The radius ρ is fixed and corresponds to the one defined by the beam line. This formula means that, by tuning the magnetic field B applied, we can chose which ions with a specific A/Z ratio follow the central trajectory of the beam line, and which ones are blocked in thick slits placed at the intermediate dispersive focal plane.

After this stage, we have a high-energy cocktail beam of radioactive isotopes containing the isotope of interest as well as some contaminants with similar A/Z ratio. The beam then impinges on the reaction target into which knockout reactions occur, producing different states of the nuclei of interest. Those states decay then by γ-ray or particle emission (unless bound states are populated) and we identify and characterize the products of the reaction using a complex detection system that we describe below in Fig. (3.3).

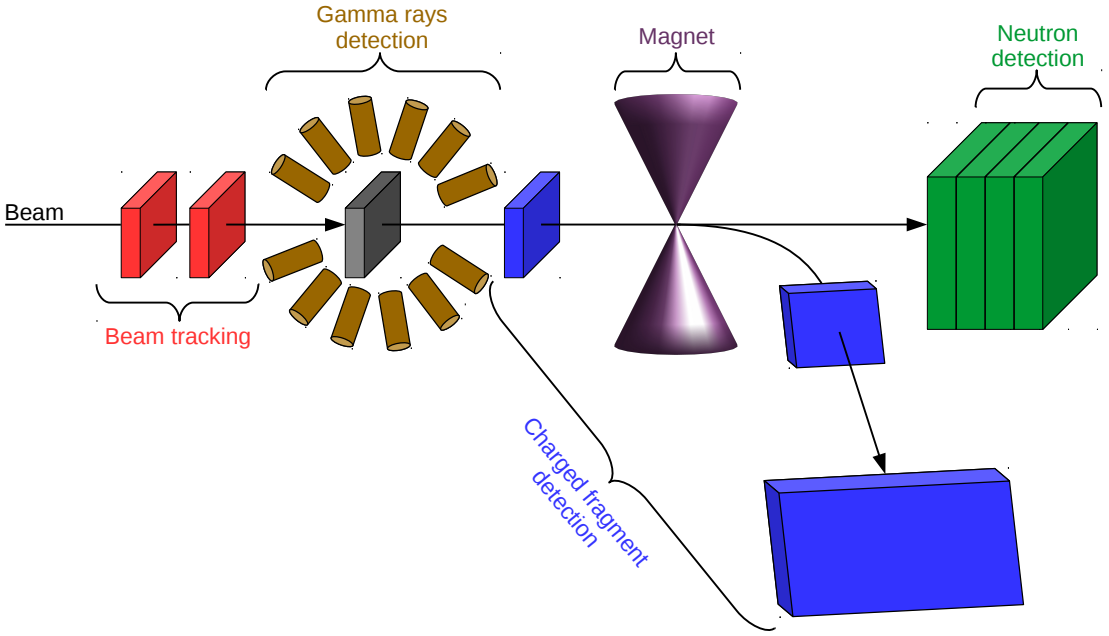

Figure 3.3: *Sketch of the typical detection setup used during our experiments, with the beam traveling from left to right. It is first going through beam trackers in order to reconstruct its trajectory before reaching the reaction target, which is surrounded by a γ-ray detector to detect eventual in flight γ rays. After the reaction, the emitted neutron(s) go straight into a neutron detector where their trajectory and time of flight are measured, while the charged fragment, deflected by a magnet, is detected and identified using a set of detectors allowing us to reconstruct its trajectory and energy loss.*

We are interested in unbound states that decay by emitting one or several neutrons. And in order to investigate them, we need to compute the relative energy (see section 2.17). To do so, we need to identify event by event the incoming nuclei and determine the energy and the momentum of each reaction product. The different quantities needed to investigate unbound states are presented below:

1. Beam velocity β_b
2. Beam charge number Z_b
3. Beam trajectory
4. Fragment velocity β_f
5. Fragment charge number Z_f
6. Fragment mass number A_f
7. Fragment trajectory
8. Neutron(s) trajectory
9. Neutron(s) velocity β_n

How these quantities are derived using the R^3B-LAND or the SAMURAI s021 setups is explained in the following sections.

3.3 GSI and R^{3}B-LAND experimental setup

We are first presenting the experiment performed at GSI. In this experiment, we used the R^{3}B-LAND experimental setup. The description of the apparatus used can be divided in two different parts. We present first the production and selection of the radioactive ion beam and then the experimental setup used for the detection of the reaction products.

3.3.1 Beam production

The s393-experimental campaign has been performed at GSI, where the radioactive ion beam (RIB) is produced via an in-flight technique, meaning the radioactive ions are produced and separated in flight. This beam production is briefly explained in the following paragraph. Moreover, a schematic view of the GSI accelerator is presented in Fig. 3.4. The production mechanism of the RIB starts with a stable primary beam. At GSI the ions of choice are injected into the "UNIversal Linear ACcelerator" (UNILAC) from an ion source. In the experiment described here, ^{40}Ar ions have been used as primary beam. From the UNILAC the ^{40}Ar^{11+} beam is injected into the "Schwer Ionen Synchrotron-18" (SIS-18), having an energy of nearly 11.5 MeV/nucleon.

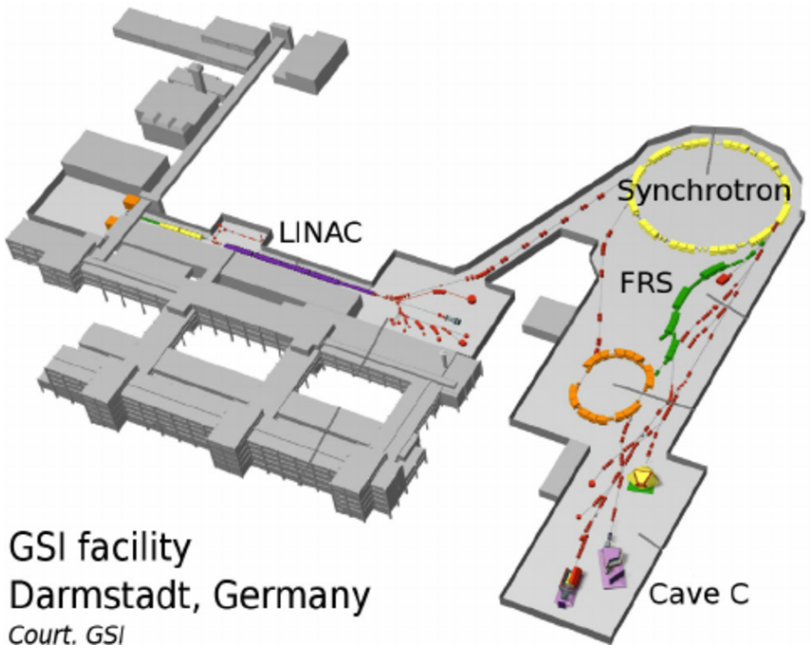

Figure 3.4: *Schematic layout of the GSI accelerator complex used during the experiment.*

Leaving the SIS-18, the ^{40}Ar ions have been accelerated to an energy of 490 MeV/nucleon and the primary beam is guided onto the production target at the entrance of the FRagment Separator (FRS) presented in Fig. 3.5. A 4 g/cm^2 thick Be production target was used to induce fragmentation reactions. The primary beam had an intensity of 6×10^{10} ions/bunch. The beam composition delivered to the experimental cave depends on the FRS settings only. For a more detailed description of the FRS, see Ref. [95]. For the purpose of our experiment, the magnetic rigidity $B\rho$ of the FRS is set to 9.05 Tm in order to favor the transmission of nuclei with $A/Z \approx 2.7$. The reaction products of the nuclear fragmentation of the incoming ^{40}Ar beam impinging on the Be target are forming the cocktail or secondary beams with an

energy of nearly 430 MeV/nucleon. A large variety of elements with masses smaller than the one of the primary beam is produced. The beam composition is then selected by means of the $B\rho$ method (3.2) which is applied in the FRS. These secondary beams are then transmitted to the R^{3}B-LAND experimental setup located in Cave C.

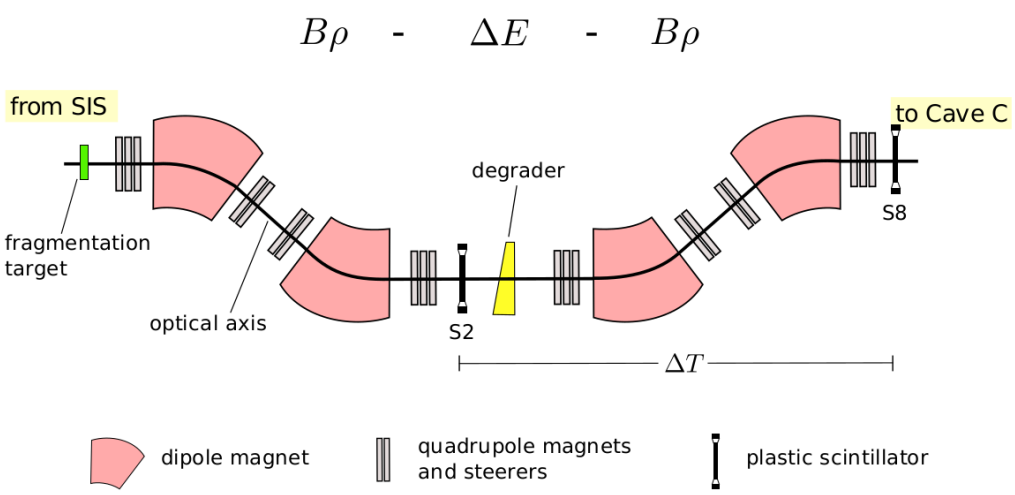

Figure 3.5: *Sketch of the FRS. The $B\rho$-ΔE-$B\rho$ method is applied using dipoles to bend the beam ($B\rho$) as well as a degrader to have a position and Z-dependent energy loss (ΔE) (figure taken from [6]).*

The FRS beam line has been equipped with two 3 mm thick scintillator paddles. Those detectors are needed to perform an incoming time of flight (ToF) measurement over a long distance (FRS to Cave C) for each ion. One scintillator paddle was placed at the middle focus (S2) and the second was situated behind the FRS (S8). Since the scintillator at the mid-plane of the FRS (S2), about 136 m upstream of the reaction target, was overloaded with the intense beam, the scintillator at the intermediate focal plane (S8) has been used, leaving us a nearly 55 m flight path to Cave C.

3.3.2 Beam identification

As mentioned in section 3.2, we need to be able to identify and characterize the incoming nuclei event by event. Therefore, the velocity of the beam β_b, its charge number Z_b and its trajectory have to be derived for each event. In order to identify incoming ions, the mass to charge ratio A_b/Z_b, as well as the charge number Z_b needs to be known. Using 3.2, we can derive:

$$\frac{A_b}{Z_b} = \frac{B\rho}{C}\frac{1}{\beta_b\gamma_b} \tag{3.4}$$

Therefore β_b and $B\rho$ are needed. The value of $B\rho$ is known from the FRS setting, so we only have to determine the velocity of the incoming ion β_b. This is done using a time of flight (ToF) method that needs two detectors (start and stop) in order to measure the time needed for a particle to travel a certain distance. In our case, we use a plastic scintillator paddle at S8 as start detector (see Fig. 3.5). This detector is read out with two photo-multiplier tubes (PMT), one at the top and one at the bottom. A square-shaped (2.5 cm×2.5 cm) plastic scintillator with thickness of 1 mm at the entrance of Cave C is used as a stop detector. The Cave C

experimental setup is shown in Fig. 3.6. This detector is called POS, and is read out with four PMTs, one for each side. Those two detectors allow us to measure the times t_{start} and t_{stop} from which we can deduce the velocity of the incoming ion β_b using the ToF method below:

$$\beta_b = \frac{d}{(t_{stop} - t_{start})c} \tag{3.5}$$

where c is the speed of light and d is the distance between these two detectors which is about 55 m, resulting in a very good velocity resolution.

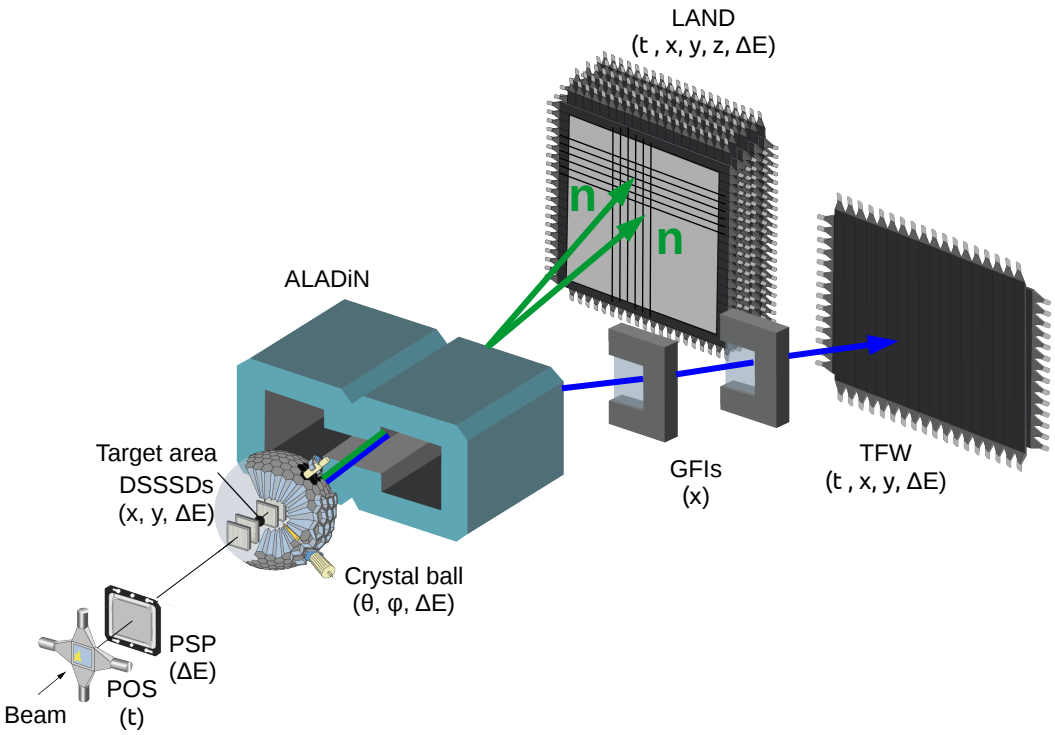

Figure 3.6: *Experimental setup in Cave C as used during the s393 campaign. The observables measured by each detector are presented in parenthesis.*

To complete the identification of the incoming ion, we also need to have access to its charge number Z_b. It is known that an ion passing through matter loses energy following the Bethe-Block formula:

$$\Delta E \propto \frac{Z_b^2}{\beta_b^2} \tag{3.6}$$

We can rearrange this formula such as:

$$Z_b \propto \beta_b \sqrt{\Delta E} \tag{3.7}$$

The charge number Z_b can therefore be derived from ΔE measurement using a position sensitive pin-diode (PSP) in front of the target. Now that we have access to Z_b and A_b/Z_b, we can select the ions of interest using two-dimensional cuts. The identification of the incoming beam is presented in Fig. 3.7.

The identification of the incoming ions is now completed but we still need the information on their trajectories. We can access this information using two double sided silicon strip detectors

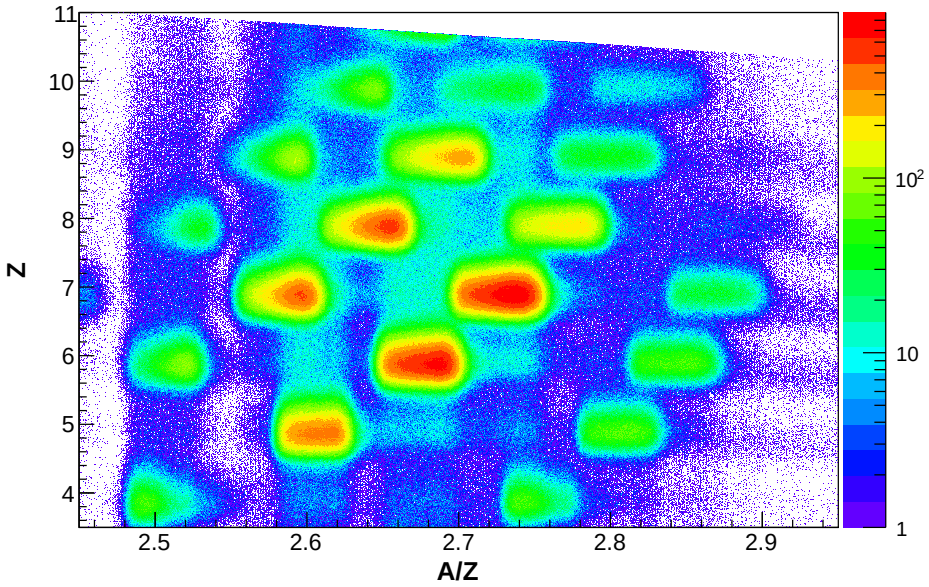

Figure 3.7: *Identification of the nuclei in the cocktail beam.*

(DSSSD) as shown in Fig. 3.6. Each DSSSD has an active area of 72×41 mm^2 and strips 300 μm thick (110 μm pitch). The coordinate system, used in the analysis presented here, is labeled in the following convention: the z-axis points in beam direction, the x-axis points to the left looking from the beam and the y-axis points to the top. Each in-beam DSSSD has two sides, the first side delivering measurement in the x-direction and the second side delivering measurement in the y-direction. Using these positions, we only need to know the distance between the two DSSSDs in order to deduce the trajectories of the incoming ions. We can then extrapolate the position of the interaction between the ion onto the reaction target, which is the next material. Two different reaction targets were used during the experiment: a 922 mg/cm^2 CH_2 target and a 935 mg/cm^2 C target. During the experiment, those two targets are mounted on a remote-controlled target wheel so they could be changed in vacuum without beam breaks.

3.3.3 Detection of the reaction products

While going through the reaction target, the incoming ion has a probability to react with a nucleus from the target. In our experiment, we are looking for knockout reactions from which unbound states can be populated. Those unbound states are decaying with the emission of one or several neutrons. We are therefore left with neutron(s), a charged fragment and possible γ-rays if excited states of the fragment are populated. In order to characterize the unbound states, we need to be able to identify and characterize all those reaction products. We specify the technique used to detect them in the following.

The outgoing fragments are detected in two DSSSDs, identical to the one in front of the target, directly behind the target (Fig. 3.6). Their charge is determined via a ΔE measurement (see equation 3.7) and the outgoing angle θ_f is measured as well. The target is surrounded by a 4π NaI sphere named crystal ball (CB). The CB is segmented into 159 crystals, each having a length of 20 cm and covering a solid angle of nearly 77 msr. The CB allows the detection

of photons ($\epsilon_\gamma \approx 60\%$ at 2 MeV) from excited fragments decaying in flight and recoil protons at angles larger than $\pm 7°$ in the laboratory frame. Each crystal is equipped with phototubes having a gain adapted for the detection of photons. Moreover, the photo-multipliers of the 64 most forward crystals have a second lower-gain readout for the detection of recoil protons originating from knockout reactions. This detector is used in our analysis to tag the recoiled proton resulting from a knockout reaction via the CB-sum trigger.

After having passed the downstream pair of DSSSDs, the reaction products leave the vacuum and enter ALADIN which is filled with helium gas. The magnetic field of ALADIN bends the charged fragments but leaves the neutrons unaffected on their straight trajectories. All detectors behind ALADIN are operated in air. In the following, we first focus on the detection of the fragments. The fragment detection branch is oriented such that the central position at each detector is at 15° with respect to the incoming beam axis. It consists of 3 detectors, two large fiber detectors (GFI-1 and GFI-2) and the time of flight wall (TFW), as shown in Fig. 3.6.

Each GFI is built of 480 vertical fibers covering in total an area of 50×50 cm^2. A position measurement in x-direction (horizontal) with a resolution of 1 mm [96] is done using this type of detectors. Having these two position measurements behind the magnet and the ones done by the DSSSDs in front of the magnetic field, the trajectory of the ions can be reconstructed. Different isotopes are deflected to different angles in the magnetic field of ALADIN according to their different mass-to-charge ratio (Eq. 3.2). Therefore, the $B\rho$ of an ion is measured by reconstruction of its track through the magnetic field. The $B\rho$ value determines the mass of the ion unambiguously if the charge is already known as we can see in Eq. 3.4. Detailed information on the GFIs can be found in [97] and the calibration procedure is described in [96].

The last detector in the fragment branch is the TFW and is located 523 cm behind the last GFI. This detector is built out of 14 horizontal scintillator paddles in the first plane and a second plane having 18 vertical paddles. Each horizontal paddle has the dimension (196.6×10.4×0.5) cm^3, while the vertical paddles have a dimension of (154.6×10.4×0.5) cm^3. All 32 paddles are read out using a PMT on each side. The time, the energy loss ΔE, as well as the position of each hit is measured. Having the ToF between target and the TFW and knowing the length of the trajectory gives the velocity β_f of the ion, while the deposited energy determines its charge Z_f. As an example, the identification in charge and mass of the fragments observed after the interaction between the target and a ^{19}N beam is presented in Fig. 3.8.

As mentionned before, when produced in an unbound state during a knockout reaction, nuclei may emit neutrons that are detected in the forward direction using the "Large Area Neutron Detector" (LAND) [98]. The detector covers an area of (2×2) m^2 and is 1 m deep. It consists of 10 planes and every plane contains 20 paddles, which have the dimensions of (200×10×10) cm^3. The detection of the neutrons is based on the use of inactive converter materials in which the neutrons create charged particles via nuclear reactions. Those secondary particles are then detected with plastic scintillators. In order not to stop too many of the created secondary charged particles in the converter material itself, the design of the detector is based on a sandwich structure using thin iron layers as converter material. One paddle has eleven iron and ten scintillator sheets of 5 mm thickness each. Only the two outermost iron layers have a thickness of 2.5 mm adding up again to 5 mm while stacking two paddles. A specific algorithm

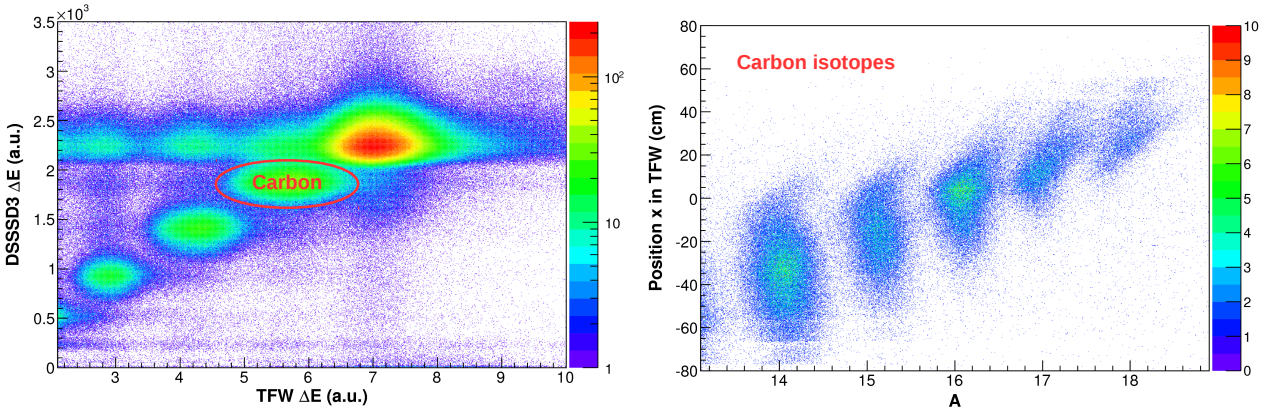

Figure 3.8: *Identification of the fragments produced from the interaction of* ^{19}N *nuclei from the beam with the target. The charge identification is presented of the left panel and the mass identification for the Carbon isotopes is presented on the right panel.*

is used to reconstruct the hit profiles in LAND [99], and obtain from them the position of the first neutron-LAND interaction (with a spatial resolution of 5 cm FWHM) and the neutron ToF (with a resolution of 370 ps FWHM). The LAND detector was placed 12 m downstream of the reaction target, covering forward angles of ±79 mrad. The $1n$ and $2n$ efficiencies are of the order of 90% and 70% up to about 4 MeV and 8 MeV fragment-neutron relative energy, respectively, and decrease smoothly beyond those values [58]. The $2n$ efficiency, that includes causality conditions for the rejection of cross-talk events, drops below 200 keV as neutrons are emitted within a very narrow cone and cannot be distinguished. The energy resolution of the observed neutron resonances degrades slowly from 200 keV at 500 keV to 700 keV at 5 MeV relative energy [58]. Using the information from LAND, the momentum of the neutron $\vec{p_n}$ is reconstructed.

3.4 RIKEN and SAMURAI experimental setup

We are presenting now the setup used during the SAMURAI 21 experiment performed at RIKEN in November 2015. In this experiment, we used the typical SAMURAI setup to which two multi-detectors have been added, the NeuLAND demonstrator and the MINOS active target. We present first the production and selection of the radioactive ion beam and then the experimental setup used for the detection of the reaction products.

3.4.1 Beam production

The SAMURAI 21 experiment has been performed at RIKEN where neutron-rich exotic beams necessary to our experiment (^{29}Ne, ^{30}Ne, ^{29}F...) are produced in several steps. The first step, as discussed in section 3.2, is to produce a stable beam (^{48}Ca here) from the ionization of a material. The ions created are then extracted from the plasma using electric fields in order to be sent to the acceleration devices (cyclotrons and linear accelerators). Like in GSI, the radioactive ions are produced and separated in-flight. In the experiment described here, the ^{48}Ca stable beam at nearly 345 MeV/nucleon impinged on the thin Beryllium target, inducing fragmentation reactions in which a large variety of radioactive ions with lighter mass and

smaller charge than the initial beam are produced. Those ions form the so-called cocktail or secondary beam.

The in-flight fragmentation is well adapted to the study of nuclei with short lifetime. Indeed, the ions produced with this technique have a velocity similar to the one of the stable beam used (nearly 60% of the speed of light) which enables their transport to the experimental area.

The primary beam at RIKEN is produced by the RIBF (Radioactive Ion Beam Factory) presented in Fig. 3.9. Its oldest part (built in the 90s [100]), called RARF (RIKEN Accelerator Research Facility), is made of two separated-sector cyclotrons (RRC) as well as two injectors: a linear accelerator (RILAC) and a cyclotron (AVF). In order to extend the capabilities of the facility to exotic nuclei, three separated-sector cyclotrons have been added (fRC, IRC and SRC). The RILAC2, a linear accelerator has also been built in order to produce very high intensity heavy-ion beams (U, Xe...). The entire facility allows the production of a large variety of stable beams with intensities of about 10^{12} particles per second (pps) [101]. The maximum energy that can be achieved goes from 350 to 440 MeV/nucleon depending on the isotope.

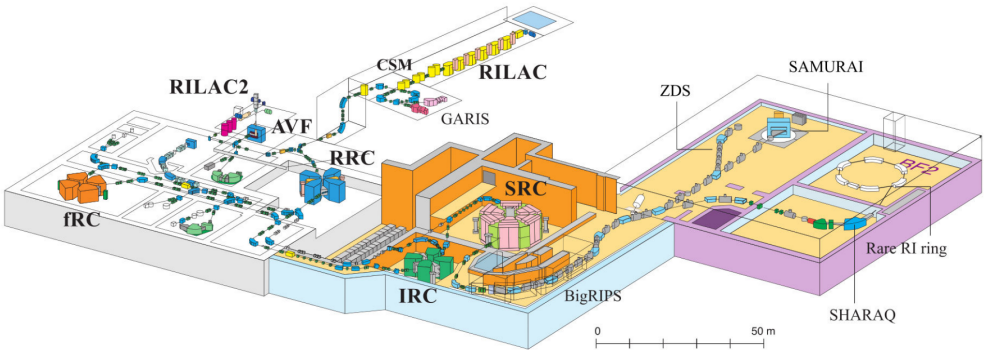

Figure 3.9: *Sketch of the RIBF facility at RIKEN. During the SAMURAI 21 experiment, the ^{48}Ca stable beam has been accelerated from the linear accelerator RILAC to the cyclotron SRC. After fragmentation on the Be target, the radioactive beam was selected using the BigRIPS fragment separator before being sent to the SAMURAI experimental area.*

As mentioned previously, the stable beam produced by the RIBF facility is fragmented in a cocktail beam containing a large diversity of nuclei with lower charges and lighter masses with respect to the primary beam. However, we are interested only by a small proportion of nuclei in the cocktail beam. The fragment separator BigRIPS, which is made of different magnets, is therefore used to select nuclei of interest by means of the $B\rho$ method developed in section 3.2. This method allows us to select the A/Z ratio of our nuclei of interest.

The BigRIPS fragment separator in presented in Fig. 3.10. Its line is nearly 75 m long and is made of seven dipoles (labeled from D1 to D7) placed between the primary target (F0) and the focal plane F7. Quadrupoles (labeled form STQ1 to STQ25) are also used in order to focus the beam and assure a good transportation of the beam in the beam line.

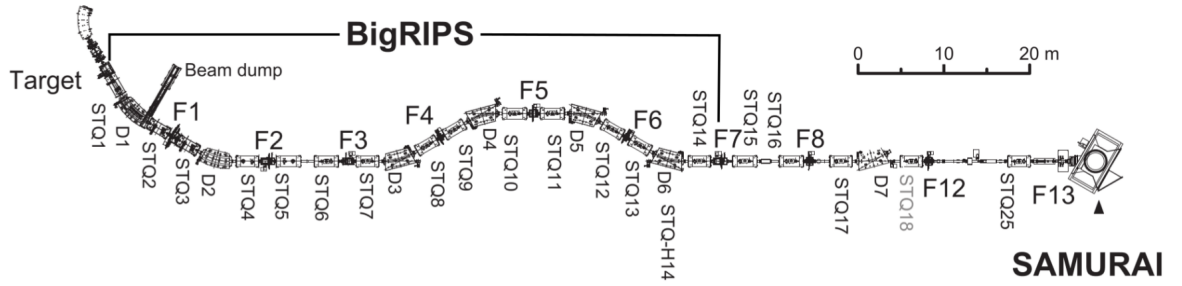

Figure 3.10: *Sketch of the BigRIPS fragment separator. The different dipoles are labeled from D1 to D7 and the quadrupoles allowing the focusing of the beam are labeled from STQ1 to STQ25.*

3.4.2 Beam identification

As mentioned before in section 3.2, we need to be able to identify and characterize incoming nuclei event by event. Therefore, the velocity of the beam β_b, its atomic number Z_b and its trajectory has to be determined for each event.

In order to identify the incoming ion, the charge number Z_b and the A_b/Z_b ratio are needed. The latter can be expressed as shown in Eq. 3.4, where only $B\rho$ and the beam velocity β_b need to be determined. The value of $B\rho$ being known from the BigRIPS setting, only the beam velocity β_b is needed. This is done using the time of flight (ToF) technique developed in section 3.3.2. This technique allows to measure the velocity of nuclei event by event. It is performed using four plastic scintillators placed along the beam line. The position of each of those plastic scintillators is detailed in Table 3.1. Knowing the distances and the time of flight between the detectors, we have access to the velocity β_b of the incoming ion and can therefore compute its A_b/Z_b ratio.

To complete the identification of the incoming ion, we also need to determine its charge number Z_b. This is done using the Bethe-Block formula (see Eq. 3.6) that links Z_b to the energy loss (ΔE) in a material. The quantity of light produced when a particle goes through a plastic scintillator being proportional to the energy loss of the particle, the amplitude of the signal measured gives us access to the charge number Z_b.

The plastics used in BigRIPS are covered with light isolation and two photo-multipliers (PM) are placed on each side (left and right). Applying coincidence conditions between the two PMs allows to reduce the background sources. During the SAMURAI21 experiment, two thin plastics called SBT (Secondary Beam Trigger) were placed 8 cm from each other along the beam line. They are much thinner than the other plastics in order to minimize the probability of reaction in the material. Their role is to trigger the data acquisition and to be the time reference for the entire setup.

The identification of the incoming ions is now completed and the identification plots obtained for the two different settings used during our experiment are presented in Fig. 3.11. However, we still need the information on their trajectories. They are determined using the drift chambers called BDC1 and BDC2 (Beam Drift Chamber) presented in Fig. 3.12. Those two chambers are separated by nearly 1 m and placed after the SBT. They are both

name	relative position (mm)	thickness (mm)
F3	-83600	3.0
F7	-36617	3.0
SBT1	-40	0.5
SBT2	40	0.5

Table 3.1: *Properties of the different plastic scintillators placed on the beam line. The relative distances are given with respect to the middle of the two SBT detectors.*

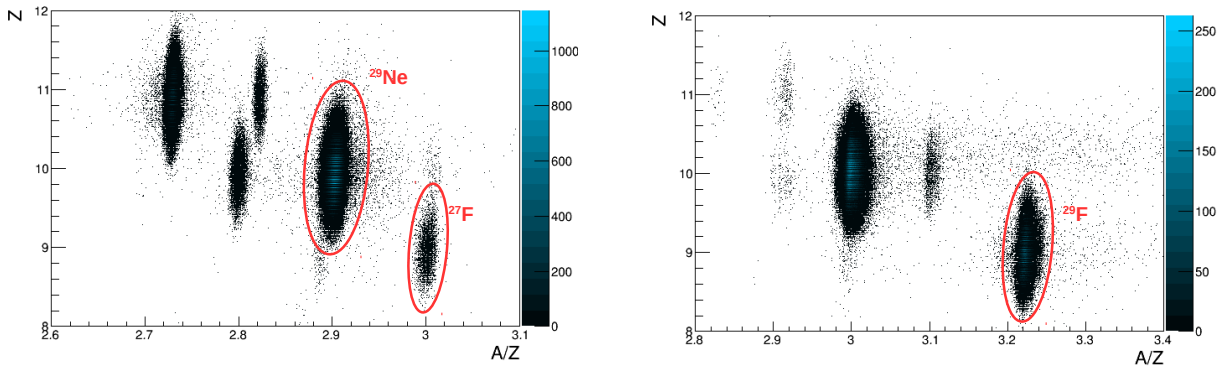

Figure 3.11: *Identification of the cocktail beam for the two different settings used in the SAMURAI21 experiment.*

identical with a square section of dimensions 320(H)×320(V)×120(T) mm^3 with an active volume of dimensions 94(H)×94(V)×90(T) mm^3. The two chambers are filled with Isobutane at a pressure of 100 Torr. They are made of 8 planes of 16 wires arranged vertically (Y) and horizontally (X). Those planes, separated by 4.8 mm, are placed successively by pairs of two with the same orientation in the following way: $X_1X_1'Y_1Y_1'X_2X_2'Y_2Y_2'$. In a same plane, wires are separated by 5 mm. For two successive planes with the same orientation, wires are shifted from one plane to the other by 2.5 mm in order to maximize the spatial covering. A 8 μm foil of aluminized Kapton is placed in between each wire plane and is used as a cathode.

During our experiment, we used MINOS (presented in Fig. 3.13) as reaction target. The MINOS device is made of a 15 cm liquid hydrogen target and a Time Projection Chamber (TPC) and is particularly adapted to proton-induced nucleon knockout experiments. It allows the tracking of the protons involved in the knockout reaction and therefore to determine the interaction point. This is of a great importance in order to achieve a good resolution as we will see in the following chapters. More details about the MINOS target can be found in Refs. [102, 103].

3.4.3 Detection of the reaction products

We described in the previous section how to identify and characterize the ions of the beam (Z_b, A_b/Z_b and trajectories). However the main interest of our study is about the reaction products from the interaction between the beam and the reaction target. More precisely, since we are dealing with unbound systems, the products of the reaction are the decay products of our

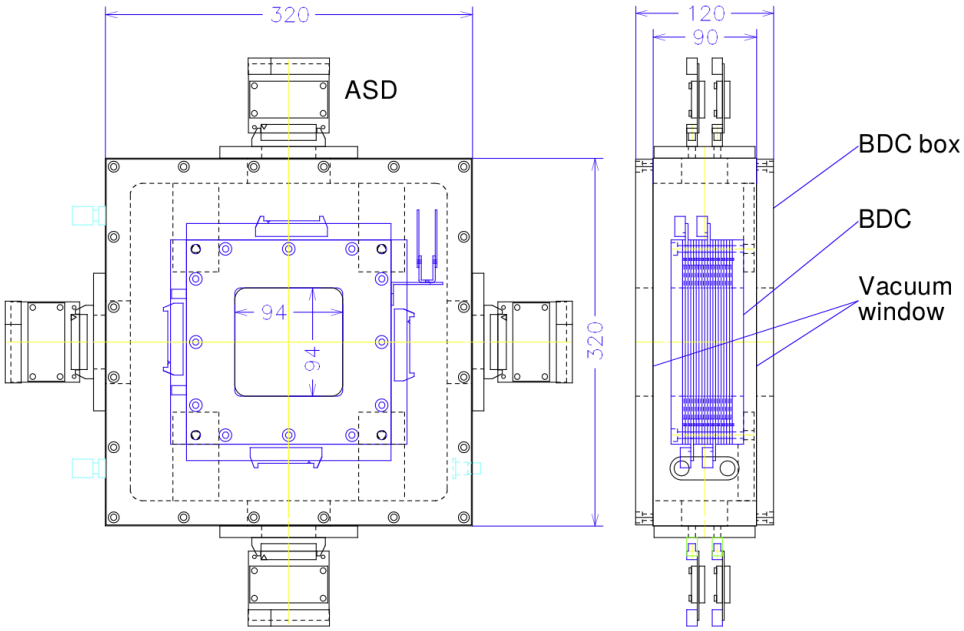

Figure 3.12: *Sketch of a Beam Drift Chamber (BDC). The dimensions are displayed in mm.*

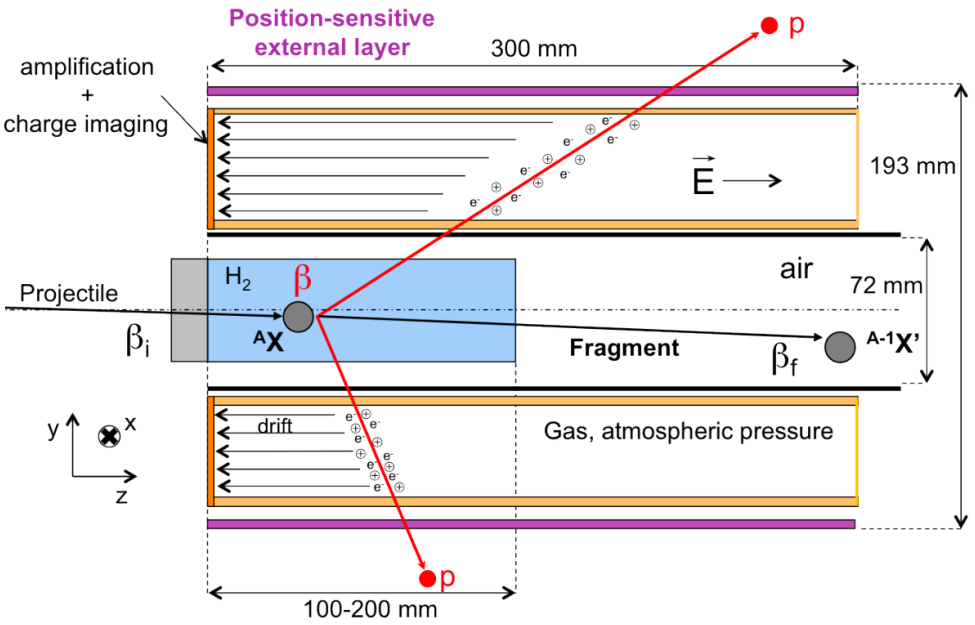

Figure 3.13: *Sketch of the MINOS device.*

nuclei of interest (fragment+neutron(s)). As we discussed in section 2.2.2, the invariant-mass method used in our study requires the detection of all the decay products in order to have access to the full kinematics of the reaction. In order to detect the decay products, the experimental setup is made of a γ-ray detector, two detector for neutrons and a set of dipole, drift chambers, and plastic detectors for the charged fragments. We are describing in this section each detector used in our experiment.

DALI2 - The fragment produced during the interaction between the beam and the target can be populated in excited states that will decay by emitting γ-rays. This is why the γ-ray

detector DALI2 has been placed around the reaction target. DALI2 is a 4π detector made of 140 independent Sodium Iodide crystals (NaI). They are placed in 13 rings perpendicular to the beam axis in order to surround the reaction chamber. The identification of the γ-rays that have deposited some energy in the crystals is done by looking at the amount of light measured. Once calibrated, DALI2 allows to reconstruct the energy of a ^{137}Cs $\gamma-$source with a resolution of nearly 9% (FWHM) for the 662 keV photons.

SAMURAI - The charged fragment travels towards SAMURAI (Superconducting Analyzer for Multi-particles from RAdio Isotopes beams) which is a supraconductor magnet that allows to reconstruct the properties of charged particles emitted during the reaction. It has been designed to be used during experiments that require the full kinematics of the reaction such as in our case in order to compute the invariant mass of unbound states. The system has been made to be adaptable in order to be used in different kinds of experiment (Coulomb breakup of neutron-rich and proton-rich nuclei, study of pygmy and giant resonances, nucleon knockout in order to study unbound states...). The magnet is made of two concentric poles of 2 m diameter separated by 88 cm, within which is installed a 80 cm high vacuum chamber. The entire setup is placed on a turning base that allows the magnet to turn from $-5°$ to $95°$.

SAMURAI allows to create a relatively homogeneous vertical field up to 3.1 T between the poles for a current of 563 A. Such a field can separate charged fragments (in mass and charge) by nearly 5σ for an energy of 250 MeV/nucleon and a $A/Z \approx 3$ ratio. The big size of the vacuum chamber allows to cover a large angular acceptance for the reaction products: $\pm$ 10° horizontally and $\pm$ 5° vertically. The chamber has two exit windows, one for the neutrons and one for the charged particles [104].

In the same way that for the beam, the identification of the charged fragment is done using the ToF and Bρ techniques. In order to have access to the Bρ, two drift chambers are placed before and after the magnet in order to reconstruct the trajectory of the charged fragment. They are called FDC1 and FDC2, respectively.

FDC1 drift chamber - The FDC1 (see Fig. 3.14) is based on a similar principle than the one of the BDC1 and BDC2. It is located in between DALI2 and the entrance window of SAMURAI. It is a rectangular chamber of dimensions 1000(H)×696(V)×336(T) mm^3 with a cylindrical active volume of dimensions 310(D)×180(T) mm^2. It is filled with Isobutane at a pressure of 50 Torr. Its large entrance window, 620(H)×340(V) mm^2, allows to minimize the interaction of the neutrons in the chamber. 14 plans of 32 wires used as anodes are placed in the detector. The planes are separated by 10 mm from each-other and the wires from a same plane are separated by 5 mm.

On the contrary to the BDCs, the FDC1 does not have any horizontal plane (due to mechanical constraints). Instead, so called U and V planes are used, in which the wires are placed at an angle of $-30°$ and $30°$, respectively, with respect to the vertical. The simultaneous use of both planes allows the reconstruction of the horizontal coordinate by interpolation.

Such as for the BDCs, the FDC1 is made of successive pairs of planes of the same type, the positions of the wires of the second plane being shifted by 2.5 mm compared to the previous

one in order to maximize the detection efficiency. The planes are therefore organized in such a way: $X_1X_1'U_1U_1'V_1V_1'X_2X_2'U_2U_2'V_2V_2'X_3X_3'$. In order to ensure an electric field inside the chamber, 15 planes of aluminized Kapton are inserted in between the anode planes. The interpolation of the positions reconstructed on those 15 planes allows the FDC1 to determine the position of the ions with a precision of 100 μm (RMS) and an efficiency of 100%.

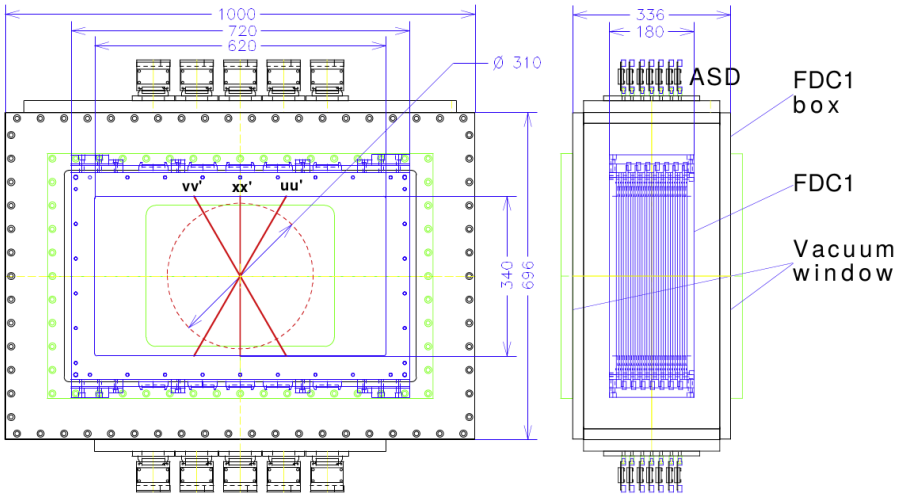

Figure 3.14: *Sketch of a FDC1 drift chamber. The dimensions are displayed in mm.*

FDC2 drift chamber - The FDC2 (see Fig. 3.15) is located after the SAMURAI spectrometer, at nearly 1 m from the SAMURAI exit window. Its principle is similar to the one described for the other drift chambers used in our experiment (BDCs and FDC1) but its size is much larger. Indeed, its dimensions are as follows: 2616(H)×1156(V)×876(T) mm^3, with an active volume of dimensions 2296(H)×836(V)×653(T) mm^3. The wires are organized in 14 planes in the configuration X, U and V. The planes are made of 112 wires and grouped by two planes of the same orientation separated by 15 mm from each other. Moreover, the second plane is shifted by 5 mm in order to maximize the spatial efficiency. In a same plane, the wires are separated by 10 mm and the groups of planes by 100 mm. Each wire is surrounded by 6 other wires forming an hexagonal shape that plays the role of the cathode.

The succession of the planes in the FDC2 can be described such as: $X_1X_1'U_1U_1'V_1V_1'X_2X_2'U_2U_2'V_2V_2'X_3X_3'$. The active area is filled with a mix of Hellium and Isobutane at atmospheric pressure. The positions of the ions in the FDC2 is reconstructed by interpolation with a precision of 120 μm (RMS) and an efficiency of 100%. Its large active area also allows to cover most of the trajectories coming out of the SAMURAI exit window.

Hodoscope - It is a wall made of 24 plastic scintillator bars of dimensions 100(H)×1200(V)×10(T) mm^3. The bars are placed vertically side by side on a frame in order for their center to be at 2 m height from the floor. A photomultiplier is placed at each extremity of each bar. The coincidence between the signals of those two PMs allows to select physics events and to access the ToF of the charged fragments as well as the charge that they deposited in the bar. Those two information allow to identify the fragments (see Fig. 3.16), and by using the Bρ obtained from their trajectories in SAMURAI, we can compute their

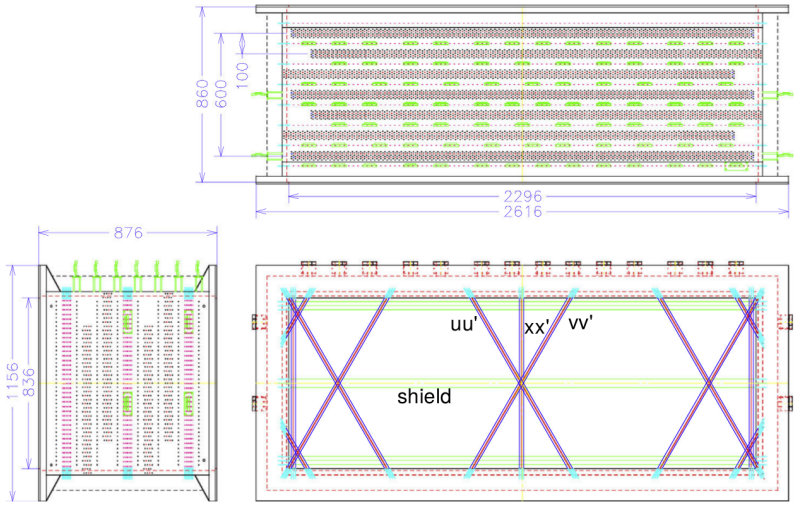

Figure 3.15: *Sketch of a FDC2 drift chamber. The dimensions are displayed in mm.*

energy-impulsion four-vector.

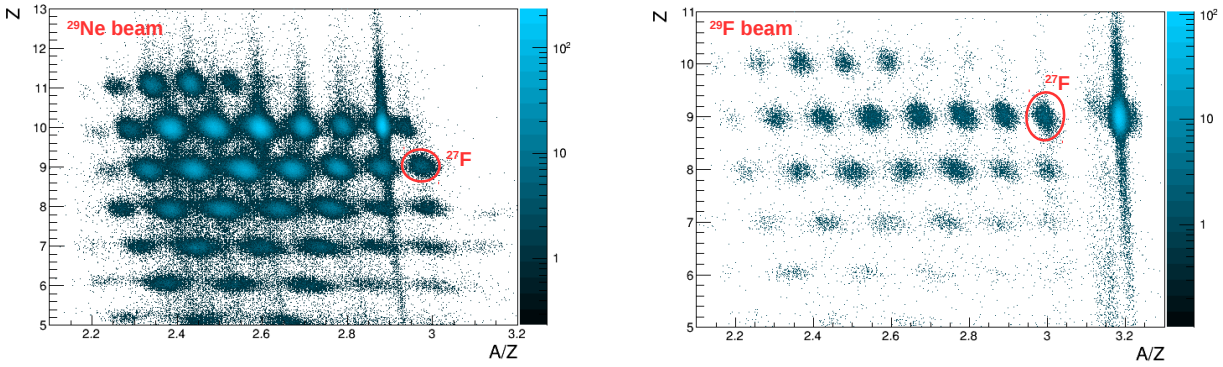

Figure 3.16: *Identification of the charged fragments produced from a ^{29}Ne (left) and ^{29}F (right) beam after its interaction with the MINOS target.*

NEBULA - It is one of the neutron detectors used during the experiment. It is made of 120 plastic scintillator bars organized in two walls separated by 85 cm. Each wall is made of two layers of 30 bars of dimensions 120(H)×1800(V)×120(T) mm^3 placed vertically. A photomultiplier is placed at the extremity of each bar. The position of the interaction of the neutron in the detector is crucial in order to reconstruct precisely the energy-impulsion four-vector of the neutron. The X and Z positions are taken as the middle of the bar where the interaction took place (leading to a ±6 cm uncertainty) and the Y position is determined from the time difference between the two PMs. The commissioning performed in March 2012 showed that the resolution on the impulsion reconstructed with such a method is $\sigma_p/p = 0.57\%$ for a neutron with an energy of 200 MeV [105].

In order to distinguish charged particles from neutrons, so called vetos are placed in front of each wall. Those vetos are plastic scintillators thinner enough to have a negligible efficiency

to neutron detection but sufficient to allow the detection of charged particles. Therefore, any event in NEBULA in coincidence with a hit in at least one of the vetos will be discarded from the analysis.

Since the magnetic field of SAMURAI does not have any effect on the neutrons, they follow their trajectory. It has been therefore chosen to place NEBULA at nearly 14 m from the MINOS target along the beam axis. The neutrons are not sensitive to Coulomb interactions, and interact only through the strong interaction. Therefore their detection is not direct but induced by the signal of the recoil nuclei coming from a nuclear reaction. This implies that the energy deposited in the detector is not proportional to the one of the incident neutron. We therefore use a ToF technique between the target and NEBULA in order to determine the energy of the neutron. A second consequence to that indirect detection is the fact that a same neutron can be detected several times in NEBULA by interacting successively in different bars. This phenomena, called cross-talk, makes more difficult the study of reaction channels where more than one neutron are observed in the final state. More details about the treatment of such reactions has been given in section 2.1.

NeuLAND - It is the second neutron detector that has been used for the first time during our experiment. Its principle is identical to the one described for NEBULA. However, its geometry and characteristics are different. NeuLAND is made of 400 plastic scintillator bars of dimensions 50(H)×2000(V)×50(T) mm^3 organized in eight successive layers of 50 bars oriented vertically (V) or horizontally (H) depending on the layer. The succession of layers can be described as follows: $H_1V_1H_2V_2H_3V_3H_4V_4$. In the case of a horizontal (vertical) layer, the position Y (X) and Z are taken as the middle of the bar and the X (Y) position is reconstructed from the time difference between the two PMs located at the extremities of the bar. The higher granularity of NeuLAND compared to NEBULA allows a better resolution on the position of the interaction and therefore on the reconstruction of the neutron energy-impulsion four-vector. During the experiment, NeuLAND was placed in front of NEBULA at nearly 11 m from the MINOS target. In the same way as for NEBULA, vetos were placed in front of NeuLAND in order to discard the charged particles during the analysis.

3.5 Monte-Carlo simulations

Due to the complexity of the experimental setups used in our experiments, the use of numerical simulations is essential for a good understanding of the experimental response of the different detectors involved. However, a simulation of the entire setup and all the processes involved in the experiment could be extremely heavy and complex. Since the response of some of the detectors is completely independent from others, we have decided to develop several simulations, each one reproducing different parts of the setup. In this section, we are presenting each of those simulations and the way they are used in the analysis. For clarity, in the following we will present only the simulations used for the analysis of the RIKEN data, but similar ones have been used in the analysis of the GSI data.

3.5.1 Trajectories of the charged fragment

The determination of the magnetic rigidity of the charged fragment is one of the key parameters in our analysis. Not only for the identification of the charged fragments but also for the determination of their momenta. The dipoles used in our experiments (SAMURAI and ALADIN) allow to separate the ions as a function of their $B\rho$, but unfortunately also introduce non linear effects, making difficult the determination of the trajectories of the fragments. In order to correct those effects, it has been chosen to use a simulation. For the analysis of the RIKEN data, the simulation has been developed using the GEANT4 software.

In order to use the simulation, the user tunes the input parameters that correspond to the properties of the ions at the exit of the target (rigidity or energy, position, incident angle...). The program is randomly generating a large number of events following the conditions of the user and propagates the particles in the experimental room until their detection or their exit of the interest area. This simulation has two main goals: predicting the trajectories before an experiment in order to determine the optimal position for the fragment detectors; and determining the relation between the positions and angles measured, before and after the dipole, and the magnetic rigidity. The simulation determines the trajectory of each particle and in particular its horizontal and vertical positions as well as the incident angles in the drift chambers. The results of the X, Y, θ_x and θ_y before the dipole (FDC1) as well as X and θ_x after the dipole (FDC2) are used to generate a multidimensional polynomial adjustment with the *TMultiDimFit* routine of ROOT. The generation of such a function can be long but once created, it allows to have access instantly to the rigidity of each charged fragment during the analysis.

3.5.2 Simulation of the γ detection

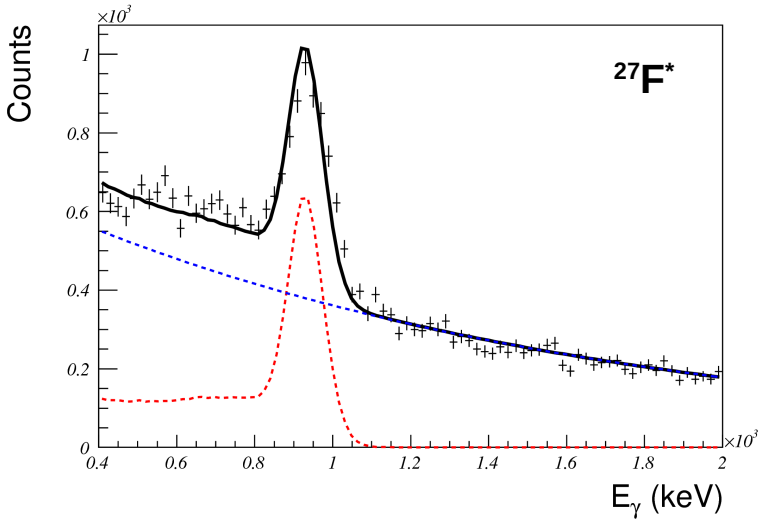

Figure 3.17: *Test of the DALI2 simulation on the γ-ray transition from $^{27}F^*$. The data (black points) are fitted using a distribution (black line) with two components: the result of the simulation (red dashed line) and a exponential (blue dashed line).*

In order to analyze the γ-ray spectra produced by the DALI2 detector, a simulation reproducing the response of the detector (interaction into the NaI crystals, Doppler effect...) has been developed. This simulation has been built in the GEANT4 framework ([106–108]). Its ability to correctly reproduce the efficiency and the resolution of DALI2 has been tested using a γ-ray transition from ^{27}F observed during the experiment (see Fig. 3.17).

3.5.3 Fragment-neutron(s) decay

Event generator

In order for the simulation to describe the reality, it needs to reproduce the properties of the ion beam before the reaction. Experimentally, the beam is characterized by a velocity distribution with a variable width and shape that can be quite complex. In the simulation, the distribution is considered uniform and its mean value and width are tuned for each reaction channel in order to reproduce as good as possible the experimental data (see Fig. 3.18).

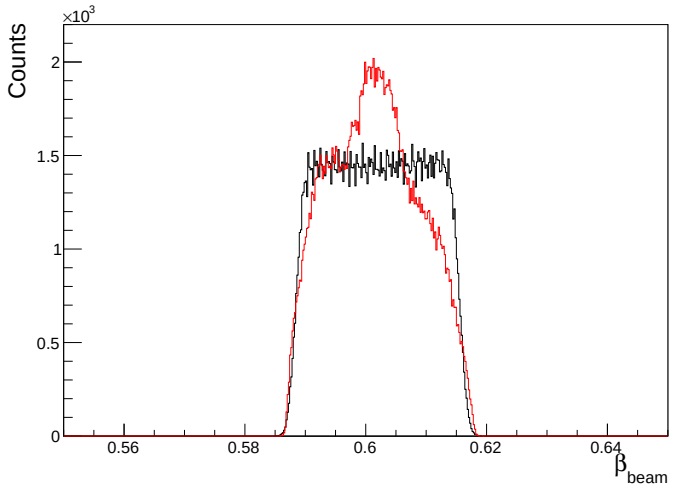

Figure 3.18: *Superposition of the beam velocity distributions from the data (red) with the distribution given as an input of the simulation (black) for the (^{29}F,^{27}F+n) reaction channel.*

In the target, the ions of the beam lose energy. This energy loss being linked to a large number of microscopic processes, it is not strictly identical for two particles with the same energy. Therefore, we observe a broadening of the energy distribution while going through the target called energy straggling. Moreover, the multiple diffusion of the ions in matter induce a slight deviation of their trajectory in the target, called angular straggling. In order to take into account those two effects, once the energy loss in the target calculated, shifts in energy and angle are randomly picked following Gaussian distributions which width was defined by the user. The values of the straggling, as well as the energy loss calculation, have been estimated using the LISE++ software.

In the simulation, we consider the decay of an unbound state of an isotope via the emission of one or several neutrons. Such decays are characterized by the energy accessible to the system, the relative energy (E_{rel}) between the fragment and the neutron.

The differential cross-section of the relative energy follows a distribution characterized by the state considered, that can be expressed using different functions presented in the previous chapter. The simulation allows to randomly pick the relative energy of an event from the probability distribution as a function of the parameters of the fragment+neutron resonance.

Once the relative energy of the event is determined, it is shared between the fragment and the neutron(s) following the two(or more)-body phase space. In the case of a two-body phase space, the momenta have, in the center of mass, same norms and same trajectories but opposite directions. In the simulation, the momenta are supposed isotropic in the center of mass and their norms are given by the following relations [85]:

$$P_{CM} = \frac{\sqrt{(E_x^2 - (m_A c^2 + m_n c^2)^2)(E_x^2 - (m_A c^2 - m_n c^2)^2)}}{2E_x} \tag{3.8}$$

$$E_x = E_{rel} + m_A c^2 + m_n c^2 \tag{3.9}$$

where E_{rel} is represents the relative energy of the system, E_x its excitation energy, m_A the mass of the fragment and m_n the mass of the neutron.

In our experiments, however, the unbound resonance has been produced through a given reaction, and during the process a momentum is communicated to the resonance. This information is easily obtained from the data by reconstructing the momentum distribution of the fragment+neutron(s) system, which shows a Gaussian shape with a characteristic width in the longitudinal and transverse directions, of the order of 50–200 MeV. In practice, we determine these widths experimentally for each reaction channel and introduce the values obtained in the simulation, that will add for each event the momentum of the resonance being generated following those distributions.

The depth of the reaction point in the target is also picked randomly following a uniform distribution. Finally, all the observables calculated in the center of mass are converted into the laboratory frame by using the speed of the incident ion corrected by the energy loss in the target and affected by the straggling. The fragment then created is affected by the same effects than the incident ion (energy loss and straggling) which are calculated for the target thickness remaining to be traveled through. As the detection efficiency of the fragments is not dependent on their momentum and is close to 100%, in order to optimize the computation time of the simulation it is considered that 100% of the fragments are detected. We then affect the measured momenta of the fragments by the resolution induced by the experimental system. The latter has been determined experimentally and is described in detail in the next section. Finally, the neutrons produced are transported to the neutron detectors where their detection (or not) is treated.

Reproduction of the momenta and the experimental resolutions

The measurement of the fragment momentum is degraded by our experimental setup. Indeed, the momenta are reconstructed from the positions in two drift chambers using a multidimensional polynomial function which makes very complex the identification of the influence of all the parameters of the measurements. Therefore it has been decided to measure this influence directly using the data. The ideal conditions for each reaction channel would be an empty

target run with the following characteristics: the fragment of interest is produced at an energy slightly below the one of the reaction studied (in order to compensate for the absence of energy loss in the target) and its momentum and angular spread are negligible. Unfortunately, such conditions are not doable in reality. Therefore, in order to reproduce artificially a pencil beam, we are selecting events in the data by applying conditions on their angle and momenta for different ions produced during the empty target runs. Due to the strict selection on the events, only the ions produced with a sufficient statistics can be studied using such a treatment. We therefore selected some of the ions produced in order to deduce a general tendency from a few examples.

The two observables affected by the experimental setup that we want to reproduce are the emission angles of the fragments and their total momenta. In order to reproduce the angular distributions, the following conditions were applied to the beam:

- Reaction centered on the target (15 mm sides square)
- $|\theta_x - \langle\theta_x\rangle|$ <0.5 mrad
- $|\theta_y - \langle\theta_y\rangle|$ <0.5 mrad
- No selection on the total momentum

The angular distributions obtained once the conditions applied to the beam are very similar for the different isotopes considered. They can be well described by a single Gaussian with a given width for the x and y directions (see Fig. 3.19).

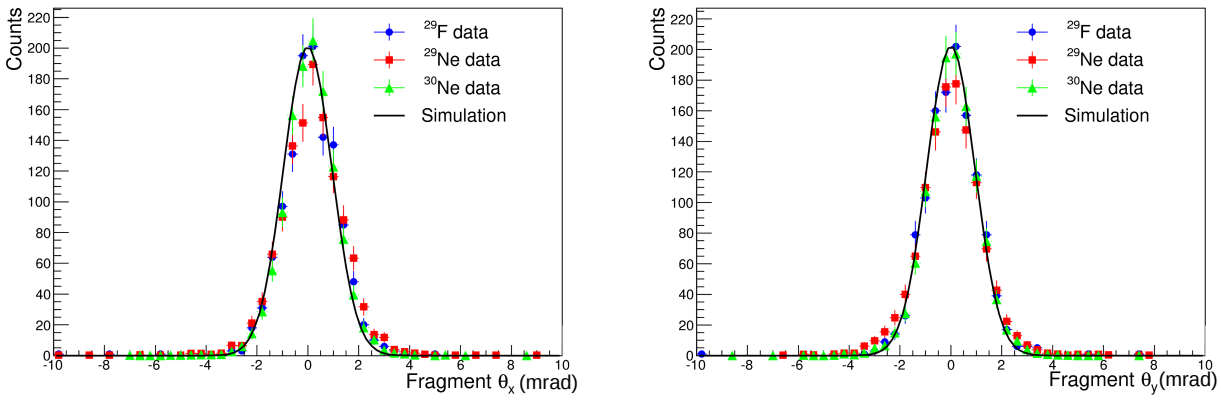

Figure 3.19: *Superposition of the angular distributions obtained for different ions by selecting a pencil beam on the empty target and the function used in the simulation to reproduce those distributions.*

Concerning the total momentum, the conditions chosen for the beam were as follows:

- No selection on the target position
- No selection on the angles
- Dispersion of the fragment momentum around the average as follows:
  $|P - \langle P\rangle|/\langle P\rangle$ <0.2‰

The momentum distributions obtained for the different fragments can be reproduced by a Gaussian. We tried to reproduce the different fragment considered using only one Gaussian width. The best results, presented in Fig. 3.20, have been obtained using a Gaussian of width σ =33 MeV/c.

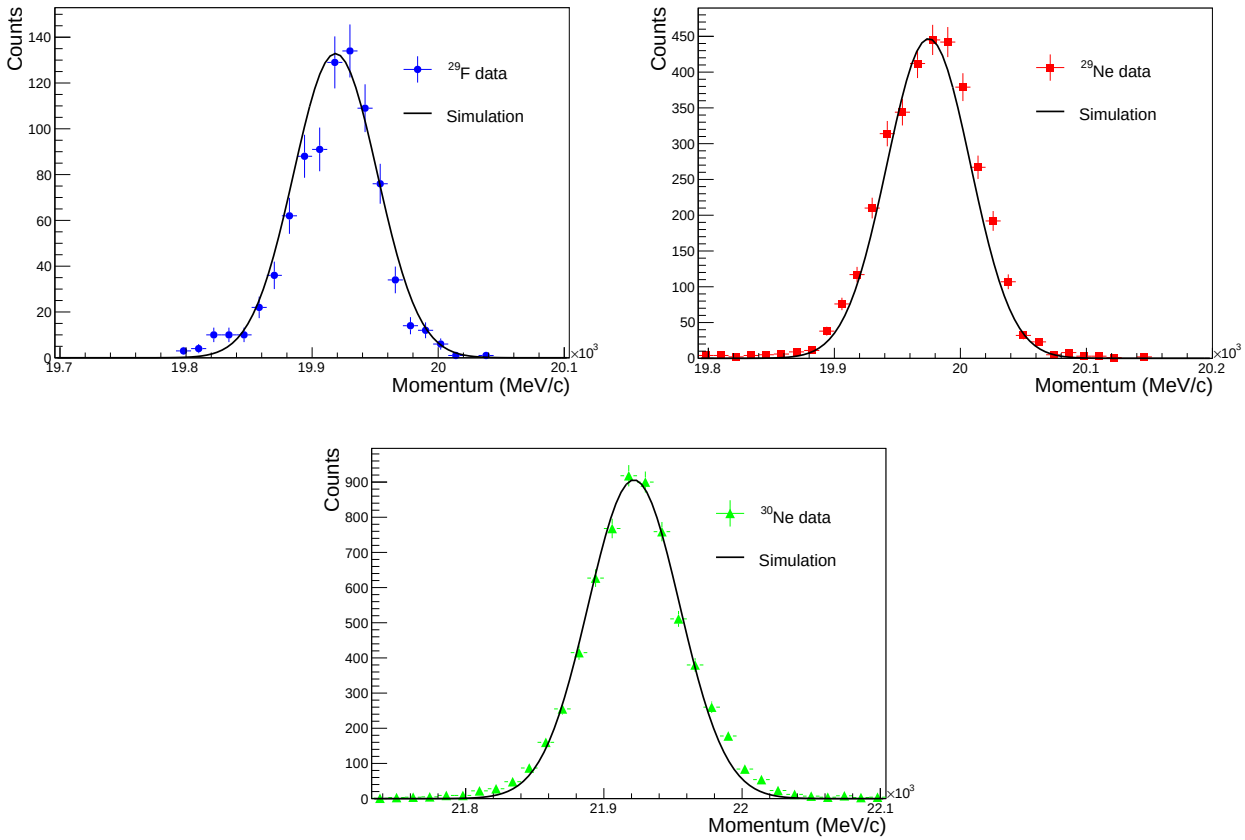

Figure 3.20: *Distributions of total momentum obtained for the ^{29}F, ^{29}Ne, ^{30}Ne pencil beams. The black curve represent the best compromise obtained to reproduce the three distributions using only one Gaussian. In each case, the simulation is normalized to the data so that their integrals match.*

Treatment of the neutrons in the simulation

Once the fragment detection taken into account by doing the convolution of the momentum by the function described in the previous section, it is necessary to simulate the detection of the neutrons. This can be decomposed as the product of a geometrical acceptance (that characterizes the probability that the neutron is reaching the detector) by a detection efficiency (that characterizes the probability that the neutron interacts with the detector).

Concerning the geometrical acceptance, the momentum of the neutron emitted by the unbound system determines entirely its trajectory in the experimental area. The geometrical acceptance for the detection of a neutron as a function of the relative energy available in the unbound system is presented Fig. 3.21. The higher the relative energy, the higher will be the energy transmitted to the neutron and therefore the more it may deviate from the beam trajectory. We observe that the geometrical acceptance is maximum and constant between

0-1 MeV. Past 1 MeV, the acceptance is decreasing as the energy transmitted to the neutron is sufficient so that its trajectory is going out of the neutron detectors. The complex shape of the acceptance is due to the use of two different detectors with different positions and dimensions. Indeed, comparing the acceptance of each detector (Fig. 3.21) allows us to understand the full acceptance of the neutron detection system. NeuLAND having a square entry face and being closer from the target compared to NEBULA, its acceptance is maximum and constant until about 3 MeV. Past that value the acceptance is smoothly decreasing as the energy transmitted to the neutron is sufficient so that its trajectory is out of NeuLAND. NEBULA, being further from the target and since it has a rectangular entry face, its acceptance is maximum and constant up to 1 MeV. Then it is decreasing between 1-3 MeV as the trajectory of the neutron is going out of the vertical acceptance of NEBULA. At 4 MeV, we observe that the acceptance is going down faster as the neutron is going out of the horizontal acceptance of NEBULA. Those phenomena explain the complexity of the acceptance observed for the full neutron detection setup (NeuLAND and NEBULA).

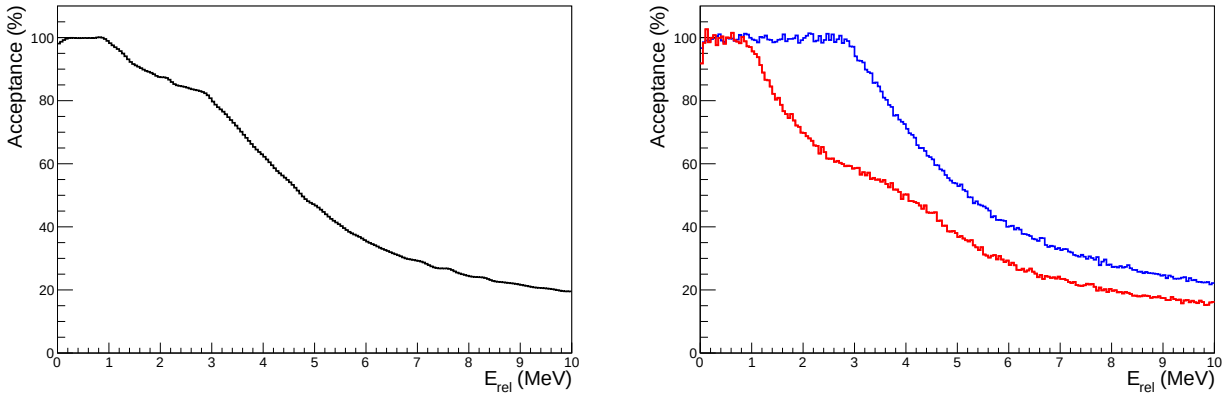

Figure 3.21: *On the left, evolution of the geometrical acceptance for the neutron detection in the SAMURAI21 experiment (NeuLAND and NEBULA) as a function of the relative energy of a fragment+n resonance formed at 230 MeV/nucleon. On the right, evolution of the geometrical acceptance for the neutron detection in NeuLAND (blue) and NEBULA (red).*

We need now to add the probability for a neutron to interact with the Carbon or Hydrogen nuclei from the plastic bars of NEBULA or NeuLAND. We used the MANGA (Multiparticle Analysis in a Neutron Geometrical Array) simulation in our analysis. In this simulation, the neutron interaction is treated in a purely effective way. We calculate the thickness of material that the neutron is going through and assume a probability of interaction per cm. The simulation is therefore depending on only one parameter that is tuned in order to reproduce the efficiency of the neutron detectors at $E_{rel} = 0$. The procedure used to determine this value is described in more detail in Ref. [5]. Once the position of interaction determined, the time needed for the light to reach the corresponding two PMs is reconstructed. Then this time is convoluted by the time resolution of each PM (obtained experimentally). The positions and the time are then treated using the same analysis procedure as the experimental data.

The MANGA simulation does not simulate the energy deposit of the neutron in the material of the detectors and does not take into consideration the possible multiple interactions

of a neutron. More complex simulations taking into account those effects have therefore been developed. However, as it is discussed in Ref. [5], the results obtained using MANGA or more complex simulations show almost identical results in the case of one neutron decays. Most importantly, taking into account the large number of simulations that will be needed for the fit of all the reaction channels that we analyze, the calculation time is much smaller using the MANGA simulation (about one order of magnitude).

The MANGA simulation allows us to determine the relative energy resolution of our experimental setup (Fig. 3.22), that has been determined by simulating the decay of delta resonances and by studying the width obtained after the convolution by the experimental response. We can see that the resolution is slowly degrading while going to higher relative energies. A phenomenological law reproducing the data is proposed following the equation: $FWHM = 0.18 \times E_{rel}^{0.63}$. The resolution is a crucial parameter since it is constraining our capacity to observe or not resonant states. We note here the large improvement on the resolution compared to previous experiments performed at MSU (Fig. 1.10) and at RIKEN during the DAYONE experiment where NeuLAND and MINOS where not part of the setup [5].

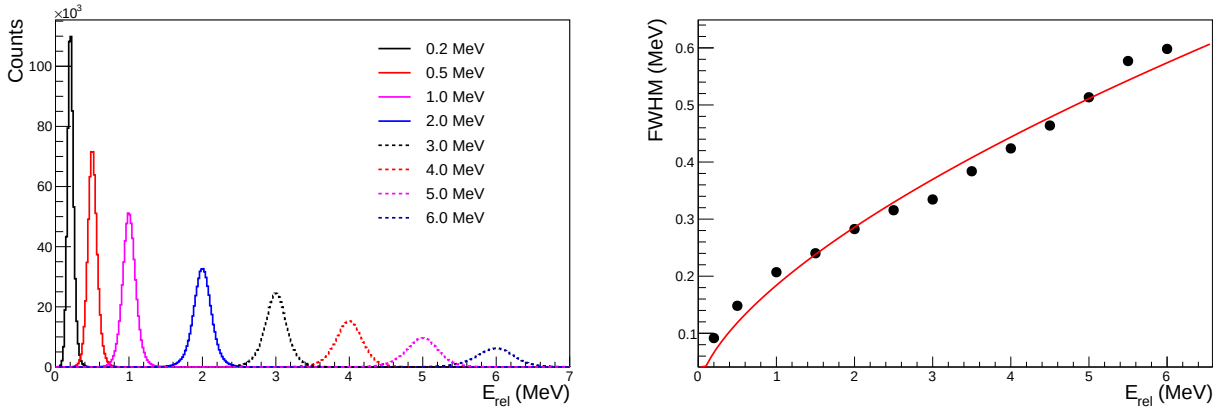

Figure 3.22: *Evolution of the experimental resolution in the SAMURAI21 as a function of the fragment-neutron relative energy for a beam at 230 MeV/nucleon. The red line on the right characterizes the evolution of the resolution.*

With this geometrical simulation, we can also study the effect of our cross-talk filters on the true n-n coincidences. The cross-talk phenomenon in a neutron detector such as the ones used in our experiment has been described in section 2.1. The filter used in order to suppress the cross-talk events is presented in Appendix A. The capacity to eliminate cross-talk events can be verified experimentally, but in order to study the effect of the cross-talk filter on the good events, the simulation is necessary.

A first information that is obtained from the simulation is the deformation of the neutron detection efficiency induced by the filter. To determine it, we simulate a three-body decay (fragment+n+n) using MANGA. Since the neutrons interact only once in this simulation, all the double coincidences obtained correspond to true $2n$ events. We can therefore apply the cross-talk rejection algorithm and compare the two spectra obtained. The result obtained is presented in Fig. 3.23. We can observe that our filter reduces the efficiency to detect two

neutrons but still lets us access true events at very low energies. This effect is due to the fact that when a nucleus decays with a low relative energy, the angle between the two neutrons emitted is small and the neutrons are therefore often detected in the same bar of the detector, which makes impossible to distinguish them. The efficiency is then increasing rapidly with the relative energy before reaching a maximum at around 1.5 MeV. Then the geometrical effects discussed in the previous section make the efficiency decrease.

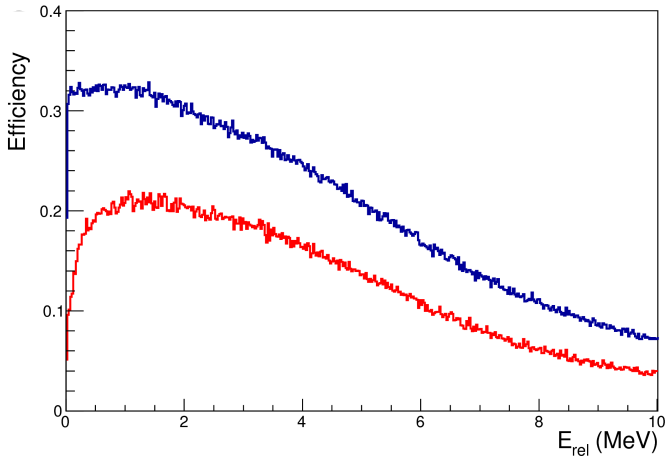

Figure 3.23: *Effects of the cross-talk rejection procedure of the true 2n events using MANGA. We show the superposition of the detection efficiency curves before (blue) and after (red) the cross-talk rejection algorithm as a function of the relative energy.*

Use of the simulated data in the analysis

In the past sections, we have been describing the different simulations used to model the entire experimental setup. However, the goal of those simulations is to help us understand physical processes. In particular, our goal is to use the results from the simulation to describe relative energy spectra obtained experimentally.

In this section, we are showing how to use the simulations in order to study the structure of nuclei taking the ^{29}F(p,pn) reaction as an example (Fig. 3.24). Before using the simulation, we following experimental data are available:

- The fragment+n relative energy spectrum that contains resonances from the unbound system as well as a non-resonant contribution.
- The shape of the non-resonant contribution but not its amplitude.
- The fragment-n correlation function, corresponding to the ratio between the relative energy and the maximized non-resonant contribution, that can help us to determine the number of resonances and their location area.

The goal is now to describe the regions of the relative energy spectrum that are not reproduced by the non-resonant component using resonances. Those resonances have three main

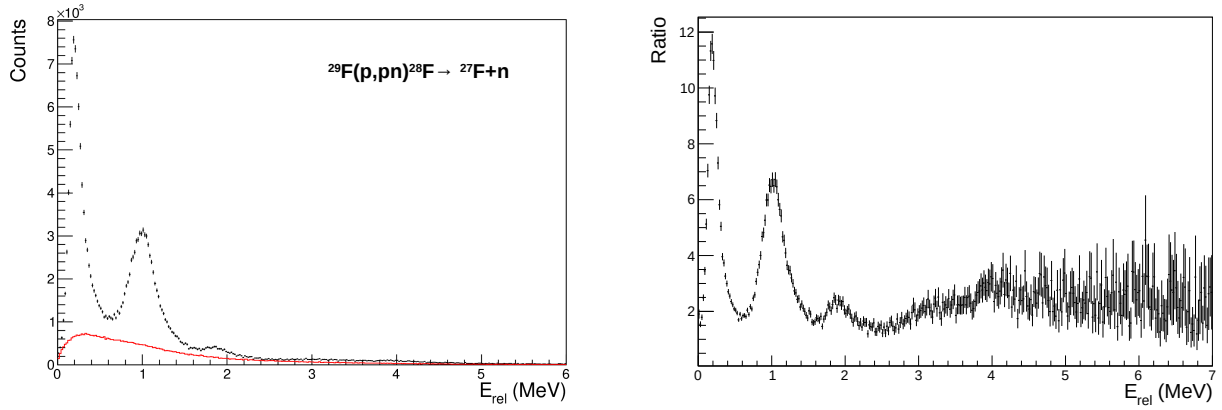

Figure 3.24: *On the left, relative energy spectrum obtained for the $^{29}F(p,pn)^{28}F$ reaction in the SAMURAI21 experiment to which the maximized non-resonant contribution has been added (red). On the right, ratio of the relative energy by the maximized non-resonant contribution for the same reaction channel.*

characteristics: the resonance energy E_r, their width Γ_r and the angular momentum ℓ of the neutron relative to the fragment. We start by determining the number of resonances needed to reproduce the relative energy spectrum and we perform simulations by varying the resonance energy and its width in reasonable ranges. In our example, several structures are observed. In particular, a low energy resonance is observed at around 200 keV and another one at around 1 MeV. The fit of the total relative energy spectra can be expressed as follows:

$$N(E_x) = \sum_i w_i R_i(E_x) + (1 - \sum_i w_i) U(E_x) \tag{3.10}$$

where N is the number of events at a given energy, R_i the i^{th} resonance used, normalized to the integral of the relative energy spectrum, w_i the weight applied to this resonance, and U the non-resonant component which is also normalized to the integral of the relative energy spectrum. The weights w_i must satisfy the condition $\sum_i w_i \leq 1$ so that the integral of the spectrum and of the fitting function are equal. The best fit is determined using the χ^2 method associated to the energy (E_r) and width (Γ_r) of the resonances.

The error bars for the energy and width of each resonance can be determined using χ^2 surface as presented in Fig. 3.25, which minimum corresponds to the best fit of the relative energy spectrum. Once the χ^2_{min} determined, we can draw an area that will allow us to calculate the error bars for E_r and Γ_r. To do so, we look for points of the χ^2 surface that satisfy the following condition : $\chi^2 \leq \chi^2_{min} + \Delta\chi^2$, where $\Delta\chi^2$ depends on the level of confidence that we want to achieve as well as the number of degrees of freedom in the fit [109]. In our example, the degrees of freedom are the energy and the width of the resonance considered, and the proportion of all the other components of the fit (resonances and non-resonant background). Due to the large number of resonances observed in our relative energy spectra, the χ^2 surfaces for each resonance are computed by fixing the energies and widths of the other resonances. For the ^{29}F(p,pn)^{28}F reaction, the fit of the relative energy spectrum is done with seven resonances meaning that we have nine degrees of freedom. A good level of confidence is achieved by taking an area with $\Delta\chi^2 = 10$.

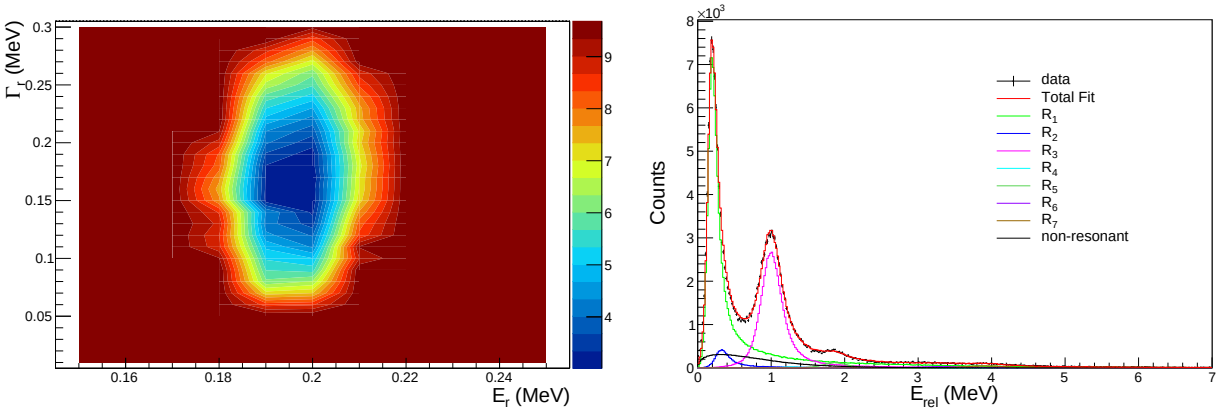

Figure 3.25: *On the left, χ^2 surface obtained by adjusting the relative energy spectrum for the first peak observed in the $^{29}F(p,pn)^{28}F$ reaction. Each area corresponds to five units of χ^2. The energy is varying from 0.15 to 0.25 MeV and the width from 0.01 to 0.3 MeV. On the right, result for the best fit of the same spectrum.*

The projection of this area on E_r and Γ_r gives us our uncertainties (see Fig. 3.26). In this case, we obtain ΔE_r ∼10 keV and $\Delta\Gamma_r$ ∼40 keV.

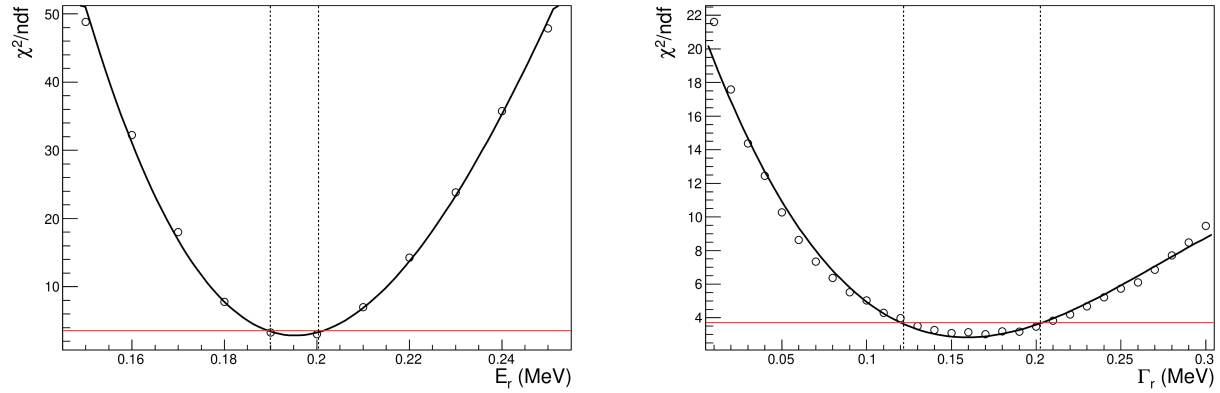

Figure 3.26: *Projections of the χ^2 surface on the resonance energy (E_r) and width (Γ_r). The red line corresponds to the limit $\chi^2 \leq \chi^2_{min} + 10$*

Chapter 4

n-*n* pairing in ^{14}C+4*n*

Contents

In this chapter, we are presenting the results from the s393 experiment that has been performed using the R^{3}B-LAND setup (see chapter 3.3) at GSI. During this experiment, a high-energy (≈430 MeV/nucleon) cocktail beam (containing ^{19}N and ^{21}O among other nuclei, see Fig. 3.7) is sent to a reaction target in which the knockout of nucleon(s) takes place. Different states of nuclei produced from such a reaction can be produced depending on where the nucleon has been knocked out. As we will see in the following sections, the ground state can be populated, but also bound excited states that will decay via the emission of gamma rays and unbound states that will decay by emitting neutron(s).

4.1 ^{18}C excited states populated from ^{19}N($-1p$)

Let us first have a look to the bound excited states of ^{18}C populated via the ^{19}N(p,2p)^{18}C* reaction. Those states decay via the emission of γ rays and can therefore be observed during the experiment using the Crystal-Ball detector that allows to detect in-flight γ-rays. The γ-ray spectrum obtained for the ^{19}N(p,2p)^{18}C* reaction is presented in Fig. 4.1. A fit has been performed using an exponential component as well as three Gaussian functions (one for each transition observed). The three transitions are found to be at the following energies: 896(19) keV, 1528(16) keV and 2340(112) keV. Those observations are in good agreement with previous studies [110] as shown in Table 4.1. In this previous study, they were able to look at γ-γ coincidences and to observe that the 896 keV and 2340 keV transitions were in coincidence with the 1528 keV transition that has been proposed as a 2^+ state. Unfortunately, in our data, such kind of study is rather difficult to perform due to the low statistics observed (especially for the 896 keV and 2340 keV transitions).

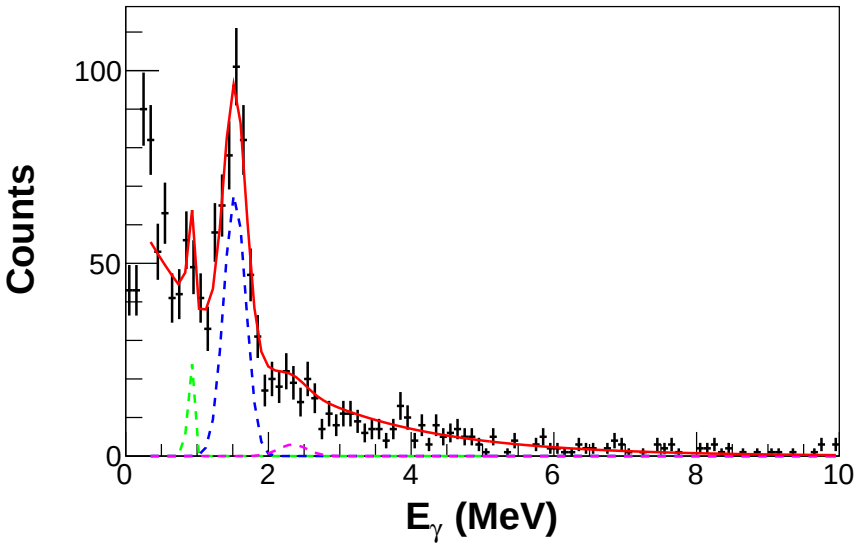

Figure 4.1: *Gamma rays observed in coincidence with the reaction $^{19}N(p,2p)^{18}C^*$. The data are fitted with an exponential component as well as three Gaussian functions.*

State	This work E(keV)	Previous work [110] E(keV)
1	896(19)	919(10)
2	1528(16)	1585(10)
3	2340(112)	2415(30)

Table 4.1: *Energies of the γ-ray transitions observed in our experiment for the reaction $^{19}N(p,2p)^{18}C^*$. The results of a previous study are also presented as comparison.*

4.2 ^{18}C unbound states populated from ^{19}N($-1p$)

Moving higher in excitation energy, we reach unbound states of ^{18}C populated via the ^{19}N(p,2p)^{18}C* reaction. Indeed, as mentioned earlier, depending on the shell from which the proton is removed during the knockout reaction, different states can be populated. The deeper is the proton knockout occurring, the higher in energy will the states populated be. In is therefore possible to populate unbound states above the one neutron emission threshold (S_n) that will decay by emitting one neutron resulting in the following reaction:

$$^{19}\mathrm{N}(p,2p)^{18}\mathrm{C}^* \rightarrow^{17} \mathrm{C}(+\gamma) + n \tag{4.1}$$

Since the setup used during the experiment allows us to have access to the full kinematics of the reaction (momenta of all the reaction products), we can compute the relative energy, using the invariant-mass method, as shown in Fig. 4.2, where we can clearly observe at least two structures. A fit of the data has been made using ℓ-dependent Breit-Wigner functions. The results of the best fit obtained are summarized in Table 4.2. A first state is observed at 1096(24) keV and a second one at 5163(133) keV. However, it is important to know if those states observed are decaying toward the ground state or toward an excited state of ^{17}C. Indeed, if a state is decaying toward an excited state of the outgoing nucleus, it is necessary to add the

ℓ	Energy (MeV)	Width (MeV)
1	1.10(3)	1.0(2)
0	5.2(2)	5.5(7)

Table 4.2: *Summary of the results obtained from the fitting of the experimental relative energy for the $^{19}N(p,2p)^{18}C^{*} \rightarrow ^{17}C+n$ reaction.*

energy of the gamma transition in coincidence to the energy obtained by fitting the relative energy in order to obtain the excitation energy of the state as follows:

$$E_{exc}^{(^{18}C)} = S_n + E_{rel}(+E_\gamma) \tag{4.2}$$

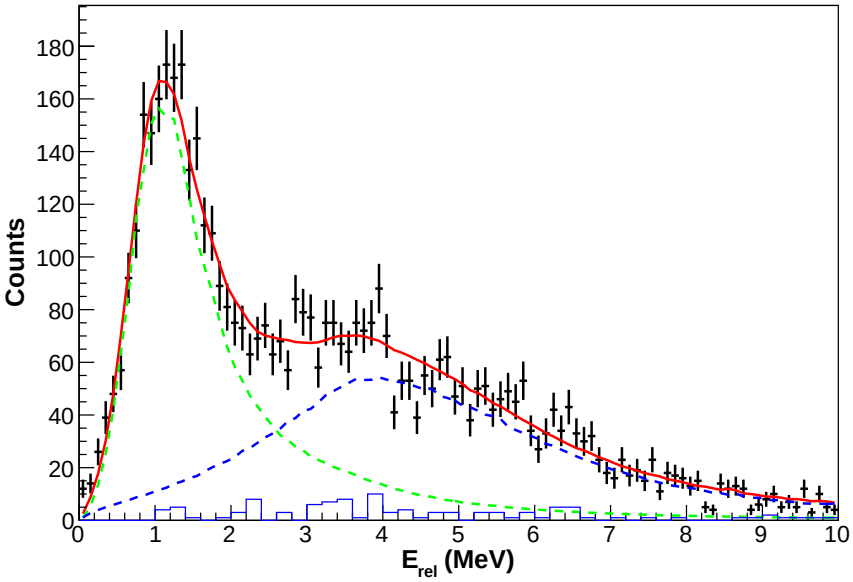

Figure 4.2: *Relative energy obtained for the $^{19}N(p,2p)^{18}C^{*} \rightarrow ^{17}C+n$ reaction. The data are fitted using two ℓ-dependent Breit-Wigner functions (green and blue dashed lines) where the response of the experimental setup is taken into account. The total fit (red line) has been found to be the best with ℓ=1 for the lower-energy resonance and ℓ=0 for the higher-energy one. The blue histogram represents events in coincidence with known γ-rays in ^{17}C taking into account the efficiency of the γ-ray detector.*

The gamma rays observed in coincidence are presented in Fig. 4.3. It is known from previous studies [110] that ^{17}C has two bound states at 207(15) and 329(5) keV. However, we observe only one transition at 314(4) keV. This could come from the fact that only one of the two known transitions is populated in our reaction or that the resolution of our detector is not sufficient to resolve the two peaks. In that case, what we observe would be a combination of the two transitions seen as one.

As we mentioned earlier, we are interested to see if those γ-rays are in coincidence with unbound states observed in the relative energy spectrum. The blue histogram presented in Fig. 4.2 corresponds to such coincidences. However, the number of coincidences is very small, which suggests that the unbound states observed are mainly decaying towards the ground state of ^{17}C.

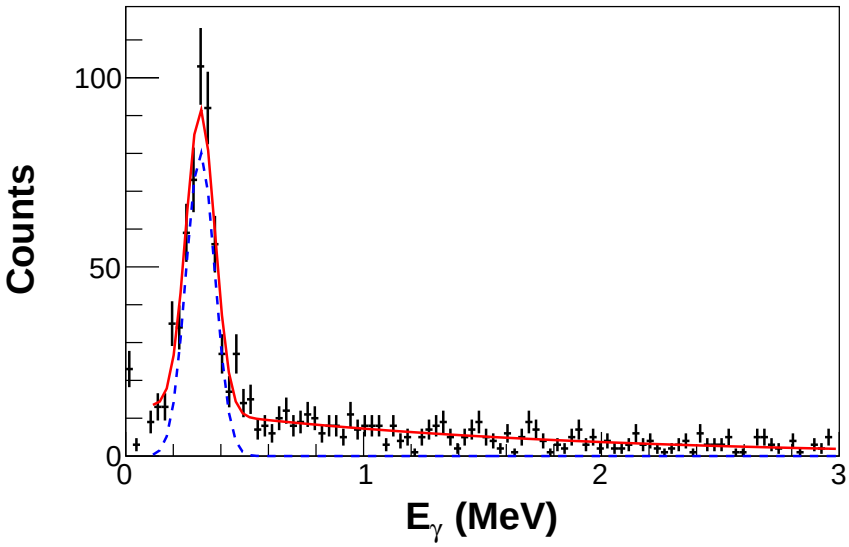

Figure 4.3: *Gamma rays observed in coincidence with the $^{19}N(p,2p)^{18}C^* \rightarrow ^{17}C+n$ reaction. The data are fitted with an exponential component as well as a Gaussian function.*

4.3 *n-n* pairing in ^{18}C and ^{20}O

During the knockout reaction, excited states higher than the ones observed previously (above S_{2n}) can also be populated and looking at the three-body decay might allow us to observe such states. As we mentioned earlier, one alternative way to reach the dripline is by populating high excited states of a nucleus. This is achieved here by knocking out a deeply bound nucleon from the beam. Such method, as we will see in the following, will allow us to investigate the *n-n* pairing inside the nucleus.

We presented in the previous section the unbound states observed when looking at ^{18}C two-body decays (fragment+n). However, it is interesting that the two-neutron emission threshold (S_{2n}) of ^{18}C is located only 735 keV above S_n. This means that all the states observed in Fig. 4.2 are actually located above S_{2n} and therefore could decay via the emission of two neutrons even if they are observed in the $1n$ decay channel. It is then interesting to look at the two-neutron decay channel to see if those same states also decay via the emission of two neutrons.

At high beam energy, the deep proton knockout reaction ^{19}N$(-1p)$ is expected to occur mainly through a quasi-free mechanism [111] and *preserve* the structure of the neutrons in ^{18}C, that can be viewed as a core of ^{14}C plus 4 neutrons in the *sd* shells (left panel of Fig. 4.4). This reaction is therefore used here as a tool to suddenly promote neutrons to the continuum, observe their decay, and trace back how they were correlated in ^{18}C.

The states produced in the ^{19}N$(p,2p)^{18}$C proton knockout should be analog in spin and energy to the $J = 1^+$, 2^+ states produced with large spectroscopic factors at energies of 7.02, 8.32, 10.44 and 11.29 MeV in ^{14}C using the ^{15}N(d,^{3}He)^{14}C reaction, likely from the pick-up of

a proton from the $p_{3/2}$ orbit.

By contrast, the deep neutron knockout reaction ^{21}O$(-1n)$ leaves a broken ^{16}O core and two unpaired neutrons in the ^{20}O residue (right panel). In this case, we expect to *hinder* the role of pairing interactions, as will be discussed in view of our observations. High energy states in ^{20}O (up to 27 MeV) are produced using the ^{21}O(p,pn)^{20}O reaction from a deeply bound $p_{3/2}$ neutron.

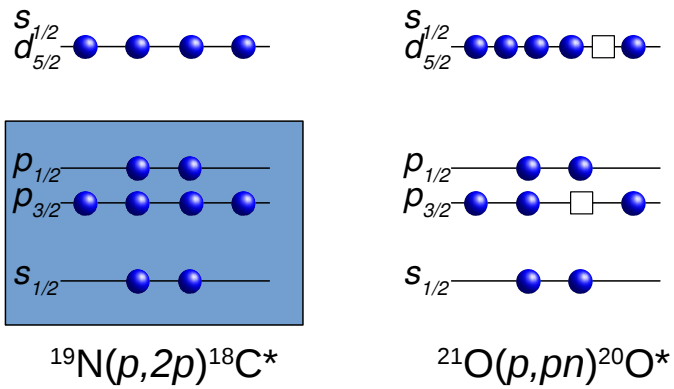

Figure 4.4: *Illustration of the shell-model configuration of the 12 neutrons in the ^{18}C (left) and ^{20}O (right) isotones. In the $(p, 2p)$ reaction the configuration of the neutrons is unchanged and all neutrons are likely paired, while in the (p, pn) reaction two neutrons are left unpaired.*

By detecting all the products of the reaction (fragment+n+n), we can study the n-n correlations in the nucleus using the method described in chapter 2. We are presenting the results obtained for the ^{18}C and ^{20}O systems using the following reactions:

$$^{19}\mathrm{N}(p, 2p)^{18}\mathrm{C}^* \rightarrow {}^{16}\mathrm{C}(+\gamma) + n + n \tag{4.3}$$

$$^{21}\mathrm{O}(p, pn)^{20}\mathrm{O}^* \rightarrow {}^{18}\mathrm{O}(+\gamma) + n + n \tag{4.4}$$

where ^{18}C and ^{20}O are populated via the knockout of a proton and a neutron, respectively.

4.3.1 Fragment+n+n relative energy

We first compute the relative energy E_{rel} (Fig. 4.5) for the ^{18}C and ^{20}O systems reconstructed from the momentum vectors of the fragment and neutrons using Eq. 2.17. This energy corresponds to the excitation energy of the total system beyond the $2n$ threshold, since no significant excitation of the fragment (blue histograms in Fig. 4.5) has been observed.

The $2n$-emission spectra of both nuclei are peaked at about the same energy of 4–5 MeV, and energies up to about 15 MeV were observed. Taking into account the S_{2n} values, this range of decay energies corresponds to $E_{exc}(^{18}\mathrm{C}) \approx 5$–$20$ MeV and $E_{exc}(^{20}\mathrm{O}) \approx 12$–$27$ MeV. To reach such high excitation energies, deep nucleon knockout must have occurred.

We can notice in Fig. 4.5 that the E_{rel} distributions for the ^{18}C$\rightarrow^{16}$C+n+n and ^{20}O$\rightarrow^{18}$O+n+n decay channel look similar even if the excitation energies (E_{exc}) explored were very different in each case. This similarity can be explained first by the fact that the neutron configurations are rather similar, as neutrons occupy the same *sd* shells in ^{18}C and ^{20}O.

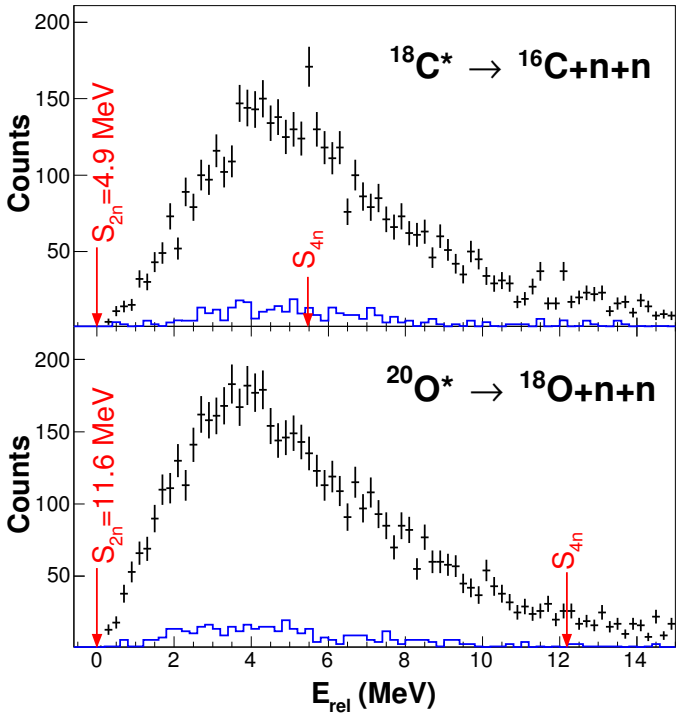

Figure 4.5: *Experimental decay energy spectra of ^{16}C+n+n and ^{18}O+n+n measured respectively in the proton/neutron knockout reactions from $^{19}N/^{21}O$ (blue histograms represent events in coincidence with known γ rays in $^{16}C/^{18}O$, corrected by ε_γ). The corresponding locations of the 2n and 4n thresholds are noted.*

Moreover, in the absence of narrow resonances, all decay-energy spectra have some common features that would apply to any system: they start at zero and increase with energy due to the opening of three-body phase space, and then at some point the experimental acceptance decreases and the high transverse momentum of the neutrons will make them escape the forward detector. And even with an infinite detector, the excitation energy provided by the reaction will drop at some point since the amplitude of the "piston" (or deep-hole process) is limited by the lowest available shell in the nuclei under study. Therefore, we must have a central bump surrounded by a low-energy rise (that can be more or less steep depending on the presence of low-energy states) and the high-energy fall down.

Within these global limitations, the two spectra of ^{18}C and ^{20}O are not strictly similar and differ in the first 5 MeV as we can observe in Fig. 4.6. Beyond 6 MeV, the shape of the spectra are dominated by the acceptance of the neutron detector. We note that the decay-energy resolution at 6 MeV is already about 2 MeV FWHM [58]. The case of the ^{15}B nucleus produced from ^{16}C knockout and decaying into ^{13}B+2n is shown in blue for comparison. In this case, low-energy structures were observed.

However, we are not able to observe any distinctive structure in the E_{rel} distributions presented in Fig. 4.5. It is therefore difficult just by looking at those distributions to distinguish if we are looking at a broad unique resonance or at a series of overlapping resonances. Let us first discuss the second scenario. If the system was populated through a series of narrow (or

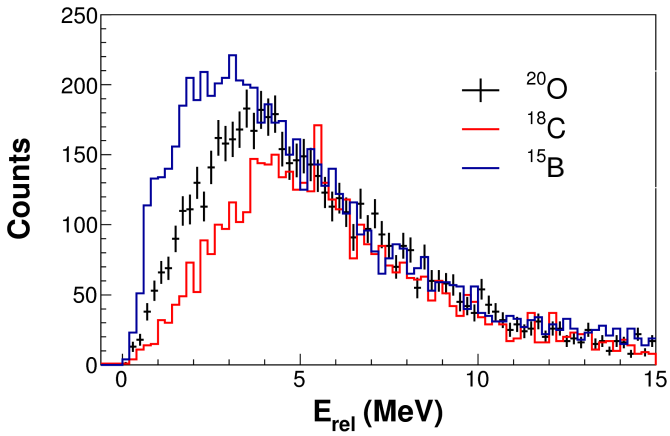

Figure 4.6: *Comparison between the E_{rel} of three different systems. The $^{21}O(p,pn)^{20}O\rightarrow^{18}O+2n$ system in black and the $^{19}N(p,2p)^{18}C\rightarrow^{16}C+2n$ system in red from Fig. 4.5, and the $^{16}C(p,2p)^{15}B\rightarrow^{13}B+2n$ system in blue.*

long-lived) overlapping resonances, all with similar strength, we might have not been able to resolve them in the decay energy spectrum. However, if resonances of different characteristics were populated, even if too broad to be distinguished on the decay energy spectrum, we would have been able to see a signature of their presence through changes in the three-body correlation patterns. The fact that the observed correlations do not change significantly (as we will see in the following sections) in the two systems as a function of the excitation energy is suggestive of the presence of a rather unique configuration that we interpret as the direct promotion of neutron pairs in the continuum.

This raises also the question about what system we are probing, initial system or high-energy resonances. From the argumentation of the previous paragraph, it was proposed that a rather unique configuration is probed. At high energy, the deeply-bound proton knockout reaction ^{19}N$(-1p)^{18}$C is expected to occur mainly through a quasi-free mechanism [111]. When deep-hole proton configurations (1p1h) are produced with this mechanism, they mix with all states present in the same (high) energy range and acquire a very broad width through this mixing, and as soon as formed these "resonances" vanish. Therefore this fast process keeps no trace of the proton particle-hole configuration and acts as a sudden promotion to the continuum of neutrons having a configuration with a strong overlap with their initial structure. Conversely, when the knockout process occurs to not-so-deeply bound states, narrower resonant states are produced and their decay is characteristic of the overlap between their configuration and those of the final state available.

As shown in Fig. 4.5, the contribution of excited ^{16}C events seems negligible. In order to check that this is not the result of a γ detection problem, the γ-ray spectra obtained in coincidence with the ^{18}C$\rightarrow^{16}$C+2n channel are presented Fig. 4.7. It is known from a previous study [112] that ^{16}C has several excited states at 1.77 MeV, 3.03 MeV, 3.99 MeV, 4.09 MeV and 4.14 MeV. It is also known that the three highest excited states are decaying in cascade through the first excited state at 1.77 MeV resulting in γ-ray transitions at the following energies: 2.22 MeV, 2.32 MeV and 2.37 MeV. Due to the resolution of the detector used during

our experiment, it is impossible to distinguish those three transitions. However, it is possible to clearly observe the cascade decay of at least one of the three highest excited states through the first excited state. Indeed, looking at the M_γ=1 events (Fig. 4.7, left) allows to clearly identify a transition at around 1.77 MeV, while looking at the M_γ=2 events (right) allows to identify not only the transition at 1.77 MeV but also a transition at around 2.39 MeV that could correspond to a transition from one of the three highest excited states to the first one.

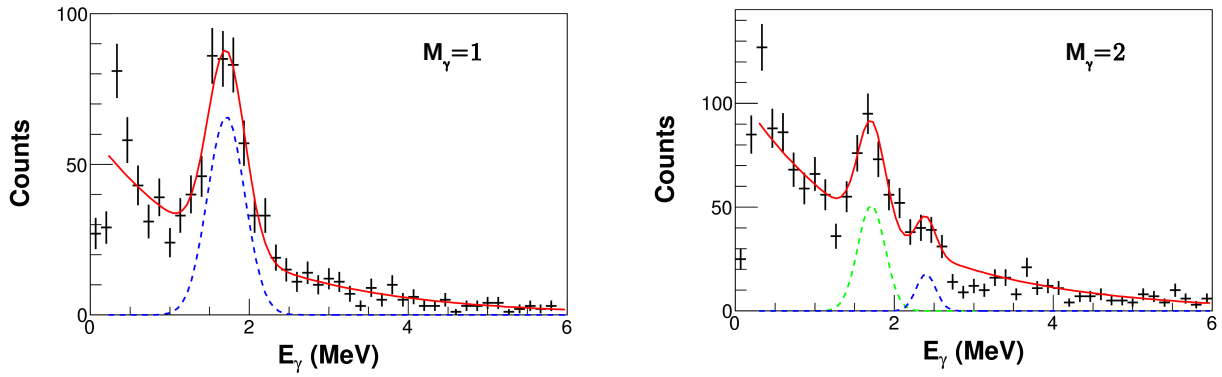

Figure 4.7: *γ-ray spectra observed in coincidence with the $^{18}C \rightarrow ^{16}C+2n$ channel for two different gamma multiplicities (M_γ).*

4.3.2 Normalized invariant masses, Dalitz plots and correlation function

Dalitz plots - As discussed in section 2.3, correlations in a three-body decay are easily revealed in Dalitz plots of the normalized squared invariant masses of particle pairs (m^2_{ij}), where FSI and resonances lead to a non-uniform population of those plots within the kinematic boundary defined by energy-momentum conservation and the relative energy. A summary of the simulation results obtained with the model developed in section 2.3 is shown in Fig. 4.8(a-c). In addition, the results of a combination of both direct and sequential decays is presented in (d), where a crescent-shaped pattern with a dip at the center appears. Prior to comparing in detail with any model, we can already note that the experimental plot of panel (e) looks almost exclusively like a direct decay, while that of panel (f) displays a mixture of direct and sequential decays.

The projections of the experimental Dalitz plots are shown in Fig. 4.9 for the two systems and four E_{rel} bins: 0–3.7, 3.7–5.3, 5.3–7.2 and 7.2–12 MeV (chosen in order to contain similar statistics). The phase-space uniform population of the Dalitz plot leads to bell-shaped projections (yellow histograms) with a maximum at about 0.5. They have been normalized to the data at $m^2_{nn} > 0.6$, where no n-n correlations are observed. Clearly, the data deviate significantly from phase space. In particular, an increase towards $m^2_{nn} = 0$ is noticeable in all panels, as already observed in Fig. 4.8(e,f). It is however much stronger in the $2n$ decay of ^{18}C, which suggests stronger pairing correlations in this system.

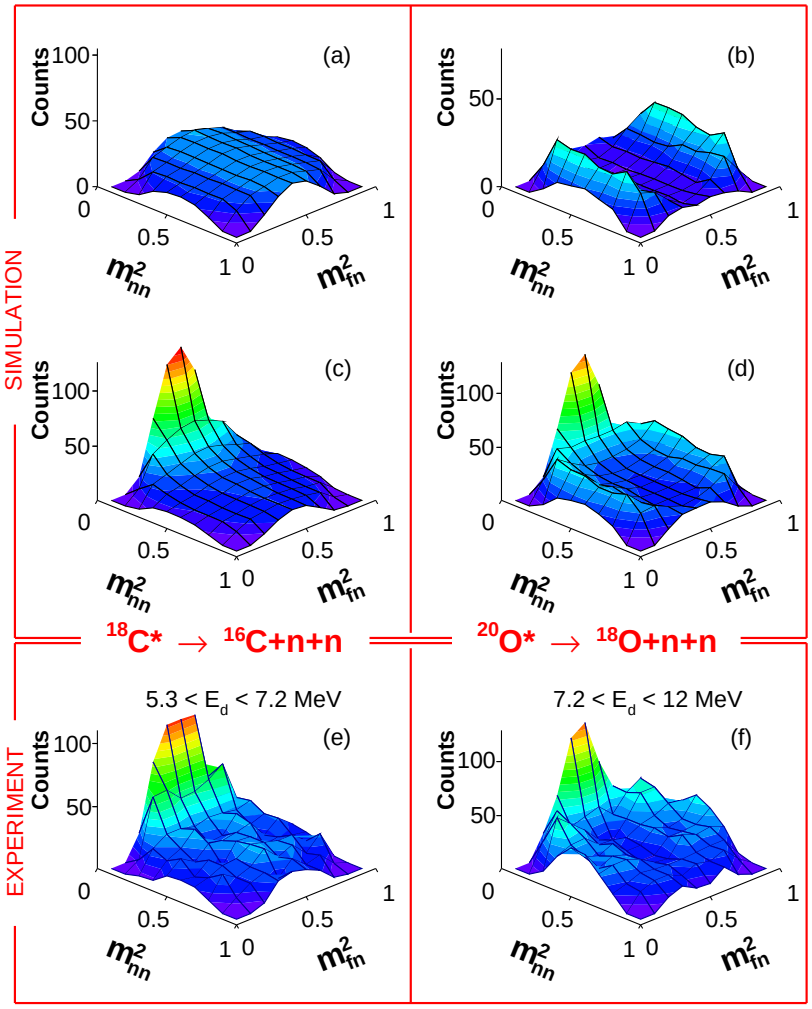

Figure 4.8: *Dalitz plots of fragment+n+n decays (fragment-n vs n-n normalized squared invariant masses). Left panels correspond to ^{16}C+n+n, right panels to ^{18}O+n+n. The four upper panels represent simulations of (a) phase space, (b) sequential decay through a fragment-n resonance, (c) direct decay with n-n FSI, and (d) a combination of the latter two. The lower panels (e,f) correspond to the experimental data for the relative energies noted.*

Concerning the fragment-n channel, which should reveal the degree of sequentiality in the decay, the expected bands in the Dalitz plot of Fig. 4.8(b) correspond to 'wings' in the projection onto m^2_{fn}. Those are clearly observed at 0.1–0.3 and 0.7–0.9 in the three higher-energy bins of ^{20}O (see Fig. 4.9). These wings and the increase of m^2_{nn} towards 0 suggest, as was noted above, that the sequential and direct decays are in competition. In order to determine the extent of this competition, we have used the phenomenological model described in chapter 2. However before moving into this, we propose to construct the correlation functions C_{nn} of the two systems studied. Indeed, the correlation function is a model-independent observable and will allow us to discuss some of the feature observed and compare our results to other studies.

Correlation functions - The experimental correlation functions C_{nn} of Fig. 4.10(a) have been constructed for ^{18}C (blue dots) and ^{20}O (red dots) from the ratio of the measured relative momentum distribution q_{nn}, that contains the interaction effects, and the one

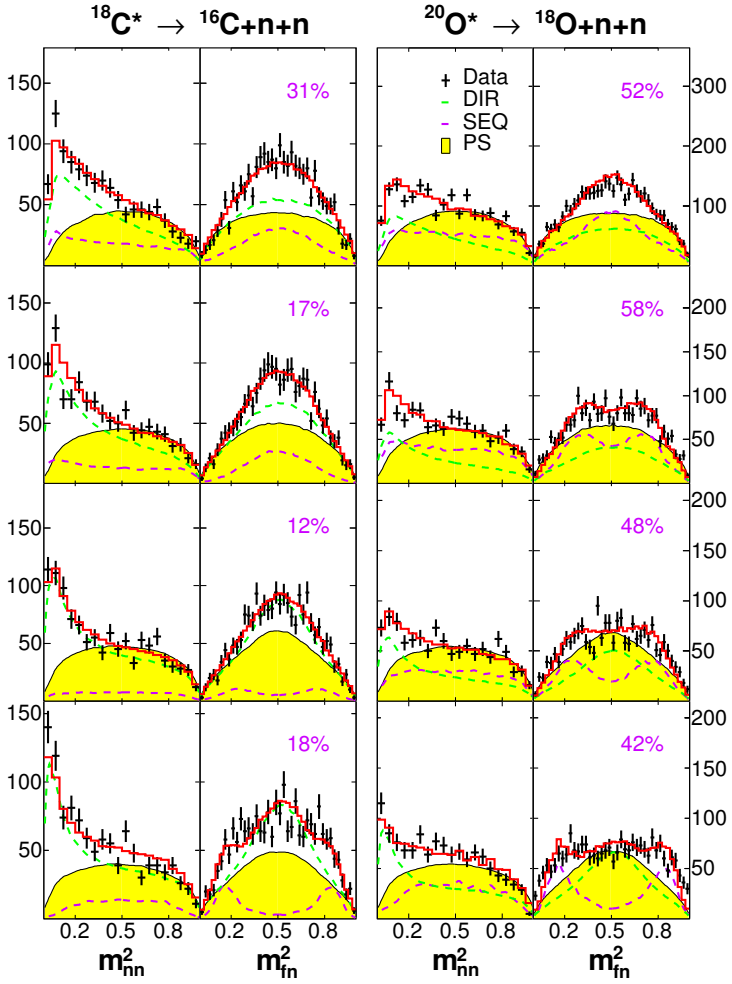

Figure 4.9: *Projection of the Dalitz plots defined in Fig. 4.8 onto either axes for the data of $^{18}C^*$ (left) and $^{20}O^*$ (right) decays. The rows correspond to the four E_{rel} bins defined in the text, from lower (top) to higher (bottom). The yellow histograms represent phase space, normalized to the data at $m^2_{nn} > 0.6$. The red histograms are the projections of the best two-dimensional fit of the plots, with their direct (green) and sequential (purple, with percentage noted) decay components.*

obtained from phase space, that contains all other effects like kinematic constraints or the experimental filter (see chapter 2). These two distributions are shown in Fig. 4.10(b) for the ^{18}C case, where the effect of the n-n FSI at q_{nn} values below 100 MeV/c becomes even clearer. In order to guide the eye, the experimental C_{nn} have been fitted with a double Gaussian. The correlation signal in ^{18}C, $C_{nn}(0) \sim 25$, is huge, actually the largest ever observed.

In order to interpret this correlation strength, the authors of Ref. [91] propose a formulation that links $C_{nn}(q_{nn})$ to the size and lifetime of a Gaussian source emitting independent neutrons. When the source of particle pairs is large and/or the emission of the two particles proceeds through a long decay time, correlations are expected to be very weak. Within this formalism, the ^{18}C data would suggest a small source and a very short decay time, or a very weak contribution of the sequential decay, as was anticipated already in Fig. 4.8(e).

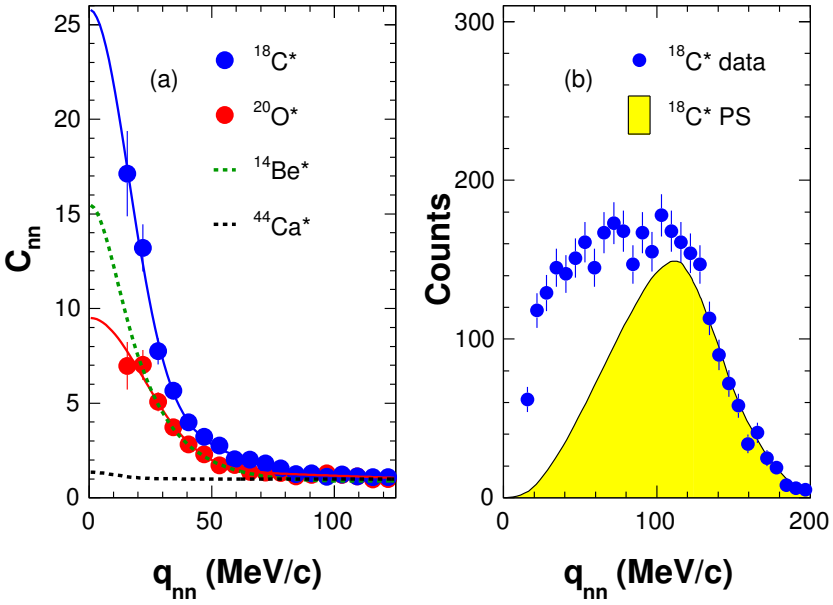

Figure 4.10: *(a) Two-neutron correlation functions from the three higher-energy bins of $^{18}C^*$ (blue) and $^{20}O^*$ (red) 2n decays. The solid lines are traced to guide the eye, while the dashed lines correspond to the fits of the experimental data from the breakup of ^{14}Be (green) [7] and the neutron evaporation from ^{44}Ca (black) [8]. (b) Numerator (measured relative momentum distribution, blue points) and denominator (phase space, yellow) of C_{nn} for the $^{18}C^*$ case.*

For comparison, we have added in Fig. 4.10(a) the correlation functions obtained for two significantly different systems. In one case (black dashed line), the source of neutron pairs was the compound nucleus formed in the collision ^{18}O+^{26}Mg [8]. The best fit of the experimental C_{nn} was obtained for a sphere of $R = 4.4 \pm 0.3$ fm and a lifetime of $\tau = 1100 \pm 100$ fm/c. For this moderately small source, the long decay time scale is responsible for shrinking the correlation to $C_{nn}(0) \sim 1.3$, a signal about a factor 80 smaller than the one measured for ^{18}C.

In the second case (green dashed line), the source was formed during the breakup of the two-neutron halo nucleus ^{14}Be [7]. Direct pair emission ($\tau = 0$) was invoked to account for the strong correlation measured, $C_{nn}(0) \sim 15$, at that time the largest ever observed. However, the relatively large size of the neutron pair in this halo nucleus, with a correlation signal described by a Gaussian source of $r_{nn}^{rms} = 5.6 \pm 1.0$ fm, accounts for a reduction of about 40% with respect to ^{18}C.

Decay model and results - As we mentioned earlier, we observe that sequential and direct decays are in competition. In order to determine the extent of this competition, we have used the phenomenological model described in chapter 2 that contains both components. We can express the general fitting function F_N for N intermediate fragment+n resonances of energy E_{r_i} and width Γ_{r_i}:

$$F_N = \sum_{i=1}^{N} \alpha_i f_i^{seq}(r_{nn}^{rms}, E_{r_i}, \Gamma_{r_i}) + (1 - \sum_{i=1}^{N} \alpha_i) f^{dir}(r_{nn}^{rms}) \qquad (4.5)$$

where α_i corresponds to the fraction of each sequential decay. f^{dir} and f^{seq} represent the

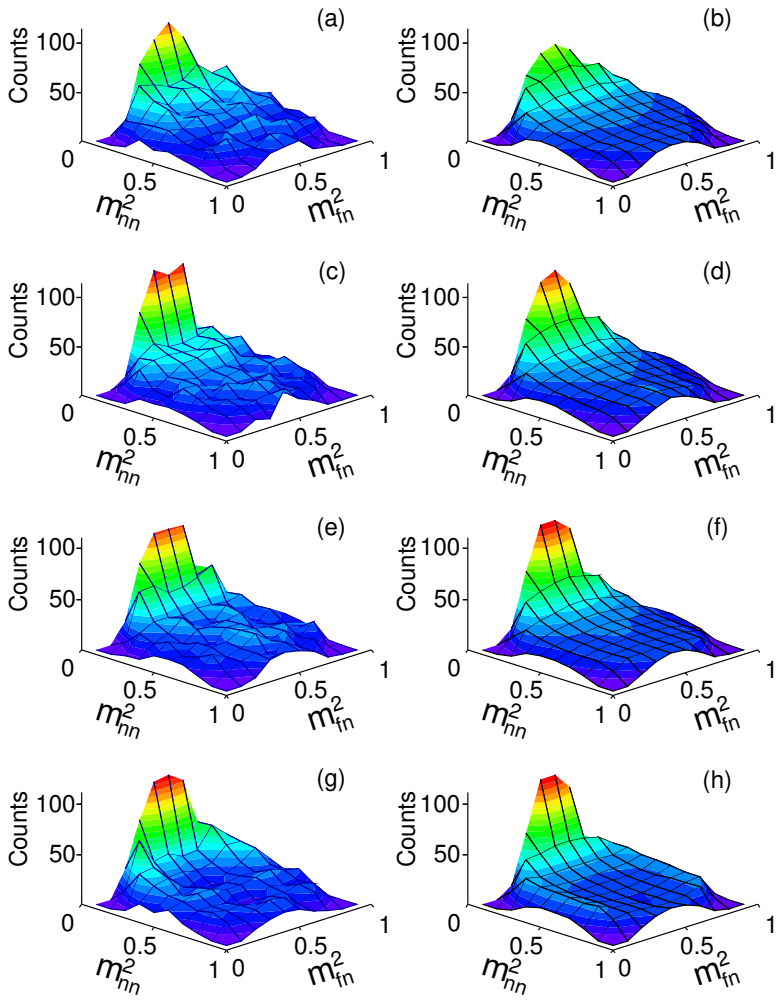

Figure 4.11: *Comparison between the Dalitz plot for ^{18}C obtained with the data (left) and the one obtained from the simulation for the best fit (right). The comparison for different E_{rel} ranges are shown: E_{rel} =0-3.7 MeV for (a) and (b), E_{rel} =3.7-5.3 MeV for (c) and (d), E_{rel} =5.3-7.2 MeV for (e) and (f) and E_{rel} =7.2-12 MeV for (g) and (h).*

direct and sequential component, respectively. In an attempt to reduce the parameters of the fit to a reasonable number, we consider that the sequential decay occurs through one fragment-n resonance of energy $\langle E_r \rangle$ and width $\langle \Gamma_r \rangle$, that can be seen as an average over individual resonances. In fact, even the fits of the higher-energy bins only require one low-energy resonance, of $\langle E_r \rangle \sim 1.5$ MeV. We can therefore express the fitting function as:

$$F_1 = \alpha f^{seq}(r_{nn}^{rms}, \langle E_r \rangle, \langle \Gamma_r \rangle) + (1-\alpha) f^{dir}(r_{nn}^{rms}) \tag{4.6}$$

The final momenta of the three generated particles are filtered to include all experimental effects (like energy resolution, angular acceptance, or cross-talk rejection). Then the different observables are reconstructed and fitted, using Eq. 4.6, to the data in the two-dimensional Dalitz surface (Fig. 4.8). An example of the goodness of the two-dimensional fit is given in the

E_d (MeV)	r_{nn}^{rms} (fm)	Seq. (%)	$\langle E_r \rangle$ (MeV)	$\langle \Gamma_r \rangle$ (MeV)
0–3.7	$4.0^{+0.6}_{-0.3}$	31 ± 14	1.5 ± 0.3	$1.0^{+0.8}_{-0.3}$
3.7–5.3	4.5 ± 0.6	17 ± 9	$2.0^{+1.3}_{-0.3}$	1.5 ± 0.3
5.3–7.2	4.2 ± 0.4	12 ± 7	$1.5^{+0.8}_{-0.3}$	$1.5^{+0.3}_{-0.8}$
7.2–12	3.7 ± 0.1	18 ± 4	1.5 ± 0.3	1.5 ± 0.3

Table 4.3: *Table summarizing the parameters obtained from the fits of the four-decay energy bins of ^{18}C shown in Fig. 4.11.*

E_d (MeV)	r_{nn}^{rms} (fm)	Seq. (%)	$\langle E_r \rangle$ (MeV)	$\langle \Gamma_r \rangle$ (MeV)
0–3.7	$4.6^{+1.1}_{-0.9}$	52 ± 9	1.5 ± 0.3	0.5 ± 0.3
3.7–5.3	4.4 ± 0.5	58 ± 10	1.5 ± 0.3	1.5 ± 0.3
5.3–7.2	4.6 ± 0.7	48 ± 7	1.5 ± 0.3	1.5 ± 0.3
7.2–12	3.7 ± 0.1	42 ± 5	1.5 ± 0.3	1.5 ± 0.3

Table 4.4: *Table summarizing the parameters obtained from the fits of the four-decay energy bins of ^{20}O shown in Fig. 4.12.*

comparison between panels (d) and (f) of Fig. 4.8, where both the n-n FSI and the wings of the sequential mode are accurately reproduced. Similar agreement is found for all the Dalitz plots (see Fig. 4.11 and Fig. 4.12) as well as for their projections shown in Fig. 4.9, further validating the different hypotheses used. The parameters obtained from the fits of the four decay energy bins of ^{18}C and ^{20}O are summarized in Table 4.3 and Table 4.4.

Considering the average over the four-energy bins (Tabs. 4.3 and 4.4), the fits denote a compact configuration in both systems, corresponding to a Gaussian source of $r_{nn}^{rms} = 4.1 \pm 0.4$ fm for ^{18}C and 4.3 ± 0.6 fm for ^{20}O. Both values are in line with the one corresponding to two nucleons independently distributed in a sphere of radius R ($r_{nn}^{rms} = \frac{3\sqrt{8}}{7}R$). Assuming a liquid drop of $R = 1.2A^{1/3}$, the r_{nn}^{rms} would read $\frac{3\sqrt{8}}{7}1.2A^{1/3}$. This gives us for $A = 20$ a distance r_{nn}^{rms} =4 fm which is very similar to what we observed experimentally. According to the fits, however, the stronger n-n signal in ^{18}C is due to the neutron pair being emitted directly in $81 \pm 9\%$ of the time, and a sequential branch is only slightly apparent in the wings of the highest-energy bin. In contrast, $50 \pm 8\%$ of the decays are sequential in ^{20}O, with wings in m_{fn}^2 that are visible in all bins, even in the lowest energy one in which they move towards $m_{fn}^2 = 0.5$ to create an enhanced central contribution there.

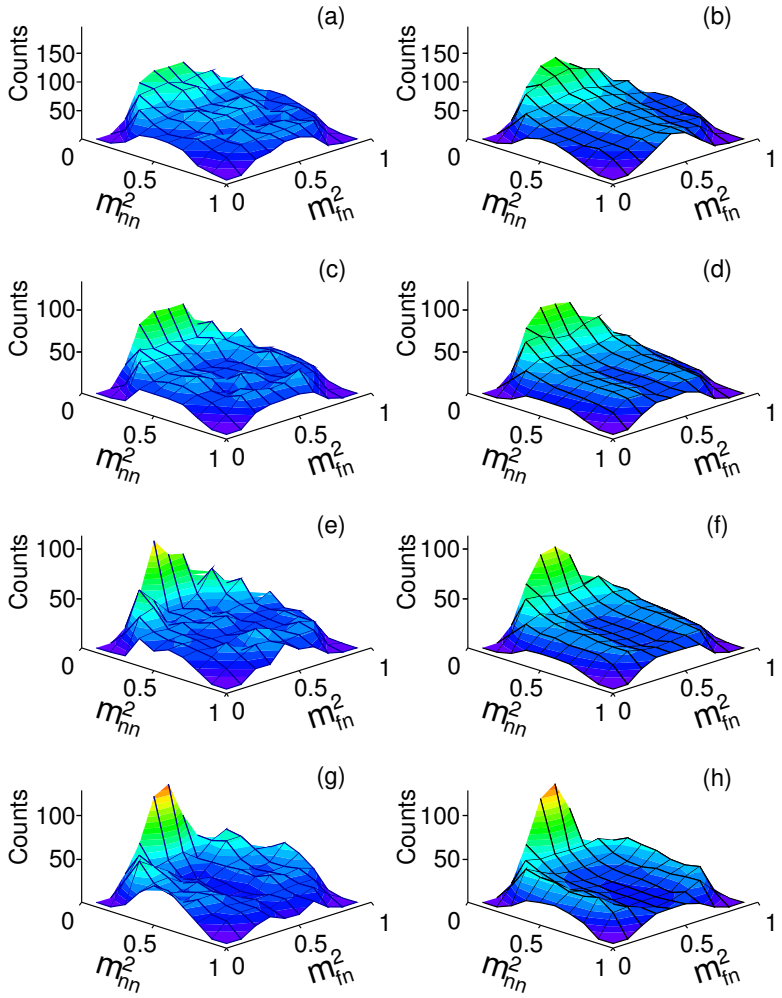

Figure 4.12: *Comparison between the Dalitz plot for ^{20}O obtained with the data (left) and the one obtained from the simulation for the best fit (right). The comparison for different E_{rel} ranges are shown: E_{rel} =0-3.7 MeV for (a) and (b), E_{rel} =3.7-5.3 MeV for (c) and (d), E_{rel} =5.3-7.2 MeV for (e) and (f) and E_{rel} =7.2-12 MeV for (g) and (h).*

4.4 Conclusion and perspective

We observed in this chapter that the decay of the core+4n isotones ^{18}C and ^{20}O displays significantly different features. In the former, extremely strong correlations persist up to 12 MeV, which we propose to be caused by the large fraction ($\sim$80%) of direct emission of correlated pairs with a relatively compact configuration. The decay of ^{20}O exhibits much weaker correlations, with about 50% occurring through sequential processes. The clear contrast between these isotones is likely due to the way they are populated: the knockout of deeply-bound neutrons from ^{21}O leaves two unpaired neutrons in ^{20}O with a broken ^{16}O core (in this way increasing the probability of sequential decay), while the knockout of deeply-bound protons from ^{19}N leaves the neutron pairs and the ^{14}C core unaffected.

The present study shows that the high-energy proton knockout reaction is a tool of choice for studying neutron correlations, be there of $2n$ or $4n$ origin, up to the neutron dripline.

Moreover, we noticed during our study that in the knockout from ^{19}N the dominant production channel leads to ^{14}C, as observed in Fig. 3.8 where the ^{14}C is the most populated fragment. While we are not able at the time being to detect $4n$ and their correlations owing to the insufficient granularity of the LAND detector, we think this feature is suggestive of a core+$4n$ structure of ^{18}C.

In the future, we wish to study the evolution of $2n$ and $4n$ correlations from the valley of stability to the dripline, and show the role of the reaction mechanism in revealing such correlations. Results shown in this chapter have suggested that the deep proton-knockout reaction provides a unique tool to suddenly promote neutrons into the continuum and study their correlations from their detection. The major drawbacks of the present study were the modest neutron energy resolution that leads to a large uncertainty on the single-particle structure of the $1n$ resonance, as well as the 500 keV efficiency cut-off for the detection of two-neutrons (due to cross-talk rejection conditions), that prevents the detection of low-energy neutrons from states possibly located right above S_{2n}. The limited granularity and efficiency of the neutron array also prevents the study of $4n$ correlations, which are rather detected as $2n$ or $3n$ at the present time. In future experiments, we wish to benefit from the increased granularity of the NeuLAND detector, as well as from the increased beam intensities, to study the ^{18}C$\rightarrow^{16}$C+$2n$ system using the ^{19}N$(-1p)$ reaction with a better resolution in order to:

- Characterize the resonance above S_{2n} (width, one- or two-neutron decay branches) to see if it is a good candidate for di-neutron decay.
- Populate and study states above S_{4n} and study if they exhibit $2n$-$2n$ or tetra-neutron correlations.
- Identify a narrow $4n$ resonance around the S_{4n} threshold to see if the Ikeda conjecture is a general feature of the continuum.

Added to this we would like to:

- Study the evolution of the pairing interaction and the extractedr_{nn}^{rms} value as a function of the excitation energy E_{exc} further from the stability using the ^{18}C$(p,2p)^{17}$B$\rightarrow^{15}$B+$2n$ reaction. Competition between gamma emission and $2n$ emission was tentatively found in the 1600 keV state, which may be a sign of $2n$ clusterization here. Having a much better energy resolution with the NeuLAND array will better constrain the energy and width of the resonance, check if its decay occurs directly or sequentially, and find if its energy matches that of the gamma-ray energy. In such a case, this would confirm this extremely rare competition between gamma and $2n$ decay.
- Study $4n$ correlations using the ^{18}C$(p,2p)^{17}$B$\rightarrow^{13}$B+$4n$ reaction channel by producing ^{17}B above the $4n$ emission threshold of 5.1 MeV.
- Identify if a candidate for $4n$ cluster (narrow resonance) exists around the corresponding emission threshold in ^{17}B, in view of a generalization of the Ikeda conjecture.

Interestingly, ^{19}C and ^{21}N are expected to be transmitted in the same experimental beam tuning. The former offers the opportunity to study the neutron correlations in ^{18}C via the one-neutron knockout reaction, and observe how they deviate when produced from the ^{19}N$(-1p)$ reaction that we presented in this chapter. Qualitatively, the neutron knockout reaction is expected to break the ^{14}C core, and may interestingly lead, as in the case of ^{20}O presented in this work, to much loose correlations and enhance sequential decays. On the other hand, the latter offers the possibility to study ^{20}O from the ^{21}N$(-1p)$ reaction to be compared with results obtained from ^{21}O$(-1n)$.

In this kind of experiment, several nuclei are produced, offering the possibility to study different systems at the same time. This is of utmost importance to understand and characterize the interplay between the reaction mechanism and the structure of the systems at the dripline.

Chapter 5

p-n interaction in Fluorine: ^{26}F and ^{28}F

Contents

In this chapter, we present the results obtained on ^{26}F and ^{28}F during the SAMURAI21 experiment performed at RIKEN. We will start by ^{26}F that has been populated from ^{27}F($-1n$), and compare our results to the ones obtained in a previous study [3]. Then we will investigate ^{28}F populated from ^{29}Ne($-1p$) and compare our results to a previous study [4] as discussed in section 1.4. In order to have a more complete picture of the ^{28}F structure, we populated it also from the knockout of a neutron in ^{29}F. Finally, we will explore the $2n$ decay (fragment+n+n) of high-energy excited states of ^{28}F populated from ^{29}Ne($-1p$).

5.1 ^{26}F: confirmation and new results

As mentioned in section 1.4, ^{26}F has already been studied using the ^{27}Ne(p,2p) reaction where an unbound state at 323(33) keV has been proposed as the $J^\pi = 3^+$ state which is part of the $J^\pi = 1^+, 2^+, 3^+, 4^+$ multiplet resulting from the $\pi d_{5/2} \otimes \nu d_{3/2}$ coupling. In this same study another state has been observed at 1790(290) keV for which no spin has been proposed. Therefore in this section, we want to compare our results, obtained with a different reaction, to those previous results. The same $J^\pi = 3^+$ state is expected to be populated using the ^{27}F(p,pn) and ^{27}Ne(p,2p) reaction. Our goal will be to confirm first that a state is observed at about 323(33) keV, and from the determination of its ℓ value confirm that this is indeed a candidate for the 3^+ of the $\pi d_{5/2} \otimes \nu d_{3/2}$ multiplet. Secondly, we will look for new states that have not been observed previously.

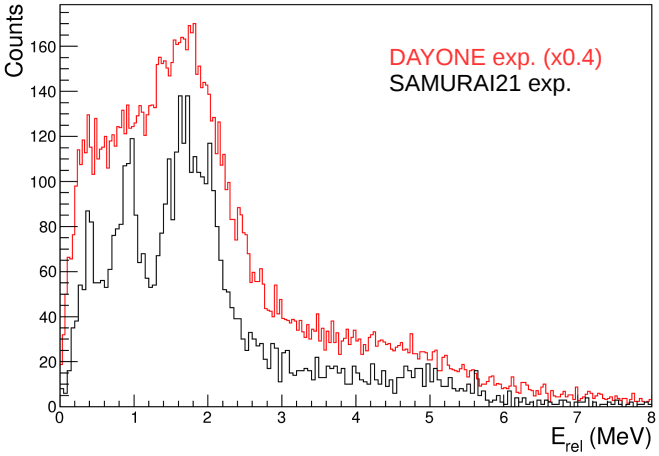

Figure 5.1: *Relative energy spectrum obtained for the $^{27}F(p,pn)^{26}F$ reaction in the SAMURAI21 experiment (black). The relative energy spectrum obtained for the same reaction in the DAYONE experiment (without the MINOS target and without the NeuLAND detector) is also shown (red).*

The relative-energy spectrum obtained for the $^{27}\mathrm{F}(p,pn)^{26}\mathrm{F}\rightarrow^{25}\mathrm{F}+n$ reaction is presented in Fig. 5.1. The spectrum obtained for the same reaction in the DAYONE experiment, in which the only differences compared to the SAMURAI21 experiment were the absence of the MINOS target and the NeuLAND detector in the setup, is also shown in the same plot. The comparison of those two results clearly shows the huge improvement on the resolution that has been made between those two experiments. Indeed, in the DAYONE experiment, only a broad structure between 0-2 MeV is observed while in the results from SAMURAI21, at least three structures can be clearly identified in this same energy range. This improvement in resolution is mainly due to two factors:

- the use of the MINOS target that allows a precise reconstruction of the position where the knockout reaction took place in the target, and therefore a precise correction for the energy loss of the fragment in the target.

- the use of the NeuLAND detector that has a higher granularity compared to the NEBULA detector and therefore allows to reach a better resolution on the reconstruction of the neutron momentum.

We start the analysis of the data by adding the maximized non-resonant contribution to the relative energy spectra as presented in Fig. 5.2 (see section 2.2.1). Then looking at the fragment-n correlation function allows us to observe four structures between 0-2.5 MeV and another structure at about 5 MeV. Moreover, it seems that another contribution could also be needed at about 3.5-4 MeV as the non-resonant component alone does not reproduce the data in this region.

We are therefore performing a fit of the data using the non-resonant contribution as well as six resonances. The results are presented in Fig. 5.3, where we can observe a good reproduction of the data by the total fit. The parameters of the fit are presented in Table 5.1.

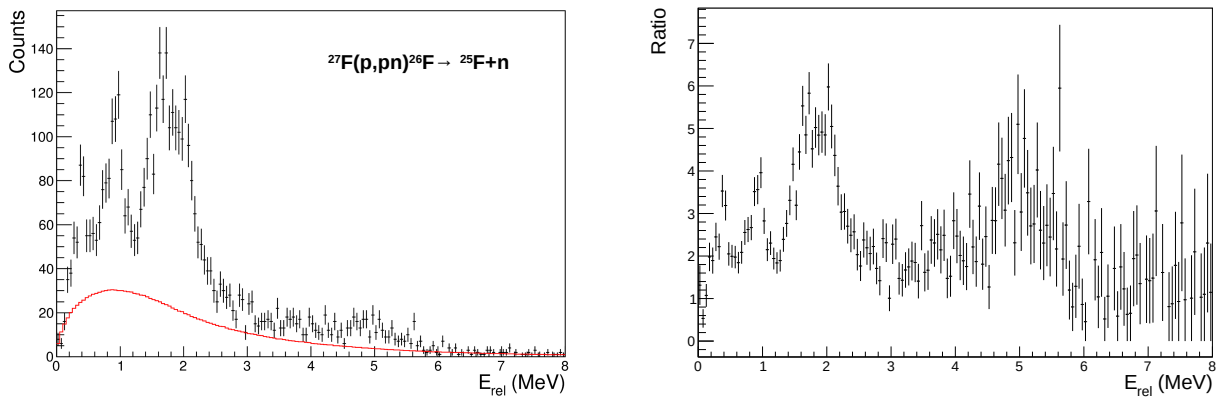

Figure 5.2: *On the left, relative energy spectrum obtained for the $^{27}F(p,pn)^{26}F$ reaction in the SAMURAI21 experiment to which the maximized non-resonant contribution as been added. On the right, ratio of the relative energy by the maximized non-resonant contribution for the same reaction channel.*

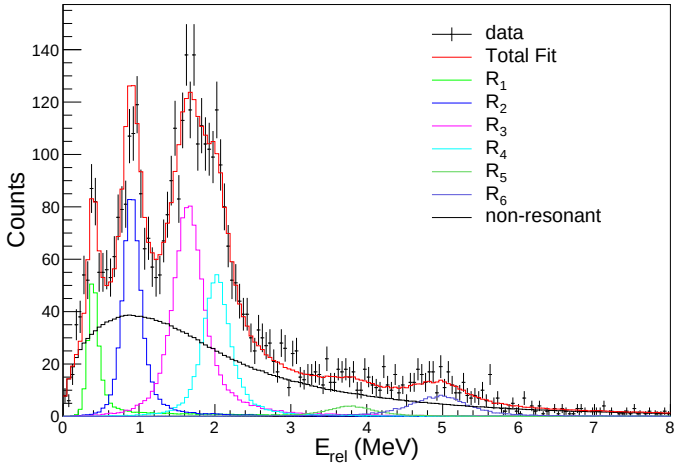

Figure 5.3: *Best fit obtained for the relative energy spectrum of the $^{27}F(p,pn)^{26}F$ reaction. The resonances are numbered as R_{1-6}.*

We observe a resonance at 0.38 MeV, which could correspond to the $J^\pi = 3^+$ state proposed in [3]. We also observe five resonances at higher energies that do not correspond to any known resonances.

However, as discussed in section 2.2.2, it is important to know if the resonances observed are decaying towards the ground state of ^{25}F or towards one of its excited states. In the first case, the excitation energy of the resonance is equal to the energy extracted from the fit to which we need to add the $S_n(^{26}\text{F})$ value, while in the second case the energy of the excited state observed in coincidence also needs to be added (see Eq. 2.19). The excited states of ^{25}F have already been studied in [9], where a precise level scheme based on particle-γ and particle-γ-γ coincidences has been established (see Fig. 5.4). Those results will be used as a reference as we will investigate correlations between γ-rays and resonances observed in the relative-energy spectrum.

R_i	E_r (MeV)	Γ_r (MeV)
1	0.38(6)	0.18(20)
2	0.90(7)	0.19(12)
3	1.65(8)	0.30(15)
4	2.02(9)	0.23(20)
5	3.81(78)	0.77(55)
6	4.98(37)	0.39(37)

Table 5.1: *Parameters obtained for the best fit of the relative energy spectrum of the $^{27}F(p,pn)^{26}F$ reaction.*

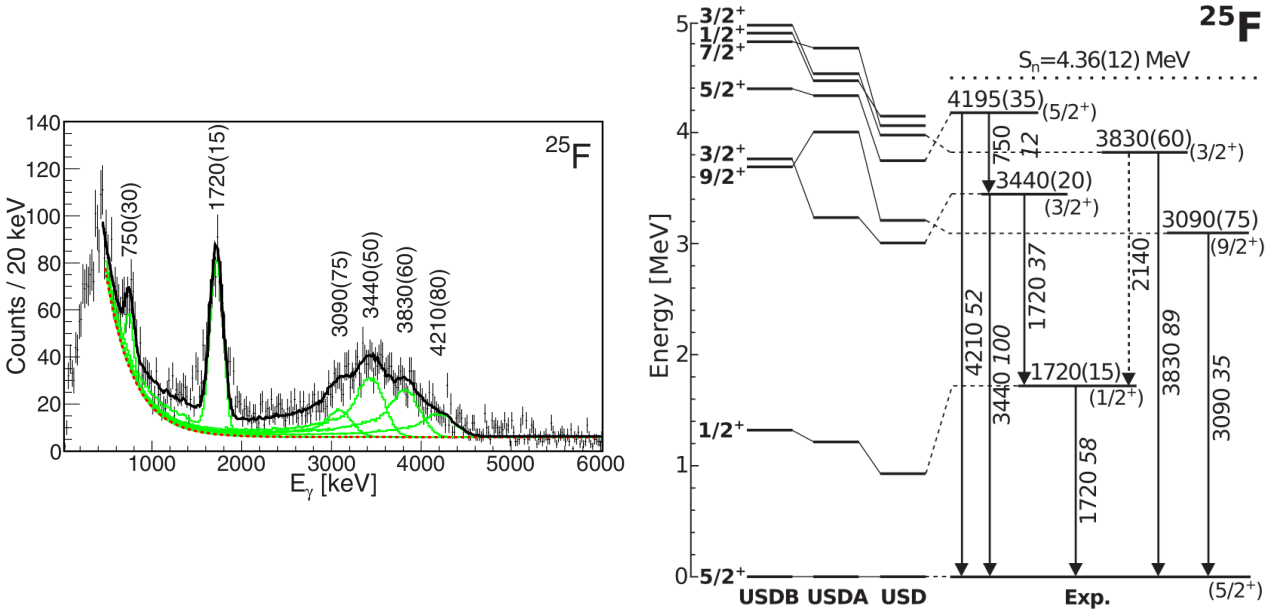

Figure 5.4: *On the left, decomposition of the γ-ray spectrum of ^{25}F. The solid black line shows the final fit which includes the response function from GEANT4 simulation (green solid curves) and the additional exponential background plotted as dashed red line. On the right, proposed level scheme of ^{25}F compared to shell-model calculations performed using USD, USDA and USDB interactions. Energies are given along the transitions as well as their relative intensities in italics. Both figures are taken from [9].*

The γ-rays observed in coincidence with ^{25}F+n events (Fig. 5.3) are presented in Fig. 5.5. Some structures that could correspond to known γ-ray transitions (Fig. 5.4) are observed in our inclusive γ-ray spectrum but it remains difficult to identify them clearly. We decided therefore to perform several cuts (corresponding approximately to the resonances found) in the relative energy spectrum of ^{26}F and to observe the corresponding coincidence events in the γ-ray spectrum (Fig. 5.6). The gates are chosen to avoid the regions where two resonances are overlapping.

We observe in Fig. 5.6 very different γ-ray spectra depending on which resonance is selected. Indeed, no clear γ-ray transition are observed in coincidence with the resonances R_1, R_4 and R_6, meaning that they are connected to the ground state of ^{25}F. A structure

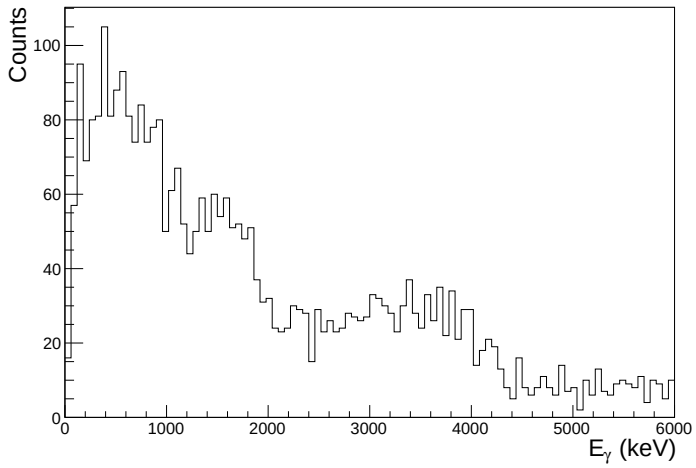

Figure 5.5: *γ-ray spectrum obtained in coincidence with ^{25}F+n events.*

that could correspond to the $9/2^+$ state in ^{25}F (Fig. 5.4) is observed in coincidence with the resonance R_5 but it is too narrow and low statistics to be consistent with the resolution of our detector. We therefore deduce that R_5 is also connected to the ground state of ^{25}F. However, structures are observed in the case of the R_2 and R_3 resonances. For the R_2 resonance, we observe γ-rays in coincidence at around 3-4 MeV that could correspond to the $3/2^+$ or $9/2^+$ states presented in Fig. 5.4. However, it is impossible, due to the resolution of our γ-ray detector and to the low statistics observed, to identify clearly which γ-ray transitions are observed in coincidence. In the γ-ray spectrum obtained in coincidence with R_3, we observe a structure at around 1.7 MeV and another one at between 3-4.2 MeV. All those transitions could be the signature of the decay through the $5/2^+$ excited state as we can see in Fig. 5.4. To summarize, we observed that the resonances R_2 and R_3 are not decaying to the ground state of ^{25}F but to its bound excited states. Indeed, R_2 seems to decay to one or several of the states from ^{25}F located between 3-4 MeV ($3/2^+$ or $9/2^+$) and the resonance R_3 seems to decay towards the $5/2^+$ state of ^{25}F. As mentioned earlier, those pieces of information need to be taken into account while building the level scheme of ^{26}F.

Now that we characterized all the resonances observed in the relative-energy spectrum of ^{26}F, we will try to assign their spin and parity (J^π). In the case of a neutron-knockout reaction, the momentum distribution allows to deduce the angular momentum of the knocked out neutron. Indeed, by comparing experimental results (shape and width of the distribution) to theoretical calculations, we are in principle able to extract the angular momentum of the knocked out neutron and therefore to deduce from which orbital it has been removed. In the following, we will compare our experimental results to eikonal-model theoretical calculations. The method used to perform those calculations is discussed in more details in Appendix B.

Before treating the unbound states previously discussed, we will test our method by looking at the ^{27}F(p,pn)^{26}F$^{(*)}$ reaction where the ground state and/or the bound excited states of ^{26}F are populated. The angular momentum of the neutron knocked out in order to populate all the $J^\pi = 1^+, 2^+, 4^+$ states is likely to be $\ell = 2$ ($\nu d_{3/2}$ orbital). We are therefore presenting in Fig. 5.7 the inclusive parallel momentum distribution of the outgoing fragment (^{26}F). The comparison

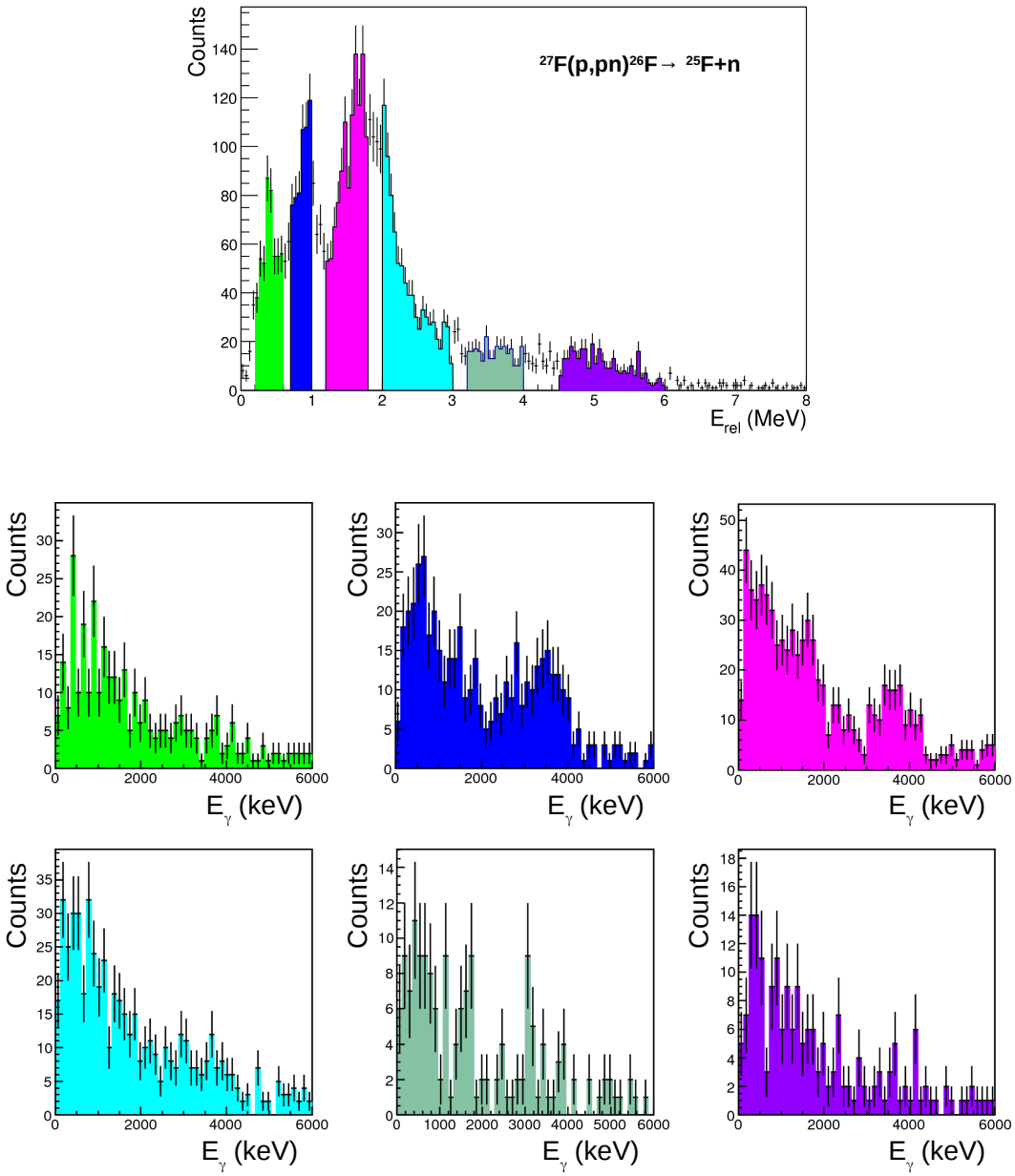

Figure 5.6: *Upper panel, relative energy gates for the ^{25}F+n events corresponding to the R_{1-6} resonances. Lower panel, γ-ray spectra corresponding to each gate (matching colors) presented in the upper panel.*

to the theoretical calculation is in good agreement with a pure $\ell = 2$ angular momentum as expected. After this cross-check, we will apply the same method to the unbound states of ^{26}F.

However, since some of the resonances are overlapping significantly, with each other and/or the non-resonant component, we need to find a way to construct the momentum distribution of a resonance without any contamination from the neighboring components. The method that we are using is discussed in Ref. [113]. The idea of this method is to build the momentum distribution of each resonance by making gates on the inclusive momentum distribution and then fitting the relative energy corresponding to each gate. For each gate in momentum,

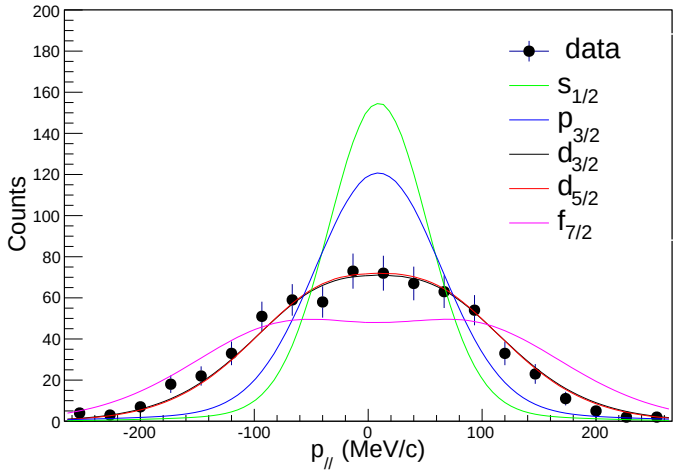

Figure 5.7: *Inclusive parallel-momentum distribution of the fragment (^{26}F) in the beam rest frame detected during the $^{27}F(p,pn)^{26}F^{(*)}$ reaction. Eikonal-model theoretical calculations are shown in different colors in order to compare them to the experimental distribution.*

one point is obtained for each resonance, the amplitude of the point corresponding to the integral of the resonance considered and its position corresponding to the center of the momentum gate. Using this method the momentum distribution for each resonance can be determined.

The result for the R_1 unbound state observed (at 0.38 keV) is shown in Fig. 5.8 and compared to theoretical calculations. Although the statistical significance is lower than in Fig. 5.7, due to the fact that the relative contribution of this resonance to the total spectrum of Fig. 5.3 is small, the best fit of the distribution is obtained for $\ell = 2$. This results confirms that this state seems to be the same than the one observed using a different reaction channel in Ref. [3] and that it is indeed a good candidate for $J^\pi = 3^+$ resulting from the $\pi d_{5/2} \otimes \nu d_{3/2}$ coupling discussed in section 1.4.

The momentum distributions for the R_2, R_3 and R_4 unbound states are also presented in Fig 5.8 and compared to theoretical calculations. For R_2, the best fit of the distribution is obtained for $\ell = 2$. Due to the relatively high energy of the resonance and to the fact that all the states from the $\pi d_{5/2} \otimes \nu d_{3/2}$ coupling have been identified. This state is probably resulting from the knockout of a neutron in the $d_{5/2}$ orbital. Therefore R_2 could be one of the states expected from the $\pi d_{5/2} \otimes \nu d_{5/2}$ coupling ($J^\pi = 0^+, 1^+, 2^+, 3^+, 4^+, 5^+$). For R_3 and R_4, the momentum distributions are best reproduced for $\ell = 1$, meaning that those two states have a negative parity.

Unfortunately, we are not able to extract the momentum distributions for the R_5 and R_6 resonances due to the low statistics observed for each of those states. We also did not observe any state corresponding to a $\ell = 0$ angular momentum even if the $s_{1/2}$ and the $d_{3/2}$ orbitals are expected to be very close. This is probably due to the fact that $\ell = 0$ states are usually very broad and therefore difficult to observed experimentally.

Following our results, we can propose a level scheme for the unbound states observed in ^{26}F using the ^{27}F$(-1n)$ reaction in Fig. 5.9. Since we are not able to distinguish which γ-ray tran-

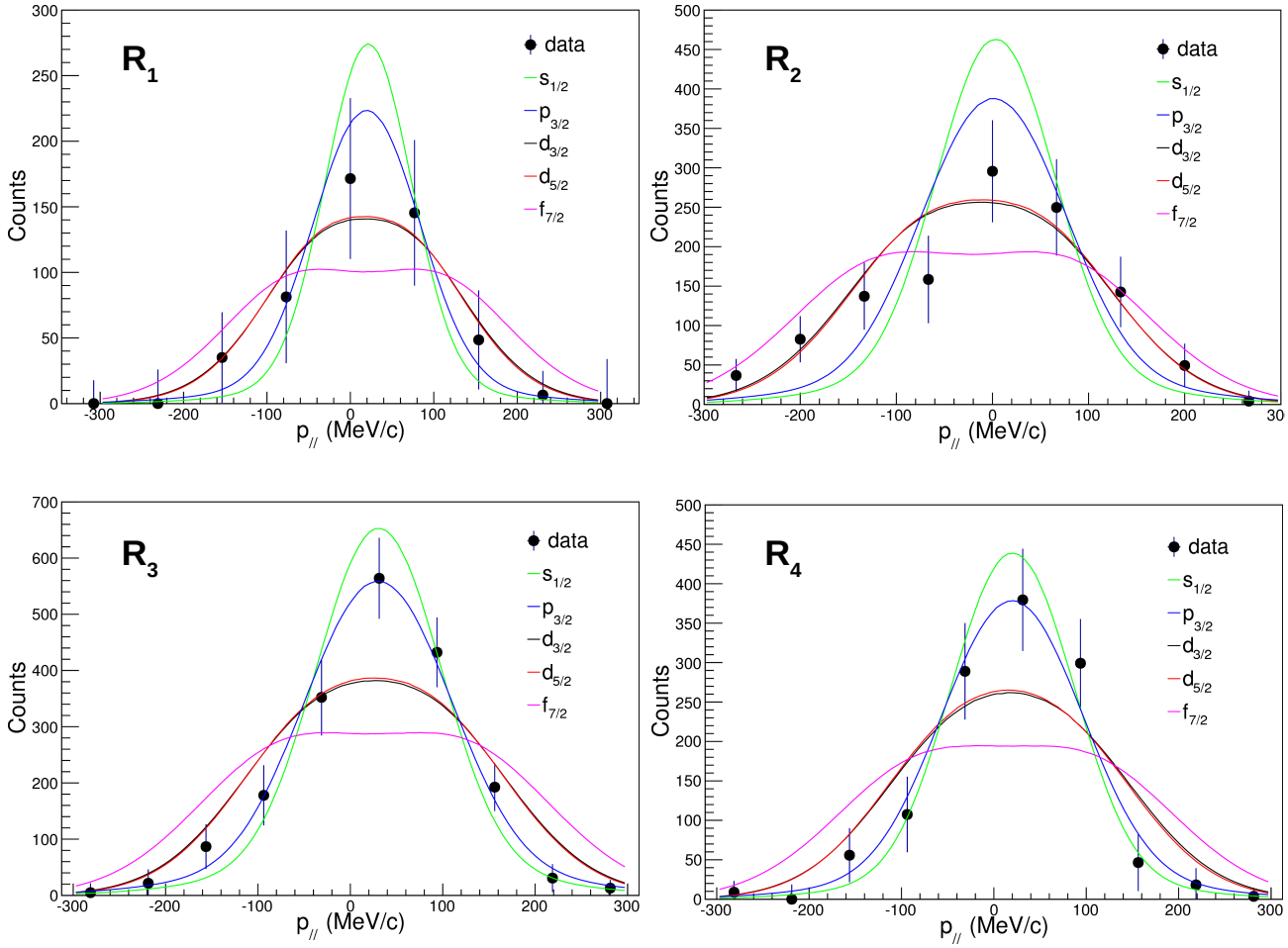

Figure 5.8: *Parallel-momentum distribution for the R_{1-4} resonances of the (^{25}F+n) unbound system in the beam rest frame. Eikonal-model theoretical calculations are shown in different colors in order to compare them to the experimental distribution.*

sitions are observed in coincidence with R_2 and R_3 we assumed an average transition of 3.5 MeV.

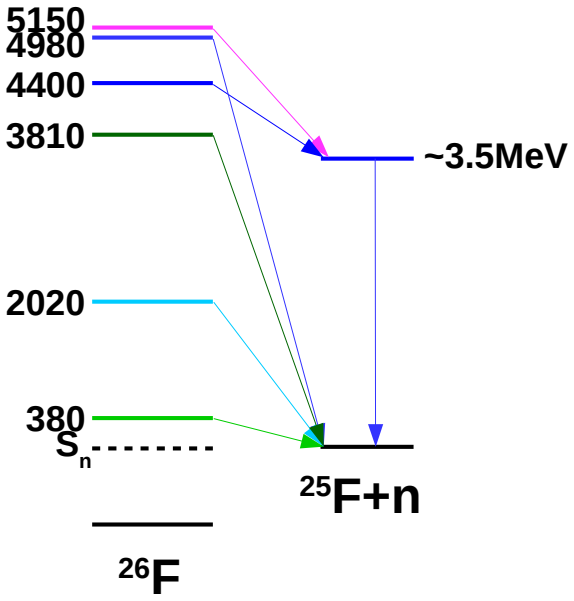

Figure 5.9: *Proposed level scheme of ^{26}F deduced from our experimental results for the $^{27}F(-1n)$ reaction.*

5.2 ^{28}F: spectroscopy from ^{29}Ne$(-1p)$

We move now to the study of ^{28}F populated from the knockout of a proton in ^{29}Ne (same reaction as in Ref. [4]). The relative energy spectrum is presented in Fig. 5.10 where the maximized non-resonant contribution has been drawn. This and the correlation function allow us to clearly observe seven resonances when only two were assumed in the previous study [4].

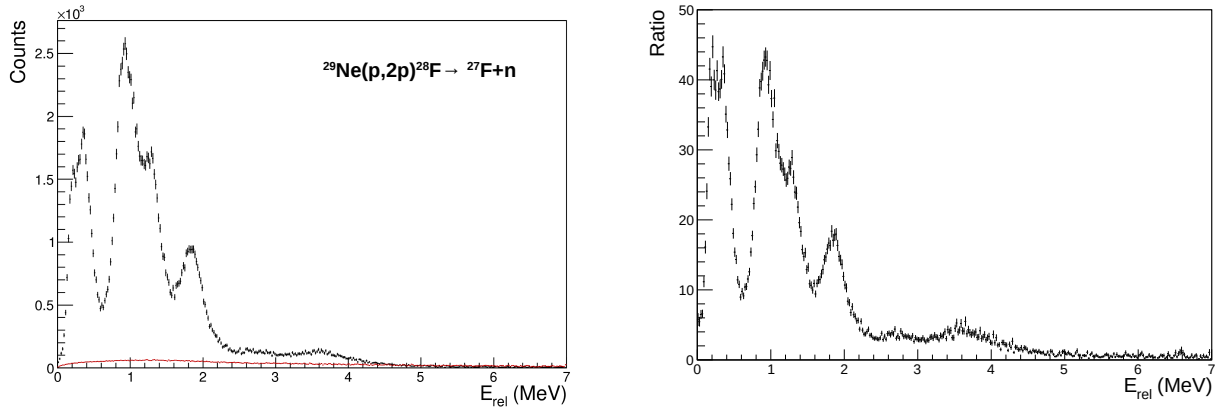

Figure 5.10: *On the left, relative-energy spectrum obtained for the $^{29}Ne(p,2p)^{28}F$ reaction in the SAMURAI21 experiment to which the maximized non-resonant contribution has been added (red). On the right, ratio of the relative energy and the maximized non-resonant contribution for the same reaction channel.*

Before moving to the fit of the relative energy spectrum, we will use this result as an example to show the resolution difference between NEBULA and NeuLAND (Fig. 5.11). The better resolution achieved using NeuLAND is explained by its enhanced granularity compared to NEBULA. Indeed, the section of the bars for NeuLAND is 5×5 cm^2 and 12×12 cm^2 for NEBULA. Even if NeuLAND is located closer to the reaction target compared to NEBULA, the resolution obtained with NeuLAND is better.

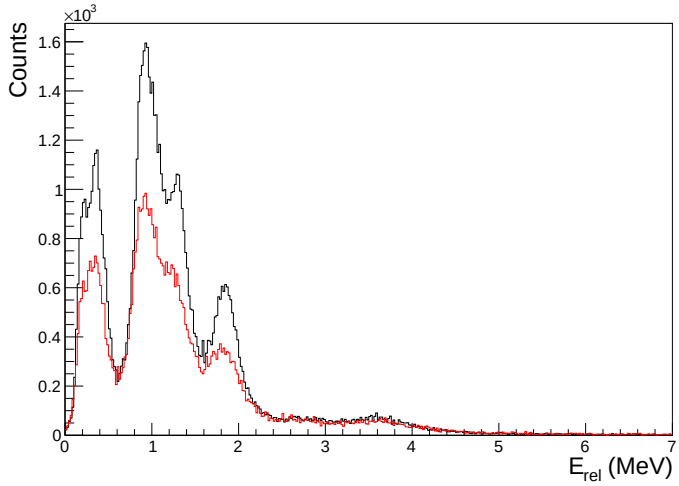

Figure 5.11: *Superposition of the relative-energy spectra for the ^{27}F+n system obtained when the neutron is detected in NeuLAND (black) or NEBULA (red).*

We are now performing the fit of the relative energy spectrum for the ^{27}F+n system. The results of the fit assuming seven resonances are presented in Fig. 5.12 and Table 5.2. The experimental data are remarkably well reproduced by the total fit, even when looking at the spectrum in logarithmic scale.

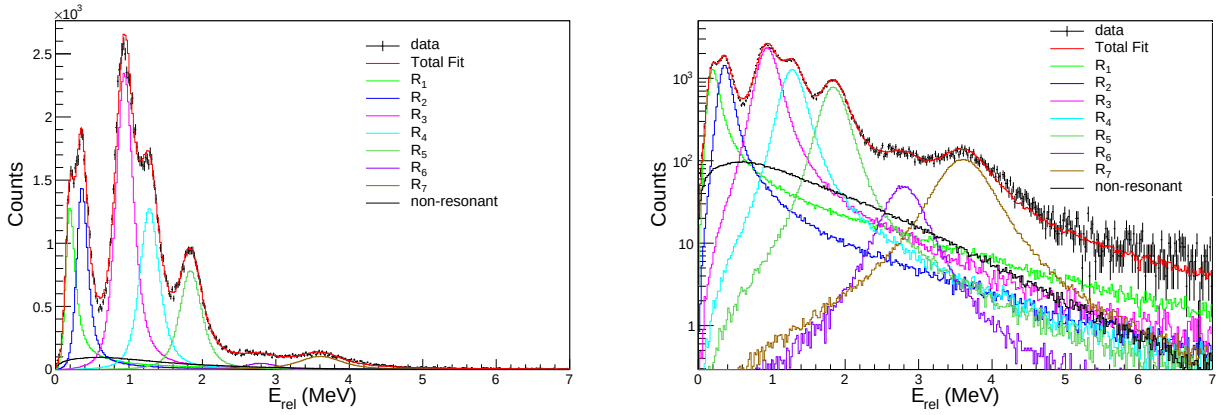

Figure 5.12: *On the left, best fit obtained for the relative-energy spectrum for the ^{27}F+n system. On the right, same figure in logarithmic scale.*

As mentioned in the previous section, it is crucial to know if the unbound states observed are decaying to the ground state of ^{27}F and/or to an excited state. The bound states of

^{27}F have been recently studied in [114] where only one excited state has been identified at 915(12) keV. This same transition is observed in the inclusive γ-ray spectrum (Fig. 5.13) obtained in coincidence with the ^{27}F+n events.

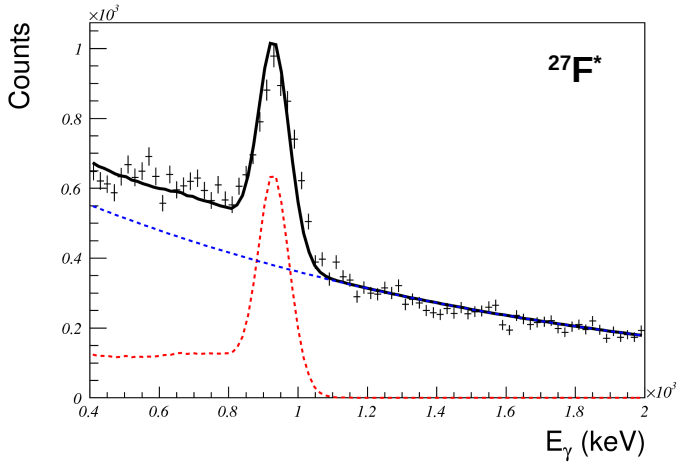

Figure 5.13: *γ-ray spectrum obtained in coincidence with ^{27}F+n events. The data (black points) are fitted using a distribution (black line) with two components: the result of the simulation (red dashed line) and an exponential (blue dashed line).*

In order to determine which state(s) are decaying to the excited state of ^{27}F, we can look for γ-ray transitions in coincidence with resonances in the ^{27}F+n system (Fig. 5.14). We observe that R_2 and R_6 are found in coincidence with a γ-ray at around 930 keV. This means that those two resonances decay to the excited state of ^{27}F while all the other resonances decay to its ground state.

As mentioned in section 2.2.2, the energy of a resonance decaying to an excited state needs to be shifted by the corresponding γ-ray transition (here 915 keV). We can do the calculation as an example for R_2 that we observed at 0.36 keV. Adding the energy of the γ-ray in coincidence, we find that this state is actually located at around 1.28 MeV above S_n, which corresponds to the energy of R_4. We can therefore propose that R_2 and R_4 are actually the same state decaying either to the ground state (59%) of ^{27}F or to its excited state (41%). We observe in the same way that R_6 and R_7 could also be only one state decaying either to the ground state of ^{27}F or to its excited state.

Following our results, we can propose a level scheme for the unbound states observed in ^{28}F using the ^{29}Ne$(-1p)$ reaction in Fig. 5.15. The ground state of ^{28}F is found to be at 0.20 MeV. We have therefore determined for the first time the energy of the ground state (and from there its mass) of ^{28}F, 200 keV. Even if this value is close to the one quoted in the previous work, the latter was the random result of the combination of the ground and second excited states, the absence of γ-ray detection, the low resolution and statistics, and a subjective fitting hypothesis. In addition, five excited states have been unambiguously determined, for the first time too, with the clear signature of one of them decaying through two different paths.

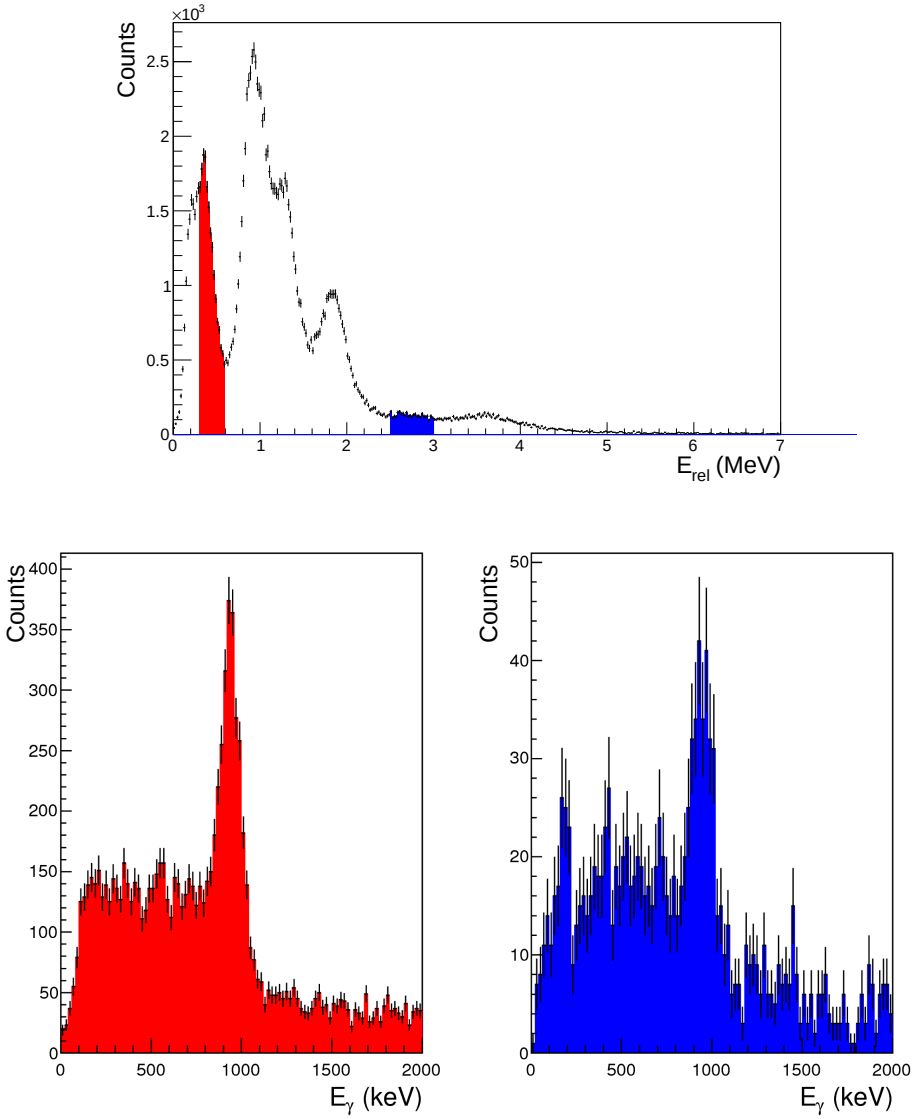

Figure 5.14: *Upper panel, relative energy gates for the ^{27}F+n events. Lower panel, γ-ray spectra corresponding to each gate (matching colors).*

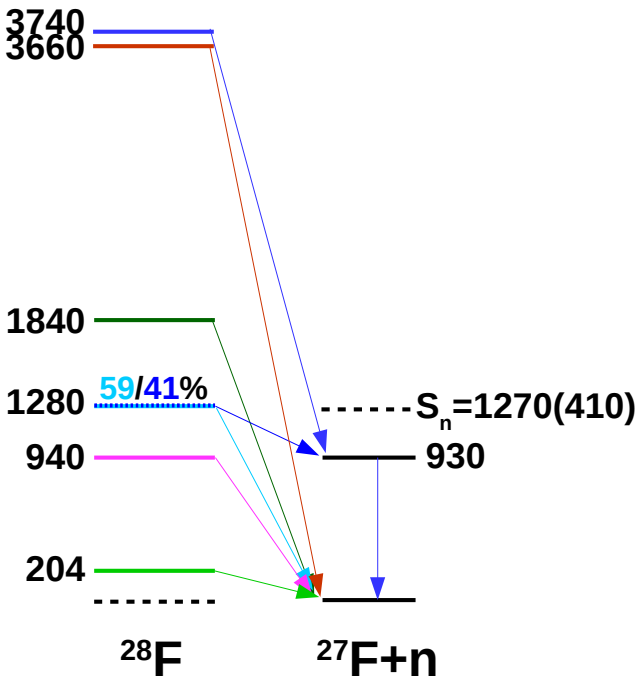

Figure 5.15: *Proposed level scheme of ^{28}F deduced from our experimental results for the $^{29}Ne(-1p)$ reaction.*

5.3 ^{28}F: spectroscopy from ^{29}F$(-1n)$

We propose now to study ^{28}F populated from the knockout of a neutron in ^{29}F, a reaction that has never been studied before and that may provide a new perspective on the structure of ^{28}F, and in particular on the spin and parity of the states observed. Like we did in the previous sections, we start first by looking at the relative energy spectrum of the ^{27}F+n system to which we added the maximized non-resonant contribution as shown in Fig. 5.16, where the correlation function is also presented. From those two plots, we can clearly identify three resonances between 0-2.5 MeV and maybe two other resonances at around 3.4 and 4 MeV, leading to a total of five contributions.

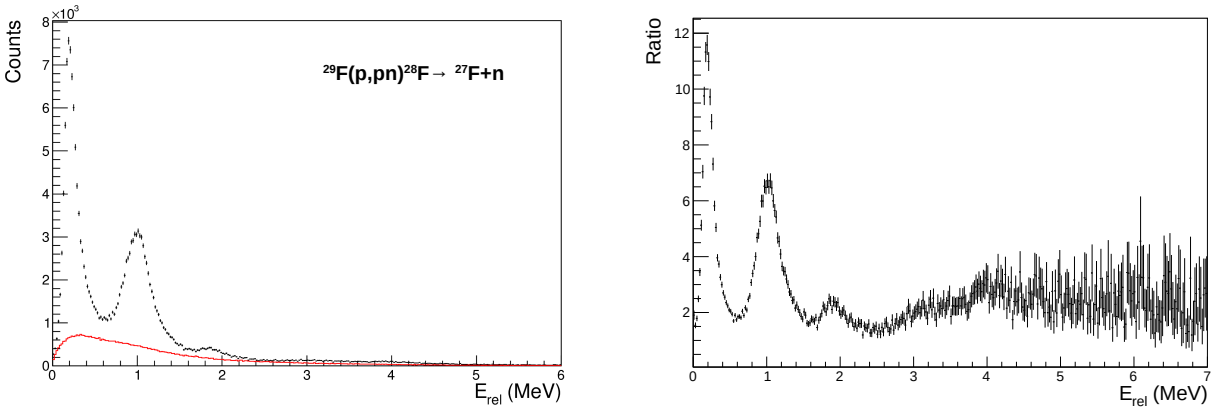

Figure 5.16: *On the left, relative energy spectrum obtained for the $^{29}F(p,pn)^{28}F$ reaction in the SAMURAI21 experiment to which the maximized non-resonant contribution has been added (red). On the right, ratio of the relative energy by the maximized non-resonant contribution for the same reaction channel.*

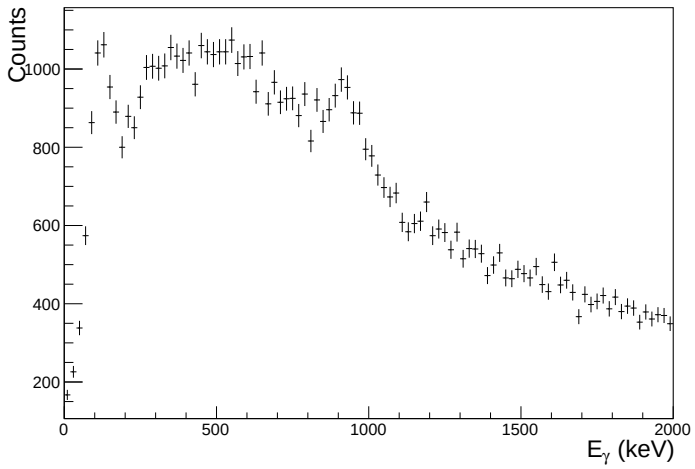

Figure 5.17: *γ-ray spectrum obtained in coincidence with ^{27}F+n events.*

Before moving to the fit of the relative energy, we check the presence of γ-rays from ^{27}F in coincidence. Indeed, we populate here the same ^{28}F nucleus than in the previous section

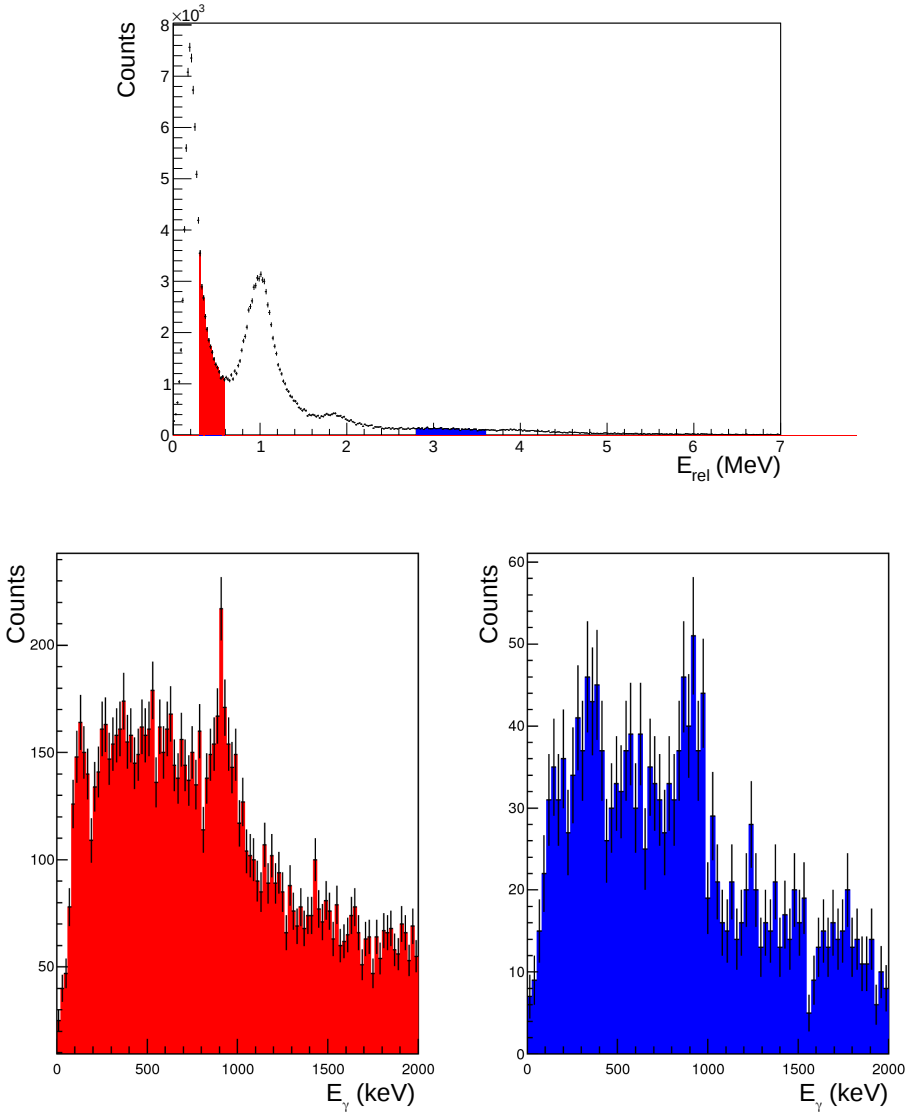

Figure 5.18: *Upper panel, relative-energy gates for the $^{27}F+n$ events. Lower panel, γ-ray spectra corresponding to each gate (matching colors).*

where seven resonances were observed. ^{28}F being populated via two different reactions, it is not surprising that the relative energy spectra are not identical. However, we note that the first state observed here at around 200 keV seems to be the ground state of ^{28}F identified in the previous section. By comparing the two spectra (Fig. 5.16 and Fig. 5.10), we observe that several structures seem to match while others seem to have disappeared, like for example the two resonances observed via the ^{29}Ne$(-1p)$ at 0.36 and 1.28 MeV. We observed in the previous section that the structure at 0.36 keV was in coincidence with γ-rays and we proposed that the structures at 0.36 and 1.28 MeV were actually the same state decaying both to the ground state and to the excited state of ^{27}F. In order to know if those two states are populated in the ^{29}F$(-1n)$ reaction, we propose to look for γ coincidences. The inclusive γ-ray spectrum presented in Fig. 5.17 shows a very weak contribution from the 915 keV transition in ^{27}F. However, some events are still observed. We therefore look in Fig. 5.18, using the same method as in previous sections, for γ-rays in coincidence with the ^{27}F$+n$.

We observe in Fig. 5.18 coincidences in the same regions than in the previous section where ^{28}F was populated from ^{29}Ne($-1p$), which proves that the 1.28 MeV resonance found in the previous section is also populated using this reaction. Therefore we should add two resonances to the fit: one corresponding to the decay of that state to the ground state of ^{27}F and the second corresponding to its decay to the excited state at 915 keV. However, we observe that this state is very weakly populated in this reaction channel compared to the one studied with the (p,2p) reaction and described in the previous section. We note that the quality of our setup has allowed us to signal unambiguously the presence of three structures that, without γ-ray detector, were almost impossible to identify at first sight in the relative energy spectrum, even with our very high resolution and acceptance.

It is clear now that we need to fit the relative-energy spectrum using seven resonances like in the previous section. The results of the fit are presented in Fig.5.19 and Table 5.2 where the data are well reproduced by the fit, even when looking at the spectrum in logarithmic scale. In order to perform that fit the extremely weak contribution of R_2 has been fixed by comparing the γ-ray observed in coincidence in the ^{29}F(p,pn)^{28}F reaction and in the ^{29}Ne(p,pn)^{28}F reaction discussed in the previous section.

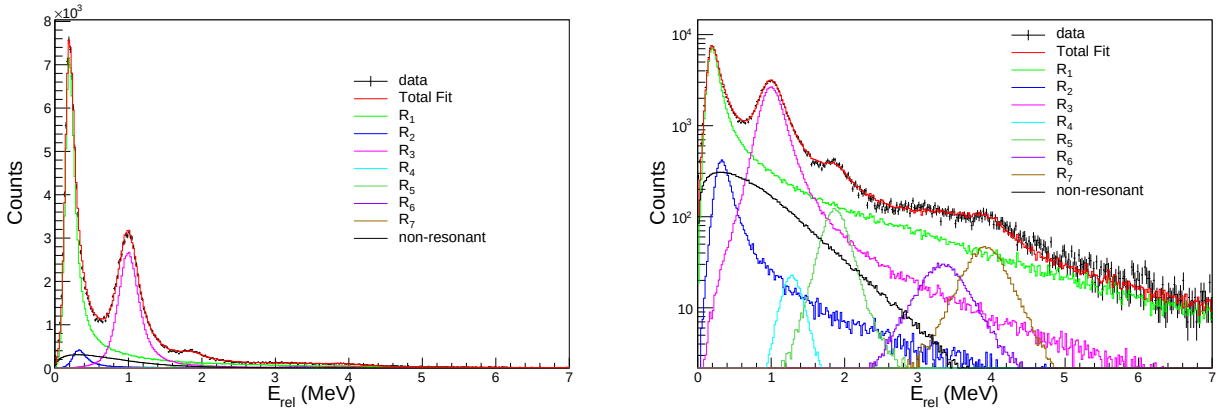

Figure 5.19: *On the left, best fit obtained for the relative energy spectrum for the $^{27}F+n$ system populated from $^{29}F(-1n)$. On the right, same figure in logarithmic scale.*

The results obtained using the two different reactions in order to populate ^{28}F can be compared. By comparing the energy position of the resonances extracted from the fit, it seems that the same states are populated using both reactions even if the population rates are varying significantly from one reaction to the other. For example, both reactions populate the ground state found at the same energy of 0.20 MeV. However, even if some states look like the same populated from two different reactions, their extracted energies sometimes differ by a few tens of keV, such as for example R_3 which was found at 0.94 MeV when populated from ^{29}Ne($-1p$) and at 1.00 MeV when populated from ^{29}F($-1n$). This might suggest that we are actually looking at two different states.

Following our results, we can propose a level scheme for the unbound states observed in ^{28}F using the ^{29}F($-1n$) reaction in Fig. 5.20.

R_i	E_r (MeV)	Γ_r (MeV)
1	0.198(6)	0.18(4)
2	0.33(21)	0.20(10)
3	0.996(13)	0.19(5)
4	1.29(15)	0.15(5)
5	1.88(8)	0.01(22)
6	3.18(26)	0.32(67)
7	3.98(26)	0.7(6)

R_i	E_r (MeV)	Γ_r (MeV)
1	0.204(16)	0.18(14)
2	0.363(17)	0.11(7)
3	0.94(2)	0.15(5)
4	1.28(3)	0.17(9)
5	1.84(3)	0.17(9)
6	2.81(36)	0.47(61)
7	3.66(10)	0.66(26)

Table 5.2: *On the left, parameters obtained for the best fit of the relative energy spectrum of the ^{27}F+n system populated from $^{29}F(-1n)$. On the right, parameters obtained for the best fit of the relative energy spectrum of the ^{27}F+n system populated from $^{29}Ne(-1p)$ are recalled in order to facilitate the comparison.*

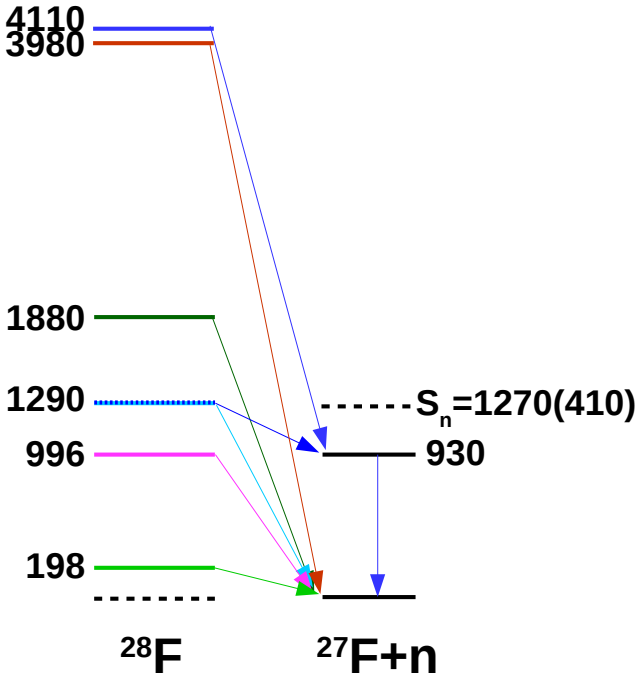

Figure 5.20: *Proposed level scheme of ^{28}F deduced from our experimental results for the $^{29}F(-1n)$ reaction.*

In the same way that in the case of ^{26}F, since ^{28}F is populated here from the knockout of a neutron in ^{29}F, looking at the momentum of the ^{27}F+n system and comparing it to theoretical calculations allows us to access the angular momentum of the knocked out neutron for each resonance. This can be very helpful in order to assign the spin parity of the unbound states observed.

We start by the ground state of ^{28}F located at 0.20 MeV. The parallel momentum distribution is presented in Fig. 5.21 and compared to theoretical calculations. We observe

an asymmetry towards the negative momenta which is related to the effects of the reaction mechanism, not considered in the calculations we use. However, the distribution above -50 MeV/c seems unaffected by this phenomenon. Therefore it has been chosen to fit the theoretical calculations to the data only in the $p_{//} \geq -50$ MeV/c region. The best agreement is found for $\ell = 1$, which suggests that the ground state of ^{28}F has a negative parity and therefore belongs to the island of inversion (see section 1.4). This is an important result, as it contradicts the main conclusion of Ref. [4].

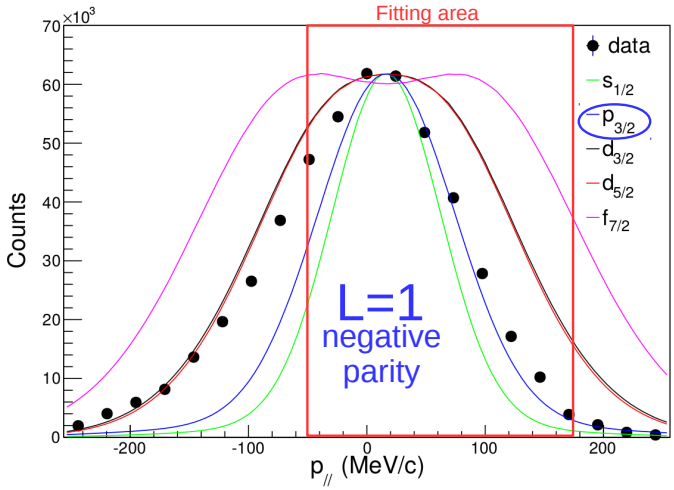

Figure 5.21: *Parallel-momentum distribution for the R_1 resonance (0.20 MeV) of the $^{27}F+n$ unbound system populated from $^{29}F(-1n)$ in the beam rest frame. Eikonal-model theoretical calculations are shown in different colors in order to compare them to the experimental distribution. The area in which theoretical and experimental distributions are compared is shown in red.*

We can also perform the same study for the R_3 resonance. The results are presented in Fig. 5.22. In this case the best fit is found for $\ell = 2$, which places this resonance as a good candidate for one of the states of the $J^\pi = 1^+ - 4^+$ multiplet resulting from the $\pi d_{5/2} \otimes \nu d_{3/2}$ coupling (see section 1.4).

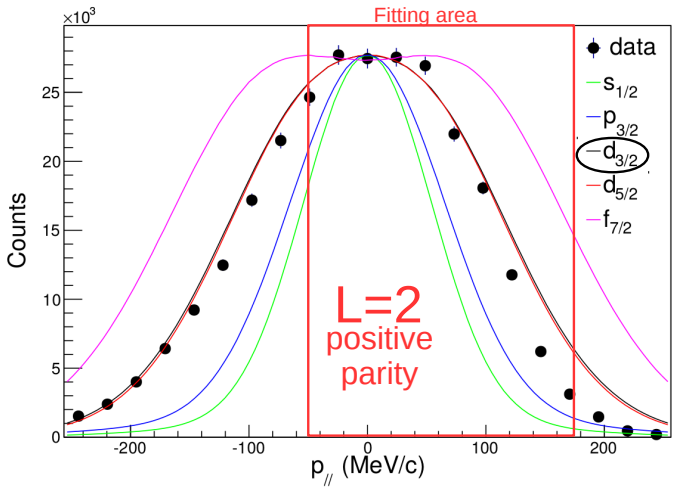

Figure 5.22: *Parallel-momentum distribution for the R_3 resonance (1.00 MeV) of the ^{27}F+n unbound system populated from $^{29}F(-1n)$ in the beam rest frame. Eikonal-model theoretical calculations are shown in different colors in order to compare them to the experimental distribution. The area in which theoretical and experimental distributions are compared is shown in red.*

5.4 Determination of $S_n(^{27}F)$

The mass is an important parameter in nuclear physics and especially in our analysis as theoretical calculations and also the mass-invariant formula depend on it. It is therefore crucial to know with a good precision the mass of the nuclei that we are studying. Unfortunately, in our case, since we are interested in nuclei far from stability, their masses usually have large uncertainties. This is the case for example for the neutron emission threshold S_n of ^{27}F, for which the AME2016 evaluation gives the value of 1270(410) keV.

In our experiment, we have been studying the excited states of ^{28}F. Among those states, some have been found to be above $S_{2n}(^{28}F)$ which might suggest that some of those states also decay by emitting two neutrons. Now if we could observe the $2n$ decay of at least two of those states, we would be able to measure the value of $S_{2n}(^{28}F)$ which is also equal to $S_n(^{27}F)$. Our results would provide in this way a precise experimental measurement of $S_n(^{27}F)$.

The first step is therefore to compare the relative energy spectrum for the one- and two-neutron decay channels of ^{28}F. They are presented in Fig. 5.23 using the value from the AME2016 evaluation. Unfortunately we do not observe any coincidence between states. However, if we slightly modify the value of $S_n(^{27}F)$ to 1600 keV (see Fig. 5.23), we observe that two of the states decaying by emitting one neutron are in perfect coincidence with two states that decay by emitting two neutrons, suggesting that they are the same states for which the one- and two-neutron decays are in competition. Once the value of 1600 keV has been determined, using the error in the energies of those two states we obtain an error for $S_n(^{27}F)$ of 50 keV, one order of magnitude smaller than the one in the AME2016.

In order to confirm that the $S_n(^{27}F)$ value is actually 1600(50) keV, several points still need to be checked. We need to confirm that the states observed in the one- and two-neutron decay channels are indeed the same states, in which both decays are in competition. If this is the

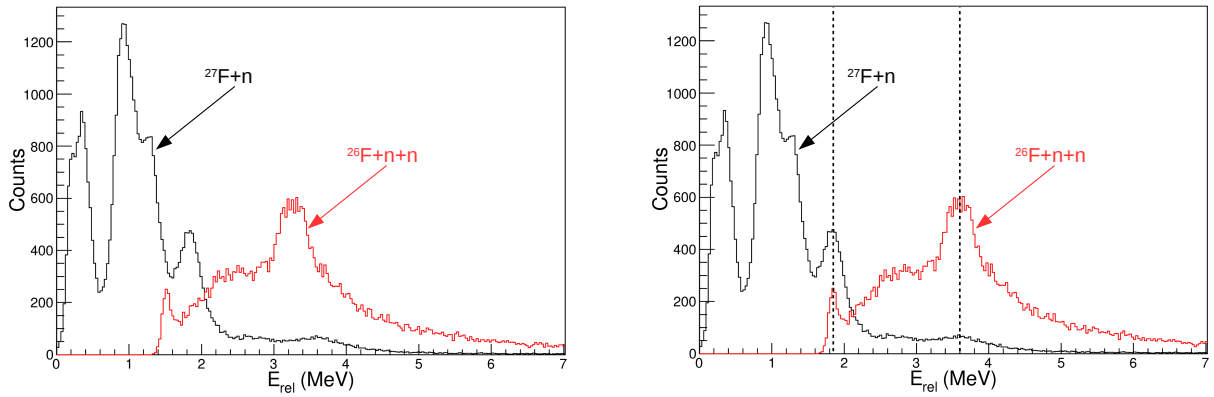

Figure 5.23: *Relative energy for one and two neutrons decay channels of ^{28}F populated from ^{29}Ne(-1p). On the left, the $S_n(^{27}F)$ value considered is the one from the AME2016 evaluation. On the right the $S_n(^{27}F)$ value is 1600 keV.*

case, the widths of the resonances should be the same in both channels, and the $1n/2n$-decay branching ratios should also be the same in the ^{29}F(-$1n$) reaction, in which these two states have also been observed.

5.5 ^{28}F: n-n decay channels

We have been interested in the previous sections by the unbound states of ^{28}F decaying by the emission of one neutron. However, higher energy states (above S_{2n}) are also populated during knockout reactions, giving us a unique opportunity to study the n-n interaction beyond the dripline (see section 1.3). We presented already, in chapters 2 and 4, techniques in order to study n-n correlations. We propose here to conduct the same kind of study in the case of ^{28}F using the ^{29}Ne(p,2p)^{28}F$\rightarrow^{26}$F+2n reaction.

Reaction channels involving the emission of two neutrons are particularly difficult to analyze due to the treatment of cross-talk events (see section 2.1). It is crucial to make sure that the cross-talk events are well treated in our data. Since in the SAMURAI21 experiment, we had two neutron detectors one behind the other separated by a few meters, cross-talk events from one detector to the other are unlikely to be missed by our rejection filter. Therefore a simple way to test the rejection procedure is to compare the three-body relative energy obtained when the 2n are detected in the same detector to the case where each neutron is detected in a different detector. If cross-talk events are completely rejected, the relative energy spectra obtained in each case should be identical. The results for such study are shown in Fig. 5.24 where no difference is observed depending on the scenario considered. We can therefore validate our treatment of the cross-talk.

The total relative-energy distribution for the ^{26}F+2n system is presented in Fig. 5.26. Compared to the three-body energy spectra of ^{18}C and ^{20}O presented in chapter 4, we note that the resolution of our experimental setup is allowing us to distinguish at least two structures at around 250 keV and 2 MeV, which introduces a qualitative step forward in our study, the

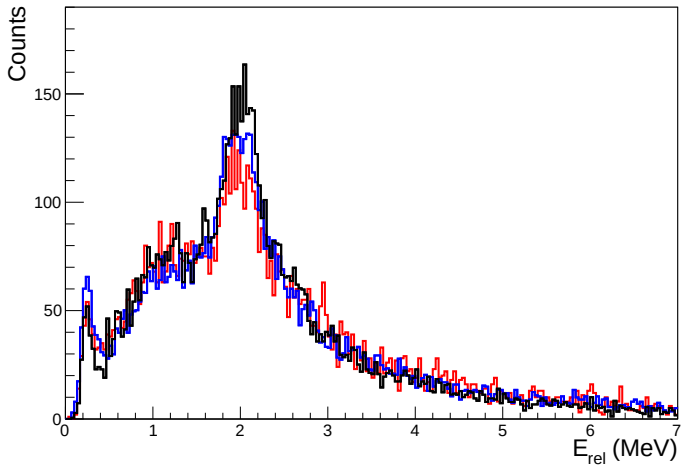

Figure 5.24: *Superposition of the relative-energy spectra for the ^{26}F+2n system populated from ^{29}Ne(-1p) when the two neutrons are detected in NeuLAND (black), the two neutrons are detected in NEBULA (red) and one neutron is detected in each detector (blue). The distributions are normalized to the red curve to facilitate the comparison.*

investigation of correlations within a given resonant state. In particular, the peak at 250 keV above S_{2n} seems to be extremely narrow. Even if only two peaks are clearly observable, the fit with only two resonances (plus the non-resonant component) was unable to reproduce the spectrum. The most straightforward hypothesis was that a third resonance was present at about 1 MeV, and this was confirmed by having a look at the same spectrum but under different conditions. For example, as shown in Fig. 5.25, events with $0.4 < m^2_{fn} < 0.6$ exhibit a clear resonance-like structure at about 1 MeV. Therefore, the spectrum was fitted with three resonances and the non-resonant continuum, leading to a very good description of the data (Fig. 5.26).

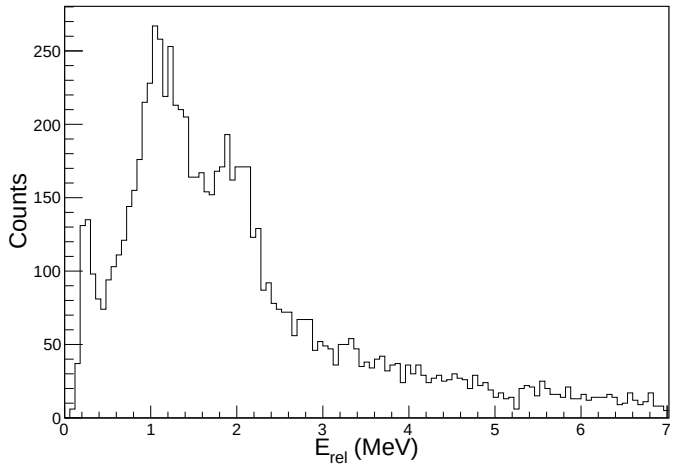

Figure 5.25: *Relative-energy spectrum for the ^{26}F+2n system populated from ^{29}Ne(-1p) with a gate such as $0.4 < m^2_{fn} < 0.6$.*

We will attempt in the following to investigate the *n*-*n* correlations of the structures at

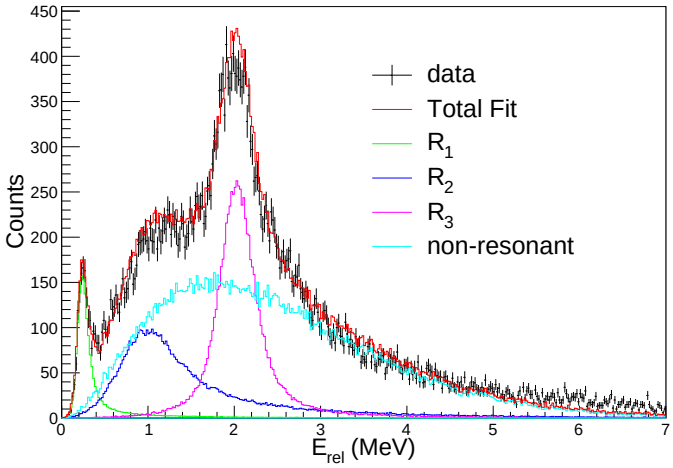

Figure 5.26: *Relative-energy spectrum for the ^{26}F+2n system populated from ^{29}Ne(-1p).*

250 keV and 2 MeV. We therefore apply gates on the relative-energy spectrum corresponding to those structures and observe the corresponding Dalitz plots in Fig.5.27. The Dalitz plot for the lower energy structure is surprisingly different to previous n-n works, since weak anti-correlations are observed (enhanced signal towards $m^2_{nn} = 1$). Indeed, in all the studies performed until now the signal observed is always towards $m^2_{nn} = 0$. However, such kind of anti-correlations have been predicted by some theoretical calculations [115], even though never observed before. Moreover, the fact that the state is located at only 250 keV can be responsible for the fact that only weak correlation signals are observed. Indeed, while moving to low energy, the n-n correlation signal is expected to vanish. Such effect is also observed in the 2^+ state of ^{14}Be located at around 280 keV, where a direct decay towards ^{12}Be+n+n without any two-body correlations is observed [116]. For the structure observed at about 2 MeV, the Dalitz plot reveals an almost pure sequential decay through an intermediate unbound state of ^{27}F at around 500 keV. We can therefore propose a level scheme for ^{28}F populated from ^{29}Ne$(-1p)$ as presented in Fig. 5.28.

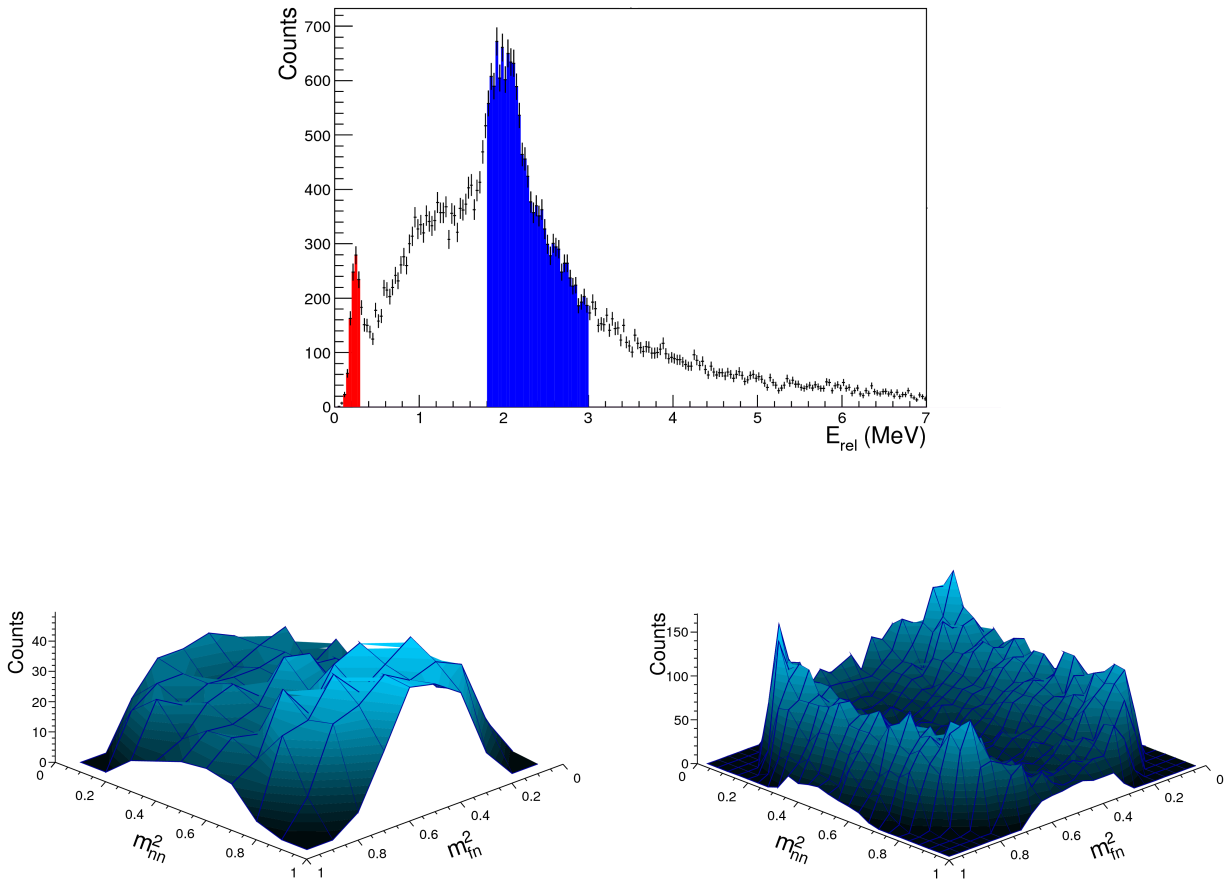

Figure 5.27: *On the upper panel, the gates applied to construct the Dalitz plots are represented on the relative-energy spectrum for the ^{26}F+2n system populated from ^{29}Ne(-1p). On the lower panel, the Dalitz plots are presented for the red and the blue gates on the left and right, respectively.*

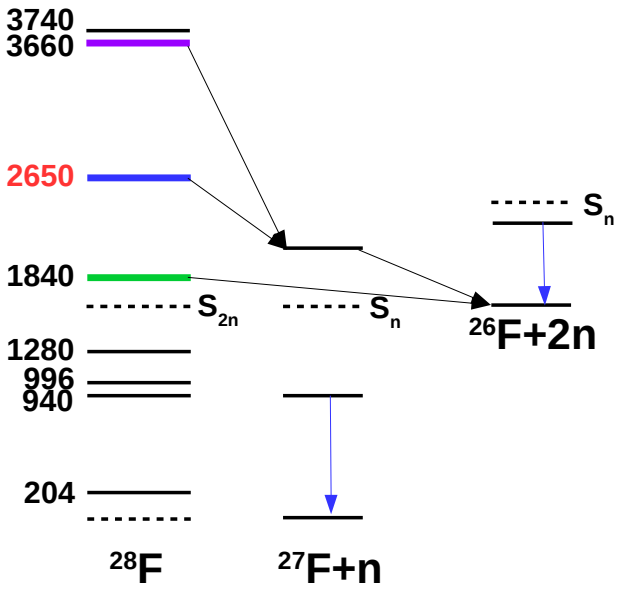

Figure 5.28: *Proposed level scheme of ^{28}F deduced from our experimental results for the ^{26}F+2n system.*

5.6 Conclusion and perspective

In this chapter, we studied ^{26}F and ^{28}F using different reaction channels. The study of ^{26}F allowed us to confirm the previous assignment of the $J^{\pi} = 3^{+}$ state and to observe new unbound states at higher energies. We also used this reaction channel to test our method before applying it to the unbound states of ^{28}F.

We studied ^{28}F populated from two different reactions: ^{29}F$(-1n)$ and ^{29}Ne$(-1p)$. The ground state of ^{28}F has been located at 200 keV and seems to be of negative parity. This result is placing ^{28}F in the island of inversion, contrary to a previous study [4]. A large number of unbound states at higher energies have also been observed.

We were also able to propose a new value of the $S_n(^{27}F)$ at 1600(50) keV by looking at states in which the one- and two-neutron decay channels are in competition.

Looking at the three-body decay of ^{28}F allowed us to discover a narrow resonance just above S_{2n} that could be a good candidate to verify if the Ikeda conjecture can hold for two-nucleon systems. We have been able to construct the Dalitz plots for this state and observed what seems to be anti-correlations. This result is not only unique due to the nature of the signal, but also to the fact that it is the n-n signal observed from the lowest-energy $2n$ state, at only 250 keV. As such, it represents a key step towards the future investigation of "dineutron" emission in the decay of ^{26}O, at 18 keV.

Apart from the experimental results, we have been able to see the power of the setup used during the SAMURAI21 experiment. We especially pointed out the large improvements of the resolution achieved due the use of the MINOS target as well as of the NeuLAND detector. Unfortunately, the NeuLAND detector is no longer available at RIKEN since it has been shipped back to GSI in order to be used in future experiments. However, the ANR EXPAND project, that will allow to increase the number of walls of NEBULA to form NEBULA-Plus, will allow us to increase the neutron detection efficiency.

Chapter 6

Conclusion and outlook

The general subject that regroups all the work presented in this document is the nucleon-nucleon interaction towards the neutron dripline. In particular, we have studied the effect of the n-n interaction in decays from the continuum of the core+4n isotones ^{18}C and ^{20}O and from narrow states of ^{28}F. The neutron-rich fluorine isotopes ^{26}F and ^{28}F were also used to study the evolution of the p-n interaction while moving towards the dripline and to determine if ^{28}F was inside the island of inversion.

The systems of interest have all been populated using nucleon knockout reactions (proton or neutron). In the case of unbound states, we used the invariant-mass method to reconstruct the relative energy of the decaying system that required the detection in coincidence of the fragment, the neutron(s) and also of eventual γ-rays emitted in flight and characterizing the population of a bound excited state of the fragment. We also used Dalitz plots in order to study the three-body decay (fragment+n+n) of systems such as ^{18}C, ^{20}O and ^{28}F.

The data presented in this document have been obtained using two very complex experimental setups, similar in principle but with very different characteristics: the R3B-LAND setup at GSI and the SAMURAI setup at RIKEN. It is noticeable that the experiment performed at RIKEN was using a state-of-the-art set of detectors including the MINOS target and the NeuLAND detector. This particular combination of detection devices allowed us to improve largely both the resolution and the statistics compared to previous studies of unbound nuclei in general.

The data have been analyzed using several simulations taking into account the experimental response of the different detectors and interpreted within different theoretical frameworks. An iterative event-mixing method has been used to determine the shape of the non-resonant contribution in fragment+n relative energy spectra, avoiding the a priori subjective analytical assumptions used in previous works.

We started first by studying the decay of the core+4n isotones ^{18}C and ^{20}O and observed that they display significantly different features. In the former, extremely strong correlations persist up to 12 MeV above S_{2n}, which we propose to be caused by the large fraction ($\sim$80%) of direct emission of correlated pairs with a relatively compact configuration. The decay of ^{20}O exhibits much weaker correlations, with about 50% occurring through sequential processes. The clear contrast between these isotones is likely due to the way they are populated: the

knockout of deeply-bound neutrons from ^{21}O leaves two unpaired neutrons in ^{20}O with a broken ^{16}O core (in this way increasing the probability of sequential decay), while the knockout of deeply-bound protons from ^{19}N leaves the neutron pairs and the ^{14}C core unaffected.

The present study shows that the high-energy proton knockout reaction is a tool of choice for studying neutron correlations, be there of $2n$ or $4n$ origin, when reaching the corresponding neutron emissions thresholds.

In the future, we wish to study the evolution of $2n$ and $4n$ correlations from the valley of stability to the dripline, and show the role of the reaction mechanism in revealing such correlations. In future experiments, we wish to benefit from the increased granularity of the NeuLAND detector at GSI, as well as from the increased beam intensities, to study the ^{18}C$\rightarrow^{16}$C+2n system using the ^{19}N(-1p) reaction with a better resolution in order to:

- Characterize the resonance above S_{2n} (width, one- or two-neutron decay branches) to see if it is a good candidate for di-neutron decay.
- Populate states above S_{4n} and study if they look like 2n-2n or tetra-neutron correlations.
- Identify a narrow 4n resonance around the S_{4n} threshold to see if the Ikeda conjecture is a general feature of the continuum.

In this kind of experiment several nuclei are produced, offering the possibility to study different systems at the same time. This is of utmost importance to understand and characterize the interplay between the reaction mechanism and the structure of the systems at the dripline.

We then looked at the fragment+n relative energy spectra for ^{26}F and ^{28}F. The interpretation, guided by theoretical calculations, allowed us to give the following conclusions on the different systems studied:

- ^{26}**F**:

  This nucleus has been produced from the knockout of a neutron in ^{27}F and six resonances were observed in the relative energy spectrum:

  - The study of the momentum distribution of the first state at 0.39 keV revealed a $\ell = 2$ angular momentum, which confirms the $J^\pi = 3^+$ assignment for this state as proposed in a previous study.
  - Several higher-energy states have been found to be in coincidence with known γ-rays of ^{25}F. The energy of those γ-rays being of about 3-4 MeV, this implies that the resonances observed in coincidence are actually very high-energy states, probably arising from the knockout of the $\nu d_{5/2}$ orbital.

- ^{28}**F**:

  This nucleus has been produced from two different reactions, the knockout of a neutron in ^{29}F and the knockout of a proton in ^{29}Ne. During this study, at least six resonances were observed in the relative energy spectra:

– The ground state of ^{28}F has been identified at 200 keV and has a negative parity. This implies that the ground state of ^{28}F is an intruder state and that therefore this nucleus is located in the island of inversion.

– The second state at 1.00 MeV is proposed as a member of the $J^\pi = 1^+ - 4^+$ multiplet resulting from the $\pi d_{5/2} \otimes \nu d_{3/2}$ coupling.

Its three-body decay has also been studied using the ^{29}Ne(-1p) reaction, where at least two resonances have been observed in the relative energy spectrum above S_{2n}:

– A narrow low-energy resonance has been observed at about 250 keV, with a Dalitz plot that reveals slight/small anti-correlations. This state is a good candidate to verify if the Ikeda conjecture can hold for two-nucleon systems.

– A second resonance at around 2 MeV has been observed where the Dalitz plot reveals a quasi-pure sequential decay through a 500 keV beyond S_n intermediate resonance in ^{27}F.

We were also able to propose a new value of the $S_n(^{27}F)$ at 1600(50) keV by looking at states in which the one- and two-neutron decay channels are in competition.

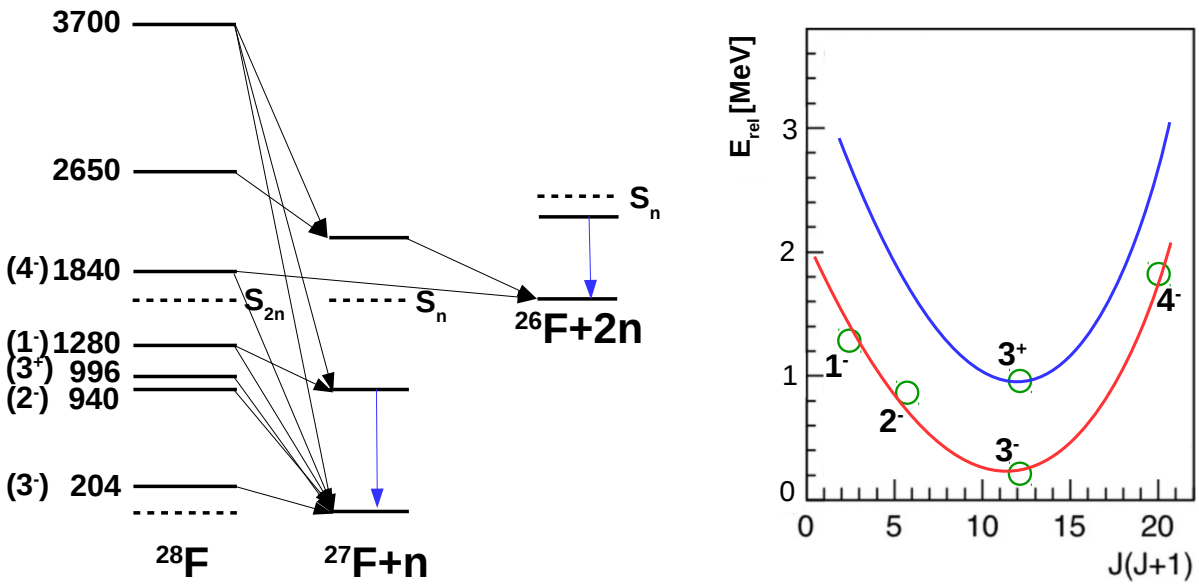

Figure 6.1: *On the left, level scheme summarizing the states observed in ^{28}F. On the right, proposed parabolas for the lower energy states observed in ^{28}F.*

A level scheme summarizing all the reaction channels studied is proposed in Fig. 6.1 as well as proposed parabolas for the lower energy states observed.

Those results are very encouraging as many new states have been observed. This has been possible due to the good resolution and efficiency/acceptance achieved with the setup of the SAMURAI21 experiment. Unfortunately the NeuLAND detector is no longer available in RIKEN as it has been shipped back to GSI for future experiments. However, a project (ANR EXPAND) is ongoing in order to expand the NEBULA detector by increasing the number of

walls to form NEBULA-Plus. This new configuration will allow us to increase the neutron detection efficiency in order to continue to investigate decay channels involving the emission of several neutrons at RIKEN.

Appendix A

Data analysis from s021 experiment

A.1 The beam

A.1.1 Geometrical alignment of the drift chambers

One of the fundamental requirements of our analysis is to know the exact position of the interaction in the target. This position along the Z-axis can be determined using the TPC surrounding the MINOS target in the case of a (p,2p) reaction since two protons are detected and therefore two tracks can be reconstructed in order to deduce the interaction point. However, in the case of (p,pn) reactions, only one proton is emitted and therefore only one track can be reconstructed, which does not allow us to deduce the position of interaction. In this case, we deduce the position of interaction using also the beam trajectory deduced from the drift chambers located before the target (BDCs). In order to insure an optimal precision on the relative position of the BDCs with respect to the others, we use the following procedure. During empty target runs, the position of the ions in BDC2 is interpolated from the one measured in BDC1 and FDC1 (see Fig. A.1). The subtraction of the interpolated position by the measured position in BDC2 must be perfectly centered at 0. If it is not the case, an offset on the BDC2 position is applied in order to align the drift chambers. The result of this procedure for an empty target run is shown in Fig. A.2.

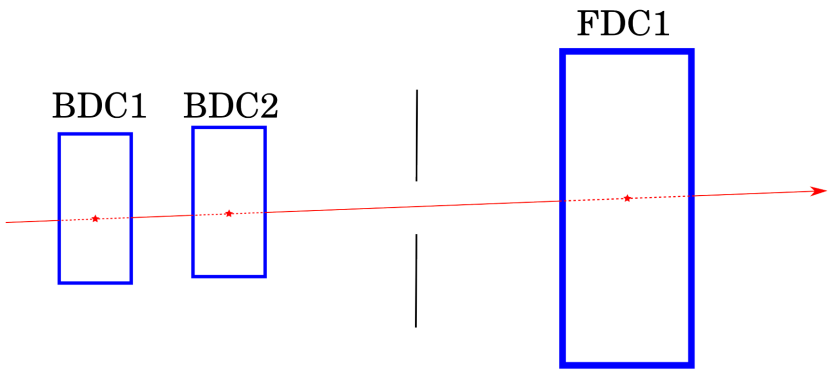

Figure A.1: *Sketch of the alignment procedure for the drift chambers (figure taken from [5]). The position measured in BDC2 is compared to the one interpolated from BDC1 and FDC1.*

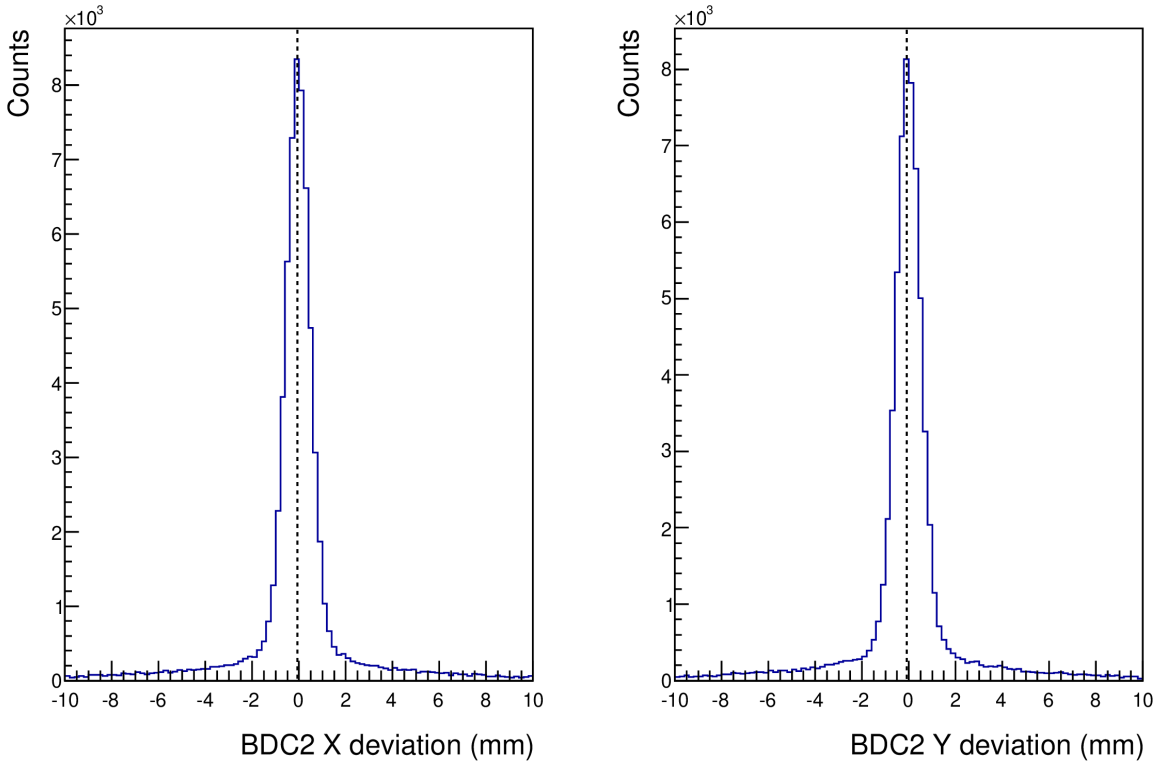

Figure A.2: *Measurement of the relative alignment of the drift chambers. The graphs represent the difference between the measured position in BDC2 and interpolated position from BDC1 and FDC1 for a ^{29}Ne beam on empty target.*

A.1.2 Time of flight and magnetic rigidity determination

The time of flight (ToF) of the beam is obtained from the time difference between the plastic detector located in F7 and the average of the time of the SBT1 and SBT2 plastics located in F13 (see Fig. 3.10). The times obtained from the plastic detectors are not absolute times and depend for example on the length of the cable connecting them to the acquisition. In order to access the physical ToF, an offset is applied to the ToF-F7F13 in order to match in average the rigidity measured by the BigRIPS team on this section of the beam line.

A.1.3 Identification of the beam

The main goal of all the techniques described in this section is to identify event by event the nature of each particle of the beam. The atomic number of the incoming ions is reconstructed from the energy loss in the plactic detector in F7 using the Bethe-Bloch formula. The determination of the A/Z ratio for the beam is done using the ToF-F7F13 and the $B\rho$ from BigRIPS. Knowing Z as well as the A/Z ratio allows us to access the identification matrices such as presented in Fig. 3.11. We observe that the different isotopes are clearly separated and therefore that the selection of the incoming ions is not causing any problem in our analysis.

A.2 Interaction point determination in MINOS

A.2.1 Drift velocity

In the TPC, the only uncertainty is the drift velocity as impurities in the TPC change over time. In order to take those changes into account, we determine the drift velocity for each run by plotting the trigger time t_{pad} measured by the TPC during a run (see Fig. A.3). Electrons which have ionized at the level of the Micromegas plane have a drift equal to 0, while those ionized at the very end of the TPC have a time corresponding to 300 mm of drift length (size of the TPC). We therefore obtain a distribution of correlated trigger events which reflects the length of the TPC.

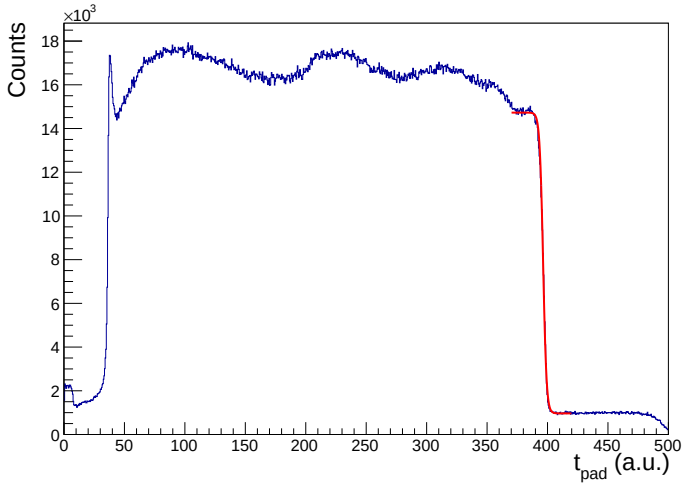

Figure A.3: *Drift time inside the TPC during a physics run.*

The minimum trigger time t_{min} does not depend on the drift velocity as it corresponds to an electron ionization at the Micromegas mesh. We can therefore set this time for the entire campaign. As for the end of the TPC with t_{max}, it directly reflects the drift velocity and has to be measured continuously. For each run, we plot the trigger times in the TPC and determine the mid-point in the downward slope which can be fitted with a Fermi function:

$$f(t) = \frac{p_0}{1 + exp((t - p_1)/p_2)} + p_3 \tag{A.1}$$

We can then determine the drift velocity as follows:

$$v_{drift} = \frac{L_{TPC}}{t_{max} - t_{min}} \tag{A.2}$$

where L_{TPC} is the length of the TPC and equal to 300 mm. The evolution of the drift velocity as a function of the run number in our experiment is presented in Fig. A.4.

A.2.2 Position calibration

After the drift velocity calibration, the TPC is calibrated and we can determine the reaction vertex using the tracking algorithm define in Ref. [102]. However, the positions that are

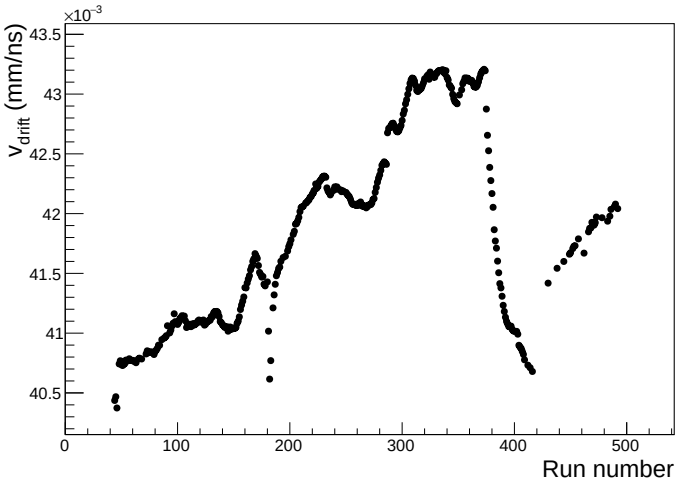

Figure A.4: *Evolution of the drift velocity as a function of the run number during the SAMURAI21 experiment.*

reconstructed need to be calibrated in order to be compatible with the other detectors used in the experiment. In our analysis, we are particularly interested by the z_{vertex} observable that corresponds to the interaction position along the z-axis. In order to calibrate this observable, we can represent the z_{vertex} reconstructed by MINOS during an empty target run (see Fig. A.5). We observe two peaks that corresponds to the entrance and exit window of the target cell. A shift on z_{vertex} has been applied so that the position of the entrance window corresponds to 0. We can notice that the size of the target cell (150 mm) is perfectly reconstructed.

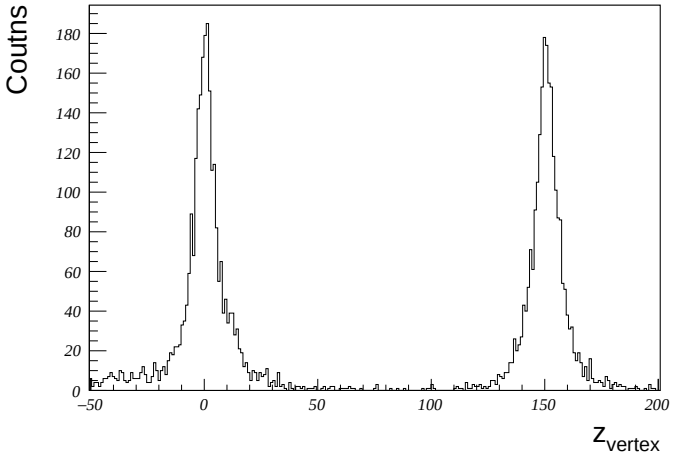

Figure A.5: z_{vertex} *distribution for an empty target run.*

In our analysis the x and y positions of the interaction have been determined from a linear interpolation from the BDCs at the z_{vertex}. However those positions (x_{vertex} and y_{vertex}) can also be reconstructed using MINOS. It is therefore necessary to determine the angle between the MINOS referential and the BDCs referential in order to have positions in the same referential. In our case a rotation of 36.4° has been applied to the MINOS referential. The MINOS calibration is now fully done and we can use the z_{vertex} position to determine the

energy loss of the beam and the fragment event by event.

A.3 The γ-ray detection

A.3.1 The calibration of DALI2

The energy calibration of DALI2 consists in finding the relation between the energy of the γ-ray and the charge deposited in each NaI crystal. This task is complicated by the different possible interactions between the photons and the material. Indeed three processes are in competition and their probability depends on several factors such as the energy of the γ-ray or the atomic number of the detector material.

The photons can first interact by photo-electric effect, this process is dominating at low energy ($\leq$ 500 keV). It consists in a transfer of the full energy of the photon to an electron of the detector. The electron therefore gains a kinetic energy equal to the total energy of the photon that is lost afterward in the material by emitting light from the scintillator. The charge obtained is then directly proportional to the energy of the incoming photon.

The Compton diffusion consists in the diffusion of the photon on one of the electrons of the material. In this case, the photon only transfers part of its energy to the electron. The rest of the process is identical to the one described for the photo-electric effect except that in this case, the collected charge is not proportional to the energy of the incoming photon. The diffused photon (less energetic) resulting from the Compton effect can eventually also interact in the detector or get out of the sensitive volume.

Finally, if the photon has an energy higher than 1022 keV (twice the mass of the electron), the materialization can occur. In this case, an electron-positron pair is produced and the excess of energy is transferred as kinetic energy. The electron created can then deposit its energy in the detector while the positron will be annihilated with an electron of the material in order to form two γ-rays of 511 keV. Three cases can then appear. The two photons are detected and the collected charge is proportional to the energy of the incoming photon. Only one photon is detected, the charge will therefore be proportional to the energy of the incoming photon minus 511 keV. The last case is that none of the photons are detected, the charge will therefore be proportional to the energy of the incoming photon minus 1022 keV.

In order to calibrate DALI2 in energy, different sources were used (shown in Table A.1).

A.3.2 The Doppler correction

The goal of DALI2 is to detect the γ-rays resulting from the decay of bound excited states of the fragments produced during the reaction in the target. The γ-rays are emitted in flight and therefore affected by the Doppler effect [117]. The energy of the photon is then linked to the incident angle, which is determined by the position of the crystal in which it is detected and by the speed of the charged fragment that produced it. The formula linking all those observables

Source type	Theoretical energy (keV)
^{88}Y	898.0
	1836.1
^{137}Cs	661.1
^{60}Co	1173.2
	1332.5

Table A.1: *List of the γ-ray sources used for the calibration of DALI2.*

is as follows:

$$E_\gamma = E_{lab}(1 + \beta cos\theta)\gamma \tag{A.3}$$

where γ represents in this formula the Lorentz factor of the radioactive ion, β its speed normalized to the speed of light and θ the angle between the trajectory of the ion and the direction in which the photon has been emitted. E_γ is the energy of the photon in the source frame and E_{lab} the one measured in the laboratory.

A.4 The fragments

The charged fragments are a crucial point of our study since the invariant-mass method requires not only their identification but also the reconstruction of their momentum. The measurement of all the observables needed is done using a set of different detectors. The position and angle measured in the drift chambers are essential to derive the trajectories of the charged fragment. The four drift chambers (BDC1, BDC2, FDC1 and FDC2) are calibrated using the same method described in the following section. The identification of the charged fragments with the Hodoscope is done using their energy loss in the plastic but also using a time of flight technique.

A.4.1 Drift chambers calibration

Drift distance calibration

The determination of the position in the drift chamber implies to measure plane by plane the distance between the incident ion and the closest wire. This observable is called drift distance and corresponds to the path taken by the electrons/ions towards the anode/cathode. If the signal induced by the charge moving overcomes a certain threshold, a time measurement is done using a TDC (Time to Digital Converter) between the SBTs and the drift chamber. The relation between the drift distance and this time is given as follows:

$$D = \int_{t_{start}}^{t_{stop}} v(t)\ dt \tag{A.4}$$

where D is the drift distance, t_{start} and t_{stop} are the trigger start and stop time, respectively, and $v(t)$ is the drift velocity of the electrons in the gas.

In order to use this equation, we need to determine the drift velocity. As a first approximation, we can suppose that we have a cylindrical symmetry around the wires, allowing us to

write:

$$v(t) = \frac{dr}{dt} = \frac{dr}{dN}\frac{dN}{dt} \tag{A.5}$$

In this case, dr/dN represents the radial distribution of the events measured and dN/dt the distribution of the drift times. Assuming that the radial distribution is not time dependent, we can write:

$$D = \int_{t_{start}}^{t_{stop}} v(t)\ dt = \int_{t_{start}}^{t_{stop}} \frac{dr}{dN}\frac{dN}{dt}\ dt = \frac{dr}{dN}\int_{t_{start}}^{t_{stop}} \frac{dN}{dt}\ dt \tag{A.6}$$

The time distribution is measured experimentally, and therefore its integral can be calculated. Moreover, the extreme values of the drift distance are known: the maximum being half of the distance between two wires and the minimum being 0. Using those two values and the fact that the time is proportional to the drift distance, we can derive the drift distance (see Fig. A.6).

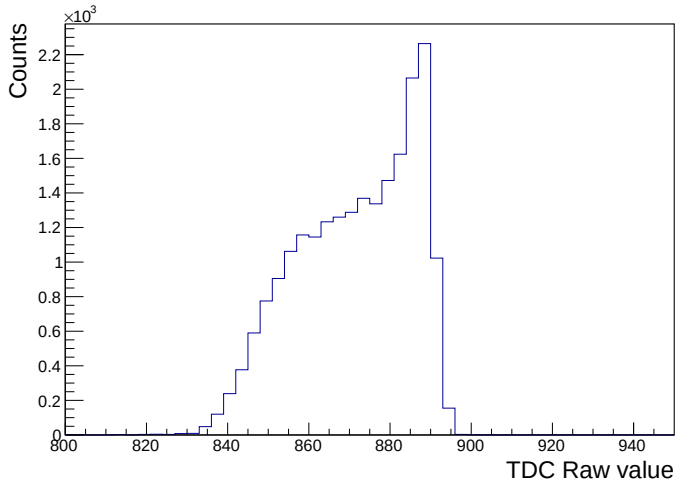

Figure A.6: *TDC distribution of the first wire plane of BDC1.*

Reconstruction of the position

In order to reconstruct the positions of the ions in the chamber, we need to determine the most probable trajectory in the chamber using the information on the position on each wire plane. Each direction (horizontal or vertical) is determined independently. We do a linear regression over all the fired wires by considering only one wire per plane. If several wires fired in the same plane, several fits are performed. For each wire fired, we know the drift distance of the incident particle but not its position with respect to the wire. Therefore, in order to improve the precision of the trajectory reconstruction, four positions are tested. The ion is always considered to be at the drift distance from the wire but either in front, behind, on the left or on the right. Once all those possibilities are tested, the fit for which the χ^2 is minimum is selected. We derive then, from the trajectory, the position at the center of the drift chamber.

Reconstruction of the angles

We saw in the previous section that the drift chambers give us access to the horizontal and vertical trajectory of the ion. It is therefore possible to determine for each of those trajectories

the angle of the ion. However, the precision on the angle inside the BDCs and the FDC1, which are quite thin chambers, is not sufficient compare to the FDC2 which is much thicker. In order to improve the precision on the angle of the ion, the information from different drift chambers has been used. The beam trajectory as well as its position of the target is then derived using the position on BDC1 and BDC2. This trajectory is characterized by the angles θ_x and θ_y as follows:

$$\theta_x = arctan\left(\frac{X_{BDC2} - X_{BDC1}}{Z_{BDC2} - Z_{BDC1}}\right) \tag{A.7}$$

$$\theta_y = arctan\left(\frac{Y_{BDC2} - Y_{BDC1}}{Z_{BDC2} - Z_{BDC1}}\right) \tag{A.8}$$

where X_{BDC1}, X_{BDC2}, Y_{BDC1} and Y_{BDC2} are the positions measured in the drift chambers and Z_{BDC1}, Z_{BDC2} are the positions of the center of the drift chambers along the beam axis.

The trajectory of the charged fragment is derived using the FDC1 and the position (x,y) extrapolated at the interaction point using BDC1 and BDC2. The θ_x and θ_y angles of the charged fragments are determined as follows:

$$\theta_x = arctan\left(\frac{X_{FDC1} - X_{Target}}{Z_{FDC1} - Z_{Target}}\right) \tag{A.9}$$

$$\theta_y = arctan\left(\frac{Y_{FDC1} - Y_{Target}}{Z_{FDC1} - Z_{Target}}\right) \tag{A.10}$$

where Z_{Target} corresponds to the z coordinate at the interaction point determined using the MINOS target while X_{Target} and Y_{Target} correspond to the positions at the interaction point extrapolated from the positions in the BDCs.

A.4.2 Hodoscope calibration

The Hodoscope is used to identify the charged fragments using their energy loss as well as a time of flight method. The use of two photomultipliers (one on each extremity of the plastic bars) allows to improve the resolution of those two observables.

Energy calibration

The measurement of the energy deposit in the bars of the Hodoscope is used to determine the nature of the ions going through. The energy deposited by the ion is converted into light that is emitted isotropically and is attenuated while traveling through the plastic. The attenuation follows the Bert-Lambert equation, which is characterized by an attenuation constant λ corresponding to the nature of the detector. The interaction being not always at the center of the bar, the light collected at the top A_u and the bottom A_d can be different and not proportional to the incident energy. Using A_u and A_d in order to compute their geometric mean allows to fix this problem since we have:

$$A_u \sim A_0 \times e^{-\lambda x_u} \tag{A.11}$$

$$A_d \sim A_0 \times e^{-\lambda x_d} \tag{A.12}$$

$$A \sim \sqrt{A_u \times A_d} \sim A_0 \times e^{-\lambda(x_u + x_d)/2} \sim A_0 \times e^{-\lambda L/2} \tag{A.13}$$

where L in the length of the bar. Therefore the geometric mean corresponds to the light emitted by the interaction of the ion, that depends on its energy and nature.

Time of flight

The calibration in time of the Hodoscope is needed in order to determine the time of flight of the charged fragments. Like all the other plastic scintillators used in the experiment, the time of each bar is derived using the arithmetic mean of the individual times obtained with the photomultipliers located at each extremity such as:

$$T = \frac{T_{up} + T_{down}}{2} \tag{A.14}$$

The observable of interest is the time of flight between the target and the Hodoscope. However, the acquisition is triggered by the beam traveling through the SBTs. It is therefore needed to correct event by event the time of flight SBT-Target by using the beam velocity and by taking into account the energy losses.

Moreover, the absolute time measured by the TDC is affected by a delay depending on the length of the wires used. The Hodoscope is made of 16 plastic bars, each having its own delay. It is therefore necessary to first align the bars between each other so that the time measured in the different bars are consistent. To do so, we choose one bar of reference and we select events with multiplicity two that also hit the neighboring bar. Those events are correlated in the two bars that got hit, therefore we apply a delay to the second bar so that in average the difference in time of the two bars is zero. The absolute ToF calibration for the entire detector is then realized by reconstructing the ToF of the ions on empty target which velocity is known and which flight path is determined by the simulation of the trajectories in SAMURAI.

Magnetic rigidity determination

The precise determination of the magnetic rigidity is essential in our analysis. Indeed, this observable is used in the reconstruction of the total momentum of the charged fragments. Since the charged fragment travels through the SAMURAI dipole, it is not possible to use the same technique than in the case of the beam where the magnetic rigidity is deduced from the positions in one plane using a linear relation. The drift chambers FDC1 and FDC2 allow us to determine the position as well as the direction of the ions before and after they travel through the dipole. The goal is therefore to determine the energy needed for a given particle to travel from a point A to a point B.

The technique chosen allows us to reach a resolution of about $\delta p/p \sim 1/800$ using only one function for all the fragments. This function, a 6^{th} order polynomial using data from FDC1 and FDC2, is calculated by adjusting a large number of trajectories produced by a simulation. A more precise description of this technique can be found in Ref. [5].

Identification of the outgoing nuclei

The identification of the charged fragments traveling in SAMURAI is done using their masses and their charges in a similar way as for the ions of the incoming beam. The charge is determined using the energy loss measured in the bars of the Hodoscope. In the case of events for which the charged fragment has deposited its energy in several bars, only the charge measured in the bar that detected the highest charge is considered. Once the energy loss estimated, the charge is reconstructed using the Bethe-Block formula (Eq. 3.6).

The mass of the fragments is reconstructed from their ToF and magnetic rigidity. The ToF measurement is performed using the Hodoscope while the $B\rho$ is determined by estimating the trajectory of the fragment in SAMURAI from the FDC1 and FDC2 data.

The identification of the fragments is then done by looking at the correlations between the charge and the mass-over-charge ratio. An example of identification is presented in Fig. 3.16. We observe that the separation in mass and charge is sufficient to identify clearly each charged fragment.

A.5 The neutrons

Even if the detection of the neutrons is more difficult than the detection of the charged particles, the determination of their momentum is more direct and is taken as a reference for the entire analysis. A precise calibration of the neutron ToF as well as a precise determination of their interaction point are therefore crucial in our work.

Determination of the positions

In our experiment, two neutron detector arrays were used: NeuLAND and NEBULA. Those detectors are made of horizontal and vertical bars (only vertical for NEBULA). In the case of a vertical (horizontal) bar, the x (y) position is directly deduced from the position of the bar that has been hit. However, the other position is calculated by the time difference between the two PMs located at each extremity of the bar. It is therefore necessary to find the correlation between this time difference and the position of the interaction.

The simplest way is making a correlation by associating the two extreme values of the time difference to the extremity of the bar and then assuming a linear relation between the time difference and the position. In the case of NEBULA, in order to improve this calibration, 8 gaseous proportional counters called HPC are used, which are cylindrical with a radius of 24 mm and a length of 4 m (see Fig A.7). They are placed horizontally and their positions are well known. During cosmic-rays runs, many muons are traveling through NEBULA and interact with the detector. The coincidence with two HPC allows us to know with a good precision the angle of the muon and therefore its position of interaction in a bar of NEBULA. Using the different combinations with two HPC, we obtain several calibration points for each bar, which allows us to achieve a good precision on the interaction position. For NeuLAND, a similar method is applied in which vertical (horizontal) bars are used to calibrate the horizontal

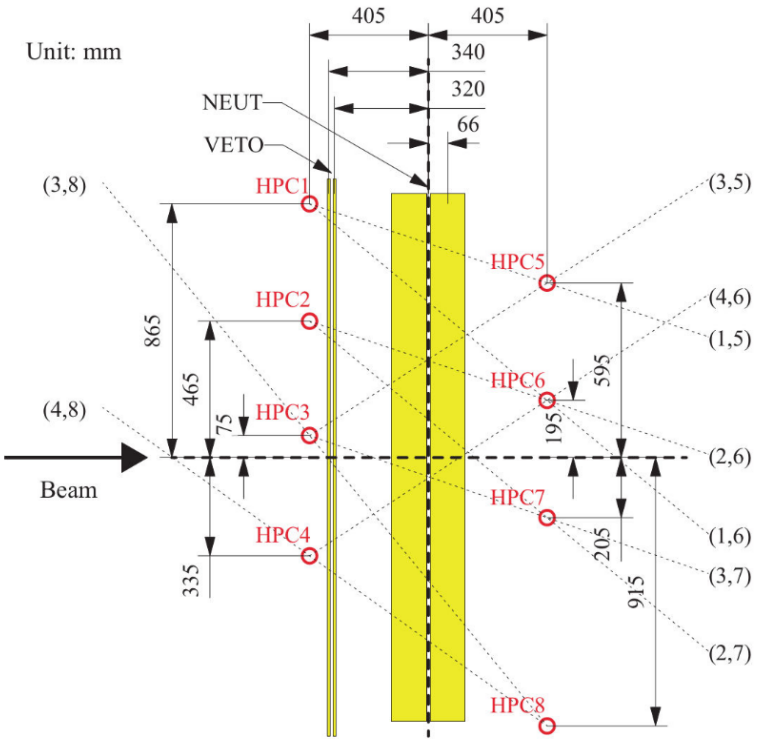

Figure A.7: *Schematic view of the position of the HPC around NEBULA (figure taken from Ref. [5]).*

(vertical) bars.

Time of flight calibration

Like all the other plastic detectors used in the experiment, the individual time for each bar of NEBULA or NEULAND is determined using the arithmetic average of the times measured at its extremity. Moreover, since the start of the ToF is given by the SBT, it is necessary to subtract the time taken by the beam to cover the SBT-Target distance from the measured time. The ToF calibration is based on a simple principle: the photons travel at the speed of light. Indeed, when we look at a ToF spectrum of NEBULA or NEULAND (see Fig. A.8), we observe two structures. A first one very narrow and a second one wider arriving a bit later. The first structure corresponds to γ-rays produced when the beam interacts with the target while the second structure corresponds to neutrons produced in the target that travel at approximately the beam velocity and arrive therefore later at the detector.

In order to calibrate the ToF of the neutrons for each bar, the peak corresponding to the γ-rays is fitted by a Gaussian. Then knowing the Target-bar distance and the speed of light, a shift is applied to the measured times so that the peak becomes centered on the theoretical value. The result of this calibration is presented in Fig. A.9. We can also check that the trigger times are following each other in the right order, meaning that the time needed to reach each wall is consistent with its distance from the target. The IDs for which no ToF is shown in the figure corresponds to the horizontal bars located on the top and bottom of NeuLAND, for which the trajectory of the neutrons are cut by the exit window of SAMURAI.

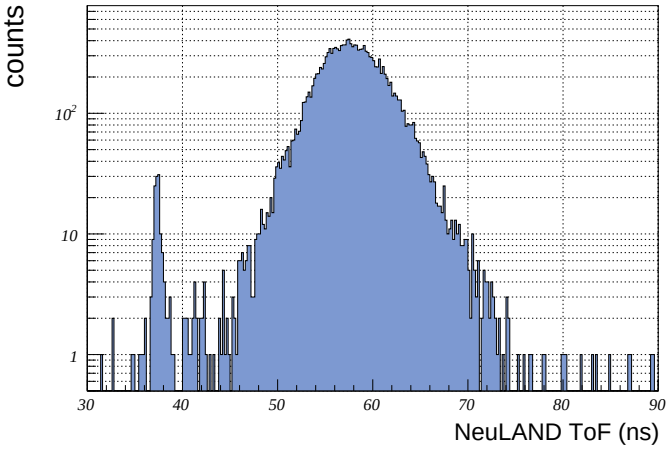

Figure A.8: *Distribution of the measured time in the bar number 315 of NeuLAND.*

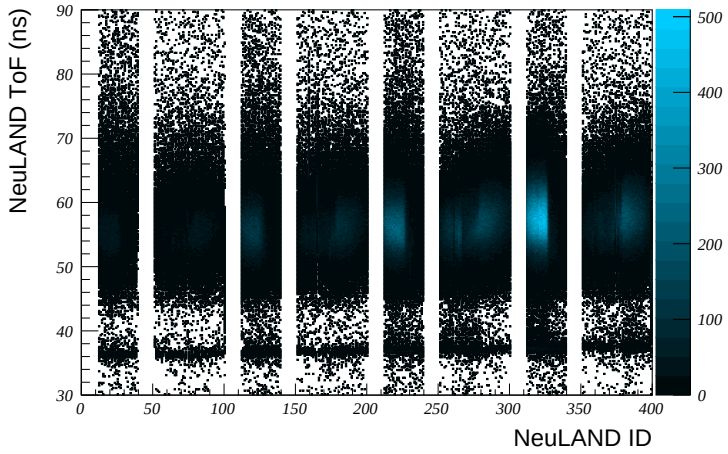

Figure A.9: *ToF of the measured particles in NeuLAND as a function of the bar ID.*

Energy calibration

We saw in the previous section that the energy of the neutrons is deduced from the ToF measurement. Indeed, the energy deposited in the detector is not proportional to the energy of the incoming neutron. However it is necessary to calibrate the energy deposited in order to discriminate neutrons from background γ-rays (arriving outside the prompt peak). Since the energy deposited is not proportional to the incident energy, it has to be less than the incident energy. However, the γ-rays produced from the decay of an excited state in exotic nuclei do not exceed a few MeV while the neutrons can have an energy close from the one of the beam. In order to get rid of the events from γ-rays, it has been chosen to take into account only particles that deposited at least 6 MeV. This cut allows to remove 80% of the photons while keeping 90% of the neutrons.

The charge calibration of the neutron detector has been performed using two points for which the energy deposited is known: the pedestal and the cosmic muons. Once these measurements are done, we perform a linear fit. The pedestal corresponds to an energy equal to 0 and the cosmic muons deposit around 29.9 MeV in each bar for NEBULA.

A.6 Fragment-n alignment

The relative energy is the central observable in our study. The determination of all the members of the relative-energy equation has already been discussed. However, since those members are reconstructed from different detectors, it is important to align the different parts of the experimental setup and especially the neutron and fragment momenta. Since the determination of the neutron momentum is performed without ambiguity, it is chosen as a reference. The alignment process consists in modifying the velocity of the fragment within a very small range. All the observables affected by this shift of velocity are then calculated again and in particular:

- the relative energy: E_{rel}
- the velocity difference between the neutron and the fragment: $\beta_n - \beta_f$
- the parallel momentum of the neutron in the fragment rest frame: $P_z^f(n)$

We then plot the evolution of the average of those three observables as a function of the velocity shift $\Delta\beta_f$ applied. The average of the relative energy evolution follows a second order polynomial which minimum corresponds to the best alignment (see Fig. A.10), while $< \beta_n - \beta_f >$ and $< P_z^f(n) >$ have a linear evolution with $\Delta\beta_f$ and are equal to 0 when fragments and neutrons are aligned. The $\Delta\beta_f$ value has been chosen in our analysis as the average of the ones obtained using the three methods. This procedure is very important because only a slight shift can have a strong effect on the measured relative energy.

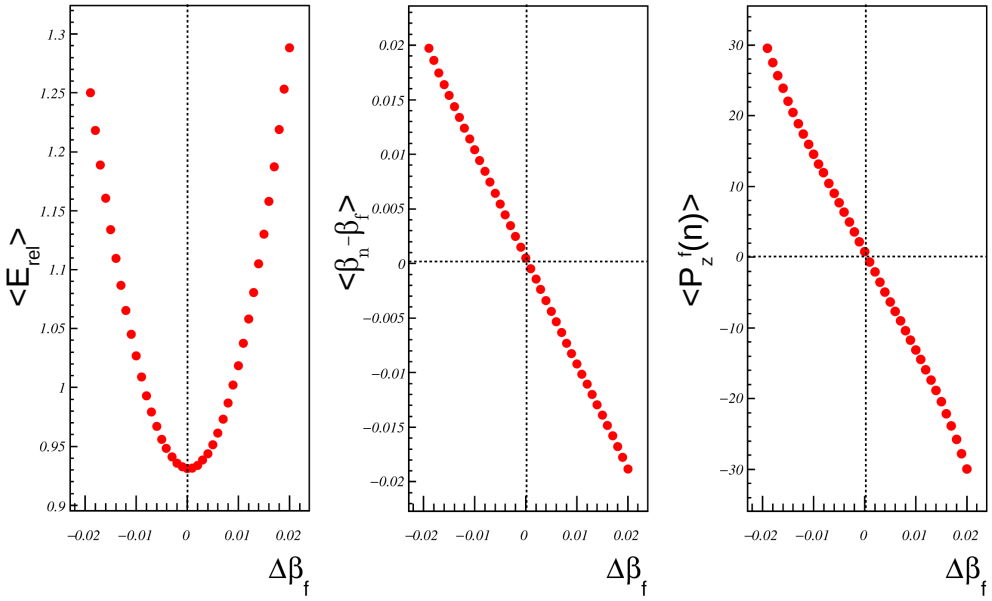

Figure A.10: *Fragment-n alignment procedure for the $^{29}F \rightarrow {}^{27}F+n$ reaction channel. Each figure represents the evolution of an observable as a function of the fragment velocity shift $\Delta\beta_f$.*

A.7 Cross-talk rejection

In the case of a reaction channel that requires the detection of more than one neutron, we discussed already the phenomenon of cross-talk where one neutron can be misidentified as several ones. It is important to try to suppress the events due to that phenomenon as much as we can. To do so, we apply several conditions on the events measured in the neutron detectors.

The procedure is made in several steps. In the first step, we determine a space-time area around a hit in which it is most likely that another hit occurring in that area is originated by the same neutron. This space-time area is tuned using a decay channel in which only one neutron is emitted and therefore all multiple hits observed correspond to cross-talk events (see Fig. A.11).

The next step is to compare the remaining hits and remove those in which the virtual velocity needed for a neutron to reach them from an earlier hit is lower than the velocity of that neutron determined from its ToF (also known as causality condition, see Ref. [118]).

Once those two steps have been performed, most of the cross-talk events are rejected (Fig. 5.24).

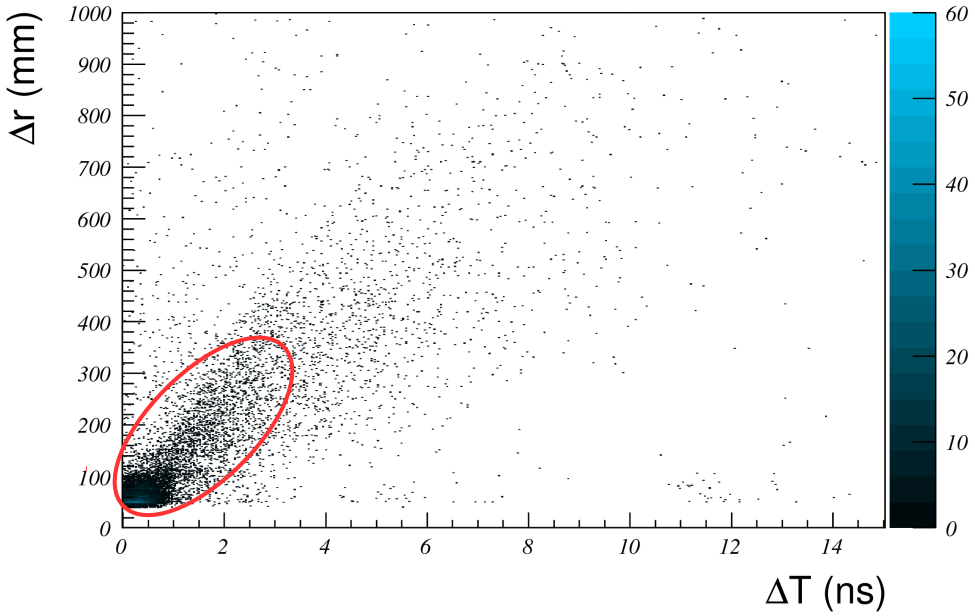

Figure A.11: *Space-time distribution of the hits detected for the* $^{29}Ne \rightarrow {}^{27}F+n$ *reaction channel. The events in the red area are considered as pure cross-talk events.*

Appendix B

Eikonal-model calculations

B.1 Introduction

Direct reaction model calculations are described here for the fast neutron removal reactions from ^{29}F and ^{27}F on a proton target at 221 and 204 MeV/nucleon, respectively, and for proton removal from ^{29}Ne at 210 MeV/nucleon. Calculations use the eikonal (forward scattering) and sudden approximations to the collision dynamics [119]. The valence neutrons are weakly bound in the neutron-rich fluorine isotopes. For n removal from ^{29}F the residual nucleus is particle unbound and $S_{2n}(^{29}\text{F})$=1.443(654) MeV with respect to the ground state of ^{27}F. According to the 2016 mass evaluation [120], the ^{28}F ground state is unbound with respect to ^{27}F+n decay with $S_n(^{28}\text{F})$=−220(50) keV. For n removal from ^{27}F, $S_n(^{27}\text{F})$=1.270(405) MeV and $S_n(^{26}\text{F})$=0.757(147) MeV [120]. On the other hand, the valence protons are very well-bound in ^{29}Ne, with $S_p(^{29}\text{Ne})$=22.631 MeV.

Exclusive n-removal cross sections and their momentum distributions are computed for the ^{28}F and ^{26}F final state energies, for different assumed orbitals occupied by the removed neutrons. The proton removal calculations are carried out assuming removal from *sd*-shell orbitals.

B.2 Formalism and parameters

B.2.1 The nucleon-nucleon system

For such inverse-kinematics reactions on a proton target, the eikonal model S-matrices entering the nucleon-removal cross-sections describe the flux loss of the forward traveling residual nuclei and the removed nucleon due to scattering and/or absorption. This is the result of their two-body interactions with the proton target. At the energies of interest here there is no absorption in the nucleon-nucleon (NN) system and the NN interactions (i.e. of the removed neutron or proton with the target proton) are entirely elastic. The NN S-matrix will be denoted $S_{jp}(b)$ where the label j denotes the species of the removed nucleon, i.e. $j = n, p$. This NN scattering operator, a function of the NN impact parameter, b, is conventionally written [121] as:

$$S_{jp}(b) = 1 - \Gamma_{jp}(b) \tag{B.1}$$

where Γ_{jp} in the np or pp profile function. This is determined by the two-dimensional (2D) Fourier transform of the NN scattering amplitude $f_{jp}(q)$, from:

$$\Gamma_{jp}(b) = \frac{1}{2i\pi k} \int d^2q \; e^{-iq\cdot b} \; f_{jp}(q) \tag{B.2}$$

where the integral is over all momentum transfer components q in the plane perpendicular to the beam direction (the usual z-axis). Thus, the inverse transform gives:

$$f_{jp}(q) = \frac{ik}{2\pi} \int d^2b \; e^{iq\cdot b} \; \Gamma_{jp}(b) \tag{B.3}$$

The NN profile functions of Eq. B.2 are parameterized, in the usual notation [121], as:

$$\Gamma_{jp}(b) = \frac{\sigma_{jp}}{2i} \; (i + \alpha_{jp}) \; g_2(\beta_{jp}, b) \tag{B.4}$$

where $g_2(\beta, b)$ is a normalized 2D Gaussian form factor:

$$g_2(\beta, b) = \frac{1}{2\pi\beta} \; exp(-b^2/2\beta) \tag{B.5}$$

representing the finite-range form factor of the NN interaction. Thus, from Eq. B.3:

$$f_{jp}(q) = \frac{k}{4\pi} \; \sigma_{jp} \; (i + \alpha_{jp}) \; exp(-\beta_{jp} q^2/2) \tag{B.6}$$

As is now evident from the optical theorem identity, namely:

$$\text{Im.}f(0^\circ) = \text{Im.}f(q = 0) = \frac{k}{4\pi}\sigma_{tot}, \tag{B.7}$$

the σ_{jp} in Eq. B.6 are the np and pp total cross sections. These were calculated here from the Charagi and Gupta parameterization [122] of the experimental NN data, giving, respectively for the three energies of 204, 210 and 221 MeV/nucleon, σ_{pp}=2.1561, 2.1595 and 2.1708 fm^2, and σ_{np}=3.9886, 3.9291 and 3.8646 fm^2.

As it is also clear from Eq. B.6, the parameters α_{jp} are the ratios of the real to the imaginary parts of the NN forward-scattering amplitudes, $f_{jp}(q = 0)$, while the β_{jp} determine the ranges of the Gaussian NN interaction (Gaussian range $\gamma_{jp} = \sqrt{2\beta_{jp}}$). These α_{jp} are computed to be, respectively for the three energies of 204, 210 and 221 MeV/nucleon, α_{np}=0.660, 0.638 and 0.598 and α_{pp}=1.161, 1.130 and 1.075, values interpolated from the published tabulation (on the interval 100-1000 MeV) of Ref. [123].

For the NN range parameters, β_{jp}, following e.g. Ref. [124], these are chosen such that the calculated NN total and total elastic cross sections derived from the S-matrices are equal, since the energies of current interest are below the pion production threshold and there is no inelasticity in the NN system. Explicitly, given the form of Eq. B.4, this requires that:

$$\beta_{jp} = \frac{\sigma_{jp}(1 + \alpha_{jp}^2)}{16\pi} \tag{B.8}$$

Calculations show that there is very little sensitivity of the calculated removal single-particle cross sections to the details of these assumed α_{jp} parameter choices, and to their corresponding derived β_{jp} ranges.

B.2.2 The nucleon-residue system

The remaining reaction inputs are the eikonal S-matrices that describe the effects of the interactions of the ^{26,28}F core/residual nuclei with the proton target. These are calculated within the optical limit of the Glauber multiple-scattering theory, also called the $t\rho$ folding approximation to the proton-residue optical potential. These potentials include the size and asymmetry of the nuclei through the point-neutron and proton densities of the residues (r). The proton-residual-nucleus optical potential used is:

$$\mathcal{U}_{pr}(R) = \sum_{j=n,p} \int dr\ \rho_r^{(j)}(r)\ t_{jp}(|R+r|) \tag{B.9}$$

Here, the NN effective interaction, t_{jp}, consistent with the NN S-matrix discussion above is:

$$t_{jp}(r) = -\frac{\hbar v}{2}\ \sigma_{jp}(i+\alpha_{jp})\ g_3(\beta_{jp}, r) \tag{B.10}$$

where the parameters σ_{jp} and α_{jp} are as discussed in the previous sections. Here v is the residual nucleus-proton target relative velocity and $g_3(\beta, r)$ is a normalized 3D Gaussian function with range parameter β.

The n and p one-body densities of the reaction residues, $\rho_r^{(j)}$, are computed using the spherical Hartree-Fock (HF) calculations with the Skyrme SkX interaction [125]. Such calculations have been shown to provide a very good global description of the root mean squared (rms) sizes [126] and radial forms of the matter and charge [127] distributions of both stable and asymmetric nuclei. In the case of reactions populating ^{28}F residues the physical nucleus is unbound whereas the HF ground state is weakly bound. The HF density is taken to provide a reasonable description of the spatial localization of the 28-nucleon system (in ^{29}F and ^{29}Ne) during the short duration of the interaction (a few times 10^{-23} seconds) with the target.

B.2.3 The bound nucleon overlaps

The geometries of the neutron bound-state potentials, that generate the normalized single-particle overlaps of the removed nucleons in the ^{27,29}F projectiles, are also constrained by Skyrme SkX interaction HF calculations. As is discussed in some detail in Ref. [128], for consistency with the range of the residue-proton optical potentials, that is determined by the $\rho_r^{(j)}$, the bound states potential geometry is adjusted to reproduce the separation energy and the rms radius of the single-particle orbital as calculated using the HF. This gives Wood-Saxon binding potential geometries with reduced radius and diffuseness parameters $(r_0, a_0) = (r_0, 0.7)$: a Thomas-form spin-orbit potential with a depth of 6 MeV and the same geometry parameters is added. The radii r_0, constrained as stated above (for full details see section III of Ref. [128]) are, respectively for ^{29}F and ^{27}F of 1.2401 and 1.2297 fm ($\nu 1d_{3/2}$), 1.2045 and 1.1966 fm ($nu1d_{5/2}$), 1.1222 and 1.0875 fm ($\nu 2s_{1/2}$) for the neutron (ν) orbitals. The lowest pf-shell orbitals are unbound in the spherical HF calculation and r_0 values 1.25 fm were assumed for the $\nu 1f_{7/2}$ and $\nu 2p_{3/2}$ orbitals. Similarly for the proton orbits in ^{29}Ne, removal calculations are performed for removal from the $\pi 1d_{3/2}$, $\pi 1d_{5/2}$ and $\pi 2s_{1/2}$ orbitals, with deduced reduced radii r_0 of 1.3915, 1.3471 and 1.2707 fm, respectively.

B.3 Reaction and calculations

The single-particle and theoretical neutron-removal cross sections to ^{28}F and ^{26}F final states (all with C^2S=1) are calculated assuming, in each case, removal from the $\nu 1d_{3/2}$, $\nu 1d_{5/2}$, $\nu 2s_{1/2}$, $\nu 1f_{7/2}$ and $\nu 2p_{3/2}$ orbitals. The shapes of the momentum distributions in each case are also calculated, all normalized to an integrated cross section of 1 mb. For unbound, mass $A-1$ final states, assuming an isotropic disintegration of the system into $(A-2)+n$, the mass $A-2$ residue momentum distribution has an additional broadening to the calculated $A-1$ momentum distribution, requiring its convolution with a rectangular distribution, see e.g. Ref. [129]. The proton removal calculations to ^{28}F final states are similarly performed.

The inelastic breakup (or stripping) contribution to the removal cross sections, the result of inelastic interactions of the removed nucleon and the target, and that usually dominates in reactions on light nuclear targets such as ^{9}Be and ^{12}C, is absent in the case of the proton target. Thus, all of the calculated removal cross sections result from the elastic breakup (or diffraction dissociation) component of the removal cross section, for details see e.g. Ref. [119]. Before being compared to experimental results, the calculated momentum distributions have been convoluted with the response of the experimental setup in order to account for the different experimental resolutions.

Bibliography

[1] A. Bohr and B.R. Mottelson. *Nuclear Structure: Single-particle motion.* Nuclear Structure. W. A. Benjamin, 1969.

[2] O. Sorlin. *Shell closure, magic and exotic nuclei.* EJC2009, 2009.

[3] M. Vandebrouck, A. Lepailleur, O. Sorlin, T. Aumann, C. Caesar, M. Holl, V. Panin, F. Wamers, S. R. Stroberg, J. D. Holt, F. de Oliveira Santos, H. Alvarez-Pol, L. Atar, V. Avdeichikov, S. Beceiro-Novo, D. Bemmerer, J. Benlliure, C. A. Bertulani, S. K. Bogner, J. M. Boillos, K. Boretzky, M. J. G. Borge, M. Caamaño, E. Casarejos, W. Catford, J. Cederkäll, M. Chartier, L. Chulkov, D. Cortina-Gil, E. Cravo, R. Crespo, U. Datta Pramanik, P. Díaz Fernández, I. Dillmann, Z. Elekes, J. Enders, O. Ershova, A. Estradé, F. Farinon, L. M. Fraile, M. Freer, D. Galaviz, H. Geissel, R. Gernhäuser, J. Gibelin, P. Golubev, K. Göbel, J. Hagdahl, T. Heftrich, M. Heil, M. Heine, A. Heinz, A. Henriques, H. Hergert, A. Hufnagel, A. Ignatov, H. T. Johansson, B. Jonson, J. Kahlbow, N. Kalantar-Nayestanaki, R. Kanungo, A. Kelic-Heil, A. Knyazev, T. Kröll, N. Kurz, M. Labiche, C. Langer, T. Le Bleis, R. Lemmon, S. Lindberg, J. Machado, J. Marganiec, F. M. Marqués, A. Movsesyan, E. Nacher, M. Najafi, E. Nikolskii, T. Nilsson, C. Nociforo, S. Paschalis, A. Perea, M. Petri, S. Pietri, R. Plag, R. Reifarth, G. Ribeiro, C. Rigollet, M. Röder, D. Rossi, D. Savran, H. Scheit, A. Schwenk, H. Simon, I. Syndikus, J. T. Taylor, O. Tengblad, R. Thies, Y. Togano, P. Velho, V. Volkov, A. Wagner, H. Weick, C. Wheldon, G. Wilson, J. S. Winfield, P. Woods, D. Yakorev, M. Zhukov, A. Zilges, and K. Zuber. Effective proton-neutron interaction near the drip line from unbound states in ^{25,26}F. *Phys. Rev. C*, 96:054305, Nov 2017.

[4] G. Christian, N. Frank, S. Ash, T. Baumann, D. Bazin, J. Brown, P. A. DeYoung, J. E. Finck, A. Gade, G. F. Grinyer, A. Grovom, J. D. Hinnefeld, E. M. Lunderberg, B. Luther, M. Mosby, S. Mosby, T. Nagi, G. F. Peaslee, W. F. Rogers, J. K. Smith, J. Snyder, A. Spyrou, M. J. Strongman, M. Thoennessen, M. Warren, D. Weisshaar, and A. Wersal. Exploring the low-z shore of the island of inversion at $n = 19$. *Phys. Rev. Lett.*, 108:032501, Jan 2012.

[5] Quentin Deshayes. *Nitrogen isotopes beyond the neutron drip line : 23N, 24N et 25N.* Theses, Normandie Université, December 2017.

[6] Christoph Langer. *Coulomb dissociation of 31Cl and 32Ar - constraining the rp process.* PhD thesis, 2012.

[7] F. M. Marqués, M. Labiche, N. A. Orr, J. C. Angélique, L. Axelsson, B. Benoit, U. C. Bergmann, M. J. G. Borge, W. N. Catford, S. P. G. Chappell, N. M. Clarke, G. Costa,

N. Curtis, A. D'Arrigo, E. de Góes Brennand, F. de Oliveira Santos, O. Dorvaux, G. Fazio, M. Freer, B. R. Fulton, G. Giardina, S. Grévy, D. Guillemaud-Mueller, F. Hanappe, B. Heusch, B. Jonson, C. Le Brun, S. Leenhardt, M. Lewitowicz, M. J. López, K. Markenroth, A. C. Mueller, T. Nilsson, A. Ninane, G. Nyman, I. Piqueras, K. Riisager, M. G. Saint Laurent, F. Sarazin, S. M. Singer, O. Sorlin, and L. Stuttgé. Three-body correlations in borromean halo nuclei. *Phys. Rev. C*, 64:061301, Nov 2001.

[8] N. Colonna, D. R. Bowman, L. Celano, G. D'Erasmo, E. M. Fiore, L. Fiore, A. Pantaleo, V. Paticchio, G. Tagliente, and S. Pratt. Measurement of compound nucleus space-time extent with two-neutron correlation functions. *Phys. Rev. Lett.*, 75:4190–4193, Dec 1995.

[9] Zs. Vajta, M. Stanoiu, D. Sohler, G. R. Jansen, F. Azaiez, Zs. Dombrádi, O. Sorlin, B. A. Brown, M. Belleguic, C. Borcea, C. Bourgeois, Z. Dlouhy, Z. Elekes, Zs. Fülöp, S. Grévy, D. Guillemaud-Mueller, G. Hagen, M. Hjorth-Jensen, F. Ibrahim, A. Kerek, A. Krasznahorkay, M. Lewitowicz, S. M. Lukyanov, S. Mandal, P. Mayet, J. Mrázek, F. Negoita, Yu.-E. Penionzhkevich, Zs. Podolyák, P. Roussel-Chomaz, M. G. Saint-Laurent, H. Savajols, G. Sletten, J. Timár, C. Timis, and A. Yamamoto. Excited states in the neutron-rich nucleus ^{25}F. *Phys. Rev. C*, 89:054323, May 2014.

[10] K.S. Krane. *Introductory Nuclear Physics*. Wiley, 1987.

[11] Isao Tanihata. Reactions with radioactive ion beams. *Nuclear Physics A*, 654(1):C235 – C251, 1999. Proceedings of the International Nuclear Physics Conference.

[12] C. Cohen-Tannoudji, B. Diu, and F. Laloë. *Mecanique quantique*. Number vol. 2 in Collection Enseignement des sciences. Hermann, 1973.

[13] F. Halzen and A.D. Martin. *Quarks and leptons: an introductory course in modern particle physics*. Wiley, 1984.

[14] Maria G. Mayer. On closed shells in nuclei. *Phys. Rev.*, 74:235–239, Aug 1948.

[15] R. Kanungo, C. Nociforo, A. Prochazka, T. Aumann, D. Boutin, D. Cortina-Gil, B. Davids, M. Diakaki, F. Farinon, H. Geissel, R. Gernhäuser, J. Gerl, R. Janik, B. Jonson, B. Kindler, R. Knöbel, R. Krücken, M. Lantz, H. Lenske, Y. Litvinov, B. Lommel, K. Mahata, P. Maierbeck, A. Musumarra, T. Nilsson, T. Otsuka, C. Perro, C. Scheidenberger, B. Sitar, P. Strmen, B. Sun, I. Szarka, I. Tanihata, Y. Utsuno, H. Weick, and M. Winkler. One-neutron removal measurement reveals ^{24}**O** as a new doubly magic nucleus. *Phys. Rev. Lett.*, 102:152501, Apr 2009.

[16] K. Tshoo, Y. Satou, H. Bhang, S. Choi, T. Nakamura, Y. Kondo, S. Deguchi, Y. Kawada, N. Kobayashi, Y. Nakayama, K. N. Tanaka, N. Tanaka, N. Aoi, M. Ishihara, T. Motobayashi, H. Otsu, H. Sakurai, S. Takeuchi, Y. Togano, K. Yoneda, Z. H. Li, F. Delaunay, J. Gibelin, F. M. Marqués, N. A. Orr, T. Honda, M. Matsushita, T. Kobayashi, Y. Miyashita, T. Sumikama, K. Yoshinaga, S. Shimoura, D. Sohler, T. Zheng, and Z. X. Cao. $n = 16$ spherical shell closure in ^{24}**O**. *Phys. Rev. Lett.*, 109:022501, Jul 2012.

[17] Y. Kondo, T. Nakamura, R. Tanaka, R. Minakata, S. Ogoshi, N. A. Orr, N. L. Achouri, T. Aumann, H. Baba, F. Delaunay, P. Doornenbal, N. Fukuda, J. Gibelin, J. W. Hwang, N. Inabe, T. Isobe, D. Kameda, D. Kanno, S. Kim, N. Kobayashi, T. Kobayashi, T. Kubo,

S. Leblond, J. Lee, F. M. Marqués, T. Motobayashi, D. Murai, T. Murakami, K. Muto, T. Nakashima, N. Nakatsuka, A. Navin, S. Nishi, H. Otsu, H. Sato, Y. Satou, Y. Shimizu, H. Suzuki, K. Takahashi, H. Takeda, S. Takeuchi, Y. Togano, A. G. Tuff, M. Vandebrouck, and K. Yoneda. Nucleus ^{26}O: A barely unbound system beyond the drip line. *Phys. Rev. Lett.*, 116:102503, Mar 2016.

[18] Elliot Warburton, JA Becker, and BA Brown. Mass systematics for a =29-44 nuclei: The deformed a≈32 region. 41:1147–1166, 04 1990.

[19] B. Alex Brown and W. A. Richter. Magic numbers in the neutron-rich oxygen isotopes. *Phys. Rev. C*, 72:057301, Nov 2005.

[20] Takaharu Otsuka, Toshio Suzuki, Jason D. Holt, Achim Schwenk, and Yoshinori Akaishi. Three-body forces and the limit of oxygen isotopes. *Phys. Rev. Lett.*, 105:032501, Jul 2010.

[21] Richard H. Stokes and P. G. Young. New isotope of helium: ^{7}He. *Phys. Rev. Lett.*, 18:611–613, Apr 1967.

[22] A. Messiah. *Mécanique quantique*. Number vol. 1 in Mécanique quantique. Dunod, 1959.

[23] C.J. Joachain. *Quantum collision theory*. North-Holland, 1975.

[24] K.W. McVoy. Virtual states and resonances. *Nuclear Physics A*, 115(3):481 – 494, 1968.

[25] M. Thoennessen, S. Yokoyama, A. Azhari, T. Baumann, J. A. Brown, A. Galonsky, P. G. Hansen, J. H. Kelley, R. A. Kryger, E. Ramakrishnan, and P. Thirolf. Population of ^{10}Li by fragmentation. *Phys. Rev. C*, 59:111–117, Jan 1999.

[26] Ricardo A Broglia and Vladimir Zelevinsky. *Fifty Years of Nuclear BCS*. WORLD SCIENTIFIC, 2013.

[27] W von Oertzen and A Vitturi. Pairing correlations of nucleons and multi-nucleon transfer between heavy nuclei. *Reports on Progress in Physics*, 64(10):1247, 2001.

[28] D. Montanari, L. Corradi, S. Szilner, G. Pollarolo, E. Fioretto, G. Montagnoli, F. Scarlassara, A. M. Stefanini, S. Courtin, A. Goasduff, F. Haas, D. Jelavic, C. Michelagnoli, T. Mijatović, N. Soić, C. A. Ur, and M. Varga Pajtler. Neutron pair transfer in ^{60}Ni+^{116}Sn far below the coulomb barrier. *Phys. Rev. Lett.*, 113:052501, Jul 2014.

[29] A.B. Migdal. Superfluidity and the moments of inertia of nuclei. *Nuclear Physics*, 13(5):655 – 674, 1959.

[30] B.R. Mottelson. Nobel lecture: Elementary modes of excitation in the nucleus. 1975.

[31] K. Hagino, H. Sagawa, J. Carbonell, and P. Schuck. Coexistence of bcs- and bec-like pair structures in halo nuclei. *Phys. Rev. Lett.*, 99:022506, Jul 2007.

[32] K. Hagino, N. Takahashi, and H. Sagawa. Strong dineutron correlation in ^{8}He and ^{18}C. *Phys. Rev. C*, 77:054317, May 2008.

[33] J. Bardeen, L. N. Cooper, and J. R. Schrieffer. Microscopic theory of superconductivity. *Phys. Rev.*, 106:162–164, Apr 1957.

[34] F. London. The λ-phenomenon of liquid helium and the bose-einstein degeneracy. *Nature*, 141:643, Dec 1938.

[35] D. J. Dean and M. Hjorth-Jensen. Pairing in nuclear systems: from neutron stars to finite nuclei. *Rev. Mod. Phys.*, 75:607–656, Apr 2003.

[36] K. Kisamori, S. Shimoura, H. Miya, S. Michimasa, S. Ota, M. Assie, H. Baba, T. Baba, D. Beaumel, M. Dozono, T. Fujii, N. Fukuda, S. Go, F. Hammache, E. Ideguchi, N. Inabe, M. Itoh, D. Kameda, S. Kawase, T. Kawabata, M. Kobayashi, Y. Kondo, T. Kubo, Y. Kubota, M. Kurata-Nishimura, C. S. Lee, Y. Maeda, H. Matsubara, K. Miki, T. Nishi, S. Noji, S. Sakaguchi, H. Sakai, Y. Sasamoto, M. Sasano, H. Sato, Y. Shimizu, A. Stolz, H. Suzuki, M. Takaki, H. Takeda, S. Takeuchi, A. Tamii, L. Tang, H. Tokieda, M. Tsumura, T. Uesaka, K. Yako, Y. Yanagisawa, R. Yokoyama, and K. Yoshida. Candidate resonant tetraneutron state populated by the ^{4}He(^{8}He,^{8}Be) reaction. *Phys. Rev. Lett.*, 116:052501, Feb 2016.

[37] F. M. Marqués, M. Labiche, N. A. Orr, J. C. Angélique, L. Axelsson, B. Benoit, U. C. Bergmann, M. J. G. Borge, W. N. Catford, S. P. G. Chappell, N. M. Clarke, G. Costa, N. Curtis, A. D'Arrigo, E. de Góes Brennand, F. de Oliveira Santos, O. Dorvaux, G. Fazio, M. Freer, B. R. Fulton, G. Giardina, S. Grévy, D. Guillemaud-Mueller, F. Hanappe, B. Heusch, B. Jonson, C. Le Brun, S. Leenhardt, M. Lewitowicz, M. J. López, K. Markenroth, A. C. Mueller, T. Nilsson, A. Ninane, G. Nyman, I. Piqueras, K. Riisager, M. G. Saint Laurent, F. Sarazin, S. M. Singer, O. Sorlin, and L. Stuttgé. Detection of neutron clusters. *Phys. Rev. C*, 65:044006, Apr 2002.

[38] N. Orr. Viewpoint: Can four neutrons tango? *Physics*, 9:14, Feb 2016.

[39] Carlos Bertulani and Vladimir Zelevinsky. Nuclear physics: Four neutrons together momentarily. 532, 04 2016.

[40] Alain Coc, Jean-Philippe Uzan, and Elisabeth Vangioni. Mirror matter can alleviate the cosmological lithium problem. *Phys. Rev. D*, 87:123530, Jun 2013.

[41] Kiyomi Ikeda, Noboru Takigawa, and Hisashi Horiuchi. The systematic structure-change into the molecule-like structures in the self-conjugate 4n nuclei. *Progress of Theoretical Physics Supplement*, E68:464–475, 1968.

[42] Jacek Okolowicz, Marek Ploszajczak, and Witold Nazarewicz. On the origin of nuclear clustering. *Progress of Theoretical Physics Supplement*, 196:230–243, 2012.

[43] Bertram Blank and Marek Ploszajczak. Two-proton radioactivity. *Reports on Progress in Physics*, 71(4):046301, 2008.

[44] M. Pfützner, M. Karny, L. V. Grigorenko, and K. Riisager. Radioactive decays at limits of nuclear stability. *Rev. Mod. Phys.*, 84:567–619, Apr 2012.

[45] B. Blank, M. Chartier, S. Czajkowski, J. Giovinazzo, M. S. Pravikoff, J.-C. Thomas, G. de France, F. de Oliveira Santos, M. Lewitowicz, C. Borcea, R. Grzywacz, Z. Janas, and M. Pfützner. Discovery of doubly magic ^{48}Ni. *Phys. Rev. Lett.*, 84:1116–1119, Feb 2000.

[46] J. Giovinazzo, B. Blank, C. Borcea, G. Canchel, J.-C. Dalouzy, C. E. Demonchy, F. de Oliveira Santos, C. Dossat, S. Grévy, L. Hay, J. Huikari, S. Leblanc, I. Matea, J.-L. Pedroza, L. Perrot, J. Pibernat, L. Serani, C. Stodel, and J.-C. Thomas. First direct observation of two protons in the decay of ^{45}Fe with a time-projection chamber. *Phys. Rev. Lett.*, 99:102501, Sep 2007.

[47] V.I. Goldansky. On neutron-deficient isotopes of light nuclei and the phenomena of proton and two-proton radioactivity. *Nuclear Physics*, 19:482 – 495, 1960.

[48] K. Miernik, W. Dominik, Z. Janas, M. Pfützner, L. Grigorenko, C. R. Bingham, H. Czyrkowski, M. Ćwiok, I. G. Darby, R. Dabrowski, T. Ginter, R. Grzywacz, M. Karny, A. Korgul, W. Kuśmierz, S. N. Liddick, M. Rajabali, K. Rykaczewski, and A. Stolz. Two-proton correlations in the decay of ^{45}Fe. *Phys. Rev. Lett.*, 99:192501, Nov 2007.

[49] P. Ascher, L. Audirac, N. Adimi, B. Blank, C. Borcea, B. A. Brown, I. Companis, F. Delalee, C. E. Demonchy, F. de Oliveira Santos, J. Giovinazzo, S. Grévy, L. V. Grigorenko, T. Kurtukian-Nieto, S. Leblanc, J.-L. Pedroza, L. Perrot, J. Pibernat, L. Serani, P. C. Srivastava, and J.-C. Thomas. Direct observation of two protons in the decay of ^{54}Zn. *Phys. Rev. Lett.*, 107:102502, Sep 2011.

[50] I. A. Egorova, R. J. Charity, L. V. Grigorenko, Z. Chajecki, D. Coupland, J. M. Elson, T. K. Ghosh, M. E. Howard, H. Iwasaki, M. Kilburn, Jenny Lee, W. G. Lynch, J. Manfredi, S. T. Marley, A. Sanetullaev, R. Shane, D. V. Shetty, L. G. Sobotka, M. B. Tsang, J. Winkelbauer, A. H. Wuosmaa, M. Youngs, and M. V. Zhukov. Democratic decay of ^{6}Be exposed by correlations. *Phys. Rev. Lett.*, 109:202502, Nov 2012.

[51] A. Azhari, R. A. Kryger, and M. Thoennessen. Decay of the ^{12}O ground state. *Phys. Rev. C*, 58:2568–2570, Oct 1998.

[52] F. Wamers, J. Marganiec, F. Aksouh, Yu. Aksyutina, H. Álvarez-Pol, T. Aumann, S. Beceiro-Novo, K. Boretzky, M. J. G. Borge, M. Chartier, A. Chatillon, L. V. Chulkov, D. Cortina-Gil, H. Emling, O. Ershova, L. M. Fraile, H. O. U. Fynbo, D. Galaviz, H. Geissel, M. Heil, D. H. H. Hoffmann, H. T. Johansson, B. Jonson, C. Karagiannis, O. A. Kiselev, J. V. Kratz, R. Kulessa, N. Kurz, C. Langer, M. Lantz, T. Le Bleis, R. Lemmon, Yu. A. Litvinov, K. Mahata, C. Müntz, T. Nilsson, C. Nociforo, G. Nyman, W. Ott, V. Panin, S. Paschalis, A. Perea, R. Plag, R. Reifarth, A. Richter, C. Rodriguez-Tajes, D. Rossi, K. Riisager, D. Savran, G. Schrieder, H. Simon, J. Stroth, K. Sümmerer, O. Tengblad, H. Weick, C. Wimmer, and M. V. Zhukov. First observation of the unbound nucleus ^{15}Ne. *Phys. Rev. Lett.*, 112:132502, Apr 2014.

[53] I. Mukha, L. Grigorenko, K. Sümmerer, L. Acosta, M. A. G. Alvarez, E. Casarejos, A. Chatillon, D. Cortina-Gil, J. M. Espino, A. Fomichev, J. E. García-Ramos, H. Geissel, J. Gómez-Camacho, J. Hofmann, O. Kiselev, A. Korsheninnikov, N. Kurz, Yu. Litvinov, I. Martel, C. Nociforo, W. Ott, M. Pfützner, C. Rodríguez-Tajes, E. Roeckl, M. Stanoiu,

H. Weick, and P. J. Woods. Proton-proton correlations observed in two-proton decay of ^{19}Mg and ^{16}Ne. *Phys. Rev. C*, 77:061303, Jun 2008.

[54] H.T. Johansson, Yu. Aksyutina, T. Aumann, K. Boretzky, M.J.G. Borge, A. Chatillon, L.V. Chulkov, D. Cortina-Gil, U. Datta Pramanik, H. Emling, C. ForssÃ©n, H.O.U. Fynbo, H. Geissel, G. Ickert, B. Jonson, R. Kulessa, C. Langer, M. Lantz, T. LeBleis, K. Mahata, M. Meister, G. MÃ¼nzenberg, T. Nilsson, G. Nyman, R. Palit, S. Paschalis, W. Prokopowicz, R. Reifarth, A. Richter, K. Riisager, G. Schrieder, N.B. Shulgina, H. Simon, K. SÃ¼mmerer, O. Tengblad, H. Weick, and M.V. Zhukov. Three-body correlations in the decay of 10he and 13li. *Nuclear Physics A*, 847(1):66 – 88, 2010.

[55] Z. Kohley, E. Lunderberg, P. A. DeYoung, A. Volya, T. Baumann, D. Bazin, G. Christian, N. L. Cooper, N. Frank, A. Gade, C. Hall, J. Hinnefeld, B. Luther, S. Mosby, W. A. Peters, J. K. Smith, J. Snyder, A. Spyrou, and M. Thoennessen. First observation of the ^{13}li ground state. *Phys. Rev. C*, 87:011304, Jan 2013.

[56] A. Spyrou, Z. Kohley, T. Baumann, D. Bazin, B. A. Brown, G. Christian, P. A. DeYoung, J. E. Finck, N. Frank, E. Lunderberg, S. Mosby, W. A. Peters, A. Schiller, J. K. Smith, J. Snyder, M. J. Strongman, M. Thoennessen, and A. Volya. First observation of ground state dineutron decay: ^{16}Be. *Phys. Rev. Lett.*, 108:102501, Mar 2012.

[57] E. Lunderberg, P. A. DeYoung, Z. Kohley, H. Attanayake, T. Baumann, D. Bazin, G. Christian, D. Divaratne, S. M. Grimes, A. Haagsma, J. E. Finck, N. Frank, B. Luther, S. Mosby, T. Nagi, G. F. Peaslee, A. Schiller, J. Snyder, A. Spyrou, M. J. Strongman, and M. Thoennessen. Evidence for the ground-state resonance of ^{26}**O**. *Phys. Rev. Lett.*, 108:142503, Apr 2012.

[58] C. Caesar, J. Simonis, T. Adachi, Y. Aksyutina, J. Alcantara, S. Altstadt, H. Alvarez-Pol, N. Ashwood, T. Aumann, V. Avdeichikov, M. Barr, S. Beceiro, D. Bemmerer, J. Benlliure, C. A. Bertulani, K. Boretzky, M. J. G. Borge, G. Burgunder, M. Caamano, E. Casarejos, W. Catford, J. Cederkäll, S. Chakraborty, M. Chartier, L. Chulkov, D. Cortina-Gil, U. Datta Pramanik, P. Diaz Fernandez, I. Dillmann, Z. Elekes, J. Enders, O. Ershova, A. Estrade, F. Farinon, L. M. Fraile, M. Freer, M. Freudenberger, H. O. U. Fynbo, D. Galaviz, H. Geissel, R. Gernhäuser, P. Golubev, D. Gonzalez Diaz, J. Hagdahl, T. Heftrich, M. Heil, M. Heine, A. Heinz, A. Henriques, M. Holl, J. D. Holt, G. Ickert, A. Ignatov, B. Jakobsson, H. T. Johansson, B. Jonson, N. Kalantar-Nayestanaki, R. Kanungo, A. Kelic-Heil, R. Knöbel, T. Kröll, R. Krücken, J. Kurcewicz, M. Labiche, C. Langer, T. Le Bleis, R. Lemmon, O. Lepyoshkina, S. Lindberg, J. Machado, J. Marganiec, V. Maroussov, J. Menéndez, M. Mostazo, A. Movsesyan, A. Najafi, T. Nilsson, C. Nociforo, V. Panin, A. Perea, S. Pietri, R. Plag, A. Prochazka, A. Rahaman, G. Rastrepina, R. Reifarth, G. Ribeiro, M. V. Ricciardi, C. Rigollet, K. Riisager, M. Röder, D. Rossi, J. Sanchez del Rio, D. Savran, H. Scheit, A. Schwenk, H. Simon, O. Sorlin, V. Stoica, B. Streicher, J. Taylor, O. Tengblad, S. Terashima, R. Thies, Y. Togano, E. Uberseder, J. Van de Walle, P. Velho, V. Volkov, A. Wagner, F. Wamers, H. Weick, M. Weigand, C. Wheldon, G. Wilson, C. Wimmer, J. S. Winfield, P. Woods, D. Yakorev, M. V. Zhukov, A. Zilges, M. Zoric, and K. Zuber. Beyond the neutron drip line: The unbound oxygen isotopes ^{25}o and ^{26}o. *Phys. Rev. C*, 88:034313, Sep 2013.

[59] B. Laurent and F. M. Marqués. Chronology of the three-body dissociation of ^{8}He. 2018.

[60] Yu. Aksyutina, T. Aumann, K. Boretzky, M. J. G. Borge, C. Caesar, A. Chatillon, L. V. Chulkov, D. Cortina-Gil, U. Datta Pramanik, H. Emling, H. O. U. Fynbo, H. Geissel, A. Heinz, G. Ickert, H. T. Johansson, B. Jonson, R. Kulessa, C. Langer, T. LeBleis, K. Mahata, G. Münzenberg, T. Nilsson, G. Nyman, R. Palit, S. Paschalis, W. Prokopowicz, R. Reifarth, D. Rossi, A. Richter, K. Riisager, G. Schrieder, H. Simon, K. Sümmerer, O. Tengblad, R. Thies, H. Weick, and M. V. Zhukov. Study of the ^{14}Be continuum: Identification and structure of its second 2^+ state. *Phys. Rev. Lett.*, 111:242501, Dec 2013.

[61] C. R. Hoffman, T. Baumann, J. Brown, P. A. DeYoung, J. E. Finck, N. Frank, J. D. Hinnefeld, S. Mosby, W. A. Peters, W. F. Rogers, A. Schiller, J. Snyder, A. Spyrou, S. L. Tabor, and M. Thoennessen. Observation of a two-neutron cascade from a resonance in ^{24}O. *Phys. Rev. C*, 83:031303, Mar 2011.

[62] M. D. Jones, N. Frank, T. Baumann, J. Brett, J. Bullaro, P. A. DeYoung, J. E. Finck, K. Hammerton, J. Hinnefeld, Z. Kohley, A. N. Kuchera, J. Pereira, A. Rabeh, W. F. Rogers, J. K. Smith, A. Spyrou, S. L. Stephenson, K. Stiefel, M. Tuttle-Timm, R. G. T. Zegers, and M. Thoennessen. Two-neutron sequential decay of ^{24}O. *Phys. Rev. C*, 92:051306, Nov 2015.

[63] F. M. Marqués, N. A. Orr, N. L. Achouri, F. Delaunay, and J. Gibelin. Comment on "first observation of ground state dineutron decay: ^{16}Be". *Phys. Rev. Lett.*, 109:239201, Dec 2012.

[64] F. de Grancey, A. Mercenne, F. de Oliveira Santos, T. Davinson, O. Sorlin, J.C. Angélique, M. AssiÃ©, E. Berthoumieux, R. Borcea, A. Buta, I. Celikovic, V. Chudoba, J.M. Daugas, G. Dumitru, M. Fadil, S. Grévy, J. Kiener, A. Lefebvre-Schuhl, N. Michel, J. Mrazek, F. Negoita, J. Okolowicz, D. Pantelica, M.G. Pellegriti, L. Perrot, M. Ploszajczak, G. Randisi, I. Ray, O. Roig, F. Rotaru, M.G. Saint Laurent, N. Smirnova, M. Stanoiu, I. Stefan, C. Stodel, K. Subotic, V. Tatischeff, J.C. Thomas, P. Ujic, and R. Wolski. An above-barrier narrow resonance in 15f. *Physics Letters B*, 758:26 – 31, 2016.

[65] G. Audi, O. Bersillon, J. Blachot, and A.H. Wapstra. The nubase evaluation of nuclear and decay properties. *Nuclear Physics A*, 729(1):3 – 128, 2003. The 2003 NUBASE and Atomic Mass Evaluations.

[66] C. R. Hoffman, T. Baumann, D. Bazin, J. Brown, G. Christian, P. A. DeYoung, J. E. Finck, N. Frank, J. Hinnefeld, R. Howes, P. Mears, E. Mosby, S. Mosby, J. Reith, B. Rizzo, W. F. Rogers, G. Peaslee, W. A. Peters, A. Schiller, M. J. Scott, S. L. Tabor, M. Thoennessen, P. J. Voss, and T. Williams. Determination of the $n = 16$ shell closure at the oxygen drip line. *Phys. Rev. Lett.*, 100:152502, Apr 2008.

[67] C.R. Hoffman, T. Baumann, D. Bazin, J. Brown, G. Christian, D.H. Denby, P.A. DeYoung, J.E. Finck, N. Frank, J. Hinnefeld, S. Mosby, W.A. Peters, W.F. Rogers, A. Schiller, A. Spyrou, M.J. Scott, S.L. Tabor, M. Thoennessen, and P. Voss. Evidence for a doubly magic 24o. *Physics Letters B*, 672(1):17 – 21, 2009.

[68] A. Lepailleur, O. Sorlin, L. Caceres, B. Bastin, C. Borcea, R. Borcea, B. A. Brown, L. Gaudefroy, S. Grévy, G. F. Grinyer, G. Hagen, M. Hjorth-Jensen, G. R. Jansen, O. Llidoo, F. Negoita, F. de Oliveira, M.-G. Porquet, F. Rotaru, M.-G. Saint-Laurent, D. Sohler, M. Stanoiu, and J. C. Thomas. Spectroscopy of ^{26}**F** to probe proton-neutron forces close to the drip line. *Phys. Rev. Lett.*, 110:082502, Feb 2013.

[69] M. Stanoiu, D. Sohler, O. Sorlin, Zs. Dombrádi, F. Azaiez, B. A. Brown, C. Borcea, C. Bourgeois, Z. Elekes, Zs. Fülöp, S. Grévy, D. Guillemaud-Mueller, F. Ibrahim, A. Kerek, A. Krasznahorkay, M. Lewitowicz, S. M. Lukyanov, J. Mrázek, F. Negoita, Yu.-E. Penionzhkevich, Zs. Podolyák, M. G. Porquet, P. Roussel-Chomaz, M. G. Saint-Laurent, H. Savajols, G. Sletten, J. Timár, and C. Timis. Spectroscopy of ^{26}f. *Phys. Rev. C*, 85:017303, Jan 2012.

[70] B. Jurado, H. Savajols, W. Mittig, N.A. Orr, P. Roussel-Chomaz, D. Baiborodin, W.N. Catford, M. Chartier, C.E. Demonchy, Z. DlouhÃ$\frac{1}{2}$, A. Gillibert, L. Giot, A. Khouaja, A. LÃ©pine-Szily, S. Lukyanov, J. Mrazek, Y.E. Penionzhkevich, S. Pita, M. Rousseau, and A.C. Villari. Mass measurements of neutron-rich nuclei near the n=20 and 28 shell closures. *Physics Letters B*, 649(1):43 – 48, 2007.

[71] A. T. Reed, O. Tarasov, R. D. Page, D. Guillemaud-Mueller, Yu. E. Penionzhkevich, R. G. Allatt, J. C. Angélique, R. Anne, C. Borcea, V. Burjan, W. N. Catford, Z. Dlouhý, C. Donzaud, S. Grévy, M. Lewitowicz, S. M. Lukyanov, F. M. Marqués, G. Martinez, A. C. Mueller, P. J. Nolan, J. Novák, N. A. Orr, F. Pougheon, P. H. Regan, M. G. Saint-Laurent, T. Siiskonen, E. Sokol, O. Sorlin, J. Suhonen, W. Trinder, and S. M. Vincent. Radioactivity of neutron-rich oxygen, fluorine, and neon isotopes. *Phys. Rev. C*, 60:024311, Jul 1999.

[72] C. Thibault, R. Klapisch, C. Rigaud, A. M. Poskanzer, R. Prieels, L. Lessard, and W. Reisdorf. Direct measurement of the masses of ^{11}Li and $^{26-32}$Na with an on-line mass spectrometer. *Phys. Rev. C*, 12:644–657, Aug 1975.

[73] C. Détraz, D. Guillemaud, G. Huber, R. Klapisch, M. Langevin, F. Naulin, C. Thibault, L. C. Carraz, and F. Touchard. Beta decay of $^{27-32}$Na and their descendants. *Phys. Rev. C*, 19:164–176, Jan 1979.

[74] D. Guillemaud-Mueller, C. Detraz, M. Langevin, F. Naulin, M. de Saint-Simon, C. Thibault, F. Touchard, and M. Epherre. β-decay schemes of very neutron-rich sodium isotopes and their descendants. *Nuclear Physics A*, 426(1):37 – 76, 1984.

[75] Takaharu Otsuka, Rintaro Fujimoto, Yutaka Utsuno, B. Alex Brown, Michio Honma, and Takahiro Mizusaki. Magic numbers in exotic nuclei and spin-isospin properties of the *NN* interaction. *Phys. Rev. Lett.*, 87:082502, Aug 2001.

[76] Takaharu Otsuka, Toshio Suzuki, Rintaro Fujimoto, Hubert Grawe, and Yoshinori Akaishi. Evolution of nuclear shells due to the tensor force. *Phys. Rev. Lett.*, 95:232502, Nov 2005.

[77] Takaharu Otsuka, Toshiaki Matsuo, and Daisuke Abe. Mean field with tensor force and shell structure of exotic nuclei. *Phys. Rev. Lett.*, 97:162501, Oct 2006.

[78] Yutaka Utsuno, Takaharu Otsuka, Thomas Glasmacher, Takahiro Mizusaki, and Michio Honma. Onset of intruder ground state in exotic Na isotopes and evolution of the $n = 20$ shell gap. *Phys. Rev. C*, 70:044307, Oct 2004.

[79] A. Poves and J. Retamosa. The onset of deformation at the n = 20 neutron shell closure far from stability. *Physics Letters B*, 184(4):311 – 315, 1987.

[80] E. Caurier, F. Nowacki, and A. Poves. Large-scale shell model calculations for exotic nuclei. *The European Physical Journal A - Hadrons and Nuclei*, 15(1):145–150, Sep 2002.

[81] Alexandra Gade and Thomas Glasmacher. In-beam nuclear spectroscopy of bound states with fast exotic ion beams. *Progress in Particle and Nuclear Physics*, 60(1):161 – 224, 2008.

[82] Z. Elekes, Zs. Dombradi, A. Saito, N. Aoi, H. Baba, K. Demichi, Zs. Fulop, J. Gibelin, T. Gomi, H. Hasegawa, N. Imai, M. Ishihara, H. Iwasaki, S. Kanno, S. Kawai, T. Kishida, T. Kubo, K. Kurita, Y. Matsuyama, S. Michimasa, T. Minemura, T. Motobayashi, M. Notani, T. Ohnishi, H.J. Ong, S. Ota, A. Ozawa, H.K. Sakai, H. Sakurai, S. Shimoura, E. Takeshita, S. Takeuchi, M. Tamaki, Y. Togano, K. Yamada, Y. Yanagisawa, and K. Yoneda. Bound excited states in 27f. *Physics Letters B*, 599(1):17 – 22, 2004.

[83] David H. Boal, Claus-Konrad Gelbke, and Byron K. Jennings. Intensity interferometry in subatomic physics. *Rev. Mod. Phys.*, 62:553–602, Jul 1990.

[84] Donald H. Perkins. *Introduction to High Energy Physics*. Cambridge University Press, 4 edition, 2000.

[85] M. Nikolić. *Kinematics and multiparticle systems*. Documents on modern physics. Gordon and Breach, 1968.

[86] E. M. Aitala, S. Amato, J. C. Anjos, J. A. Appel, D. Ashery, S. Banerjee, I. Bediaga, G. Blaylock, S. B. Bracker, P. R. Burchat, R. A. Burnstein, T. Carter, H. S. Carvalho, N. K. Copty, L. M. Cremaldi, C. Darling, K. Denisenko, S. Devmal, A. Fernandez, G. F. Fox, P. Gagnon, C. Gobel, K. Gounder, A. M. Halling, G. Herrera, G. Hurvits, C. James, P. A. Kasper, S. Kwan, D. C. Langs, J. Leslie, B. Lundberg, J. Magnin, A. Massafferri, S. MayTal-Beck, B. Meadows, J. R. T. de Mello Neto, D. Mihalcea, R. H. Milburn, J. M. de Miranda, A. Napier, A. Nguyen, A. B. d'Oliveira, K. O'Shaughnessy, K. C. Peng, L. P. Perera, M. V. Purohit, B. Quinn, S. Radeztsky, A. Rafatian, N. W. Reay, J. J. Reidy, A. C. dos Reis, H. A. Rubin, D. A. Sanders, A. K. S. Santha, A. F. S. Santoro, A. J. Schwartz, M. Sheaff, R. A. Sidwell, A. J. Slaughter, M. D. Sokoloff, J. Solano, N. R. Stanton, R. J. Stefanski, K. Stenson, D. J. Summers, S. Takach, K. Thorne, A. K. Tripathi, S. Watanabe, R. Weiss-Babai, J. Wiener, N. Witchey, E. Wolin, S. M. Yang, D. Yi, S. Yoshida, R. Zaliznyak, and C. Zhang. Experimental evidence for a light and broad scalar resonance in $d^+ \to \pi^-\pi^+\pi^+$ decay. *Phys. Rev. Lett.*, 86:770–774, Jan 2001.

[87] R. J. Charity, J. M. Elson, J. Manfredi, R. Shane, L. G. Sobotka, B. A. Brown, Z. Chajecki, D. Coupland, H. Iwasaki, M. Kilburn, Jenny Lee, W. G. Lynch, A. Sanetullaev, M. B. Tsang, J. Winkelbauer, M. Youngs, S. T. Marley, D. V. Shetty, A. H. Wuosmaa, T. K. Ghosh, and M. E. Howard. Investigations of three-, four-, and five-particle decay

channels of levels in light nuclei created using a ^{9}C beam. *Phys. Rev. C*, 84:014320, Jul 2011.

[88] R. Hanbury Brown and R.Q. Twiss. Lxxiv. a new type of interferometer for use in radio astronomy. *The London, Edinburgh, and Dublin Philosophical Magazine and Journal of Science*, 45(366):663–682, 1954.

[89] G.I. Kopylov. Like particle correlations as a tool to study the multiple production mechanism. *Physics Letters B*, 50(4):472 – 474, 1974.

[90] F. M. Marqués et al. Two-neutron interferometry as a probe of the nuclear halo. *Phys. Lett.*, B476:219–225, 2000.

[91] R. Lednicky and V. L. Lyuboshits. Final State Interaction Effect on Pairing Correlations Between Particles with Small Relative Momenta. *Sov. J. Nucl. Phys.*, 35:770, 1982. [Yad. Fiz.35,1316(1981)].

[92] G. Normand. *Investigation of correlations in light neutron-rich nuclei*. Theses, Université de Caen, October 2004.

[93] J.K. Smith, T. Baumann, D. Bazin, J. Brown, P.A. DeYoung, N. Frank, M.D. Jones, Z. Kohley, B. Luther, B. Marks, A. Spyrou, S.L. Stephenson, M. Thoennessen, and A. Volya. Neutron correlations in the decay of the first excited state of 11li. *Nuclear Physics A*, 955:27 – 40, 2016.

[94] T Baumann, A Spyrou, and M Thoennessen. Nuclear structure experiments along the neutron drip line. *Reports on Progress in Physics*, 75(3):036301, 2012.

[95] H. Geissel, P. Armbruster, K.H. Behr, A. BrÃ¼nle, K. Burkard, M. Chen, H. Folger, B. Franczak, H. Keller, O. Klepper, B. Langenbeck, F. Nickel, E. Pfeng, M. PfÃ¼tzner, E. Roeckl, K. Rykaczewski, I. Schall, D. Schardt, C. Scheidenberger, K.-H. Schmidt, A. Schroter, T. Schwab, K. Summerer, M. Weber, G. Munzenberg, T. Brohm, H.-G. Clerc, M. Fauerbach, J.-J. Gaimard, A. Grewe, E. Hanelt, B. Knodler, M. Steiner, B. Voss, J. Weckenmann, C. Ziegler, A. Magel, H. Wollnik, J.P. Dufour, Y. Fujita, D.J. Vieira, and B. Sherrill. The gsi projectile fragment separator (frs): a versatile magnetic system for relativistic heavy ions. *Nuclear Instruments and Methods in Physics Research Section B: Beam Interactions with Materials and Atoms*, 70(1):286 – 297, 1992.

[96] K. Mahata, H.T. Johansson, S. Paschalis, H. Simon, and T. Aumann. Position reconstruction in large-area scintillating fibre detectors. *Nuclear Instruments and Methods in Physics Research Section A: Accelerators, Spectrometers, Detectors and Associated Equipment*, 608(2):331 – 335, 2009.

[97] J. Cub, G. Stengel, A Grunschloss, K Boretzky, T Aumann, W Dostal, B Eberlein, Th.W Elze, H Emling, G Ickert, J Holeczek, R Holzmann, J.V Kratz, R Kulessa, Y Leifels, H Simon, K Stelzer, J Stroth, A Surowiec, and E Wajda. A large-area scintillating fibre detector for relativistic heavy ions. *Nuclear Instruments and Methods in Physics Research Section A: Accelerators, Spectrometers, Detectors and Associated Equipment*, 402(1):67 – 74, 1998.

[98] Th. Blaich, Th.W. Elze, H. Emling, H. Freiesleben, K. Grimm, W. Henning, R. Holzmann, G. Ickert, J.G. Keller, H. Klingler, W. Kneissl, R. Konig, R. Kulessa, J.V. Kratz, D. Lambrecht, J.S. Lange, Y. Leifels, E. Lubkiewicz, M. Proft, W. Prokopowicz, C. SchÃ¼tter, R. Schmidt, H. Spies, K. Stelzer, J. Stroth, W. Walus, E. Wajda, H.J. Wollersheim, M. Zinser, and E. Zude. A large area detector for high-energy neutrons. *Nuclear Instruments and Methods in Physics Research Section A: Accelerators, Spectrometers, Detectors and Associated Equipment*, 314(1):136 – 154, 1992.

[99] P. Pawlowski, J. Brzychczyk, Y. Leifels, W. Trautmann, P. Adrich, T. Aumann, C.O. Bacri, T. Barczyk, R. Bassini, S. Bianchin, C. Boiano, K. Boretzky, A. Boudard, A. Chbihi, J. Cibor, B. Czech, M. De Napoli, J.-E. Ducret, H. Emling, J.D. Frankland, T. Gorbinet, M. Hellstrom, D. Henzlova, S. Hlavac, J. ImmÃ¨, I. Iori, H. Johansson, K. Kezzar, S. Kupny, A. Lafriakh, A. Le FÃ¨vre, E. Le Gentil, S. Leray, J. Lukasik, J. LÃ¼hning, W.G. Lynch, U. Lynen, Z. Majka, M. Mocko, W.F.J. MÃ¼ller, A. Mykulyak, H. Orth, A.N. Otte, R. Palit, S. Panebianco, A. Pullia, G. Raciti, E. Rapisarda, D. Rossi, M.-D. Salsac, H. Sann, C. Schwarz, H. Simon, C. Sfienti, K. SÃ¼mmerer, M.B. Tsang, G. Verde, M. Veselsky, C. Volant, M. Wallace, H. Weick, J. Wiechula, A. Wieloch, and B. Zwieglinski. Neutron recognition in the land detector for large neutron multiplicity. *Nuclear Instruments and Methods in Physics Research Section A: Accelerators, Spectrometers, Detectors and Associated Equipment*, 694:47 – 54, 2012.

[100] T. Kubo, M. Ishihara, N. Inabe, H. Kumagai, I. Tanihata, K. Yoshida, T. Nakamura, H. Okuno, S. Shimoura, and K. Asahi. The riken radioactive beam facility. *Nuclear Instruments and Methods in Physics Research Section B: Beam Interactions with Materials and Atoms*, 70(1):309 – 319, 1992.

[101] H. Okuno, N. Fukunishi, and O. Kamigaito. Progress of ribf accelerators. *Progress of Theoretical and Experimental Physics*, 2012(1):03C002, 2012.

[102] Clémentine Santamaria. *Quest for new nuclear magic numbers with MINOS*. Theses, Université Paris Sud - Paris XI, September 2015.

[103] A. Obertelli, A. Delbart, S. Anvar, L. Audirac, G. Authelet, H. Baba, B. Bruyneel, D. Calvet, F. Château, A. Corsi, P. Doornenbal, J. M. Gheller, A. Giganon, C. Lahonde-Hamdoun, D. Leboeuf, D. Loiseau, A. Mohamed, J. Ph. Mols, H. Otsu, C. Péron, A. Peyaud, E. C. Pollacco, G. Prono, J. Y. Rousse, C. Santamaria, and T. Uesaka. Minos: A vertex tracker coupled to a thick liquid-hydrogen target for in-beam spectroscopy of exotic nuclei. *The European Physical Journal A*, 50(1):8, Jan 2014.

[104] Y. Shimizu, H. Otsu, T. Kobayashi, T. Kubo, T. Motobayashi, H. Sato, and K. Yoneda. Vacuum system for the samurai spectrometer. *Nuclear Instruments and Methods in Physics Research Section B: Beam Interactions with Materials and Atoms*, 317:739 – 742, 2013. XVIth International Conference on ElectroMagnetic Isotope Separators and Techniques Related to their Applications, December 2-7, 2012 at Matsue, Japan.

[105] T. Kobayashi, N. Chiga, T. Isobe, Y. Kondo, T. Kubo, K. Kusaka, T. Motobayashi, T. Nakamura, J. Ohnishi, H. Okuno, H. Otsu, T. Sako, H. Sato, Y. Shimizu, K. Sekiguchi, K. Takahashi, R. Tanaka, and K. Yoneda. Samurai spectrometer for ri beam experiments. *Nuclear Instruments and Methods in Physics Research Section B: Beam Interactions with*

Materials and Atoms, 317:294 – 304, 2013. XVIth International Conference on Electro-Magnetic Isotope Separators and Techniques Related to their Applications, December, 2012 at Matsue, Japan.

[106] S. Agostinelli et al. Geant4-a simulation toolkit. *Nuclear Instruments and Methods in Physics Research Section A: Accelerators, Spectrometers, Detectors and Associated Equipment*, 506(3):250 – 303, 2003.

[107] J. Allison et al. Geant4 developments and applications. *IEEE Transactions on Nuclear Science*, 53(1):270–278, Feb 2006.

[108] S. Takeuchi, T. Motobayashi, Y. Togano, M. Matsushita, N. Aoi, K. Demichi, H. Hasegawa, and H. Murakami. Dali2: A nai(tl) detector array for measurements of γ-rays from fast nuclei. *Nuclear Instruments and Methods in Physics Research Section A: Accelerators, Spectrometers, Detectors and Associated Equipment*, 763:596 – 603, 2014.

[109] William H. Press, Brian P. Flannery, Saul A. Teukolsky, and William T. Vetterling. *Numerical Recipes in C: The Art of Scientific Computing*. Cambridge University Press, New York, NY, USA, 1988.

[110] M. Stanoiu, D. Sohler, O. Sorlin, F. Azaiez, Zs. Dombrádi, B. A. Brown, M. Belleguic, C. Borcea, C. Bourgeois, Z. Dlouhy, Z. Elekes, Zs. Fülöp, S. Grévy, D. Guillemaud-Mueller, F. Ibrahim, A. Kerek, A. Krasznahorkay, M. Lewitowicz, S. M. Lukyanov, S. Mandal, J. Mrázek, F. Negoita, Yu.-E. Penionzhkevich, Zs. Podolyák, P. Roussel-Chomaz, M. G. Saint-Laurent, H. Savajols, G. Sletten, J. Timár, C. Timis, and A. Yamamoto. Disappearance of the $n = 14$ shell gap in the carbon isotopic chain. *Phys. Rev. C*, 78:034315, Sep 2008.

[111] T. Aumann, C. A. Bertulani, and J. Ryckebusch. Quasifree (p,2p) and (p,pn) reactions with unstable nuclei. *Phys. Rev. C*, 88:064610, Dec 2013.

[112] D.R. Tilley, H.R. Weller, and C.M. Cheves. Energy levels of light nuclei a = 16-17. *Nuclear Physics A*, 564(1):1 – 183, 1993.

[113] J.W. Hwang, S. Kim, Y. Satou, N.A. Orr, Y. Kondo, T. Nakamura, J. Gibelin, N.L. Achouri, T. Aumann, H. Baba, F. Delaunay, P. Doornenbal, N. Fukuda, N. Inabe, T. Isobe, D. Kameda, D. Kanno, N. Kobayashi, T. Kobayashi, T. Kubo, S. Leblond, J. Lee, F.M. Marqués, R. Minakata, T. Motobayashi, D. Murai, T. Murakami, K. Muto, T. Nakashima, N. Nakatsuka, A. Navin, S. Nishi, S. Ogoshi, H. Otsu, H. Sato, Y. Shimizu, H. Suzuki, K. Takahashi, H. Takeda, S. Takeuchi, R. Tanaka, Y. Togano, A.G. Tuff, M. Vandebrouck, and K. Yoneda. Single-neutron knockout from 20c and the structure of 19c. *Physics Letters B*, 769:503 – 508, 2017.

[114] P. Doornenbal, H. Scheit, S. Takeuchi, Y. Utsuno, N. Aoi, K. Li, M. Matsushita, D. Steppenbeck, H. Wang, H. Baba, E. Ideguchi, N. Kobayashi, Y. Kondo, J. Lee, S. Michimasa, T. Motobayashi, T. Otsuka, H. Sakurai, M. Takechi, Y. Togano, and K. Yoneda. Low-z shore of the "island of inversion" and the reduced neutron magicity toward ^{28}O. *Phys. Rev. C*, 95:041301, Apr 2017.

[115] L. V. Grigorenko, J. S. Vaagen, and M. V. Zhukov. Exploring the manifestation and nature of a dineutron in two-neutron emission using a dynamical dineutron model. *Phys. Rev. C*, 97:034605, Mar 2018.

[116] T. Sugimoto, T. Nakamura, Y. Kondo, N. Aoi, H. Baba, D. Bazin, N. Fukuda, T. Gomi, H. Hasegawa, N. Imai, M. Ishihara, T. Kobayashi, T. Kubo, M. Miura, T. Motobayashi, H. Otsu, A. Saito, H. Sakurai, S. Shimoura, A.M. Vinodkumar, K. Watanabe, Y.X. Watanabe, T. Yakushiji, Y. Yanagisawa, and K. Yoneda. The first 2+ state of 14be. *Physics Letters B*, 654(5):160 – 164, 2007.

[117] Oleg Tarasov and D Bazin. Lise++: Radioactive beam production with in-flight separators. 266:4657–4664, 10 2008.

[118] T. Nakamura and Y. Kondo. Large acceptance spectrometers for invariant mass spectroscopy of exotic nuclei and future developments. *Nuclear Instruments and Methods in Physics Research Section B: Beam Interactions with Materials and Atoms*, 376:156 – 161, 2016. Proceedings of the XVIIth International Conference on Electromagnetic Isotope Separators and Related Topics (EMIS2015), Grand Rapids, MI, U.S.A., 11-15 May 2015.

[119] P.G. Hansen and J.A. Tostevin. Direct reactions with exotic nuclei. *Annual Review of Nuclear and Particle Science*, 53(1):219–261, 2003.

[120] W.J. Huang, G. Audi, Meng Wang, F.G. Kondev, S. Naimi, and Xing Xu. The ame2016 atomic mass evaluation (i). evaluation of input data; and adjustment procedures. *Chinese Physics C*, 41(3):030002, 2017.

[121] J. S. Al-Khalili and J. A. Tostevin. Few-body calculations of proton-^{6,8}He scattering. *Phys. Rev. C*, 57:1846–1852, Apr 1998.

[122] S. K. Charagi and S. K. Gupta. Coulomb-modified glauber model description of heavy-ion reaction cross sections. *Phys. Rev. C*, 41:1610–1618, Apr 1990.

[123] L. Ray. Proton-nucleus total cross sections in the intermediate energy range. *Phys. Rev. C*, 20:1857–1872, Nov 1979.

[124] B. Abu-Ibrahim, W. Horiuchi, A. Kohama, and Y. Suzuki. Reaction cross sections of carbon isotopes incident on a proton. *Phys. Rev. C*, 77:034607, Mar 2008.

[125] B. Alex Brown. New skyrme interaction for normal and exotic nuclei. *Phys. Rev. C*, 58:220–231, Jul 1998.

[126] W. A. Richter and B. A. Brown. Nuclear charge densities with the skyrme hartree-fock method. *Phys. Rev. C*, 67:034317, Mar 2003.

[127] B. A. Brown, S. Typel, and W. A. Richter. Interaction cross sections for light neutron-rich nuclei. *Phys. Rev. C*, 65:014612, Dec 2001.

[128] A. Gade, P. Adrich, D. Bazin, M. D. Bowen, B. A. Brown, C. M. Campbell, J. M. Cook, T. Glasmacher, P. G. Hansen, K. Hosier, S. McDaniel, D. McGlinchery, A. Obertelli, K. Siwek, L. A. Riley, J. A. Tostevin, and D. Weisshaar. Reduction of spectroscopic strength: Weakly-bound and strongly-bound single-particle states studied using one-nucleon knockout reactions. *Phys. Rev. C*, 77:044306, Apr 2008.

[129] N. Kobayashi, T. Nakamura, J. A. Tostevin, Y. Kondo, N. Aoi, H. Baba, S. Deguchi, J. Gibelin, M. Ishihara, Y. Kawada, T. Kubo, T. Motobayashi, T. Ohnishi, N. A. Orr, H. Otsu, H. Sakurai, Y. Satou, E. C. Simpson, T. Sumikama, H. Takeda, M. Takechi, S. Takeuchi, K. N. Tanaka, N. Tanaka, Y. Togano, and K. Yoneda. One- and two-neutron removal reactions from the most neutron-rich carbon isotopes. *Phys. Rev. C*, 86:054604, Nov 2012.

Nuclear forces at the extremes

Résumé

L'émission de paires de neutrons par les noyaux riches en neutrons ^{18}C et ^{20}O (isotones $N = 12$) est étudié par réactions de knock-out d'un nucléon des faisceaux secondaires ^{19}N et ^{21}O, peuplant ainsi des états non liés jusqu'à 15 MeV au-dessus de leur seuil d'émission deux neutrons. L'analyse des corrélations des triples coincidences fragment+n+n montre que la décroissance ^{19}N$(-1p)^{18}$C$^* \rightarrow^{16}$C+n+n est clairement dominée par l'émission directe de paires. Les corrélations n-n, les plus grandes jamais observées, suggèrent la prédominance d'un coeur de ^{14}C entouré de quatre neutrons arrangés en paires très corrélées. De plus, une importante compétition du mode de décroissance séquentiel est observée dans la décroissance ^{21}O$(-1n)^{20}$O$^* \rightarrow^{18}$O+n+n, interprétée par la déformation causée par le knock-out d'un neutron très lié ayant pour effet de casser le coeur de ^{16}O et ainsi de réduire le nombre de paires.

De plus, les états non liés du ^{26}F et ^{28}F sont étudiés. Les deux systèmes étant peuplés par knock-out d'un nucléon du ^{27}F dans le cas du ^{26}F et du ^{29}Ne ou du ^{29}F pour ^{28}F. Cinq états ont été observés pour ^{26}F avec en particulier l'état de plus basse énergie (0.39 MeV) identifié comme l'état 3^+ résultant du couplage $\pi d_{5/2} \otimes \nu d_{3/2}$. Pour ^{28}F, cinq états ont aussi été observés et l'état fondamental (200 keV) a été identifié comme étant de parité négative, plaçant ainsi ^{28}F dans l'îlot d'inversion.

Mots clés: Physique nucléaire, Structure nucléaire, Spectroscopie nucléaire, Réactions directes, Isotopes radioactifs, Analyse de données, Simulation par ordinateur.

Abstract

The emission of neutron pairs from the neutron-rich $N = 12$ isotones ^{18}C and ^{20}O has been studied by high-energy nucleon knockout from ^{19}N and ^{21}O secondary beams, populating unbound states of the two isotones up to 15 MeV above their two-neutron emission thresholds. The analysis of triple fragment-n-n correlations shows that the decay ^{19}N$(-1p)^{18}$C$^* \rightarrow^{16}$C+n+n is clearly dominated by direct pair emission. The two-neutron correlation strength, the largest ever observed, suggests the predominance of a ^{14}C core surrounded by four neutrons arranged in strongly correlated pairs. On the other hand, a significant competition of a sequential branch is found in the decay ^{21}O$(-1n)^{20}$O$^* \rightarrow^{18}$O+n+n, attributed to its formation through the knockout of a deeply-bound neutron that breaks the ^{16}O core and reduces the number of pairs.

Moreover, unbound states in ^{26}F and ^{28}F have been studied. The two systems were probed using single-nucleon knockout reaction from secondary beams of ^{27}F respectively in the case of ^{26}F, and ^{29}Ne and ^{29}F for ^{28}F. Five possible states have been identified in ^{26}F, with in particular the lowest energy one (0.39 MeV) being identified as the 3^+ state resulting from the $\pi d_{5/2} \otimes \nu d_{3/2}$ coupling. In the case of ^{28}F, five unbound state have also been observed and in particular its ground state (200 keV) has been identified as a negative parity state, meaning that ^{28}F is located inside the island of inversion.

Keywords: Nuclear physics, Nuclear structure, Nuclear spectroscopy, Direct reactions, Radioactive isotopes, Data analysis, Computer simulations.